NASA TECHNICAL MEMORANDUM

NASA TM X-3343

NASA TM X-3343

EFFECT OF WING BEND ON THE EXPERIMENTAL FORCE AND MOMENT CHARACTERISTICS OF AN OBLIQUE WING

Edward J. Hopkins and Edgar R. Nelson

Ames Research Center
Moffett Field, Calif. 94035

NATIONAL AERONAUTICS AND SPACE ADMINISTRATION • WASHINGTON, D. C. • MARCH 1976

1. Report No.	2. Government Accession No.	3. Recipient's Catalog No.
NASA TM X-3343		

4. Title and Subtitle	5. Report Date
EFFECT OF WING BEND ON THE EXPERIMENTAL FORCE AND MOMENT CHARACTERISTICS OF AN OBLIQUE WING	March 1976
	6. Performing Organization Code

7. Author(s)	8. Performing Organization Report No.
Edward J. Hopkins and Edgar R. Nelson *	A-6068
	10. Work Unit No.
9. Performing Organization Name and Address	505-06-31
NASA Ames Research Center, Moffett Field, Calif. 94035	11. Contract or Grant No.
	13. Type of Report and Period Covered
12. Sponsoring Agency Name and Address	Technical Memorandum
National Aeronautics and Space Administration Washington, D. C. 20546	14. Sponsoring Agency Code

15. Supplementary Notes

*Project engineer, ARO, Inc., Moffett Field, Calif. 94035

16. Abstract

Static longitudinal and lateral/directional force and moment characteristics are presented for an elliptical oblique wing mounted on top of a Sears-Haack body of revolution. The wing had an aspect ratio of 6 (based on the unswept span) and was tested at various sweep angles relative to the body axis ranging from 0 to 60°. In an attempt to create more symmetrical spanwise wing stalling characteristics, both wing panels were bent upward to produce washout on the trailing wing panel and washin on the leading wing panel. Small fluorescent tufts were attached to the wing surface to indicate the stall progression on the wing. The tests were conducted throughout a Mach number range from 0.6 to 1.4 at a constant unit Reynolds number of 8.2×10^6 per meter.

The test results indicate that upward bending of the wing panels had only a small effect on the linearity of the moment curves and would require an impractical wing-pivot location at low lift to eliminate the rolling moment resulting from this bending.

17. Key Words (Suggested by Author(s))	18. Distribution Statement
Oblique wings, Skewed wings, Asymmetric wings, Static longitudinal stability, Swept wings, Linear theory-matrix-panel method	Unlimited STAR Category 02

19. Security Classif. (of this report)	20. Security Classif. (of this page)	21. No. of Pages	22. Price*
Unclassified	Unclassified	164	$6.25

For sale by the National Technical Information Service, Springfield, Virginia 22161

NOMENCLATURE

The axes systems and sign conventions are presented in figure 1. Lift, drag, and pitching moments are presented in the stability axis coordinate system; side force, rolling moments and yawing moments are presented in both the stability axis and body axis coordinate systems.

b	wing span
c	wing chord
c_{root}	wing root chord
c_{aft}	portion of wing chord aft of the $0.25c$ line
c_{fwd}	portion of wing chord forward of the $0.25c$ line
$\bar{c}$	wing mean aerodynamic chord
C_D	drag coefficient, $\frac{\text{drag}}{qS}$
$C_{D_{min}}$	minimum drag coefficient
C_{l_s}	rolling-moment coefficient about the stability axes, $\frac{\text{rolling moment}}{qSb}$
C_l	rolling-moment coefficient about the body axes, $\frac{\text{rolling moment}}{qSb}$
C_L	lift coefficient, $\frac{\text{lift}}{qS}$
C_{L_α}	lift-curve slope, $\frac{dC_L}{d\alpha}$, per deg
C_m	pitching-moment coefficient (see fig. 2 for moment-center location), $\frac{\text{pitching moment}}{qS\bar{c}}$
C_{m_α}	pitching-moment curve slope at $\alpha = 0$, $\frac{dC_m}{d\alpha}$, per deg
C_{n_s}	yawing-moment coefficient about the stability axes, $\frac{\text{yawing moment}}{qSb}$
C_n	yawing-moment coefficient about the body axes, $\frac{\text{yawing moment}}{qSb}$
C_Y	side-force coefficient about either the stability axes or the body axes, $\frac{\text{side force}}{qS}$
H	vertical distance from wing reference plane to base line (see fig. 3(a))
$\frac{L}{D}$	lift-to-drag ratio
$\left(\frac{L}{D}\right)_{max}$	maximum lift-to-drag ratio
M	Mach number

q	freestream dynamic pressure
r	body radius
S	wing area
$\left(\frac{t}{c}\right)_{max}$	maximum thickness-to-chord ratio
x	chordwise distance along airfoil
x_1	axial distance along body from the 57.47 cm longitudinal station
y	distance along wing span (see fig. 3(a))
z	vertical distance above the horizontal plane containing the airfoil chord at the wing root
α	angle of attack, deg
β	angle of sideslip, deg
Λ	sweep angle measured between a perpendicular to the body axis and the $0.25c$ line of the wing in a horizontal plane (the right wing tip is forward for positive Λ's), deg

EFFECT OF WING BEND ON THE EXPERIMENTAL FORCE AND MOMENT CHARACTERISTICS OF AN OBLIQUE WING

Edward J. Hopkins and Edgar R. Nelson*

Ames Research Center

SUMMARY

Static longitudinal and lateral/directional force and moment characteristics are presented for an elliptical oblique wing mounted on top of a Sears-Haack body of revolution. The wing had an aspect ratio of 6 (based on the unswept span) and was tested at various sweep angles relative to the body axis ranging from 0 to 60°. In an attempt to create more symmetrical spanwise wing stalling characteristics, both wing panels were bent upward to produce washout on the trailing wing panel and washin on the leading wing panel. Small fluorescent tufts were attached to the wing surface to indicate the stall progression on the wing. The tests were conducted throughout a Mach number range from 0.6 to 1.4 at a constant unit Reynolds number of 8.2×10^6 per meter.

The test results indicate that upward bending of the wing panels had only a small effect on the linearity of the moment curves and would require an impractical wing-pivot location at low lift to eliminate the rolling moment resulting from this bending.

INTRODUCTION

Experimental results in reference 1 indicate that a low aspect-ratio oblique wing-body combination (suitable as a highly maneuverable vehicle) with the wing at its optimum sweep angle for a given Mach number has higher lift-to-drag ratios than a conventional sweptback wing-body combination throughout a Mach number range from 0.6 to 1.4. The theoretical analysis made in reference 2 confirms the experimental results. It was found that the amount of spanwise upward bending of the oblique wing (or washout for the trailing wing panel and washin for the leading wing panel) produced initial flow separation on either the rearward or forward wing panel, thereby creating either pitch-up or pitch-down tendencies and nonlinear rolling and yawing moment curves. These results are related to the asymmetric spanwise distribution of local lift coefficient due to an increase in angle of attack associated with oblique wings, the trailing wing panel having the larger lift coefficients. It can be conjectured from the results of reference 2 that an optimum spanwise bend is feasible that will result in more nearly linear moment curves at high angles of attack.

In the present experimental study, therefore, an oblique wing having an upward bend between the two bends used for the oblique wing of reference 1 was investigated throughout a Mach number range from 0.6 to 1.4. Primary emphasis in this study is placed on the flow separation progression

*Project engineer, ARO, Inc., Moffett Field, Calif. 94035

on the wing with angle of attack and its effect on the linearity of the moment curves. The moment curves for the oblique wing of the present investigation (having an intermediate bend) are compared with those of the oblique wing of reference 1 (having a small bend). Lateral/directional characteristics from investigating the oblique wing-body combination in sideslip are also presented.

CONFIGURATION CODE

(Note: The third and fourth numerals designate the amount of sweep (e.g., 3W45B stands for the oblique wing with small bend mounted on the body and swept 45°.)

3W	oblique wing with small bend
5W	oblique wing with intermediate bend
B	body

TEST FACILITY

The Ames 6- by 6-Foot Wind Tunnel is a variable pressure, continuous flow, closed return type facility. The nozzle ahead of the test section consists of an asymmetric sliding block which permits a continuous variation of Mach number from 0.6 to 2.3. The test section has a perforated floor and ceiling for boundary-layer removal to permit transonic testing.

MODEL DESCRIPTION

The model consisted of an oblique wing mounted on top of a Sears-Haack body of revolution designed to have minimum wave drag for a given length and volume. With different fairing blocks, installed under the wing (fig. 2), it could be swept 0, 45°, 50°, 55°, and 60°. Details of the body and of the fairing blocks are given in table 3 of reference 1. Note in figure 2 that the wing pivot point and the moment center are located at 0.40 c_{root} ($\Lambda = 0$). The wing planform consisted of two semiellipses having the same major axis but different minor axes in the ratio of 4:1 so that the major axis is the quarter chord line. Effective *geometric twist* was accomplished by bending the wing panels upward so that the chord lines perpendicular to the quarter chord line remain in horizontal planes. This type of bending is equivalent to wing twist when the oblique wing is swept – that is, washout on the downstream panel and washin on the upstream panel. Figure 3(a) shows the equations for the bend lines of the wing with intermediate bend of the present investigation, and for those of the wing with small bend of reference 1 and the wing planform. Additional geometric wing and body details are presented in table 1.

A subcritical Garabedian profile (designed for a lift coefficient of 1.3 for a maximum $t/c = 0.1016$ at a Mach number of 0.6) was used perpendicular to the quarter chord line. This profile, shown in figure 3(b), varied in maximum thickness from 0.11c at the wing root to 0.06c at the wing tip according to the elliptical equation given in figure 3(a). Coordinates for the Garabedian profile are given in table 2.

DATA REDUCTION AND TEST PROCEDURE

The model was sting supported through the base of the model on a 6-component electrical strain-gage balance as shown in figure 4. Measured drag forces were corrected to a condition corresponding to having the freestream static pressure on the base of the fuselage. Moment data are presented about a center located on the body axis at 0.4 c_{root} ($\Lambda = 0$). See figure 2. Reference lengths and the wing area used in the reduction of the data are given in table 1.

Boundary-layer transition strips (0.1905 cm wide), consisting of a random distribution of 0.01905 cm diam glass spheres, were placed on the upper and lower surface of the wing, 0.762 cm downstream of the leading edge and on the body 2.54 cm behind its tip. Sublimation studies made at wing sweep angles of 0 and 45° indicate that the boundary layer was tripped by the 0.01905 cm diam spheres near the roughness strips at $\alpha = 0$ and 10° at Mach numbers of 0.6 and 0.9. Estimates of the required size of roughness to trip the boundary layer at other sweep angles and higher Mach numbers indicate that the chosen size should be adequate.

Tuft studies were made to indicate the flow-separation progression with angle of attack. Tufts consisting of monofilament fluorescent thread (0.0038 cm diam) about 1.0 cm long were cemented to the wing at spanwise intervals of 1.27 to 2.54 cm. Cameras mounted in the wind tunnel upper plenum chamber and outside the Schlieren window provided a permanent record of the local airflow near the surfaces indicated by the tufts, which were illuminated by blacklights.

The unit Reynolds number was held constant at 8.2×10^6 per meter. For the static longitudinal stability data, the model was mounted on a sting bent 10° to increase the maximum angle of attack, the resulting angle-of-attack range being from −3° to 28°. A limited number of runs were also made with the model inverted with the wing swept 45° so that for these runs the angle-of-attack range was decreased to −28°. Static lateral/directional stability data were obtained throughout a sideslip angle range of −6° to 6° at angles of attack of 0 and 10°. With the wing swept 45°, 50°, 55°, and 60°, data were obtained at Mach numbers of 0.6, 0.7, 0.8, 0.9, 0.95, 1.1, 1.2, and 1.4, but with the wing unswept data were obtained at only subsonic Mach numbers. See table 3 for a complete summary of the test conditions.

Angle of attack or angle of sideslip, depending upon the model orientation, was indicated by an electrical dangleometer mounted in the support located downstream of the sting. Corrections were applied to the indicated angles for balance and sting deflections.

RESULTS AND DISCUSSION

Static longitudinal stability characteristics for the oblique wing model with intermediate bend on the wing mounted right side up are presented in figures 5 through 12 at Mach numbers from 0.6 through 1.4. These characteristics for the model mounted upside down are shown in figure 13. The static lateral/directional stability characteristics are presented in figures 14 and 15 ($\alpha = 0°$ and 10°, respectively). For the oblique wing with intermediate bend, figure 16 summarizes the variation of maximum L/D, minimum drag coefficient, lift-curve slope, and pitching-moment curve slope with Mach number. For oblique-wing sweep angles of 45° and 60°, the effects of changing the wing bend

from small (data from ref. 1) to intermediate (data herein) on the static longitudinal stability characteristics are shown in figures 17 through 24 at Mach numbers from 0.6 through 1.4. For these same sweep angles, the effects of wing bend on maximum lift/drag ratio and the pitching-moment curve slope at Mach numbers from 0.6 to 1.4 are presented in figure 25.

Longitudinal Stability Characteristics

Oblique wing (intermediate bend)– Examination of the pitching-moment results presented in figures 5(c) through 12(c) indicates that the oblique wing with intermediate bend has a pitch-up tendency at moderate lift coefficients. This pitch-up tendency was generally aggravated by increases in sweep, causing a pitch-up tendency at lower lift coefficient. Tuft studies indicated that the pitch-up tendency was caused by asymmetrical spanwise flow separation as the angle of attack was increased, separation first being observed on the downstream panel near the trailing edge. It can be concluded, therefore, that the intermediate bend was insufficient to prevent initial stalling on the trailing wing panel. In reference 2, the oblique wing with much larger bend had a pitch-down tendency associated with premature flow separation from the forward wing panel. Apparently, a bend between the intermediate bend and large bend could produce more nearly linear pitching-moment curves, but the rolling moment resulting from bending at low lift coefficients would have to be trimmed, probably by changing the wing pivot location. An estimate was made of the wing-pivot movement required to eliminate the rolling moment at small lift for the oblique wing with the intermediate bend. The results of this calculation, shown in figure 2(b) for the oblique wing swept 45° at a Mach number of 0.95, indicate that the rearward pivot shift required is 0.49 c_{root}, probably to an impractical location too close to the wing trailing edge. With the oblique wing in a swept position, the nonlinearity of rolling moment, yawing-moment and sideslip curves associated with the unsymmetrical spanwise wing stall can be observed in figures 5(e) through 12(e).

A comparison of the lift/drag results in figure 5(d) for a Mach number of 0.6 with those in figure 9(d) for a Mach number of 0.95 illustrates the benefits for the oblique wing not employing sweep at low Mach numbers but employing about 50° of sweep at a Mach number of 0.95 for maximum efficiency.

Inverted oblique wing (intermediate bend)– These results correspond to the oblique wing-body combination being pitched in a negative direction up to about −28°. Therefore, the signs on all the forces, moments, and angle of attack were changed except for drag and rolling moment. In comparing the lift results in figures 9(a) and 13(b) at a given angle of attack for a Mach number of 0.95, it is evident that the lift is lower for the inverted model. Furthermore, the pitch-up tendency at a Mach number of 0.95 occurred at a lower lift coefficient for the inverted model as shown by comparing results in figure 9(c) with those in figure 13(f). Maximum lift/drag ratio was considerably lower with the model inverted. Compare figure 9(d) with figure 13(h).

Effect of Wing Bend on the Longitudinal Stability Characteristics

As shown in figures 17(c) through 24(c), changing the bend of the oblique wing from small to intermediate had only slightly beneficial to negligible effect on the linearity of the pitching-moment curves. A similar result was found for the rolling-moment and yawing-moment curves in figures 17(e) through 24(e). At all Mach numbers, the oblique wing with small bend had generally

the higher lift/drag ratios as shown in figures 17(d) through 24(d) and the higher maximum lift/drag ratios as shown in figure 25(a) compared to the oblique wing with intermediate bend.

CONCLUDING REMARKS

Increasing the upward bending of the wing panels along the span of the oblique wing from the previously investigated small bend to the present intermediate bend had only a small effect on the linearity of the pitching-moment, rolling-moment, or yawing-moment curves. At low lift at a Mach number of 0.95, an impractical wing pivot location, very close to the wing trailing edge, would be required to eliminate the rolling moment resulting from bending the oblique wing upward to form the intermediate bend. Use of the intermediate or larger bend on this oblique wing in an attempt to linearize the moment curves, therefore, does not appear feasible. The swept oblique wing with small bend had higher maximum lift/drag ratios than the swept oblique wing with intermediate bend throughout the Mach number range of 0.6 to 1.4.

Ames Research Center
National Aeronautics and Space Administration
Moffett Field, California, 94035, May 23, 1975

REFERENCES

1. Hopkins, Edward J.; Meriwether, Frank D.; and Pena, Douglas F.: Experimental Aerodynamic Characteristics of Low Aspect Ratio Swept and Oblique Wings at Mach Numbers Between 0.6 and 1.4. NASA TM X-62,317, November 1973.

2. Hopkins, Edward J.; and Levin, Alan D.: An Experimental and Theoretical Study of Low-Aspect Ratio Swept and Oblique Wings at Mach Numbers Between 0.6 and 1.4. AIAA Preprint 74-771, AIAA Mechanics and Control of Flight Conference, August 5–9, 1974.

TABLE 1.– MODEL GEOMETRY

Body	
Radius	$r = 3.856[1 - (1 - 2x_1/114.94)^2]^{3/4}$ cm
Length	
Closed	114.94 cm
Cutoff	91.44 cm
Maximum diameter	7.71 cm
Wing	
Planform ellipticity about 0.25c line	4.7:1
Span	90.50 cm
Span (reference)	71.12 cm
Area (reference)	1365.09 cm
Mean aerodynamic chord (reference), $\bar{c}$	20.88 cm
Root chord	19.20 cm
Aspect ratio ($\Lambda = 0$)	6.0
Aspect ratio ($\Lambda = 45°$)	3.2
Incidence relative to body centerline	0
Profile perpendicular to 0.25c line	Garabedian, subcritical (see table 2)

TABLE 2.– COORDINATES FOR GARABEDIAN PROFILE

[$(t/c)_{max}$ = 0.1016, design lift coefficient = 1.3 at M = 0.6]

x/c	z/c	x/c	z/c
0	0	0	0
−.00045	.00079	.00048	−.00058
−.00073	.00146	.00104	−.00120
−.00086	.00191	.00165	−.00176
−.00097	.00244	.00257	−.00249
−.00103	.00290	.00343	−.00308
−.00106	.00345	.00467	−.00382
−.00104	.00403	.00592	−.00445
−.00098	.00463	.00674	−.00481
−.00077	.00572	.00774	−.00519
−.00052	.00653	.00943	−.00570
−.00021	.00732	.01149	−.00620
.00026	.00830	.01539	−.00694
.00073	.00909	.02583	−.00837
.00163	.01033	.03967	−.00970
.00276	.01161	.06022	−.01116
.00464	.01340	.09339	−.01288
.00709	.01538	.13965	−.01462
.01197	.01878	.19880	−.01601
.02179	.02443	.25034	−.01684
.03187	.02928	.31761	−.01738
.04250	.03373	.38597	−.01735
.06373	.04113	.45495	−.01657
.09353	.04969	.50010	−.01568
.13389	.05882	.54359	−.01456
.17545	.06597	.57465	−.01363
.22415	.07249	.61351	−.01232
.28227	.07822	.65330	−.01090
.34741	.08236	.68122	−.00988
.41444	.08434	.71655	−.00865
.48168	.08406	.74682	−.00771
.55738	.08094	.77611	−.00702
.62052	.07591	.82243	−.00642
.68276	.06852	.87054	−.00698
.72012	.06288	.89717	−.00810
.75413	.05684	.91595	−.00941
.82318	.04227	.94348	−.01235
.85663	.03370	.96854	−.01674
.89115	.02388	.98615	−.02126
.92448	.01327	.99596	−.02434
.95410	.00145	1.00000	−.02600
.97175	−.00538		
.99163	−.01450		
1.00000	−.01900		

TABLE 3.– TEST CONDITIONS

Configuration	Mach Numbers									
	α	β	0.6	0.7	0.8	0.90	0.95	1.1	1.2	1.4
5W0B	var.	0	x	x	x	x	x			
5W45B	var.	0	x	x	x	x	x	x	x	x
5W50B	var.	0	x	x	x	x	x	x	x	x
5W55B	var.	0	x	x	x	x	x	x	x	x
5W60B	var.	0	x	x	x	x	x	x	x	x
5W45B (inverted)	var.	0	x	x	x	x	x	x	x	x
5W0B	0	var.	x	x	x	x	x			
5W45B	0	var.	x	x	x	x	x	x	x	x
5W50B	0	var.	x	x	x	x	x	x	x	x
5W55B	0	var.	x	x	x	x	x	x	x	x
5W60B	0	var.	x	x	x	x	x	x	x	x
5W0B	10	var.				x	x			
5W45B	10	var.	x	x	x	x	x	x	x	x
5W50B	10	var.	x	x	x	x	x	x	x	x
5W55B	10	var.	x	x	x	x	x	x	x	x
5W60B	10	var.	x	x	x	x	x	x	x	x

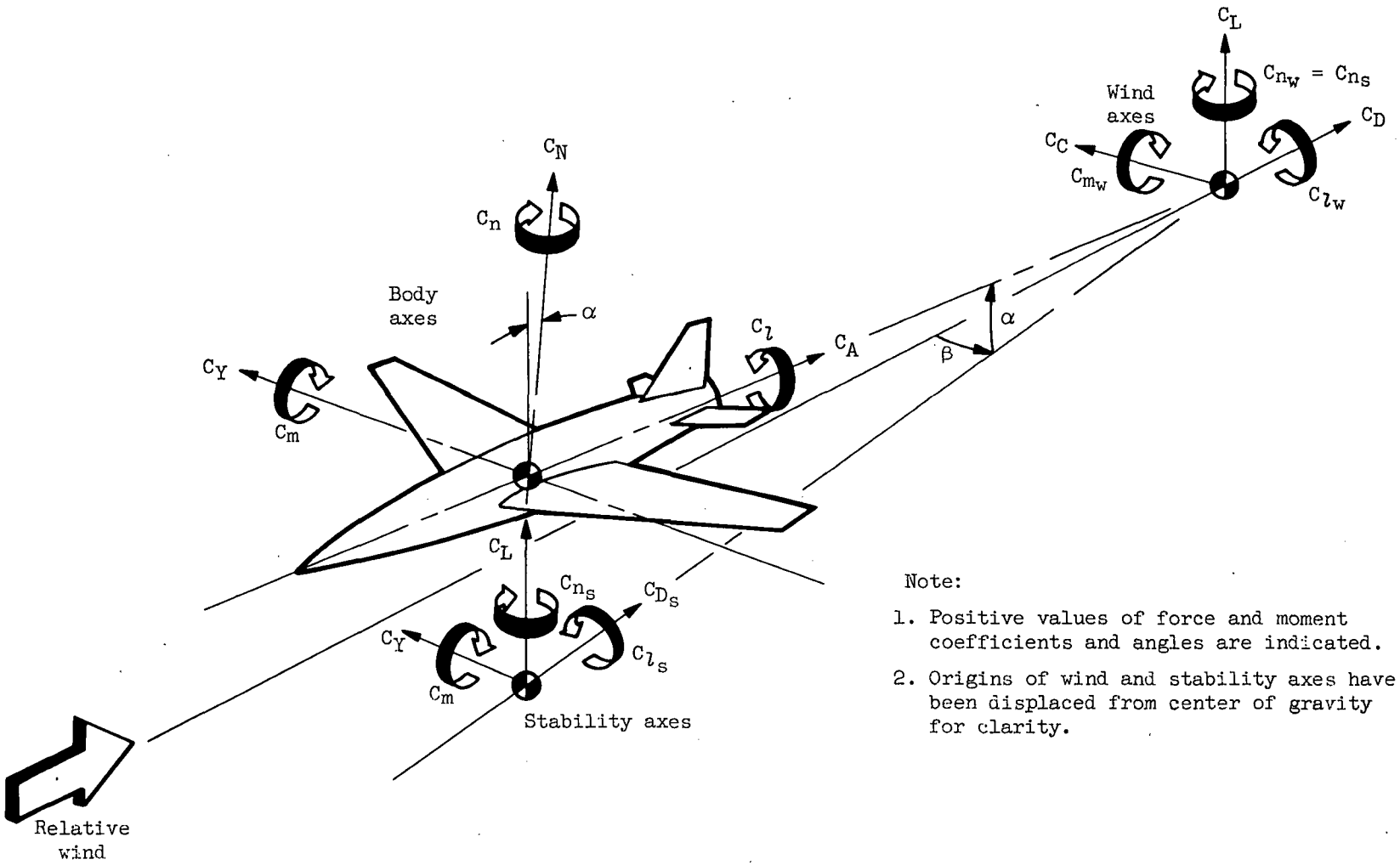

Figure 1.— Axes systems.

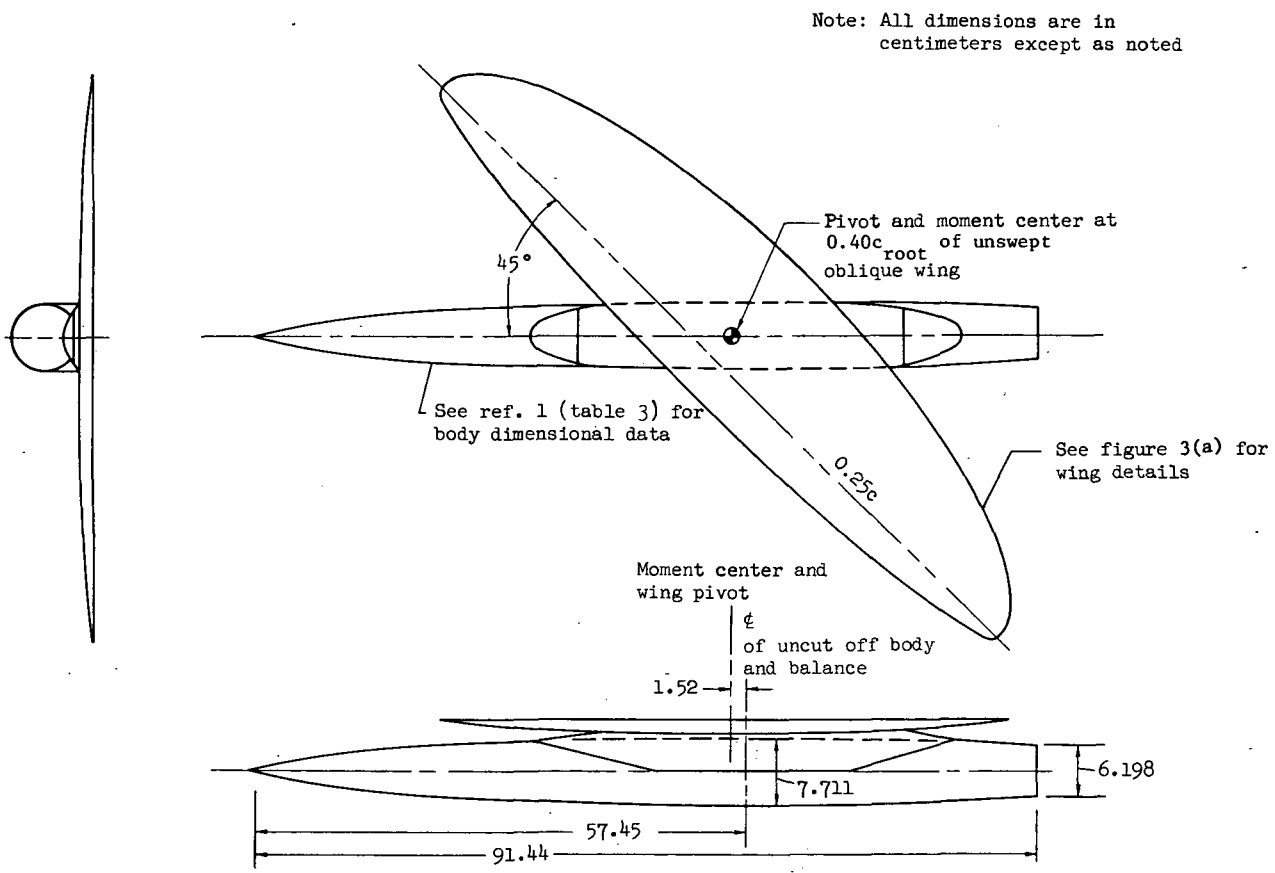

(a) Oblique wing with body.

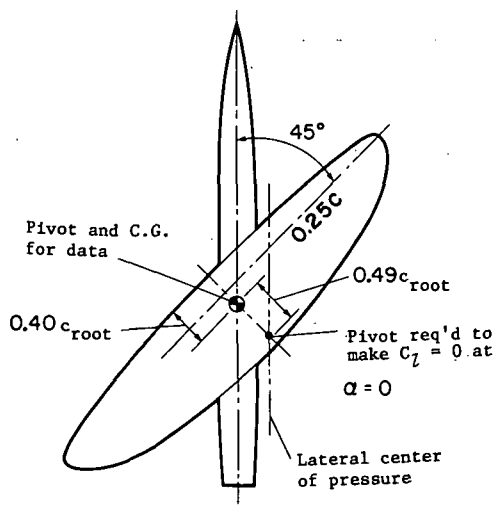

(b) Pivot location required to trim the rolling moment at $\alpha = 0$ ($M = 0.95$)

Figure 2.– Pivot and moment-center locations for the oblique wing mounted on top of the body of revolution.

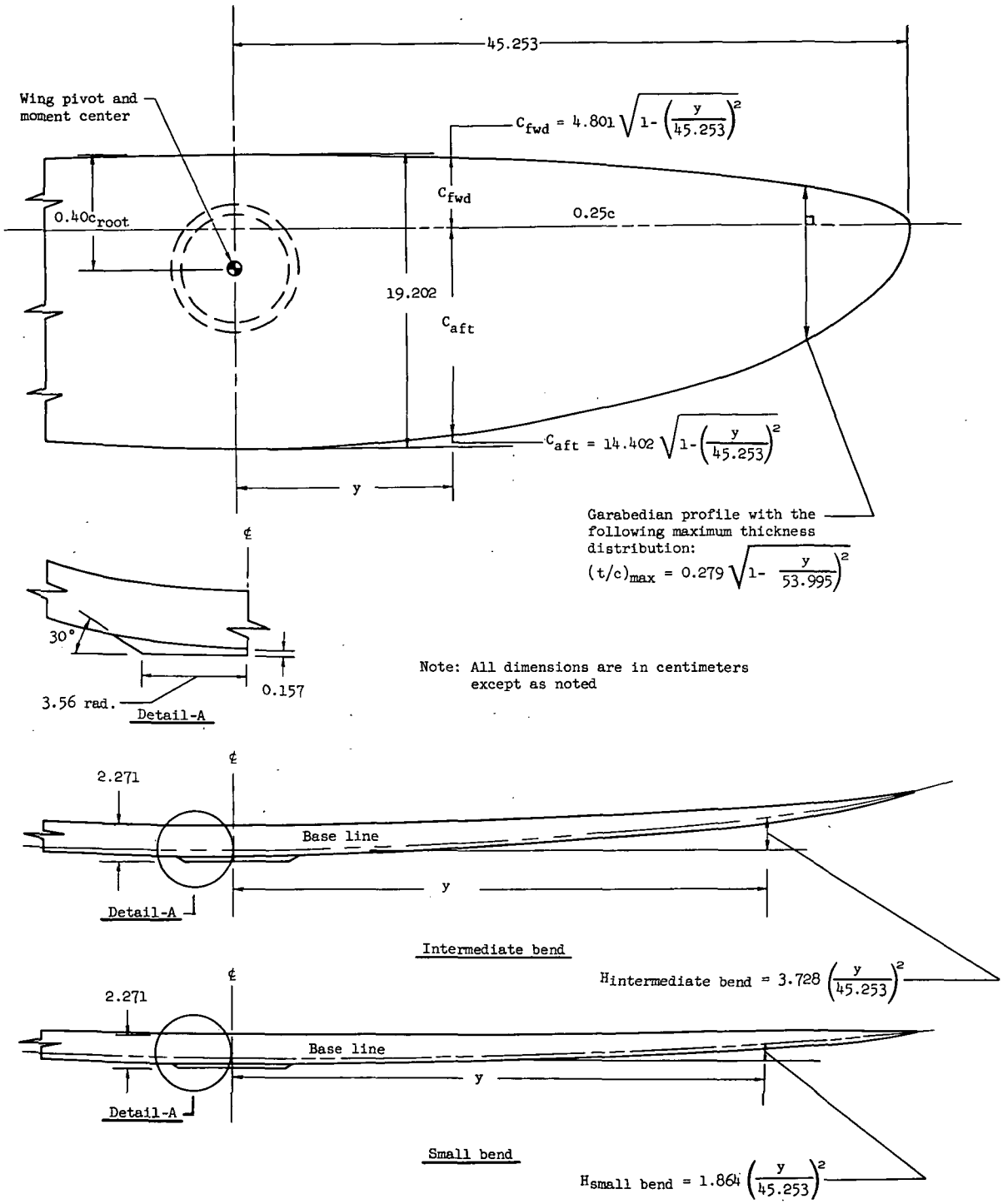

(a) Planform and bend lines.

Figure 3.– Geometry of the oblique wings.

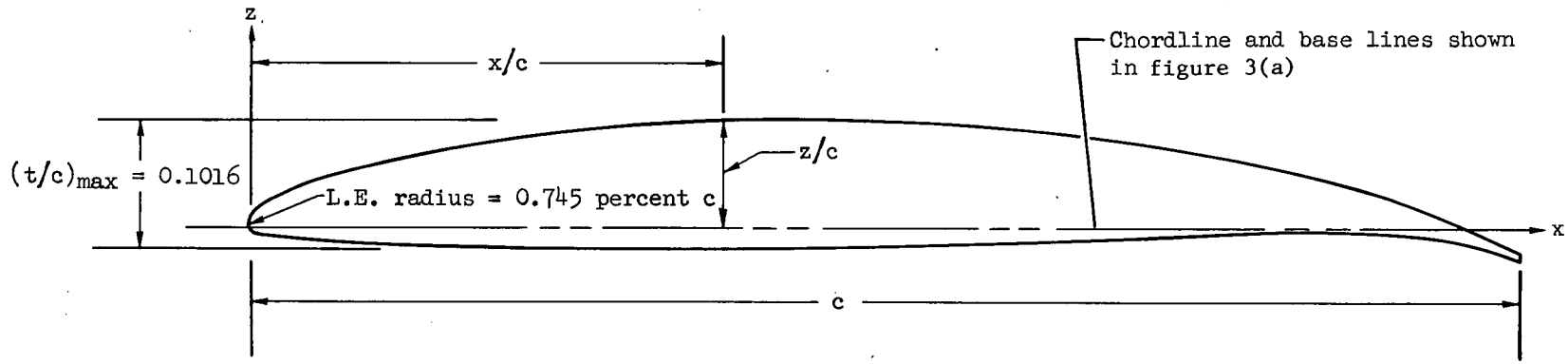

(b) Garabedian profile.

Figure 3.– Concluded.

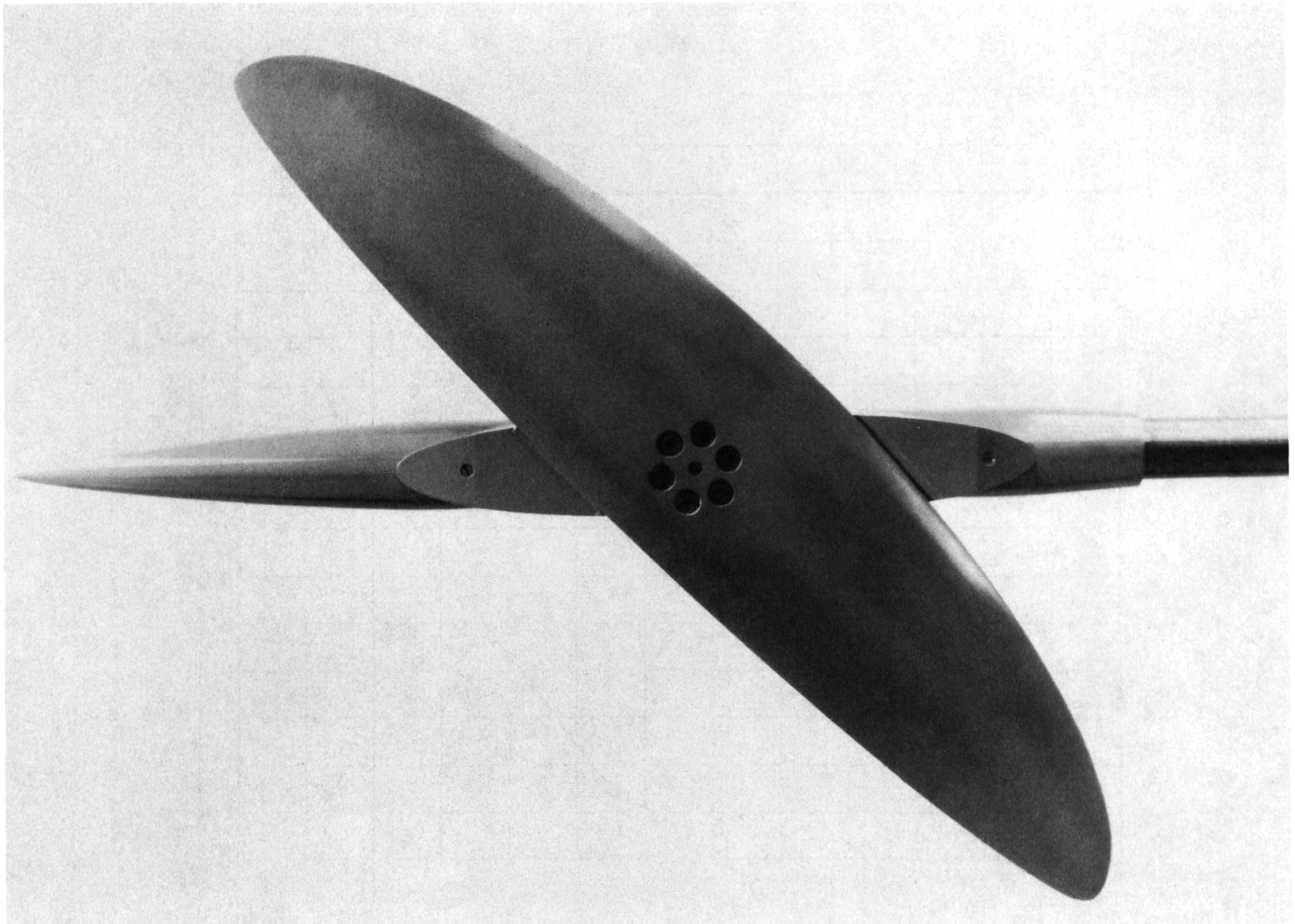

Figure 4.– Photograph of the oblique wing ($\Lambda = 45°$) mounted on top of the body of revolution.

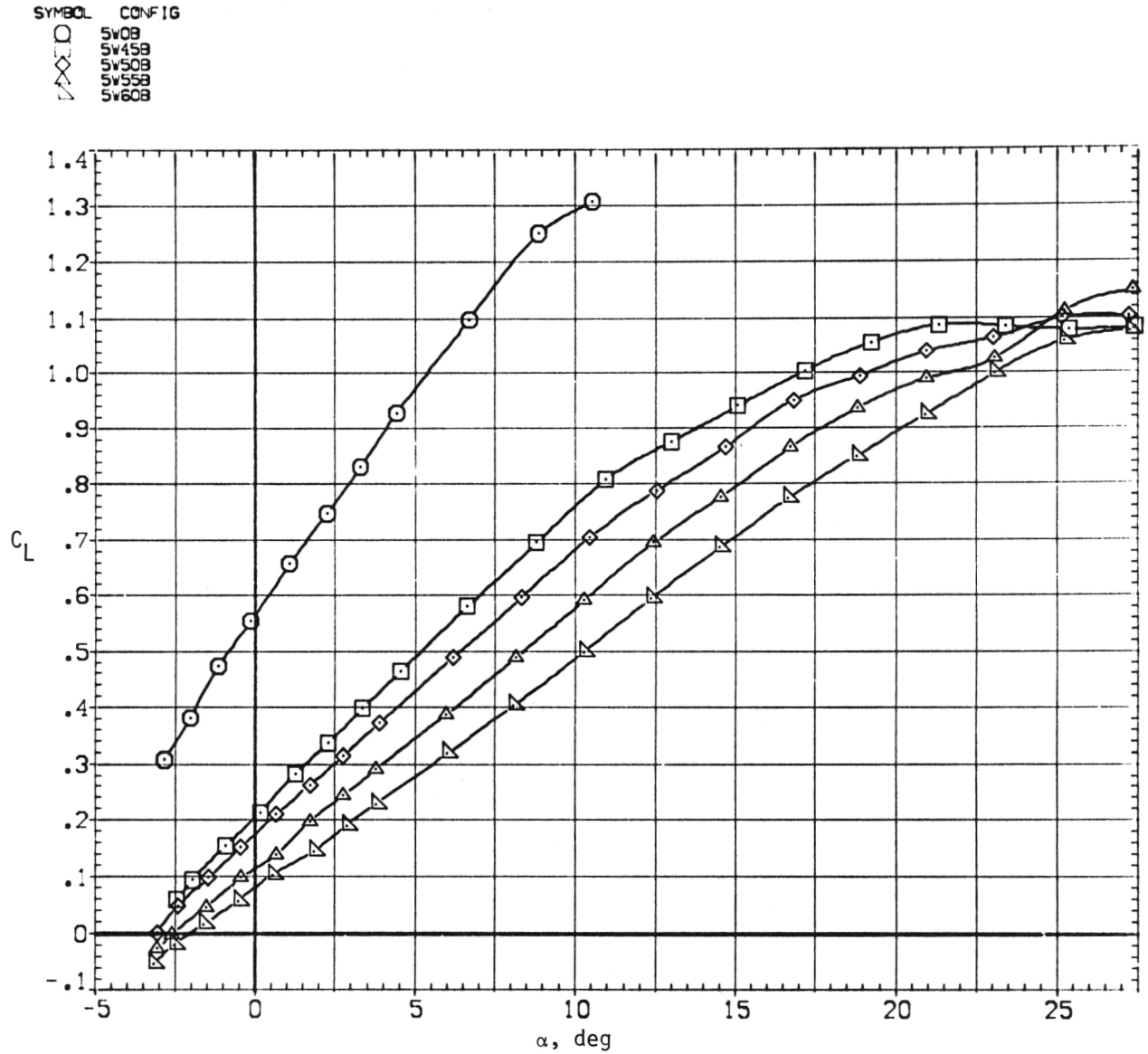

(a) C_L versus α.

Figure 5.– Longitudinal stability characteristics of the oblique wing with intermediate bend, $M = 0.6$, $\beta = 0$.

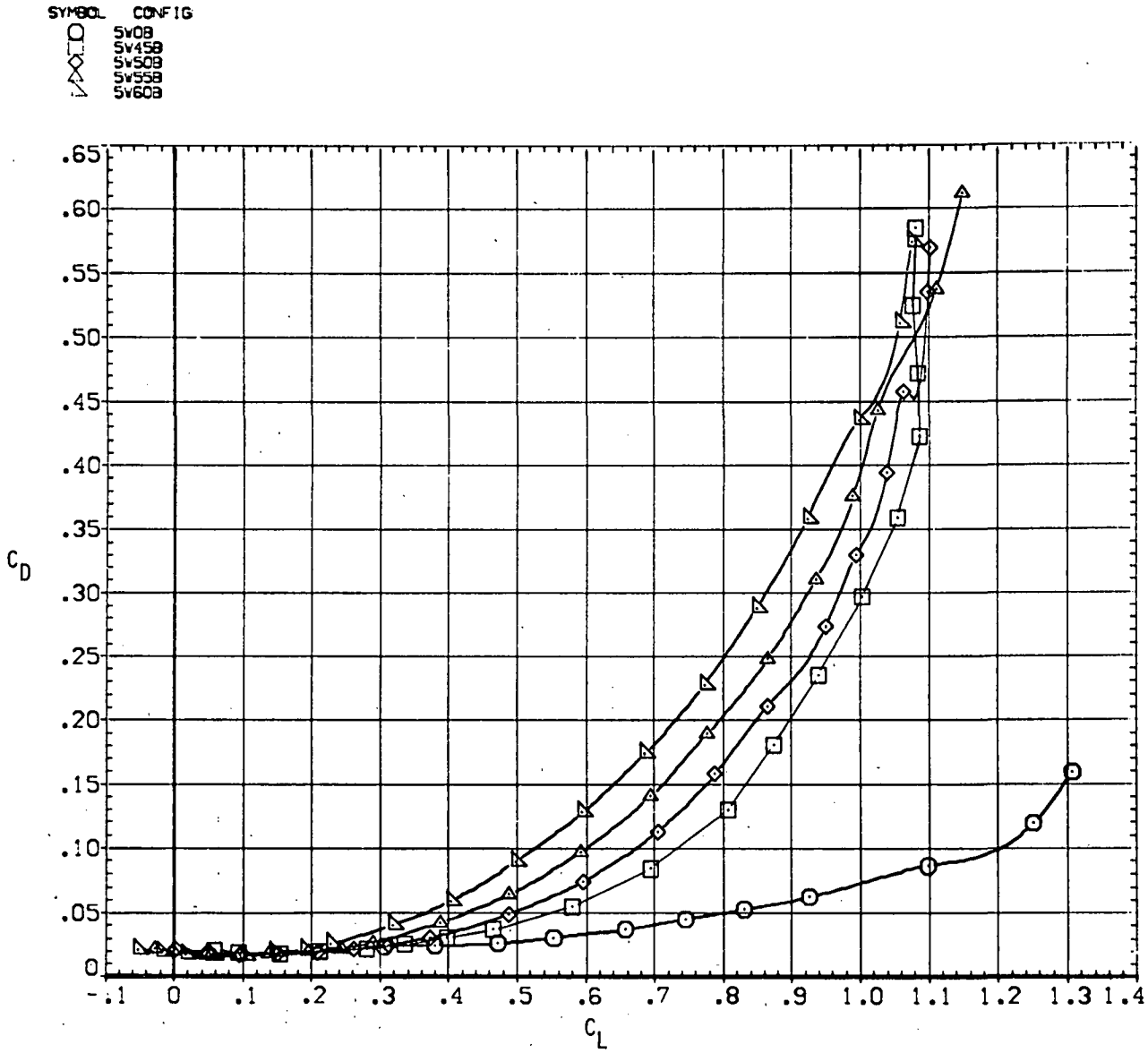

(b) C_D versus C_L.

Figure 5.– Continued.

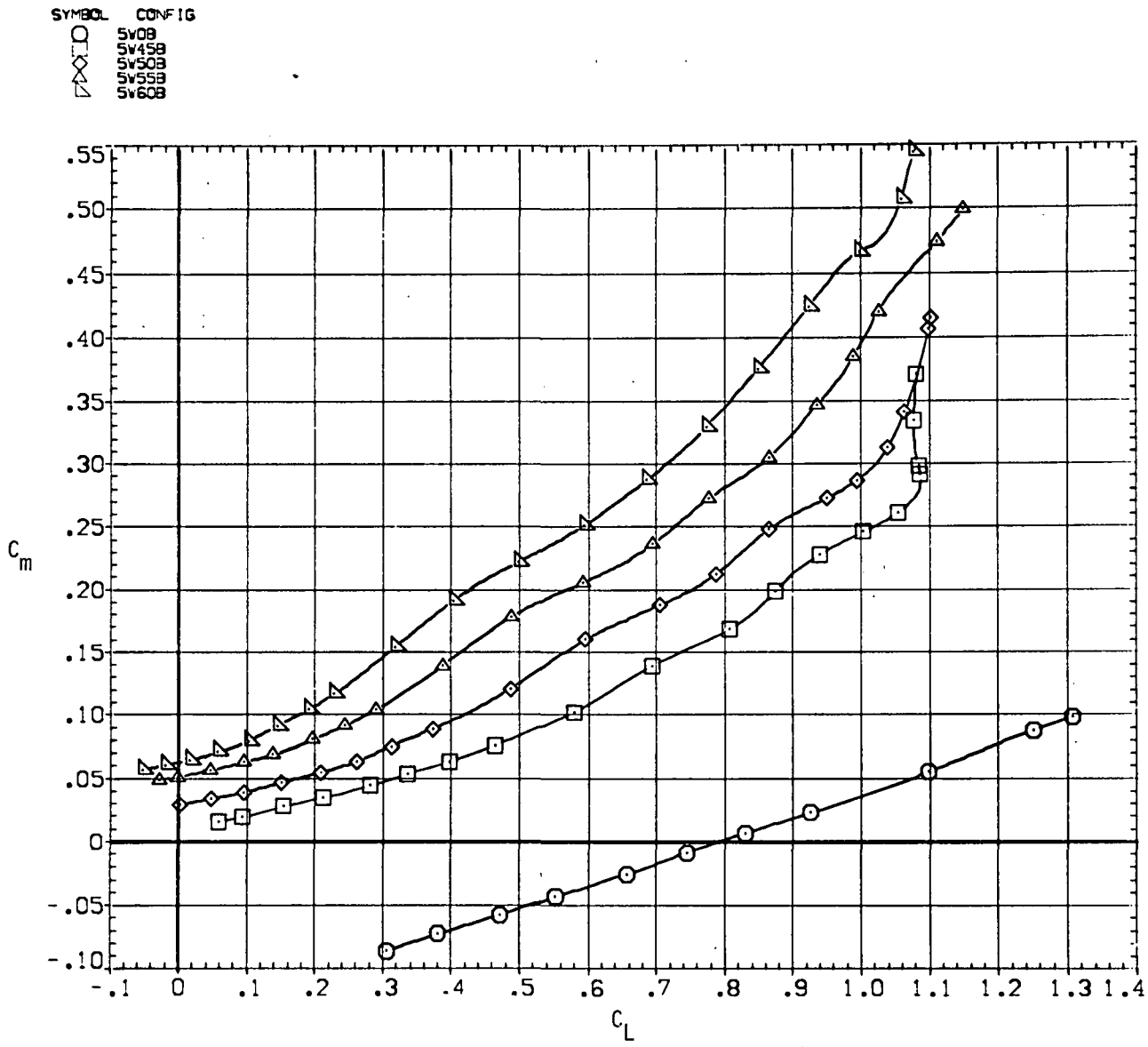

(c) C_m versus C_L.

Figure 5.– Continued.

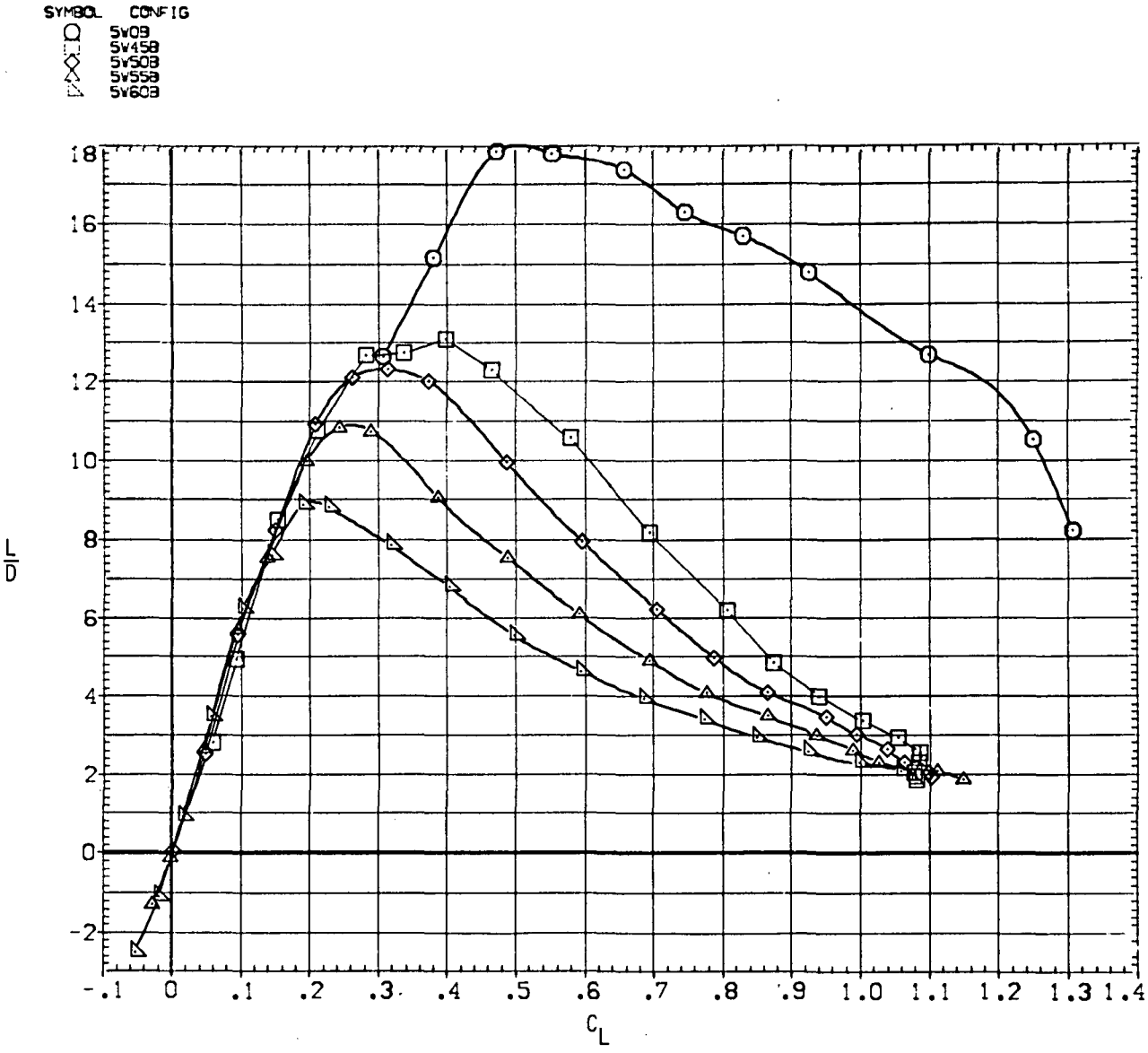

(d) L/D versus C_L.

Figure 5.– Continued.

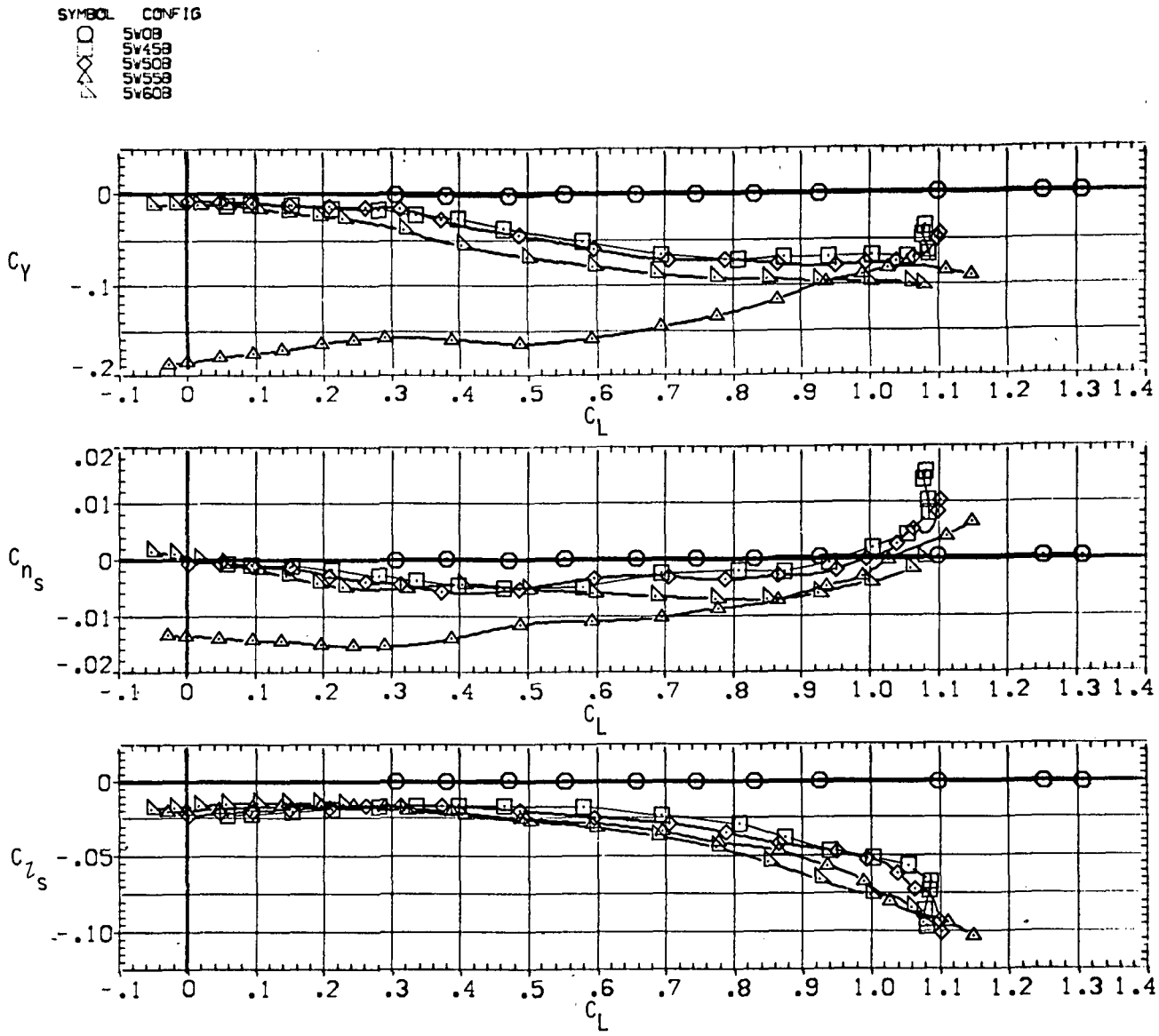

(e) C_Y, C_{n_s} and C_{l_s} versus C_L.

Figure 5.– Continued.

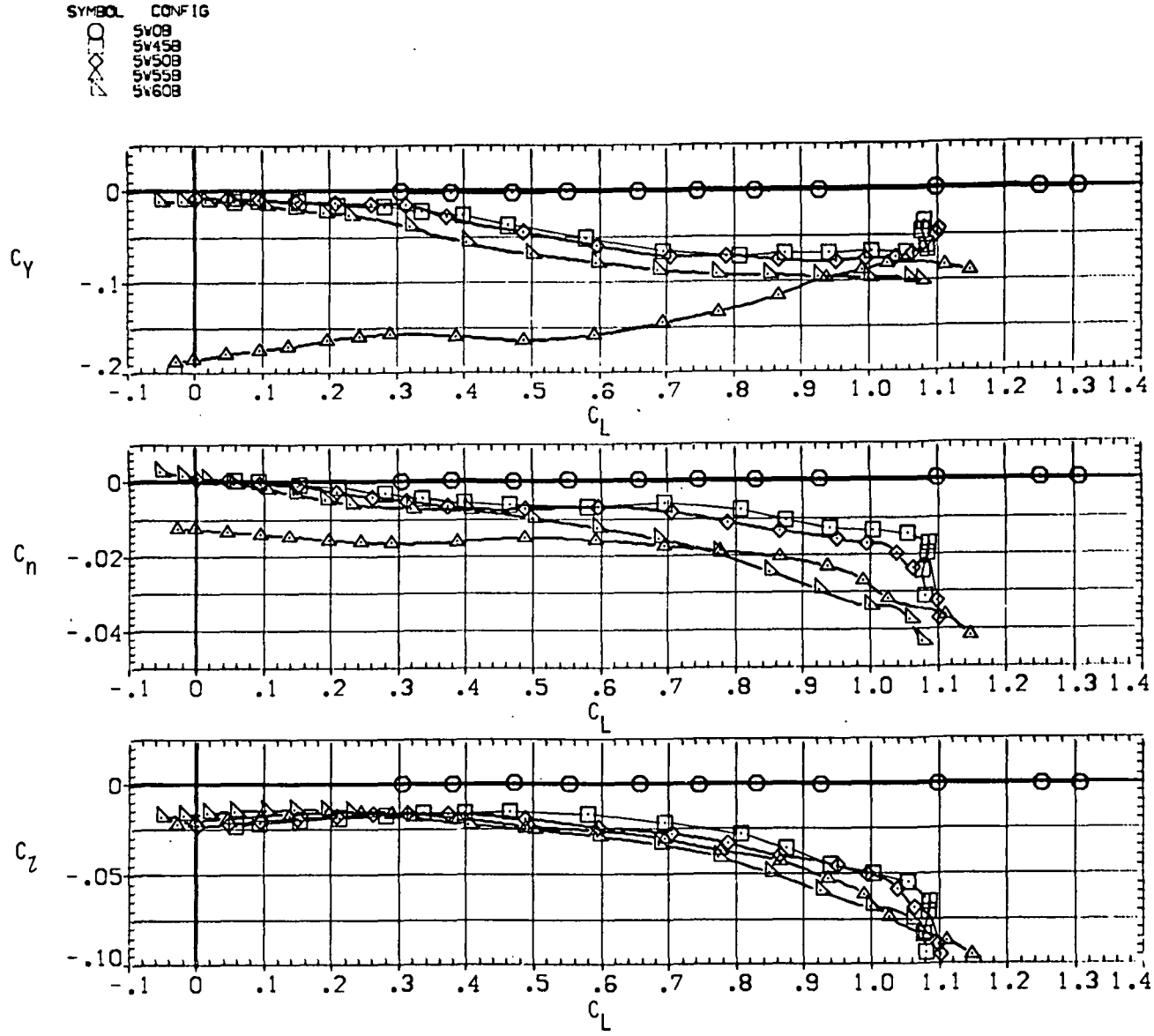

(f) C_Y, C_n and C_l versus C_L.

Figure 5.– Concluded.

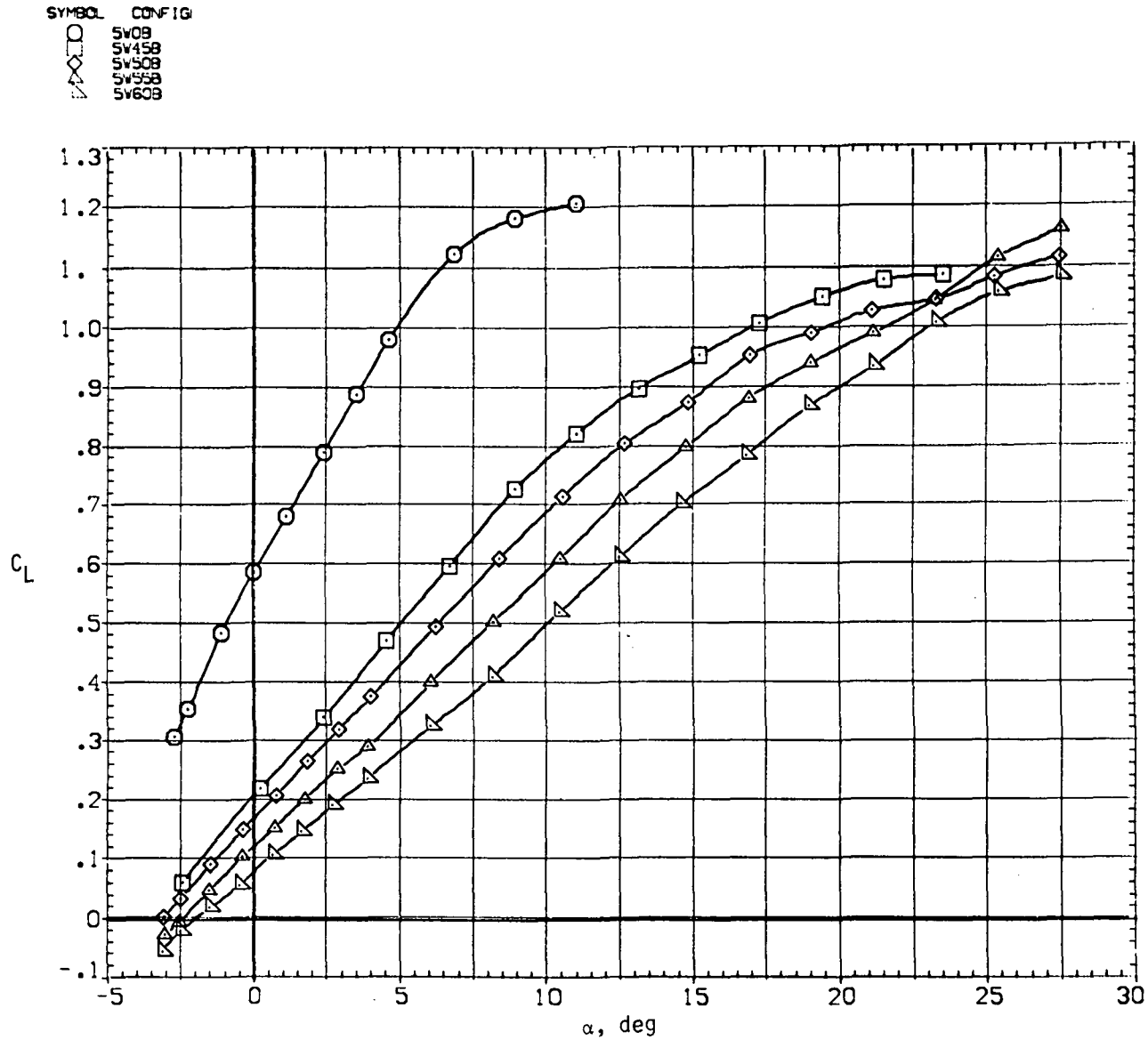

(a) C_L versus α.

Figure 6.– Longitudinal stability characteristics of the oblique wing with intermediate bend, $M = 0.7$, $\beta = 0$.

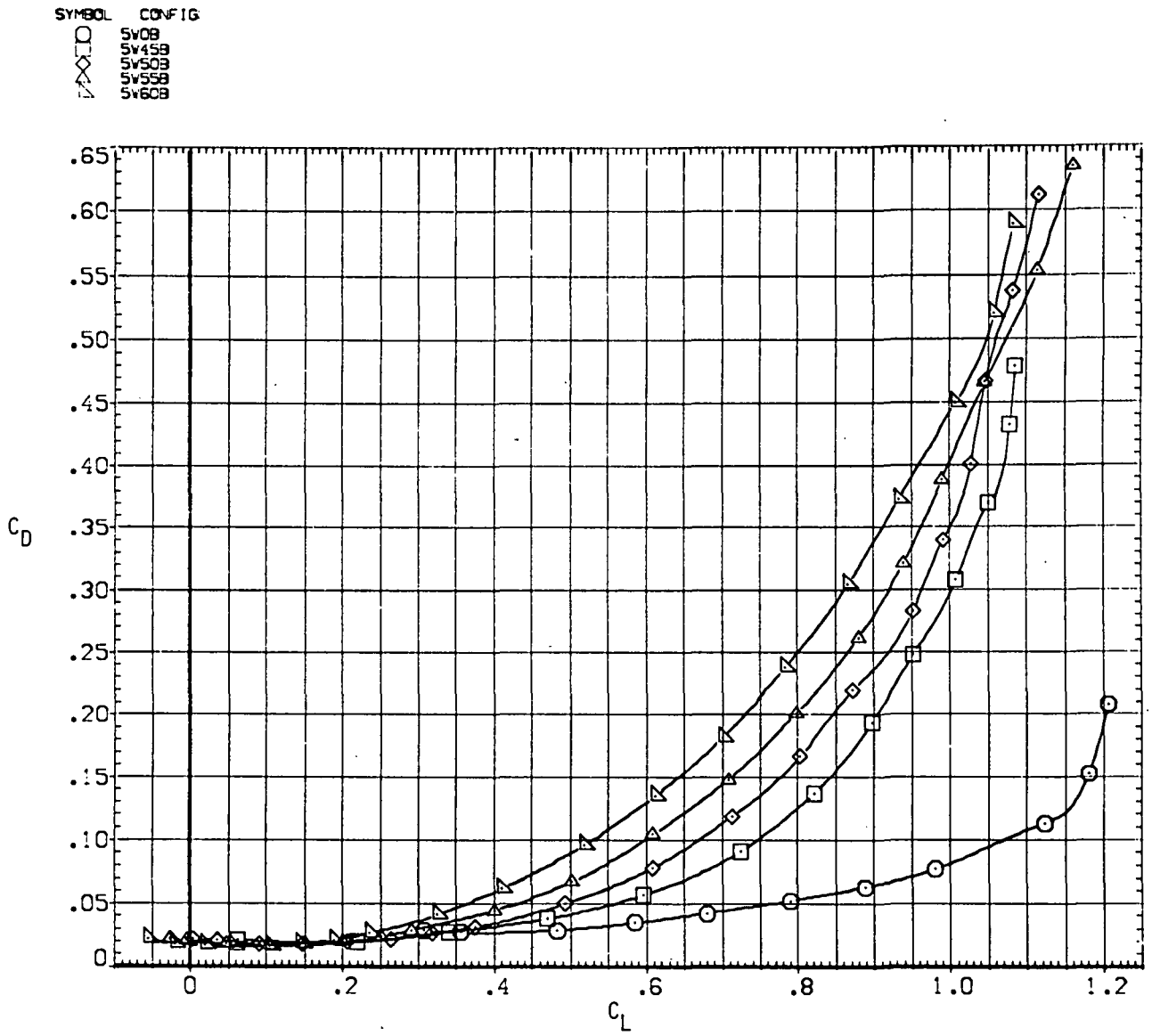

(b) C_D versus C_L.

Figure 6.– Continued.

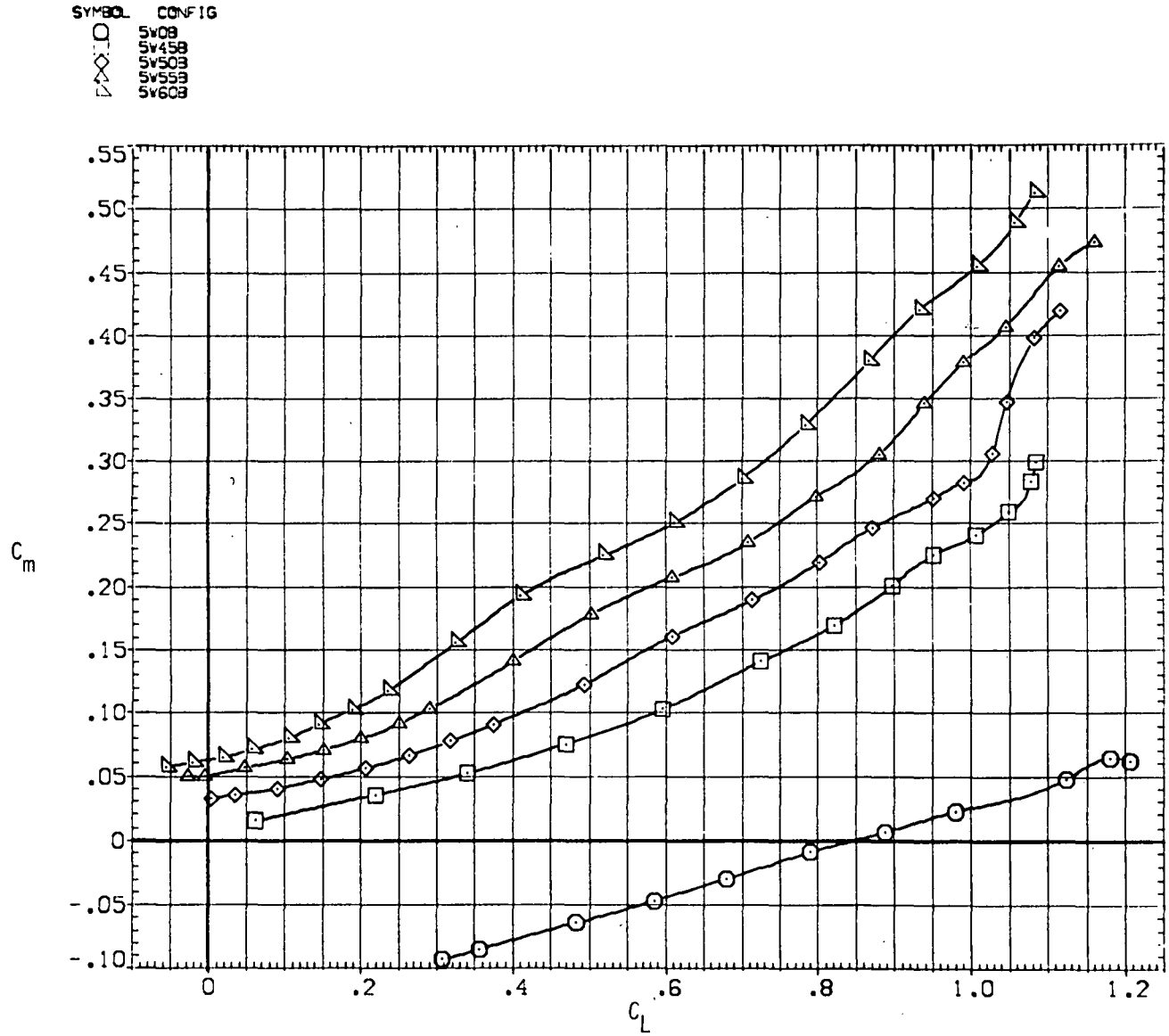

(c) C_m versus C_L.

Figure 6.– Continued.

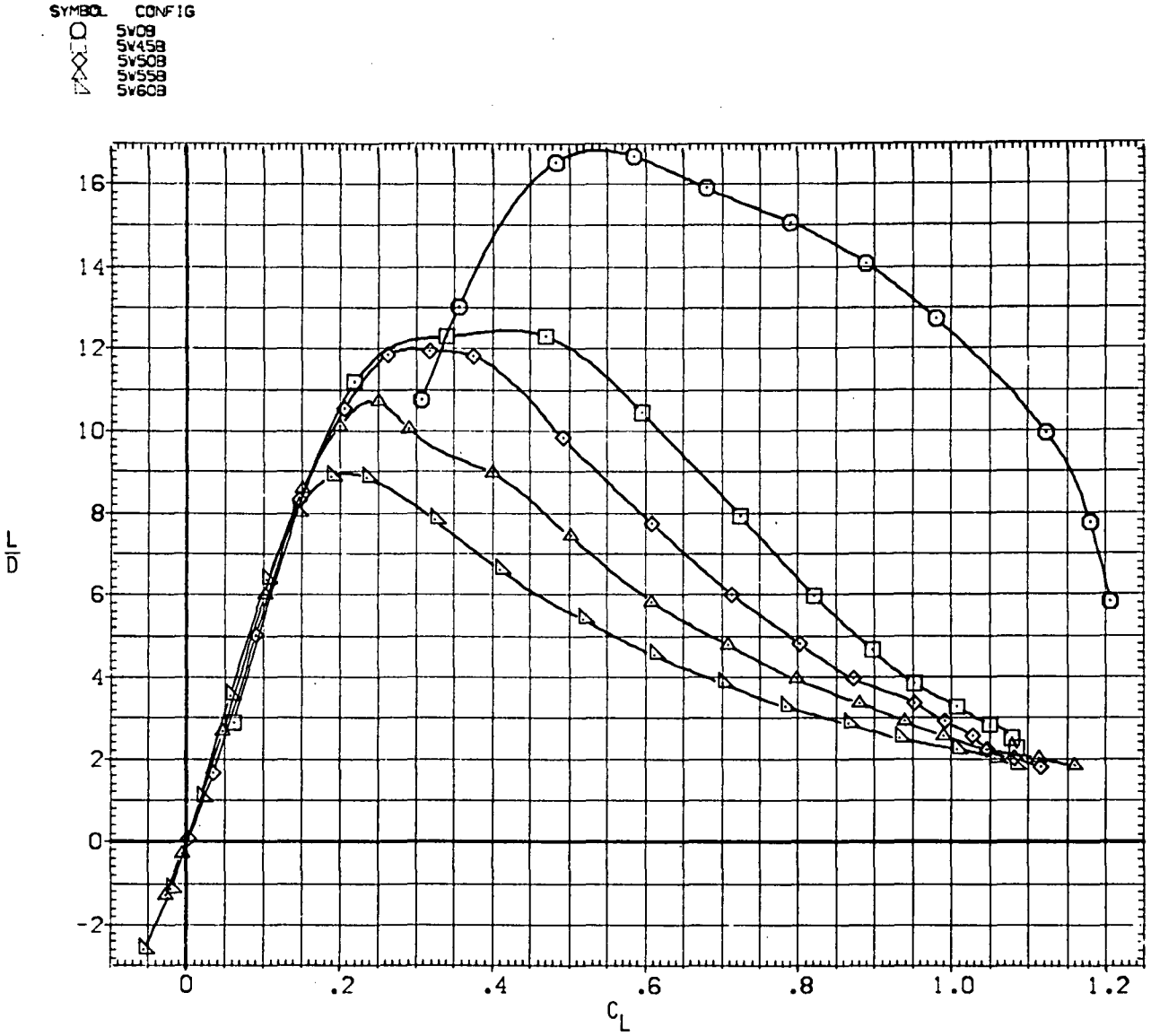

(d) L/D versus C_L.

Figure 6.– Continued.

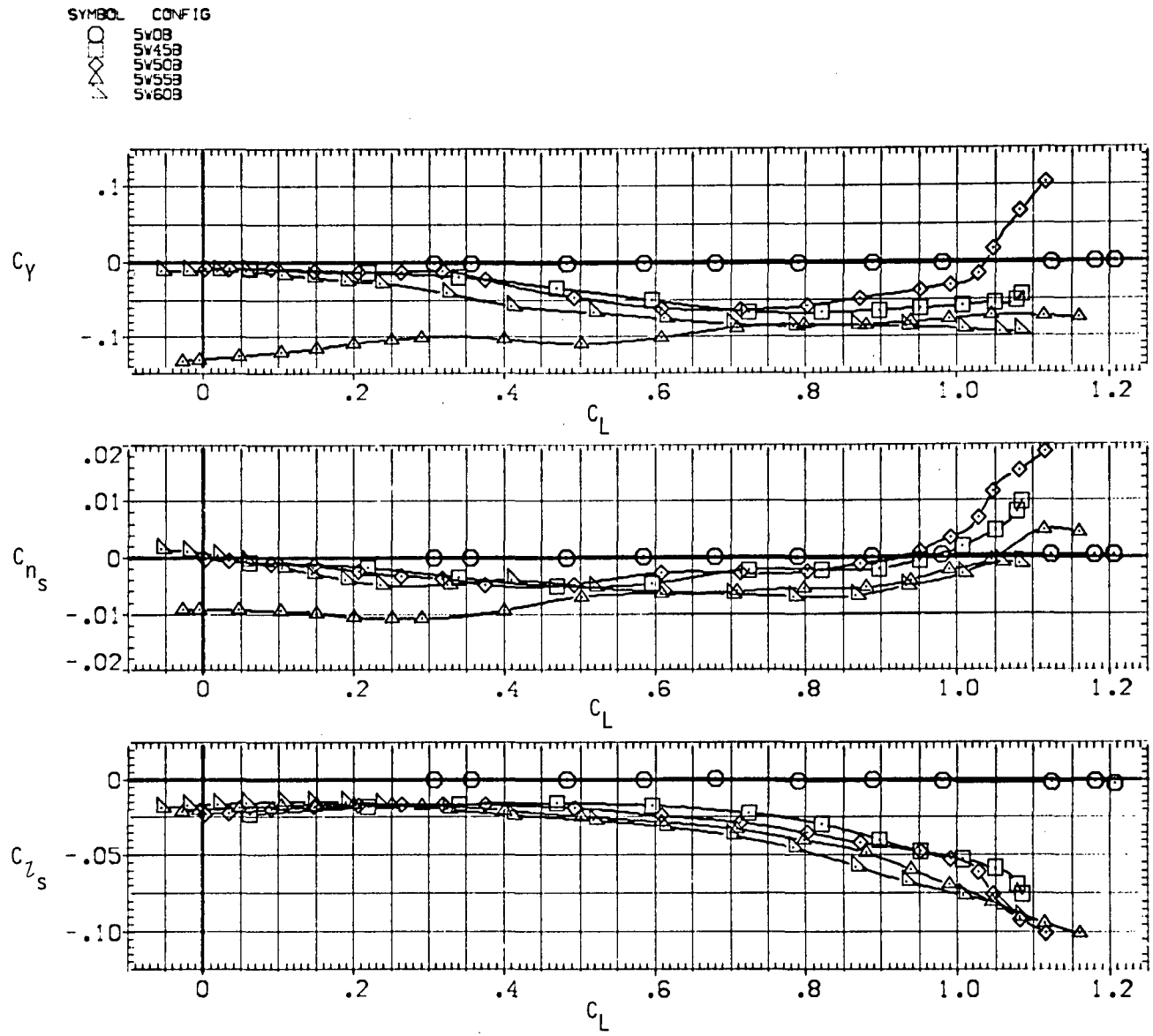

(e) C_Y, C_{n_s} and C_{l_s} versus C_L.

Figure 6.– Continued.

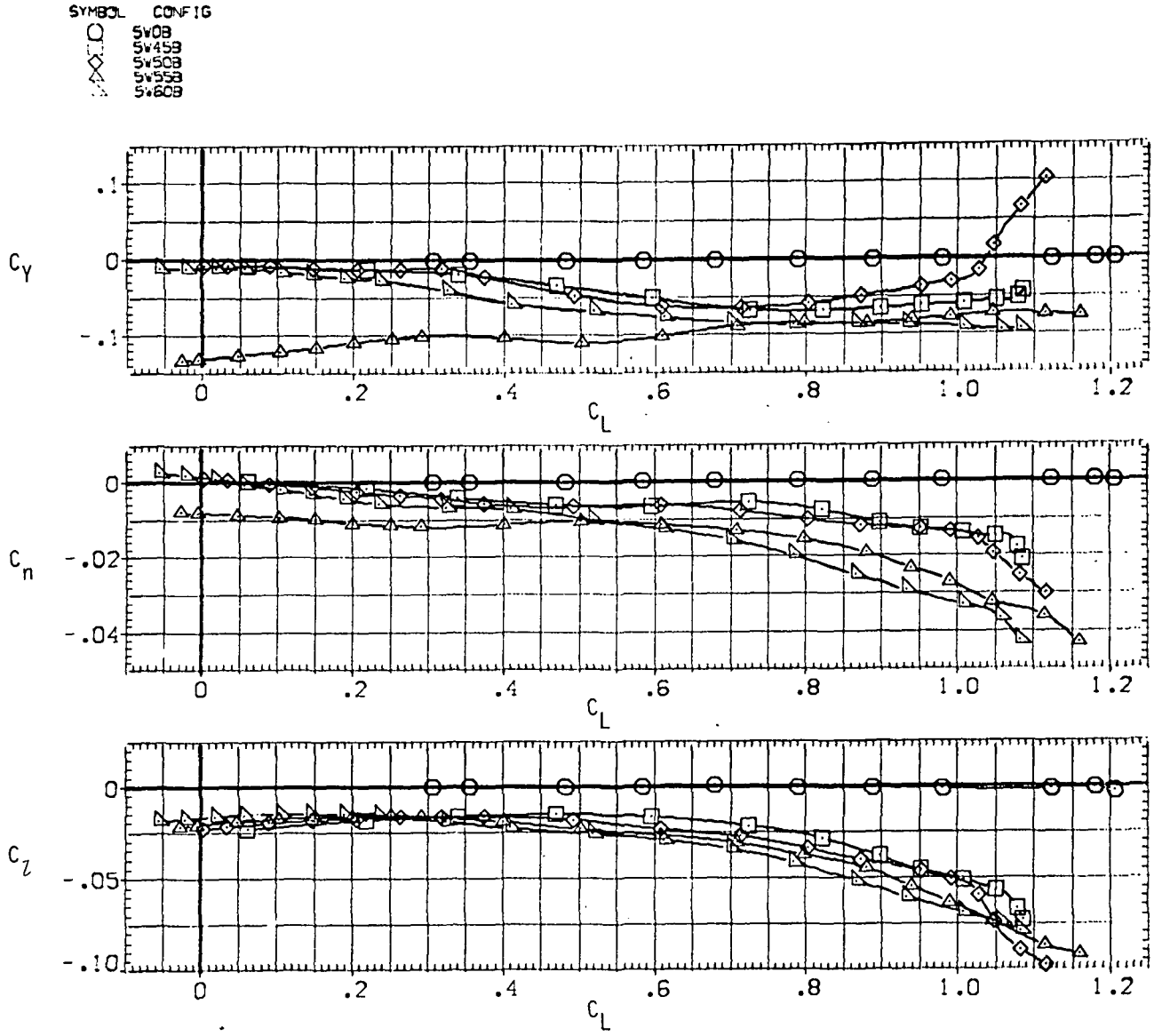

(f) C_Y, C_n and C_l versus C_L.

Figure 6.– Concluded.

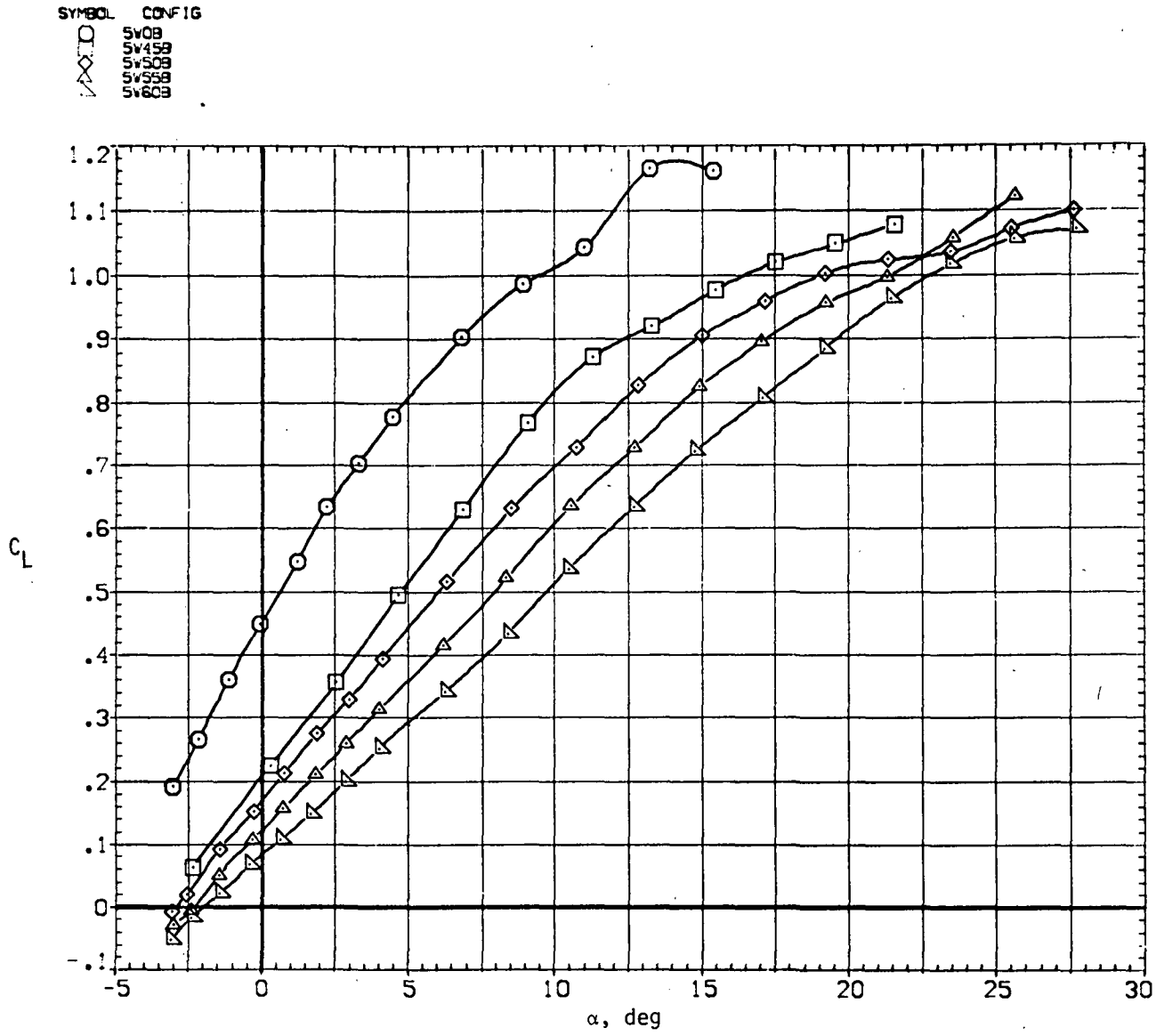

(a) C_L versus α.

Figure 7.– Longitudinal stability characteristics of the oblique wing with intermediate bend, $M = 0.8$, $\beta = 0$.

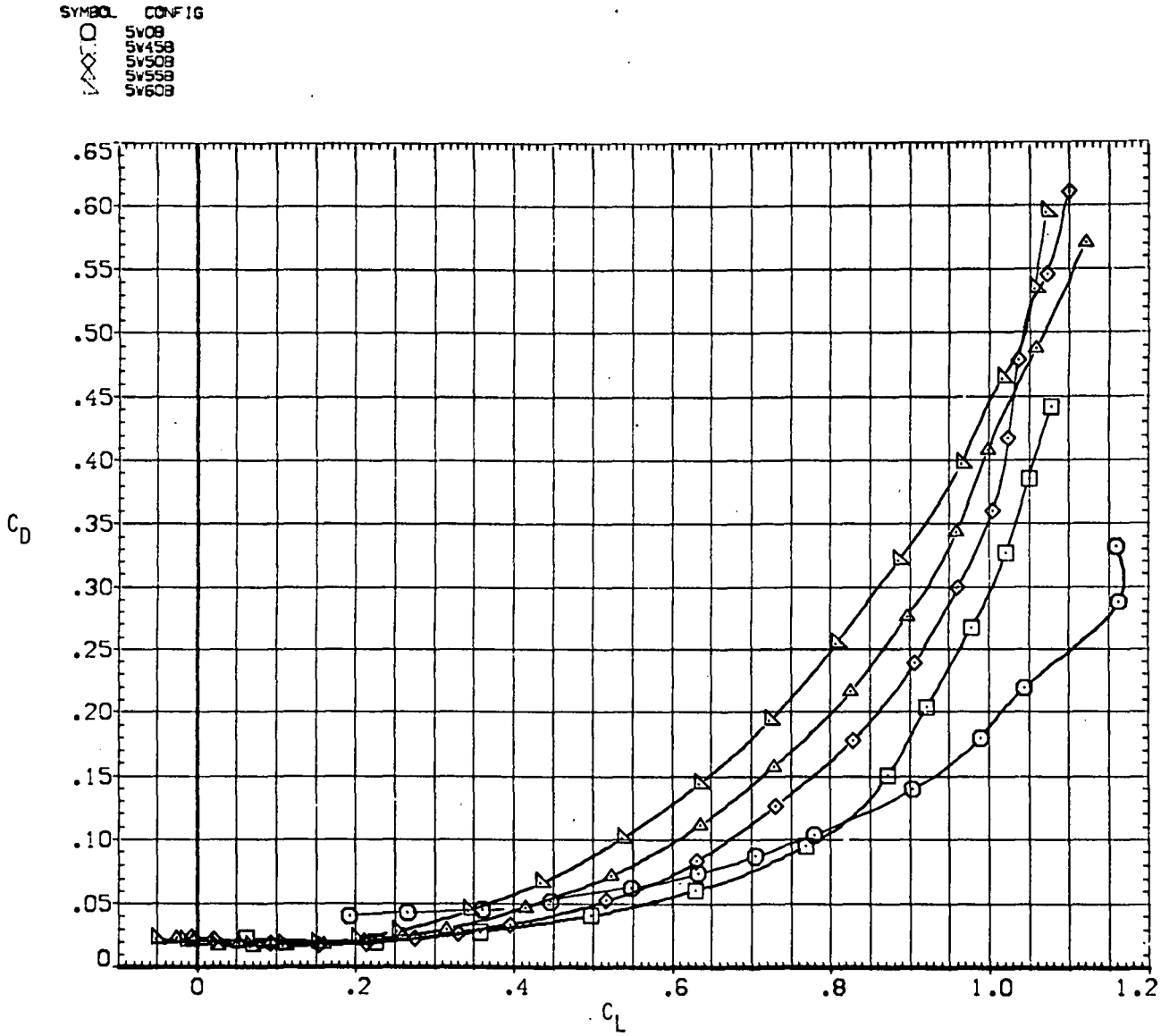

(b) C_D versus C_L.

Figure 7.– Continued.

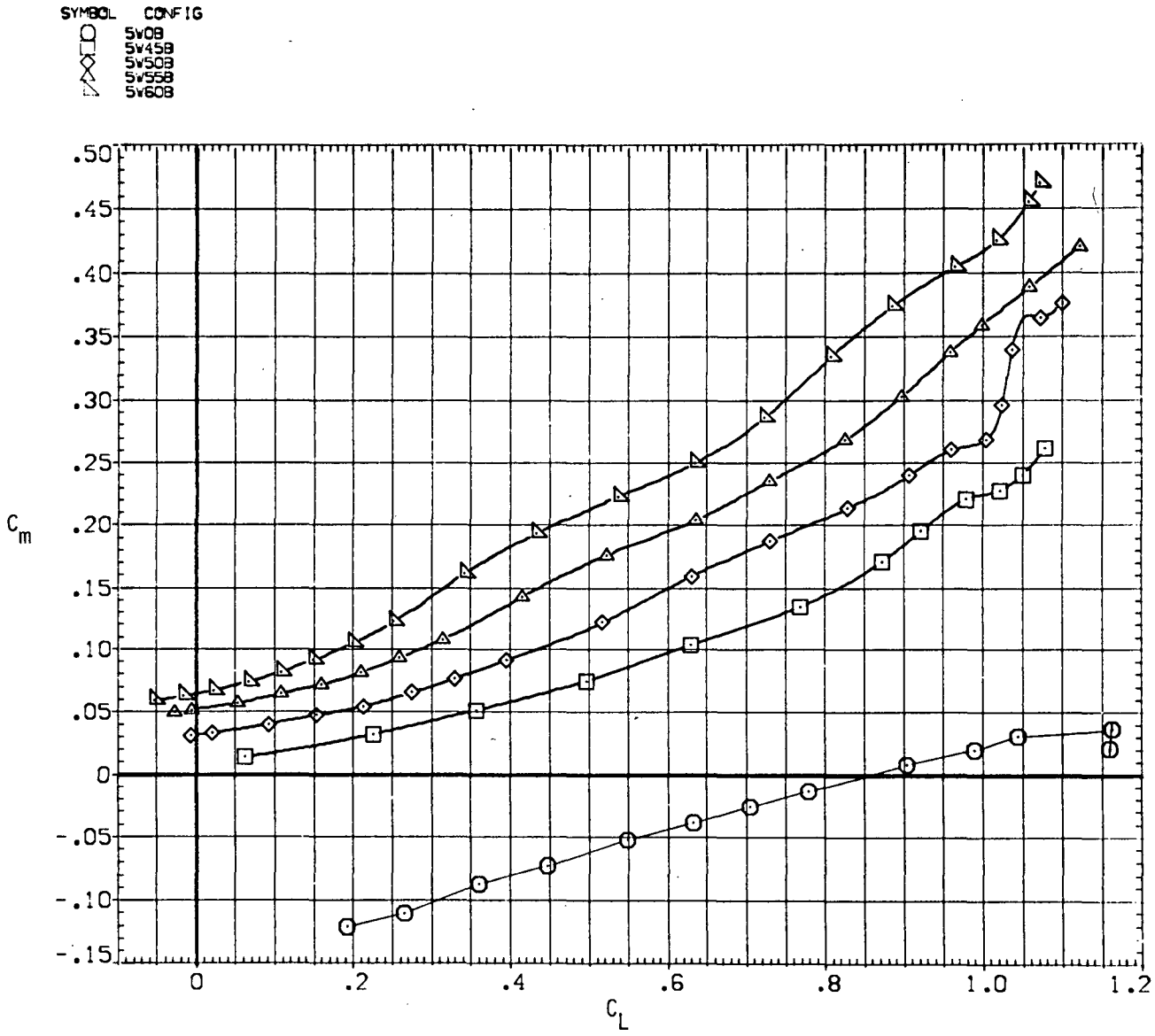

(c) C_m versus C_L.

Figure 7.– Continued.

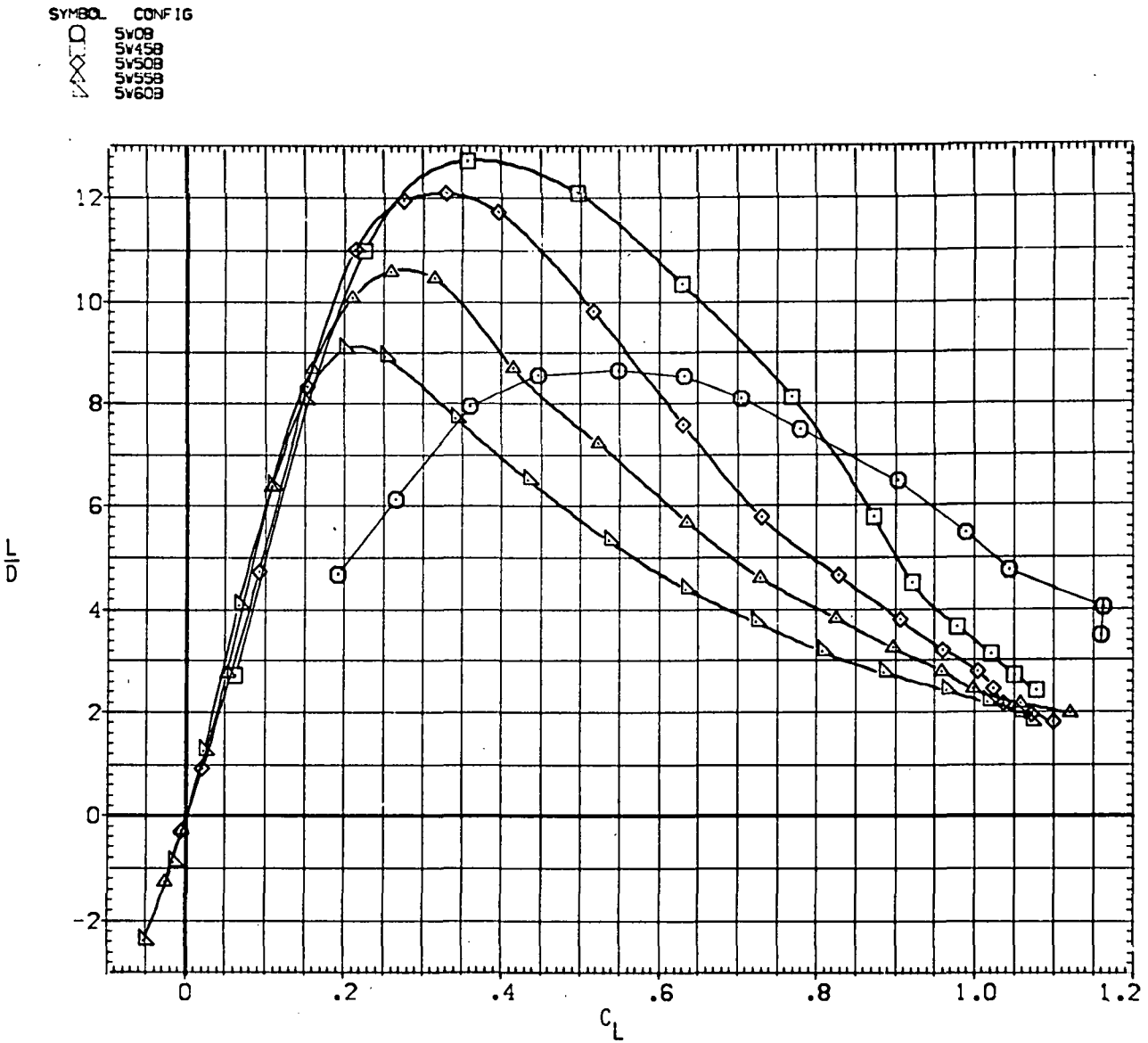

(d) L/D versus C_L.

Figure 7.– Continued.

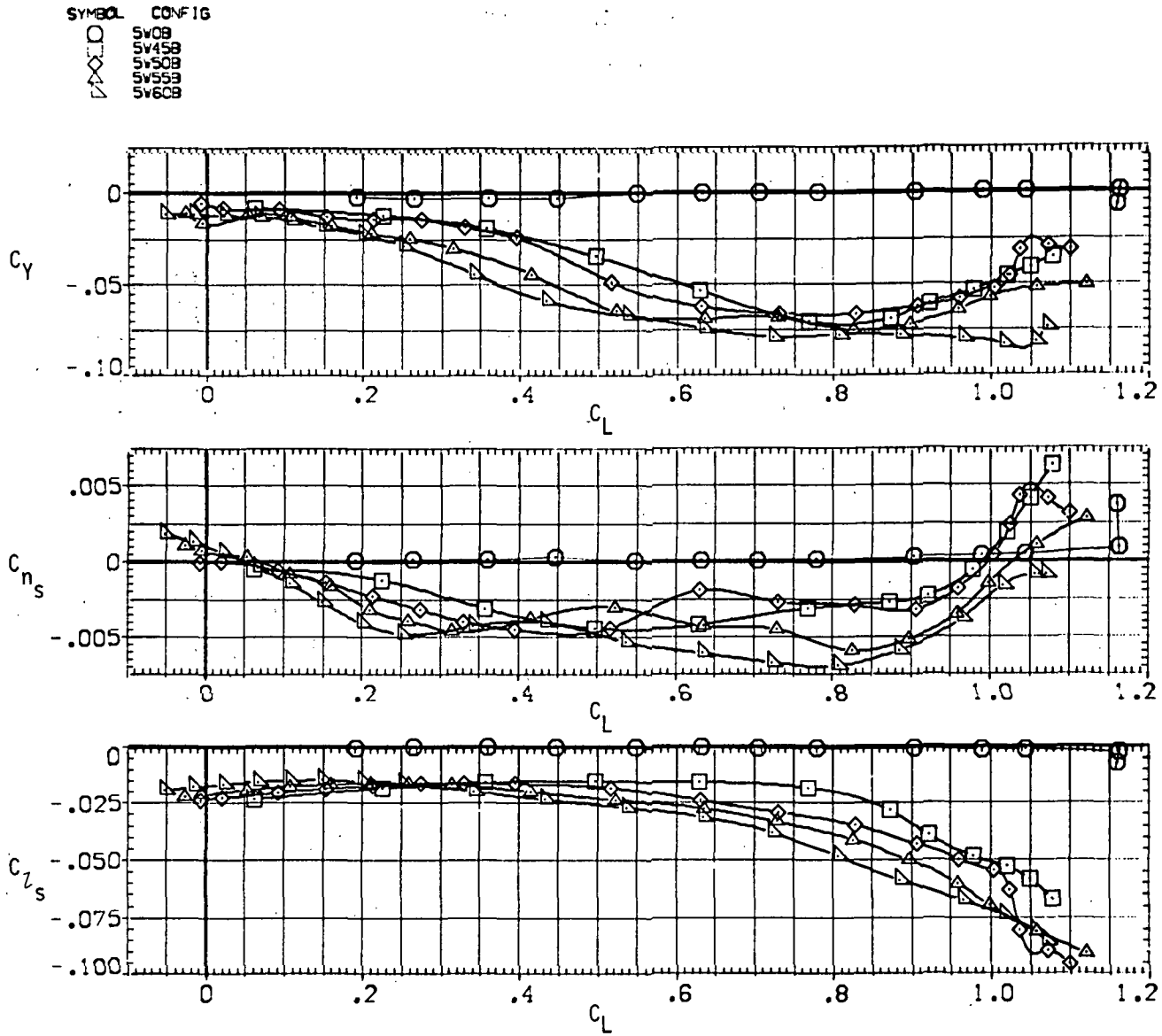

(e) C_Y, C_{n_s} and C_{l_s} versus C_L.

Figure 7.– Continued.

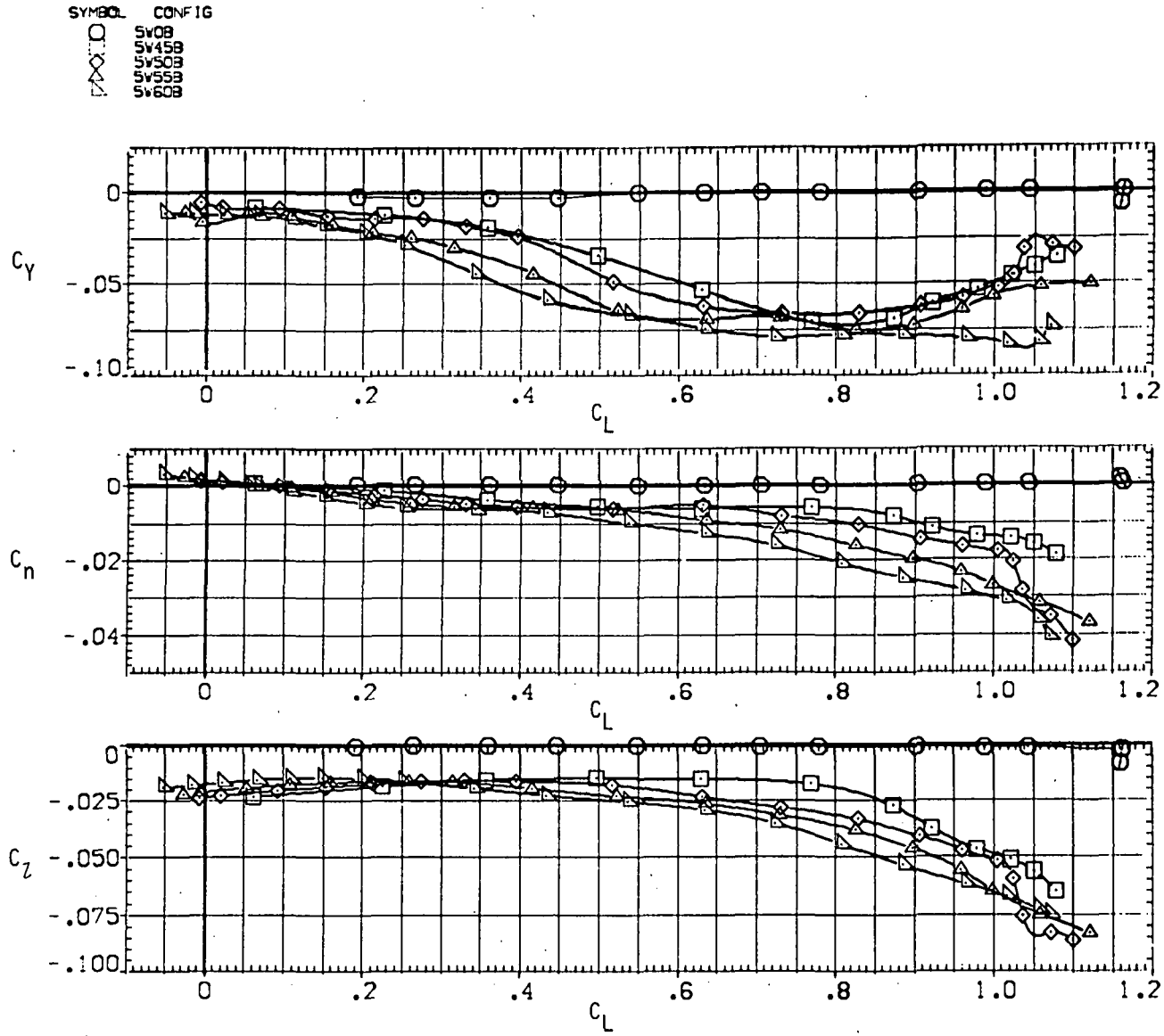

(f) C_Y, C_n and C_l versus C_L.

Figure 7.– Concluded.

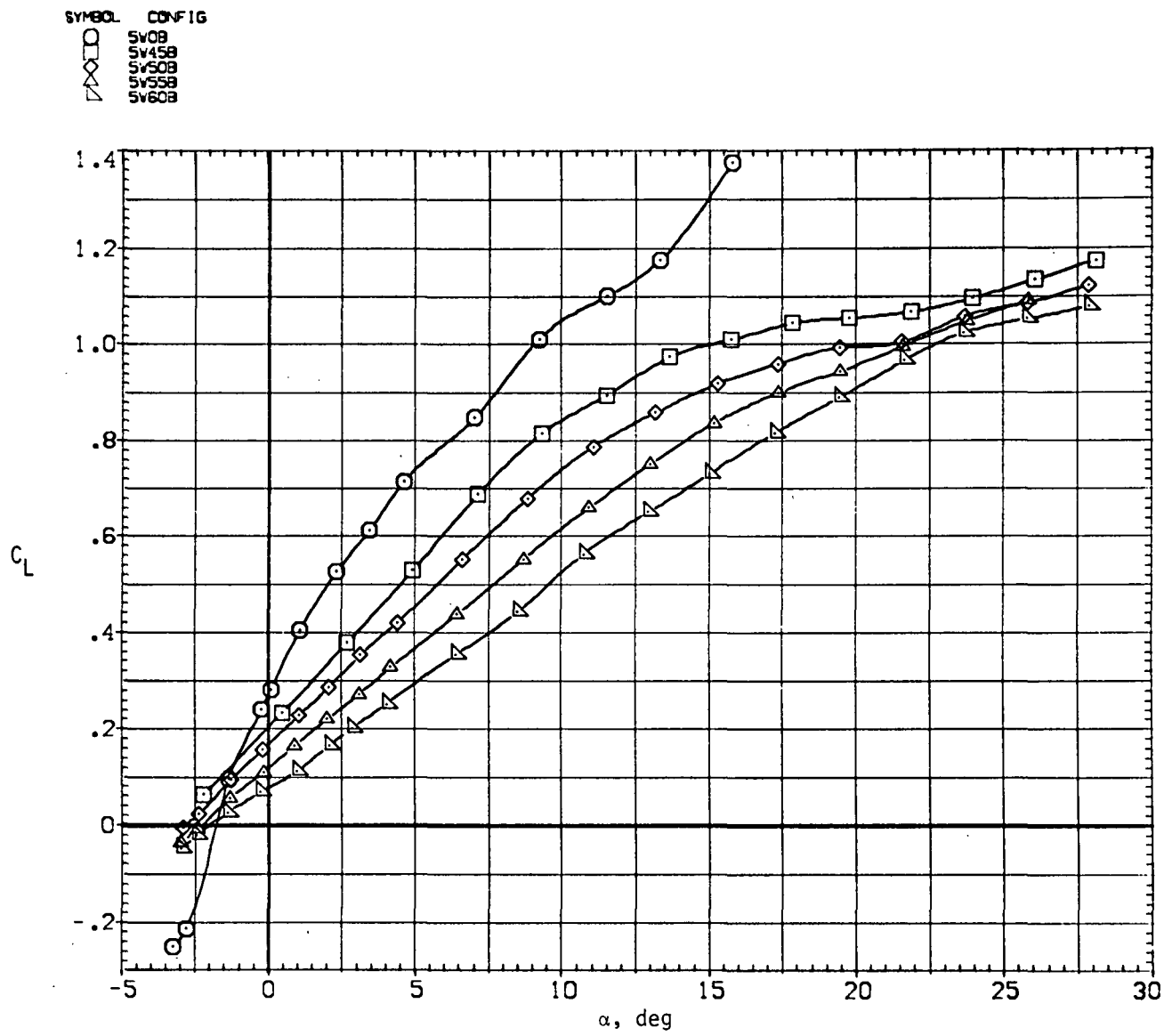

(a) C_L versus α.

Figure 8.– Longitudinal stability characteristics of the oblique wing with intermediate bend, $M = 0.9$, $\beta = 0$.

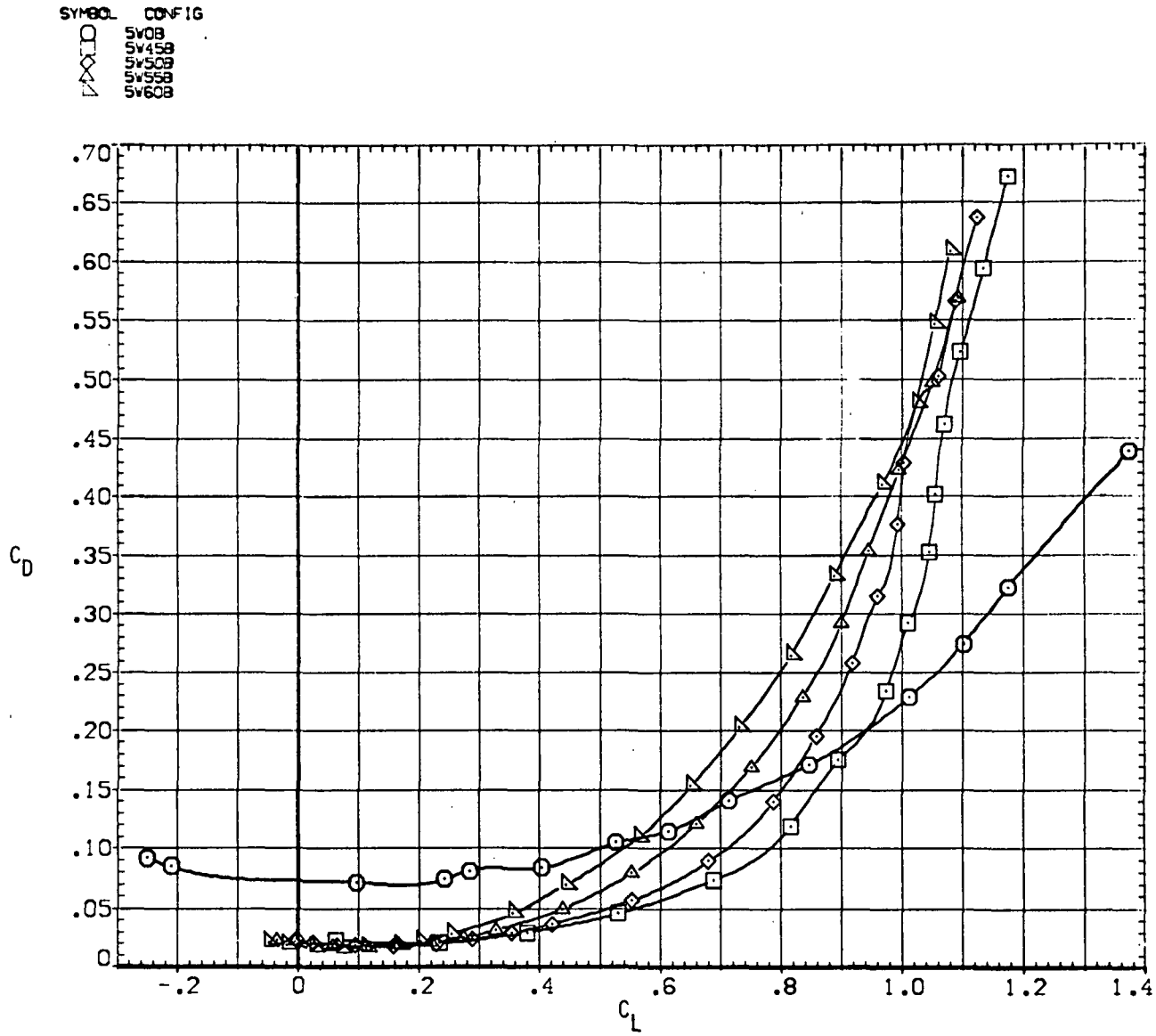

(b) C_D versus C_L.

Figure 8.– Continued.

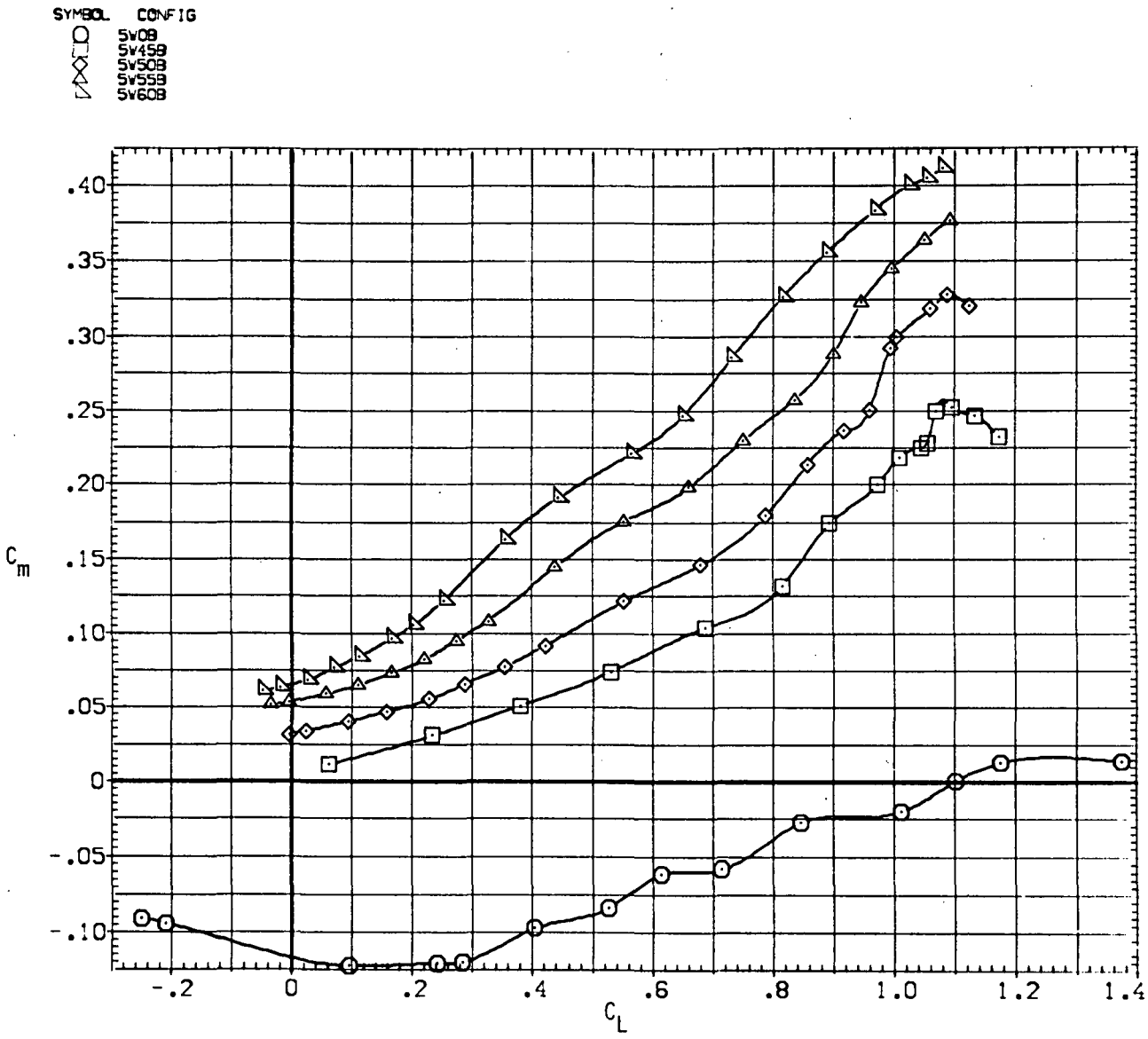

(c) C_m versus C_L.

Figure 8.– Continued.

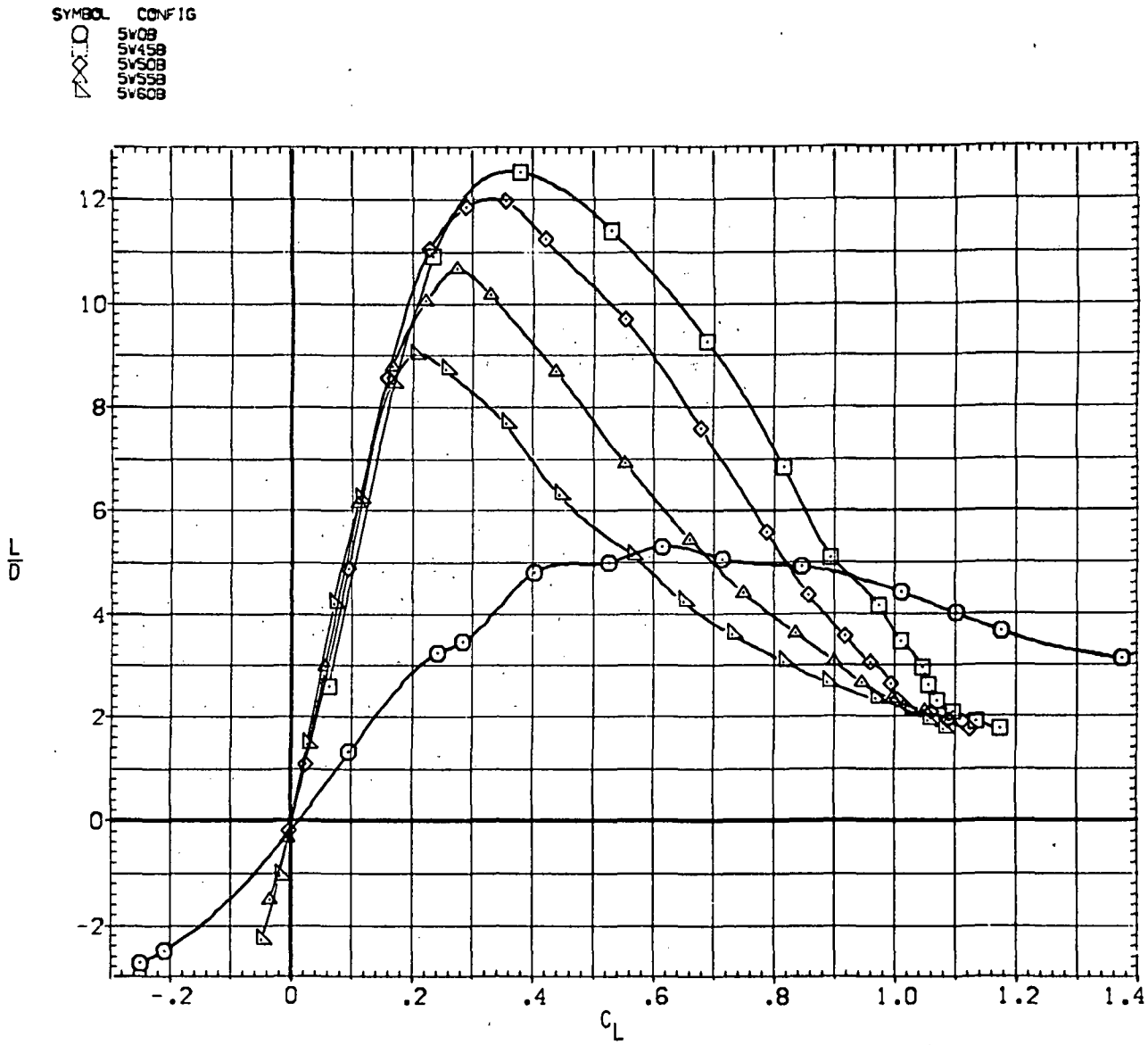

(d) L/D versus C_L.

Figure 8.– Continued.

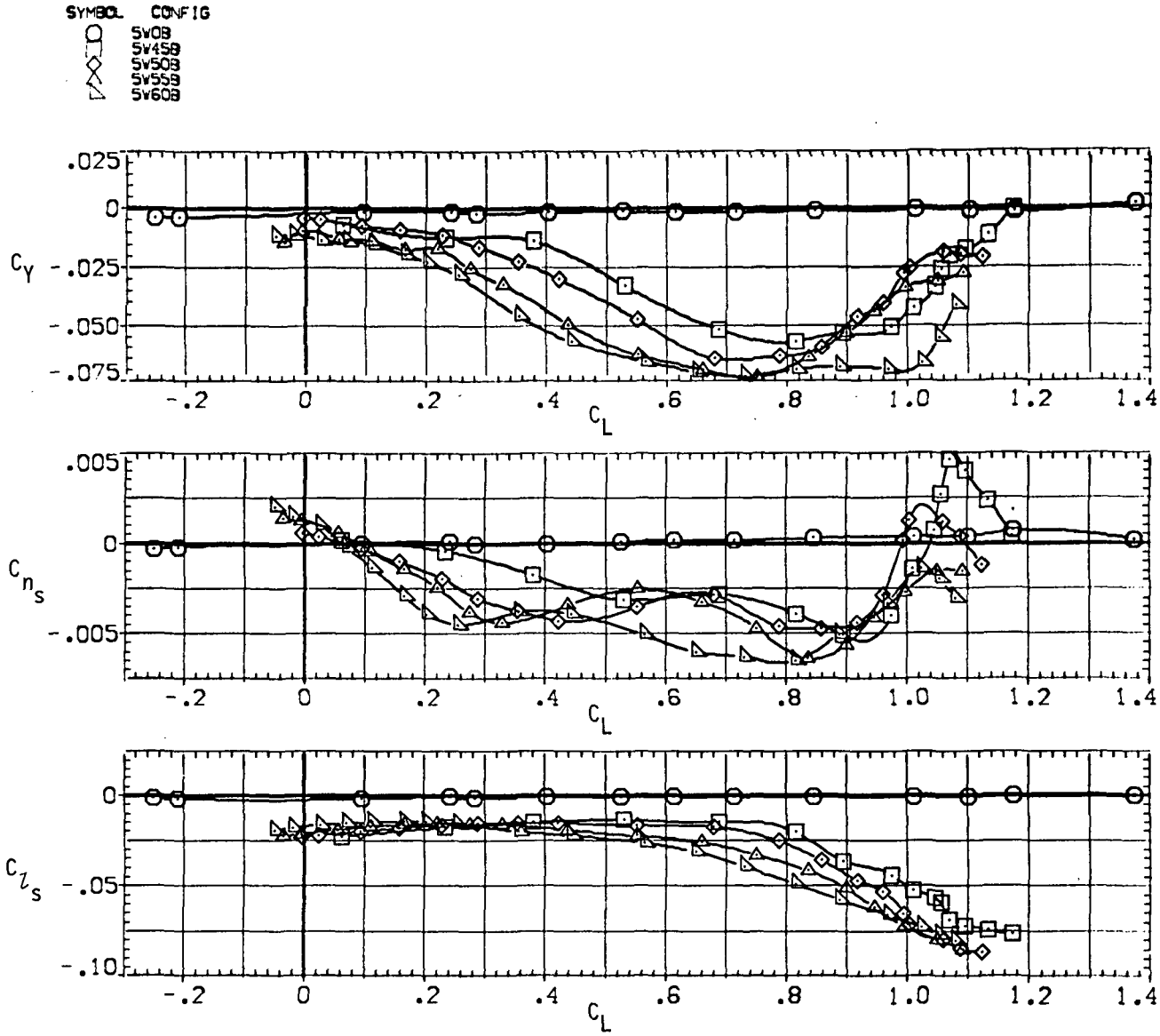

(e) C_Y, C_{n_s} and C_{l_s} versus C_L.

Figure 8.– Continued.

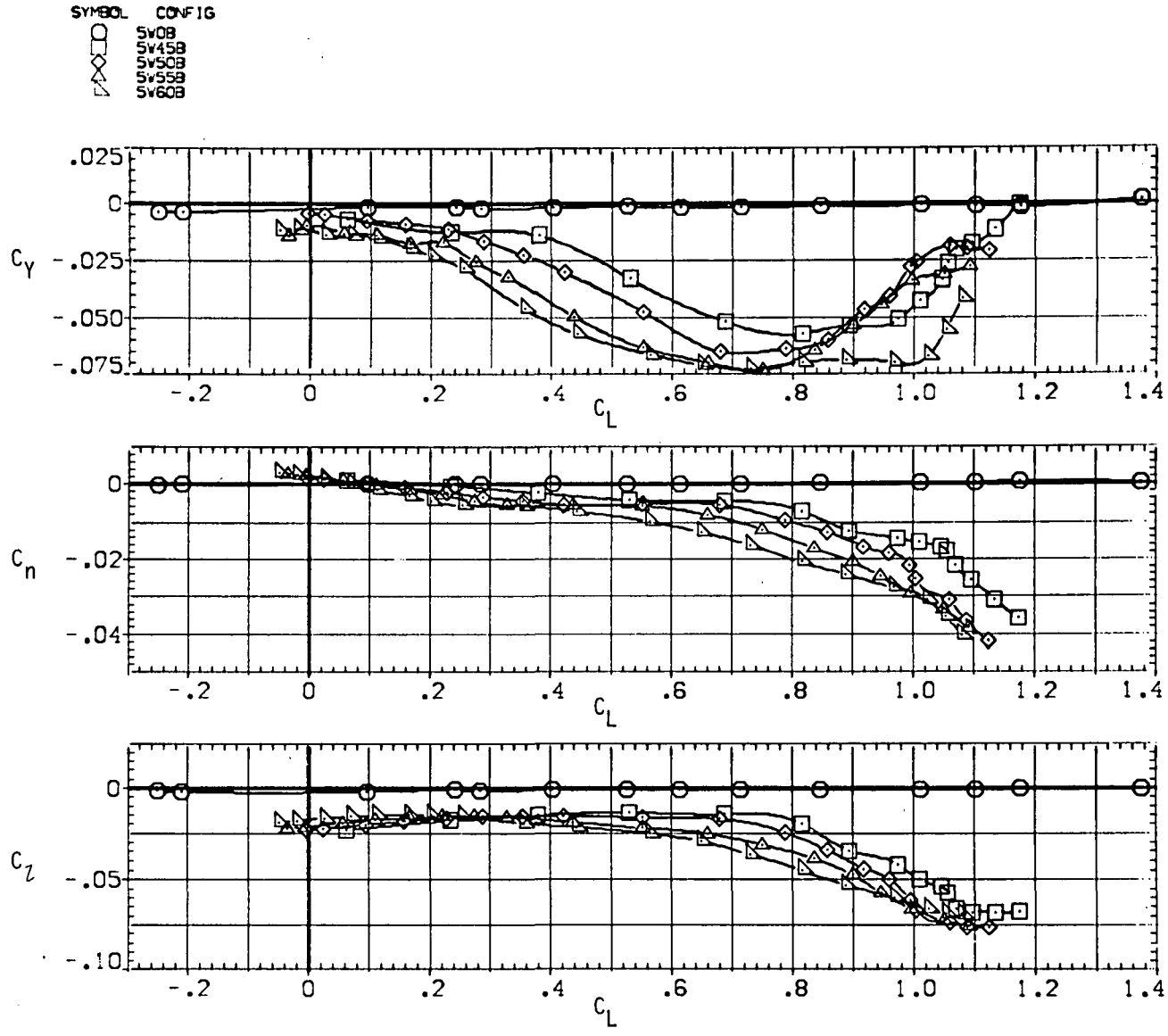

(f) C_Y, C_n and C_l versus C_L.

Figure 8.– Concluded.

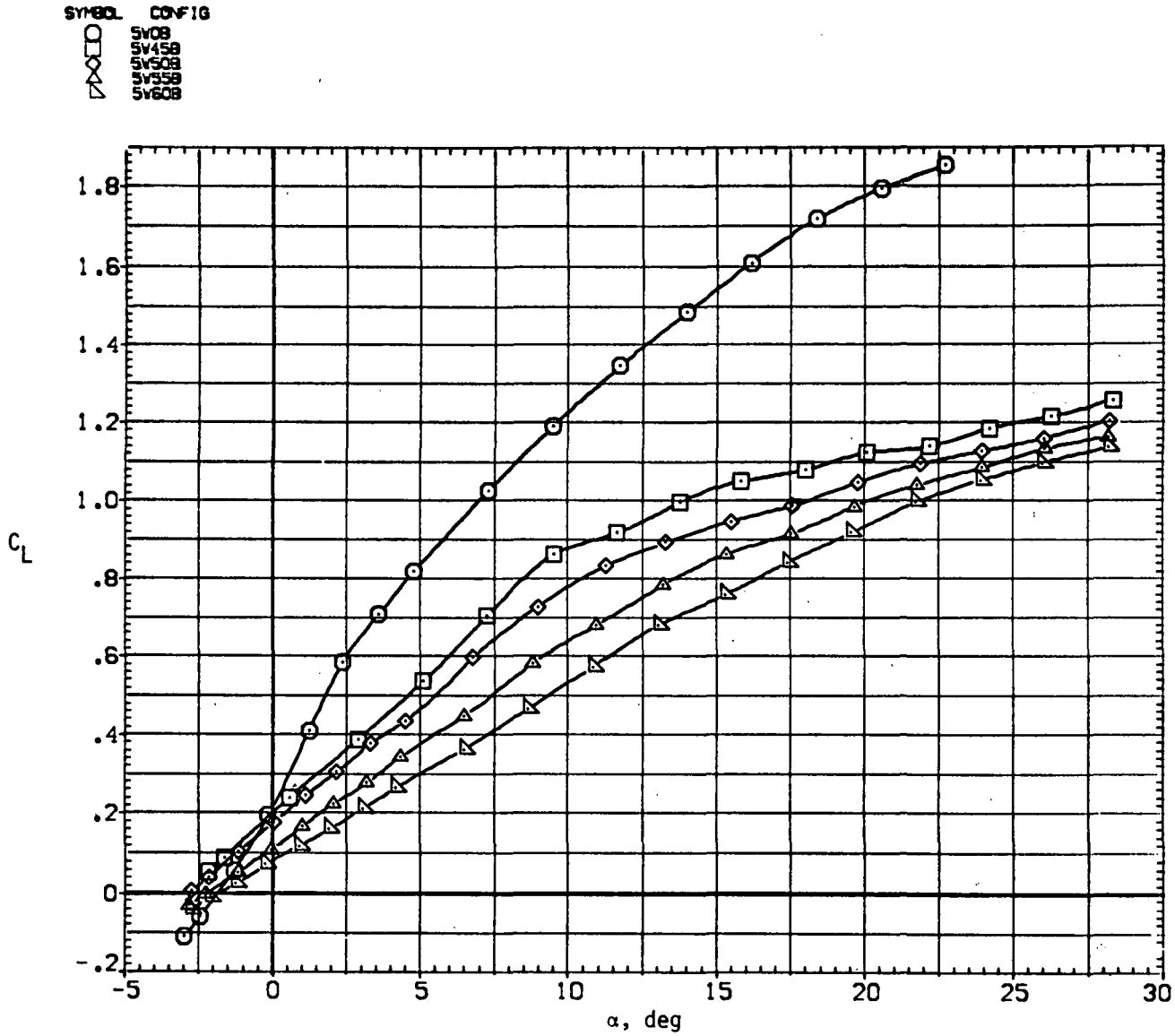

(a) C_L versus α.

Figure 9.– Longitudinal stability characteristics of the oblique wing with intermediate bend, $M = 0.95$, $\beta = 0$.

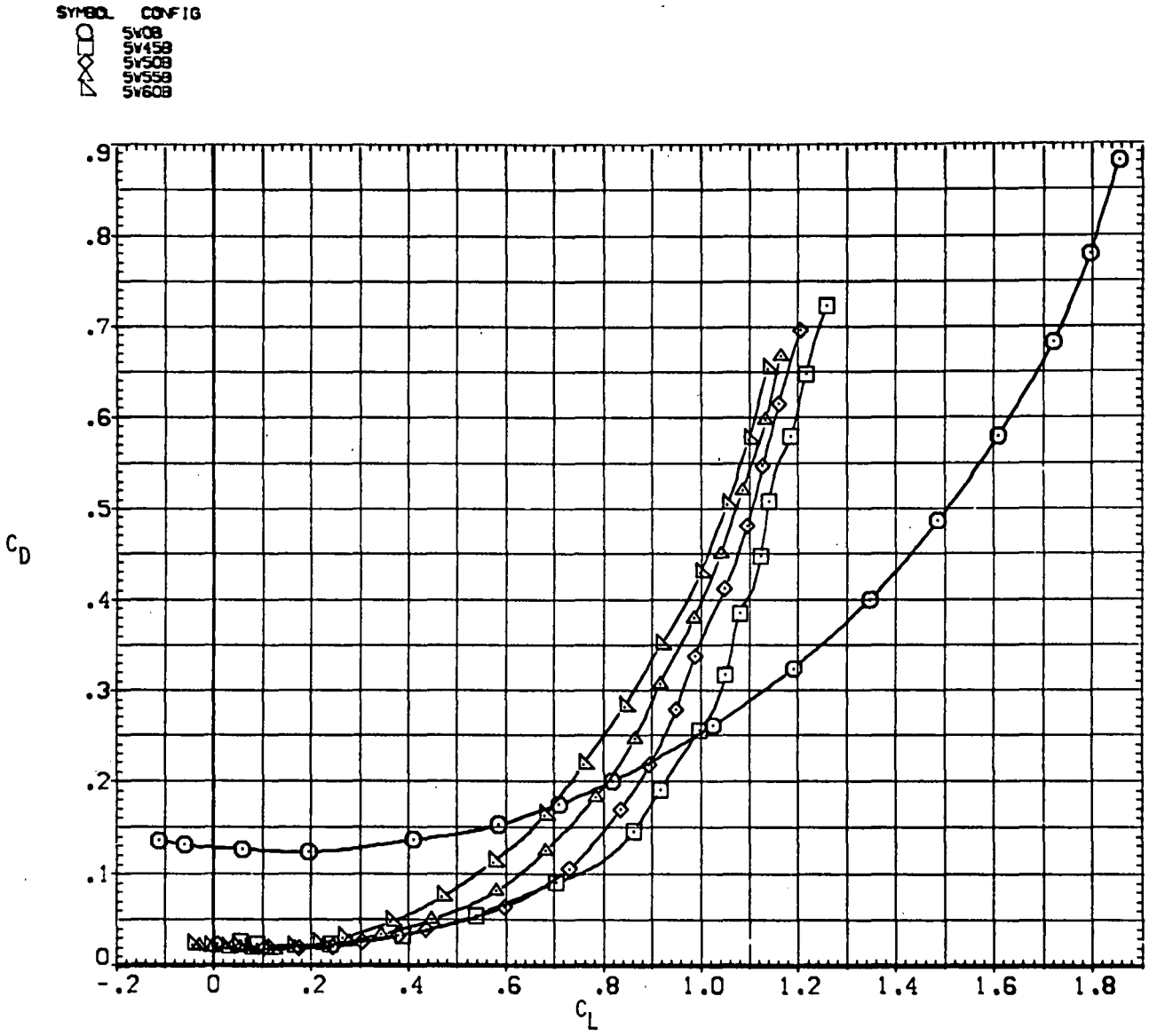

(b) C_D versus C_L.

Figure 9.— Continued.

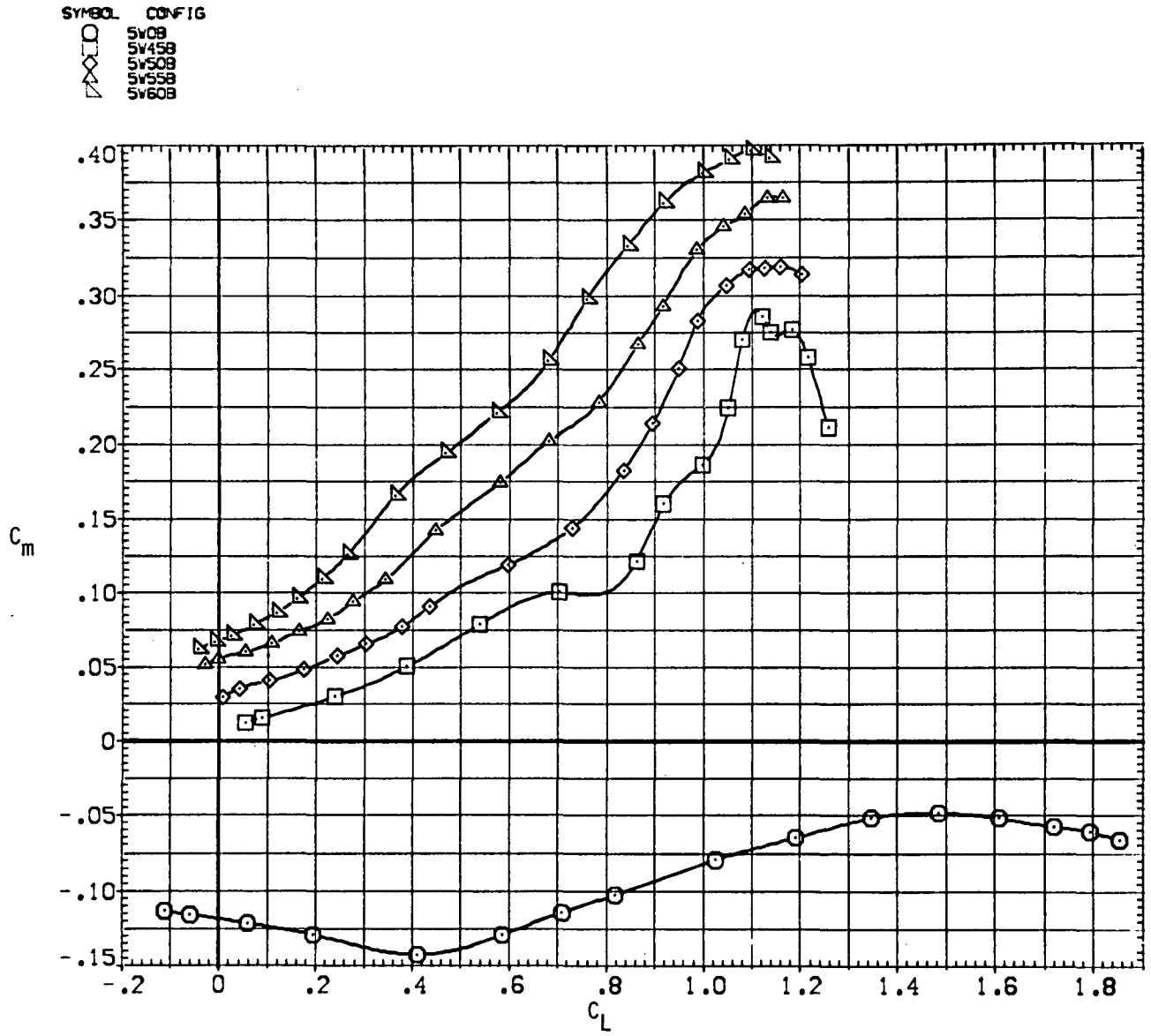

(c) C_m versus C_L.

Figure 9.– Continued.

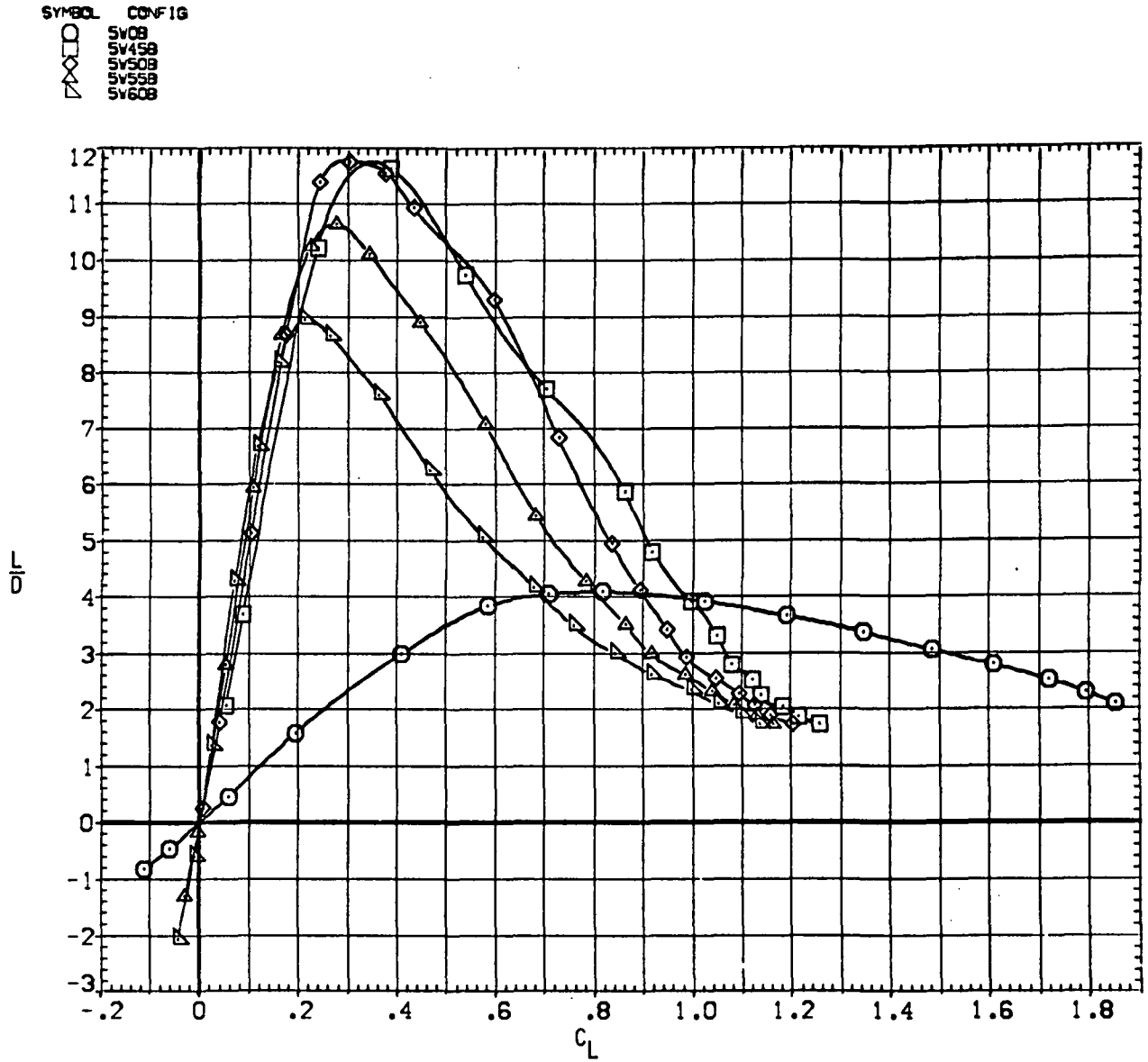

(d) L/D versus C_L.

Figure 9.– Continued.

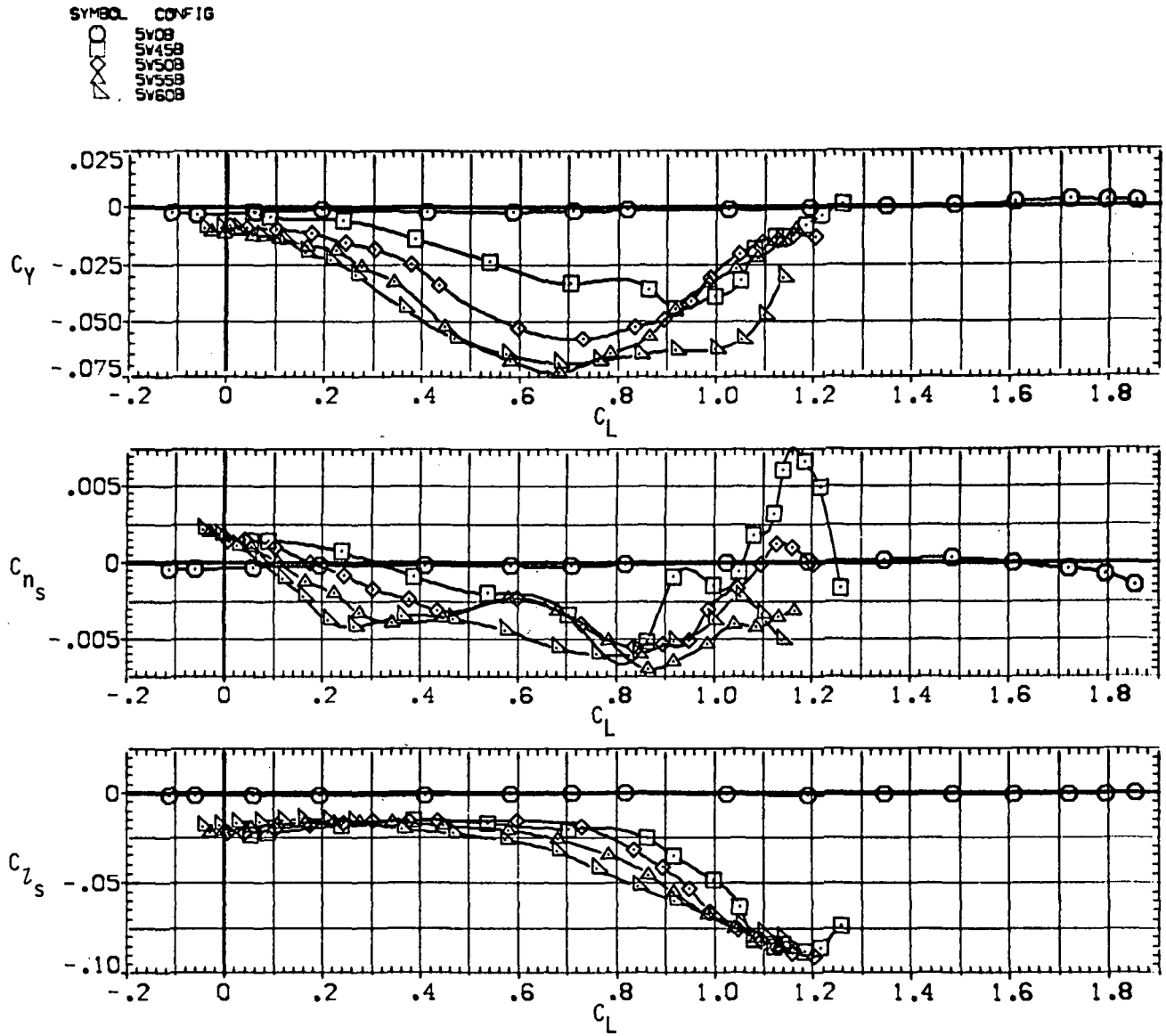

(e) C_Y, C_{n_s} and C_{l_s} versus C_L.

Figure 9.– Continued.

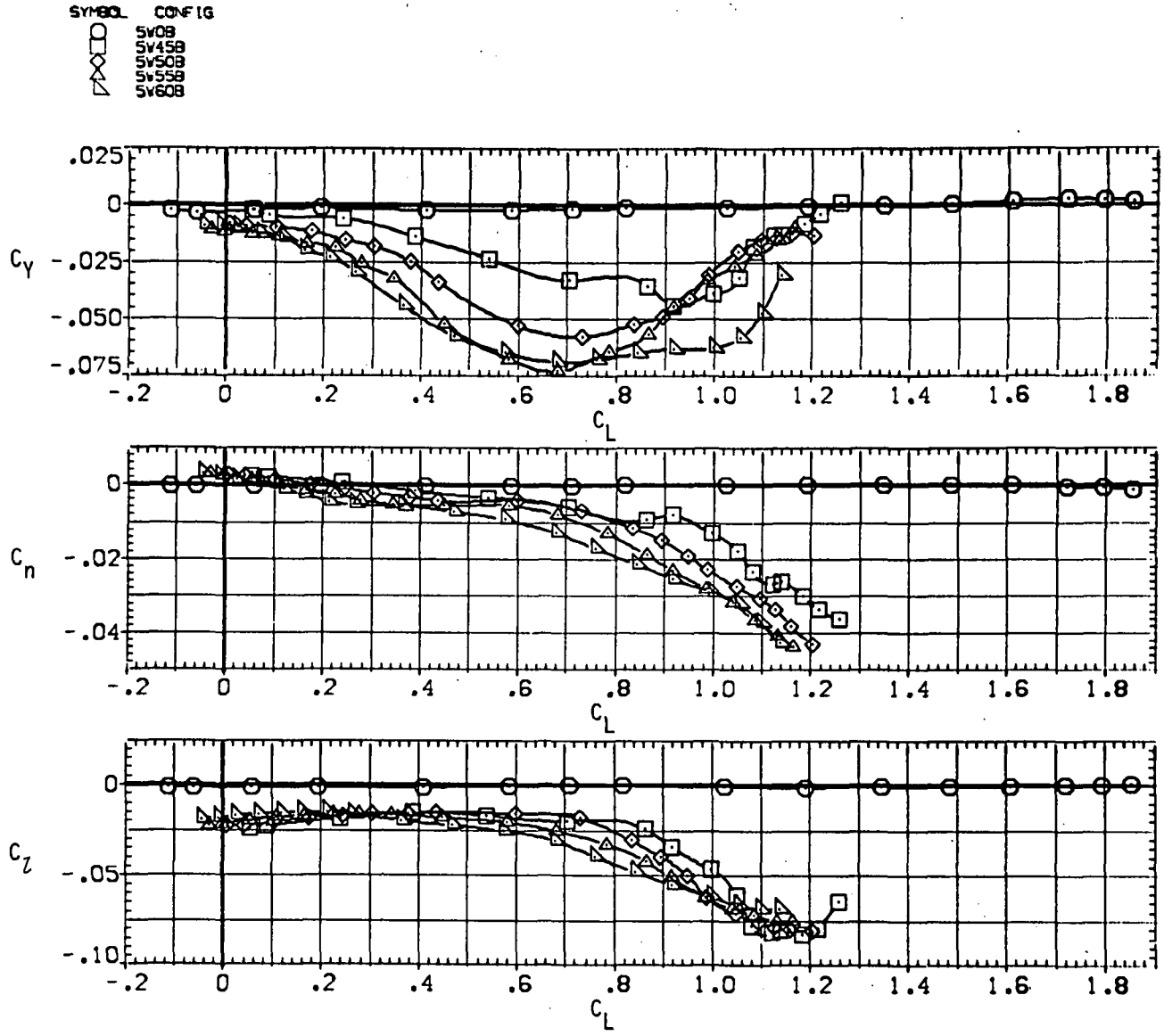

(f) C_Y, C_n and C_l versus C_L.

Figure 9.– Concluded.

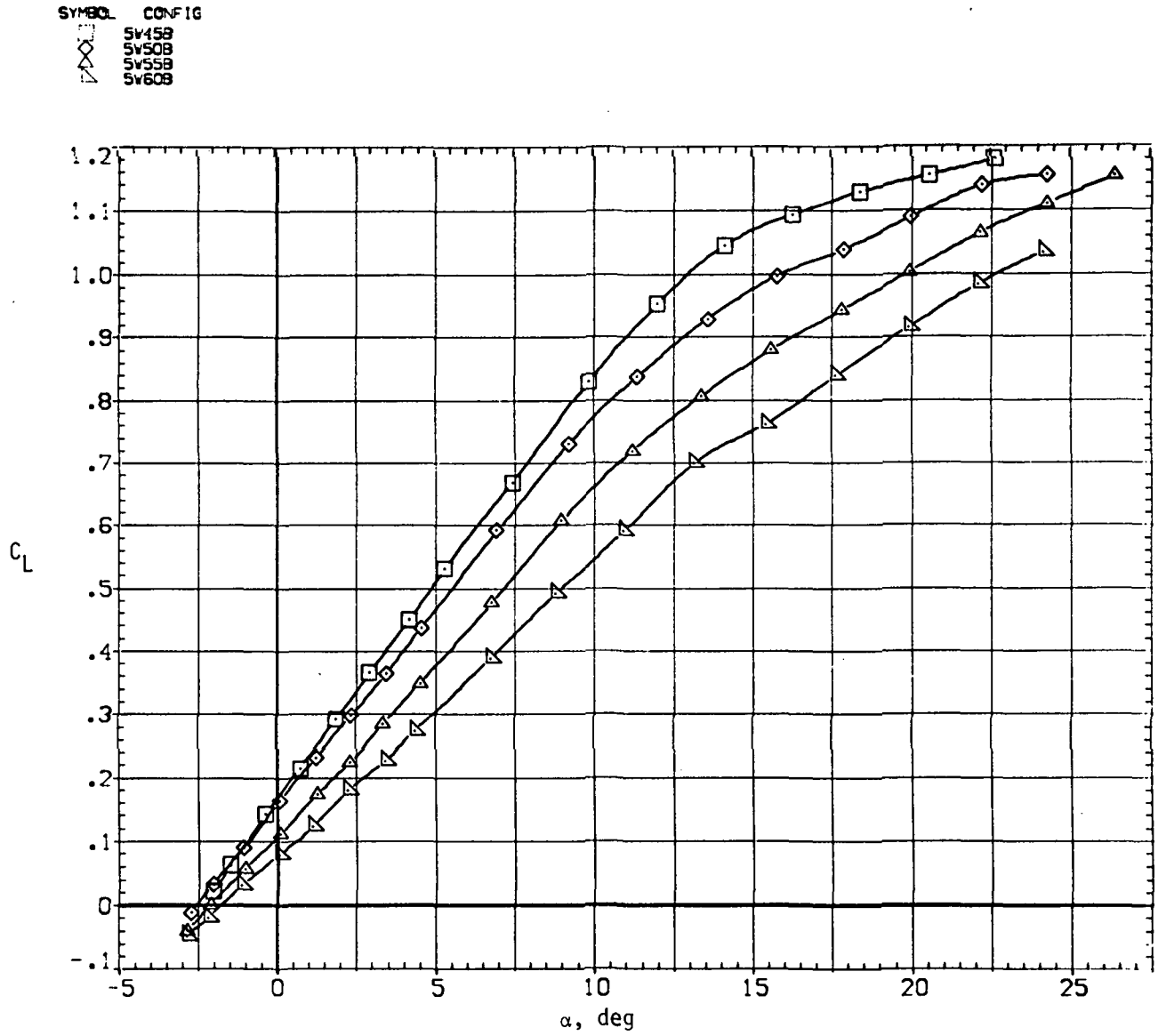

(a) C_L versus α.

Figure 10.– Longitudinal stability characteristics of the oblique wing with intermediate bend, $M = 1.1$, $\beta = 0$.

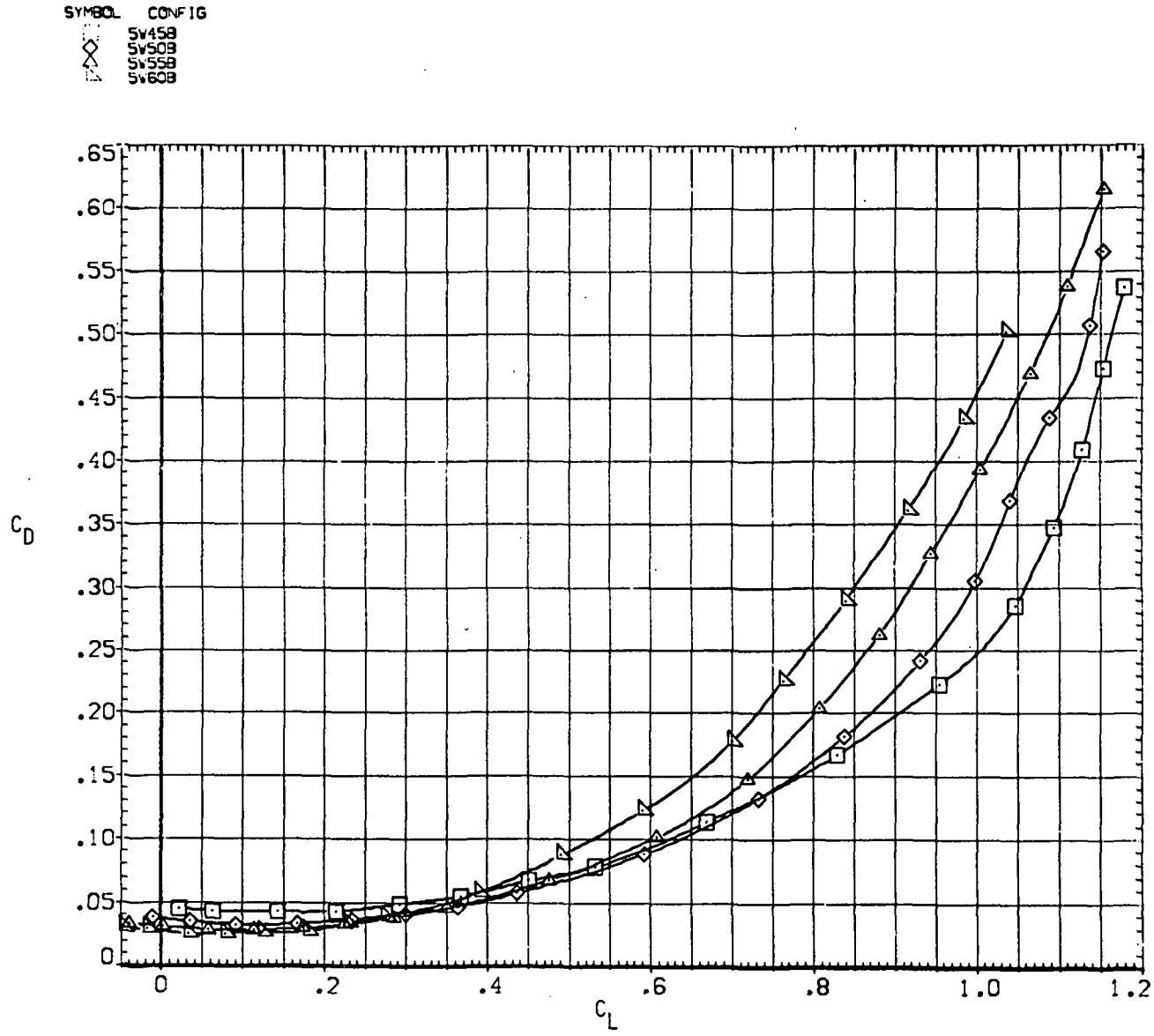

(b) C_D versus C_L.

Figure 10.– Continued.

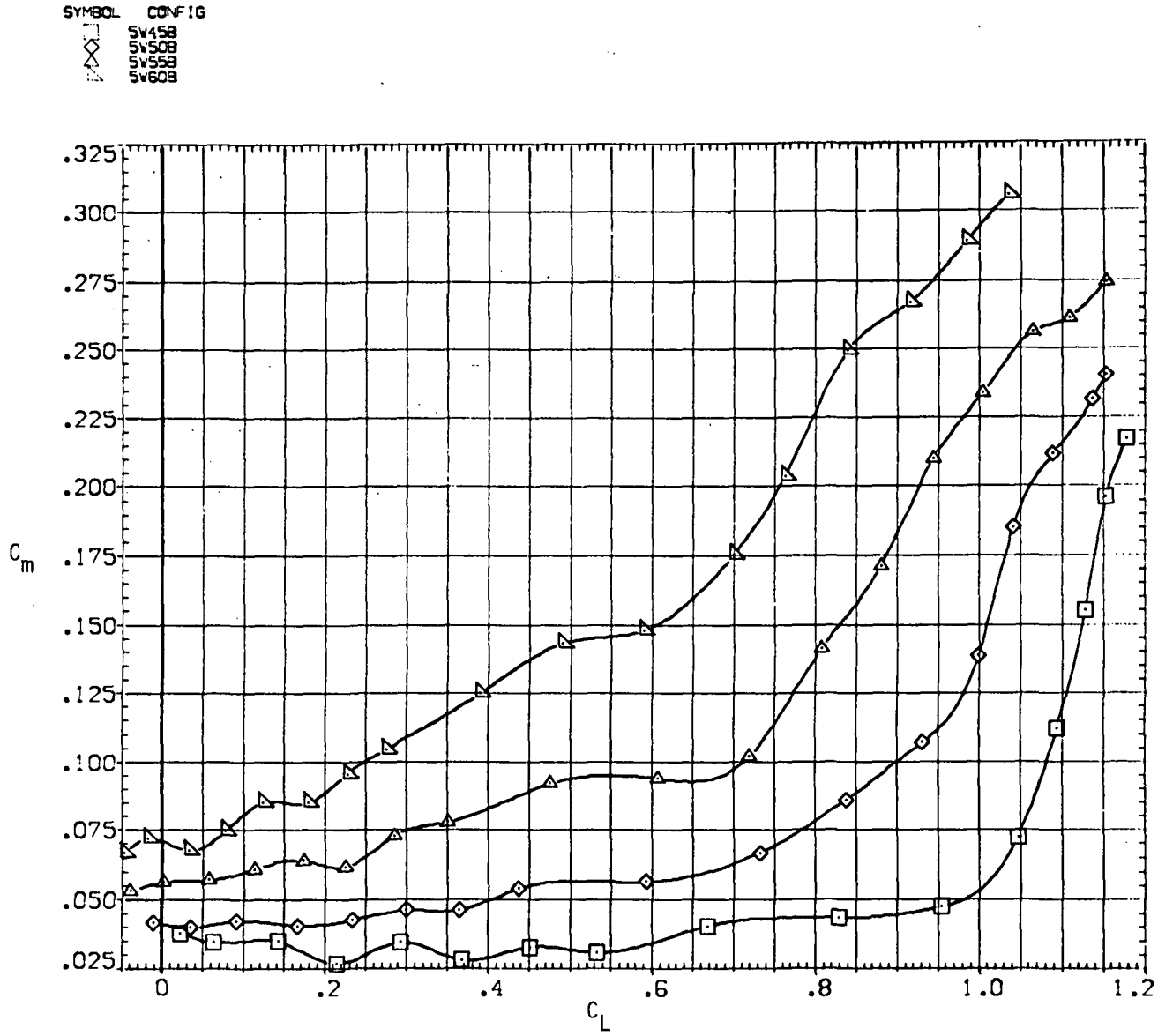

(c) C_m versus C_L.

Figure 10.– Continued.

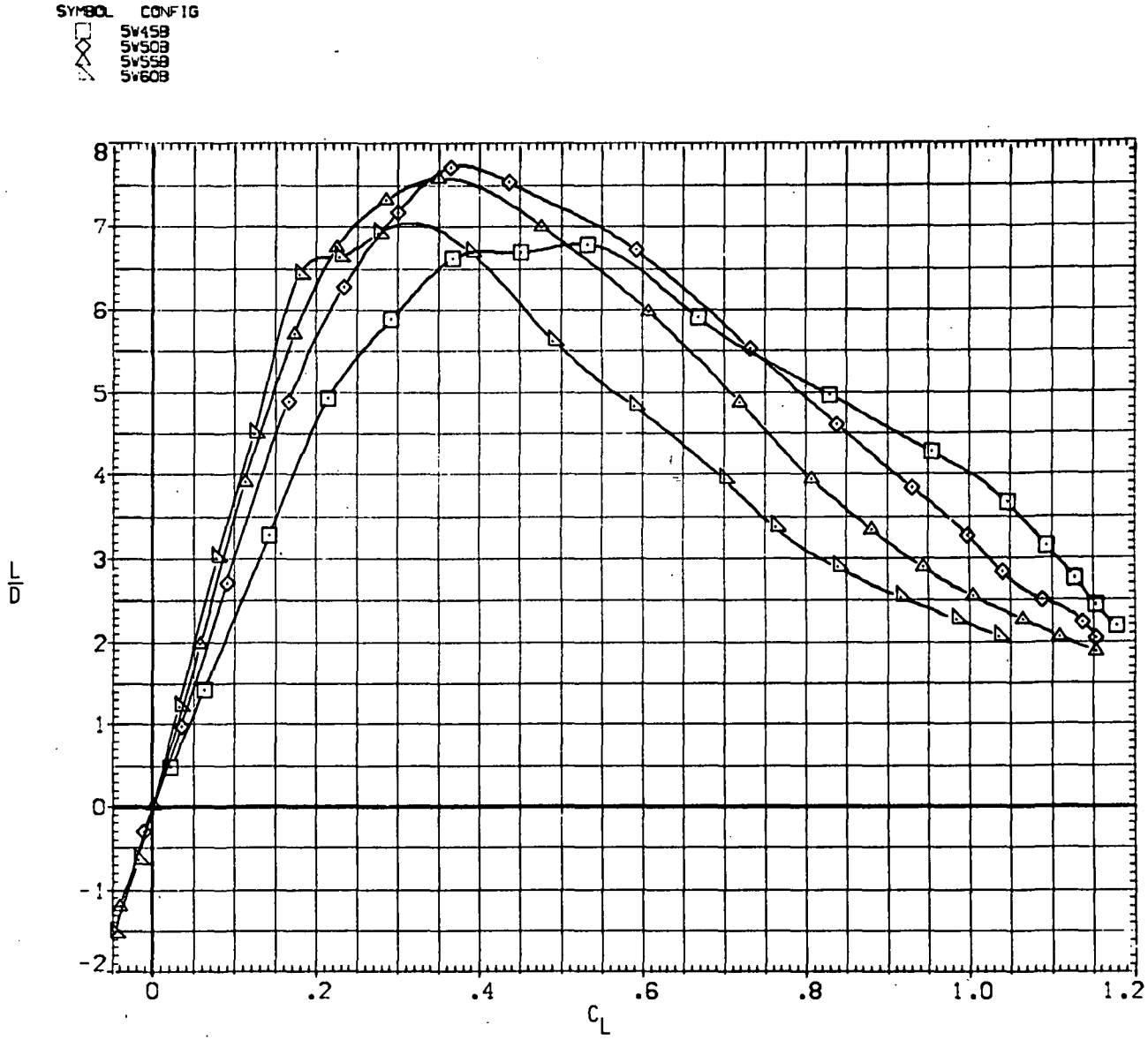

(d) L/D versus C_L.

Figure 10.– Continued.

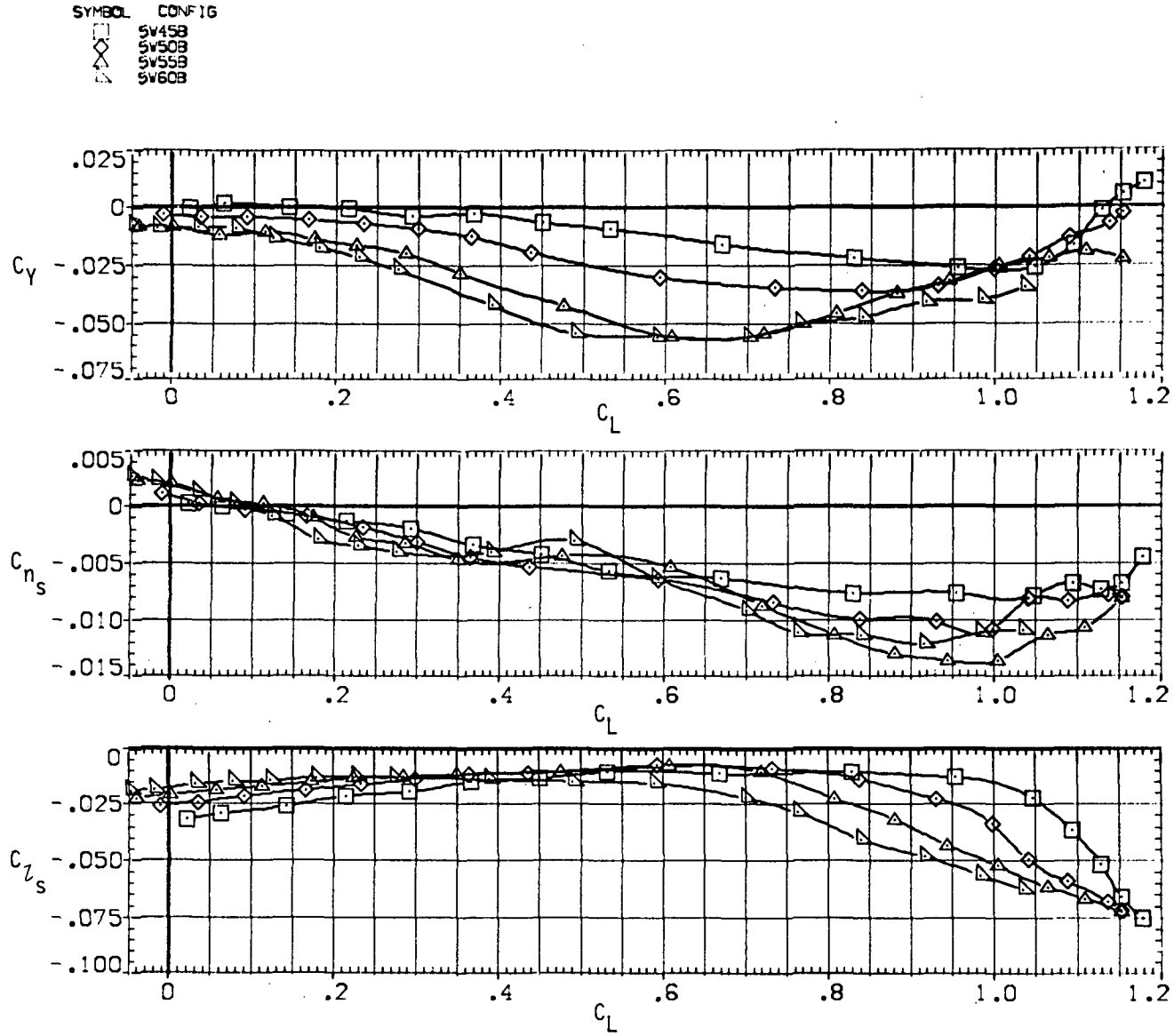

(e) C_Y, C_{n_s} and C_{l_s} versus C_L.

Figure 10.– Continued.

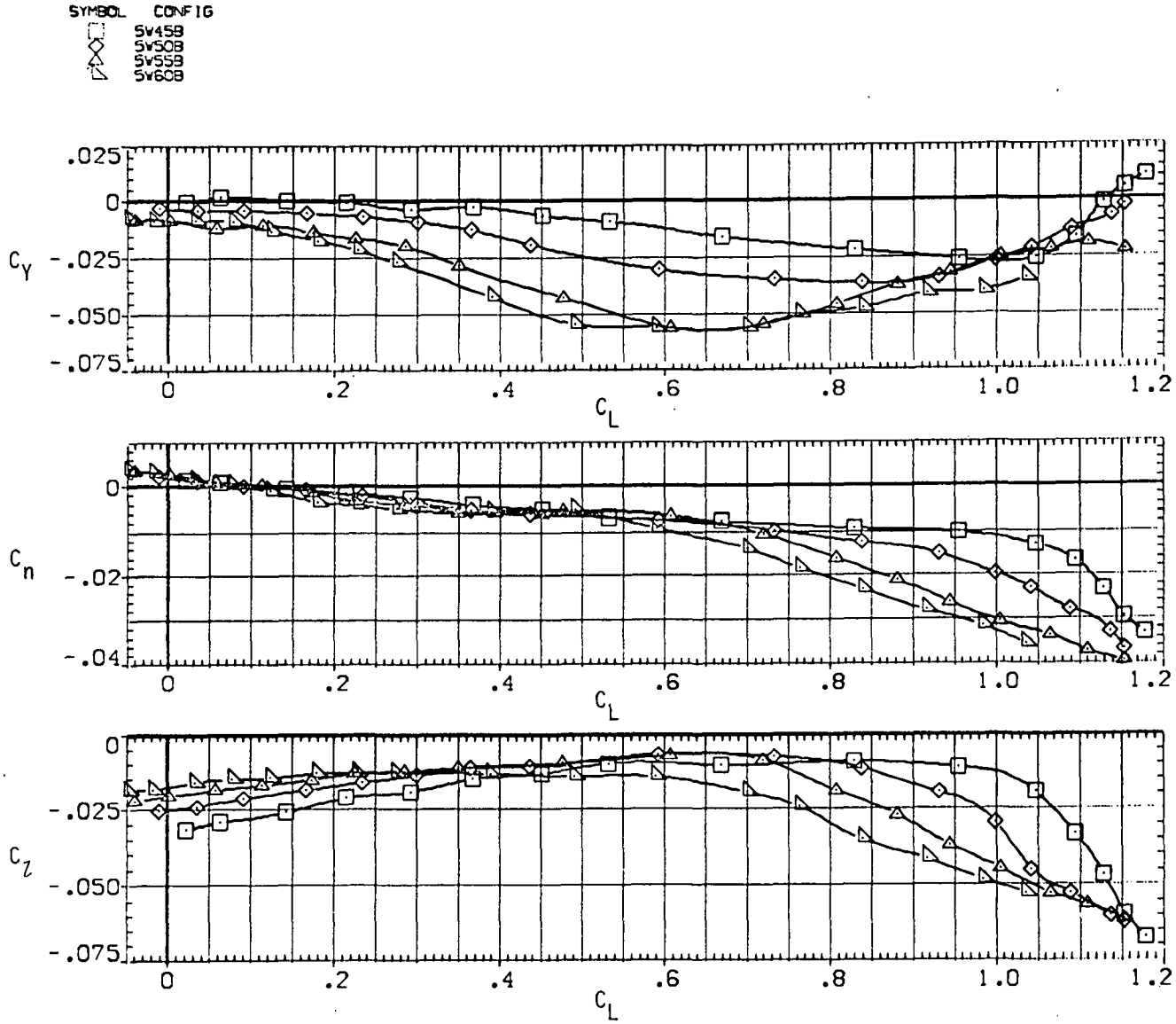

(f) C_Y, C_n and C_l versus C_L.

Figure 10.– Concluded.

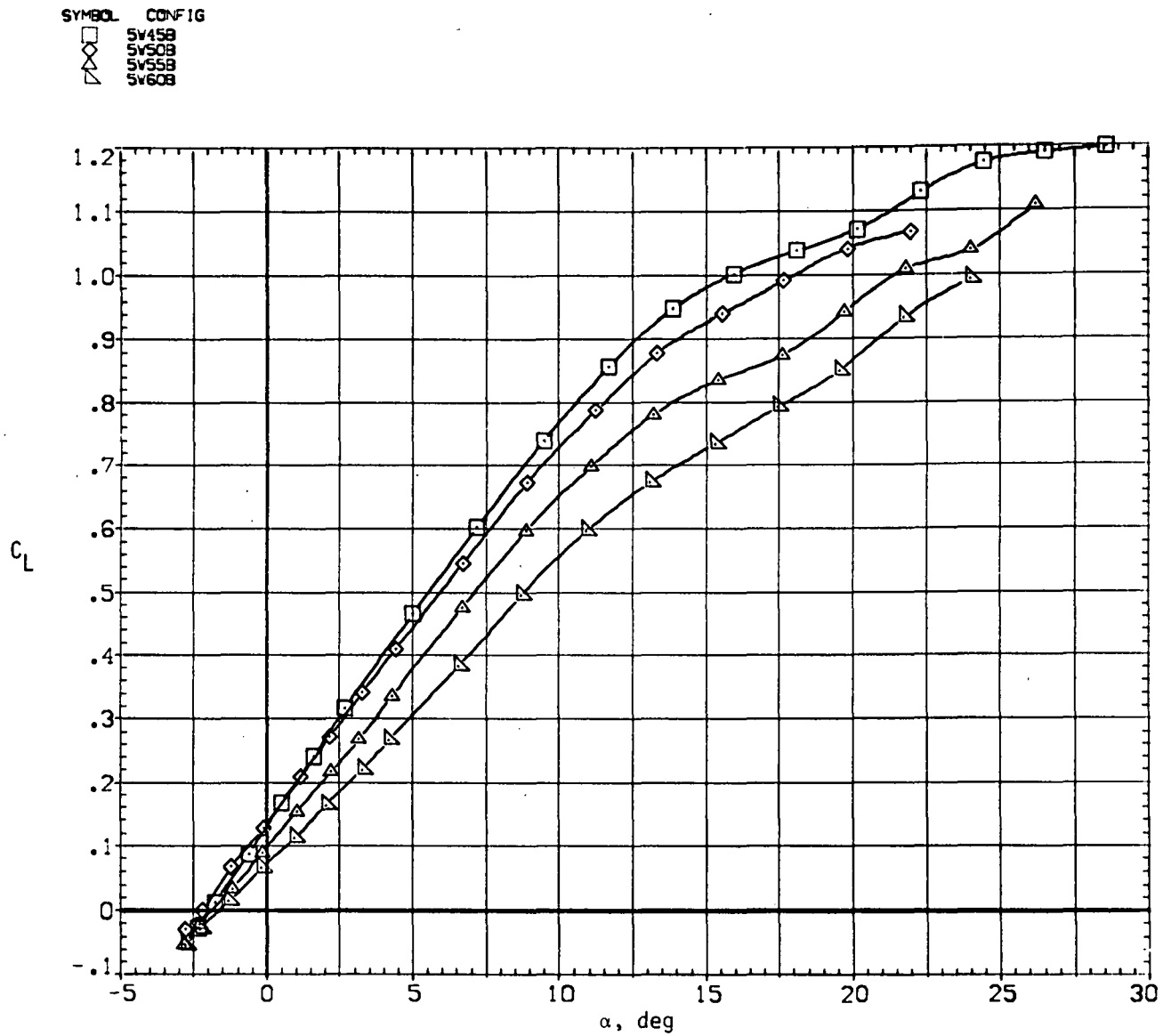

(a) C_L versus α.

Figure 11.— Longitudinal stability characteristics of the oblique wing with intermediate bend, $M = 1.2$, $\beta = 0$.

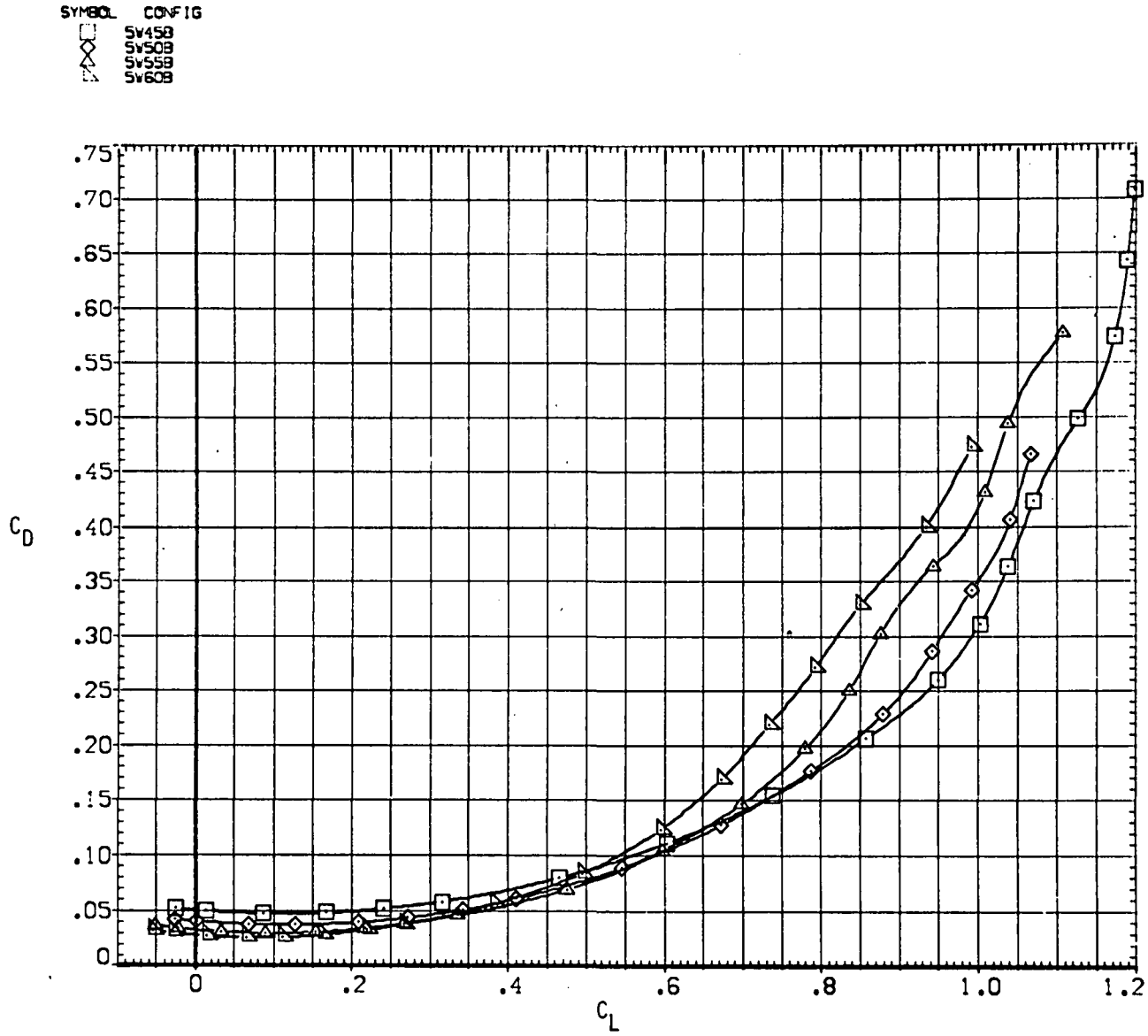

(b) C_D versus C_L.

Figure 11.– Continued.

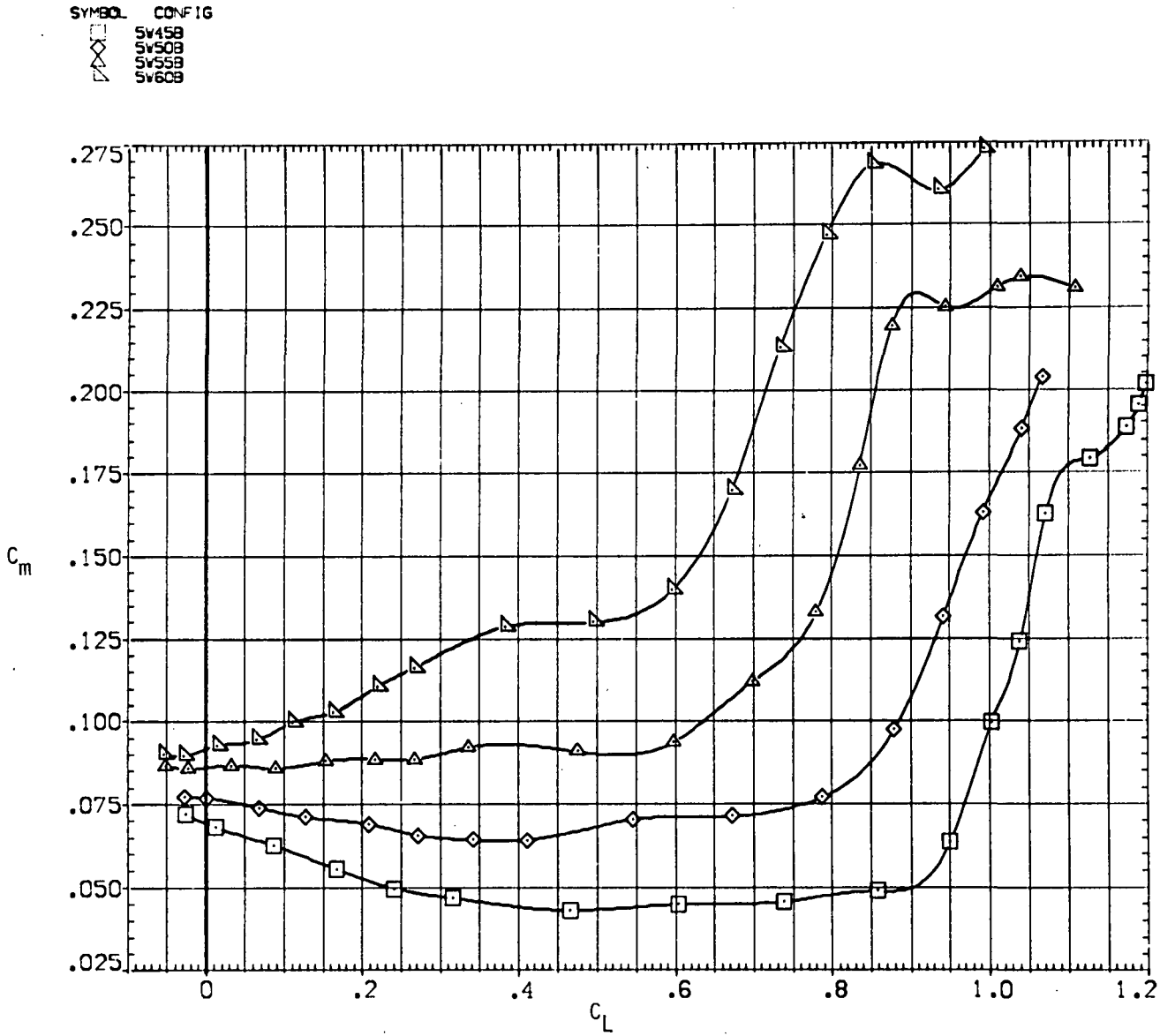

(c) C_m versus C_L.

Figure 11.– Continued.

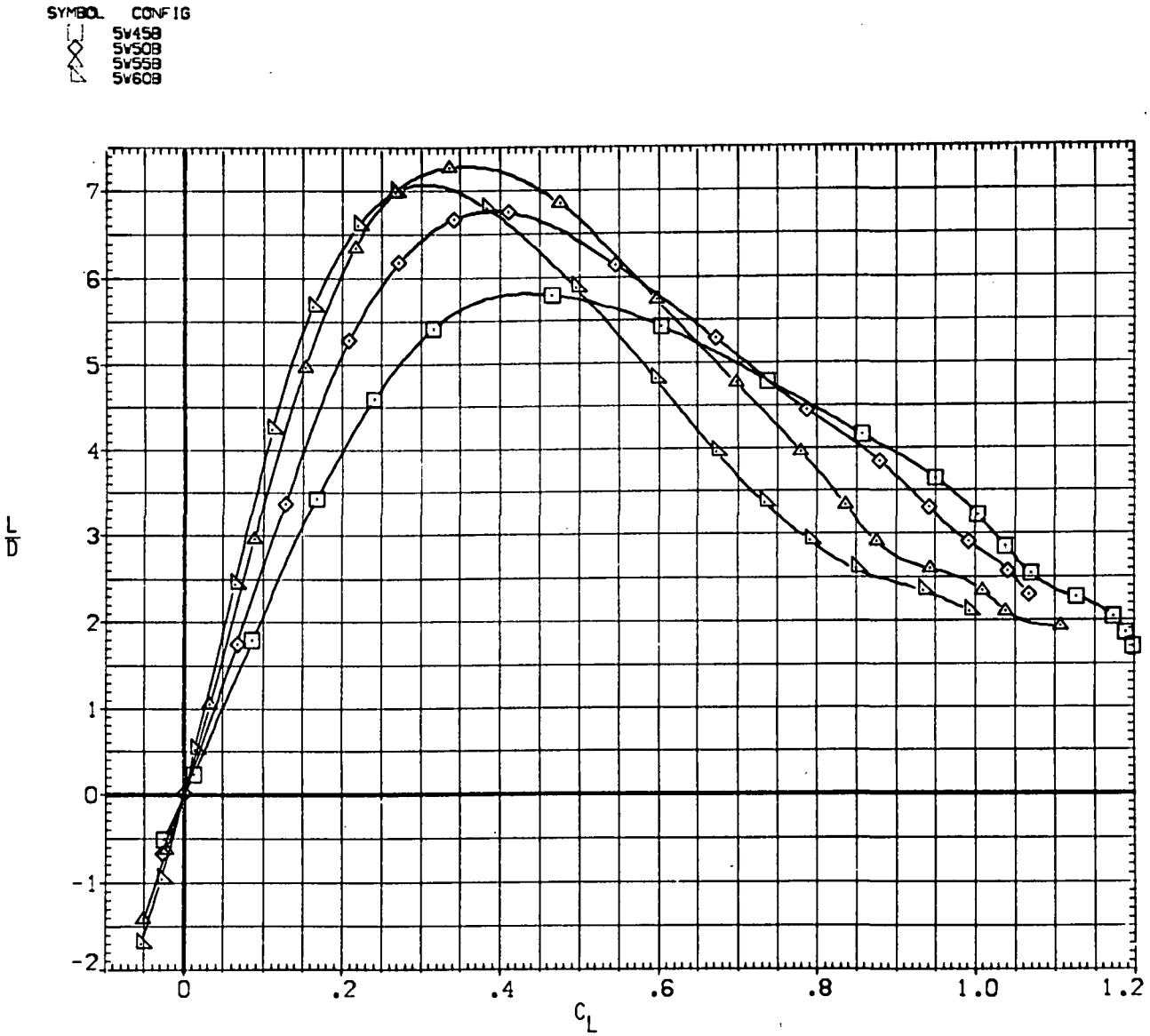

(d) L/D versus C_L.

Figure 11.– Continued.

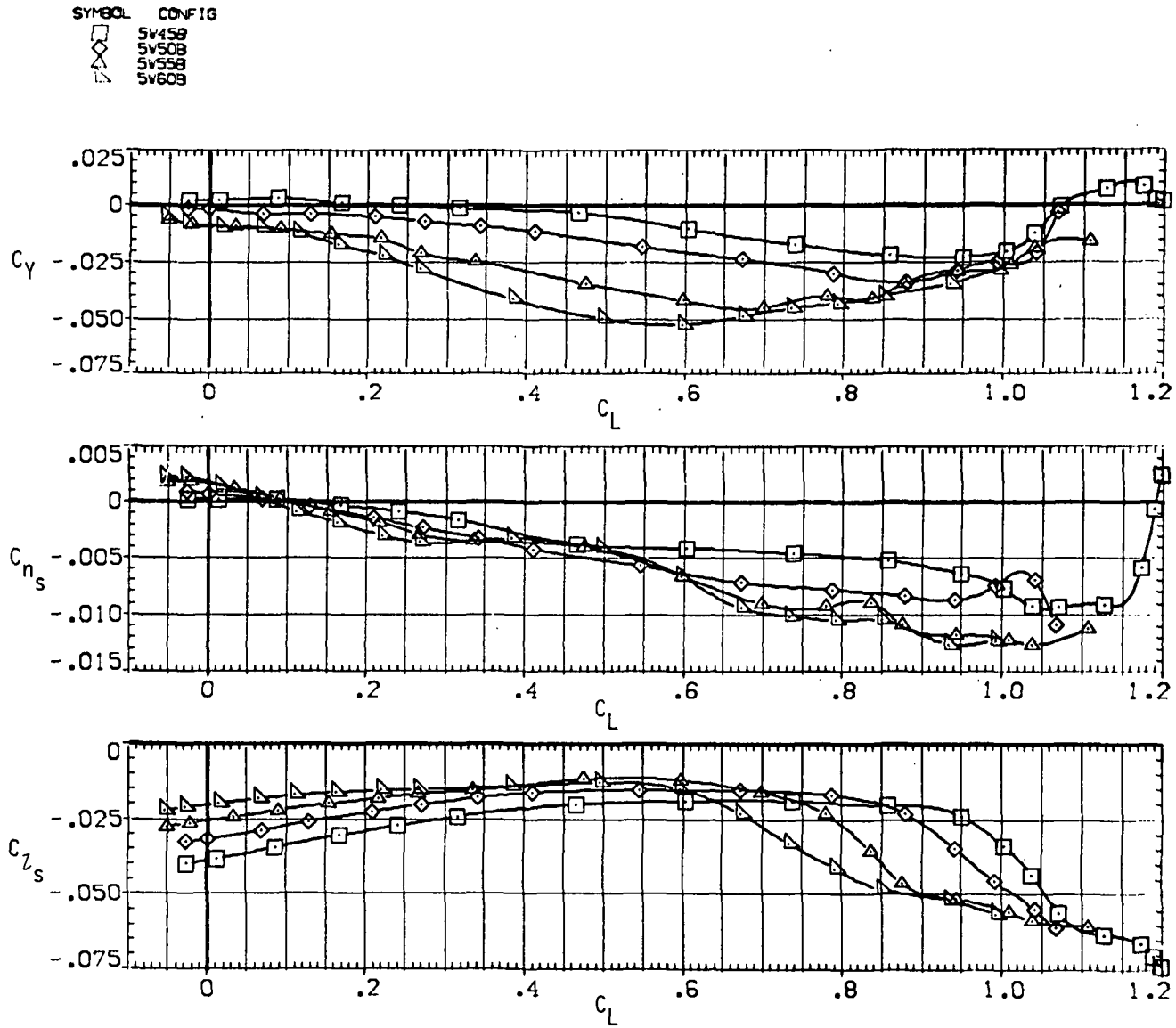

(e) C_Y, C_{n_s} and C_{l_s} versus C_L.

Figure 11.– Continued.

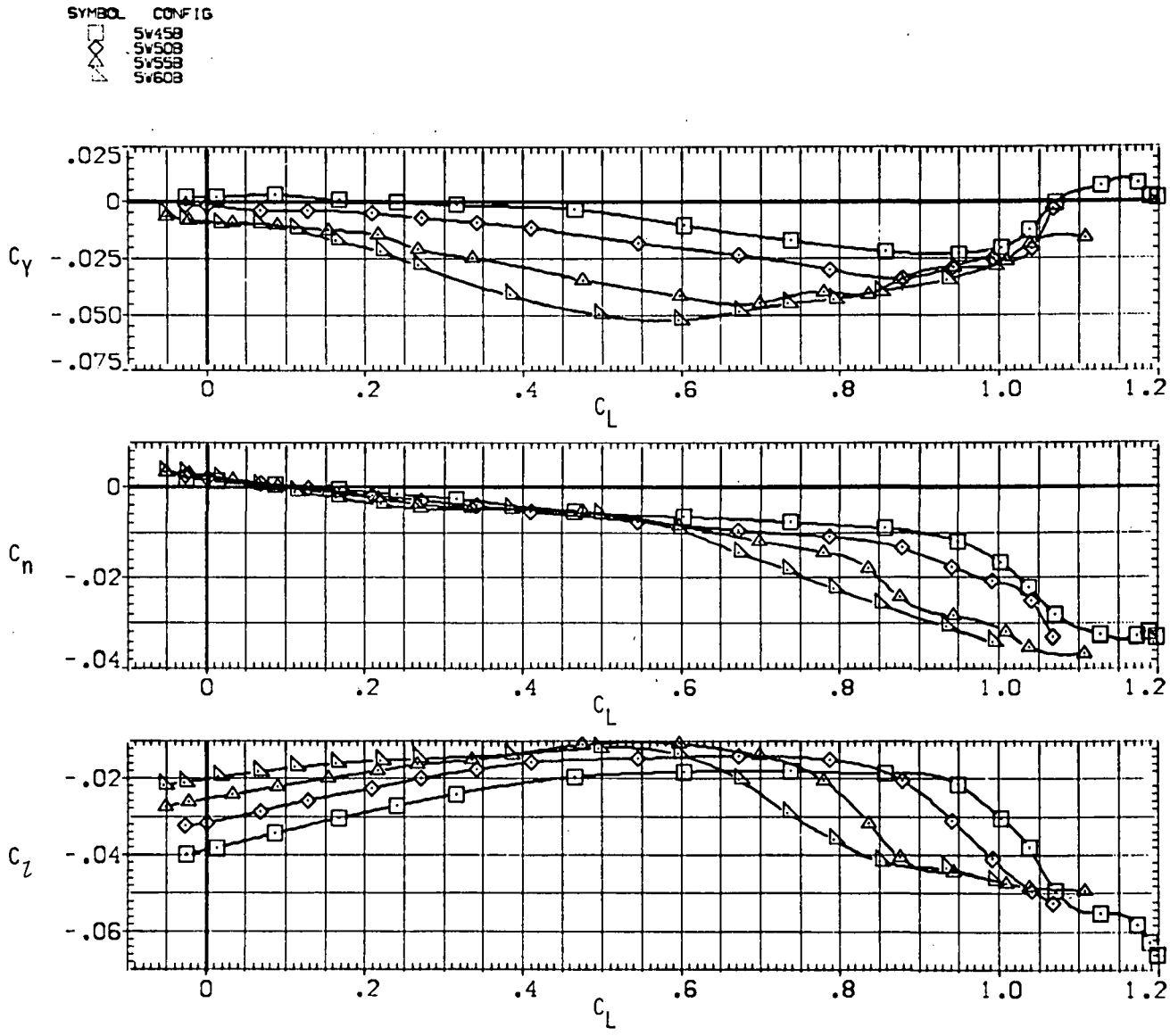

(f) C_Y, C_n and C_l versus C_L.

Figure 11.– Concluded.

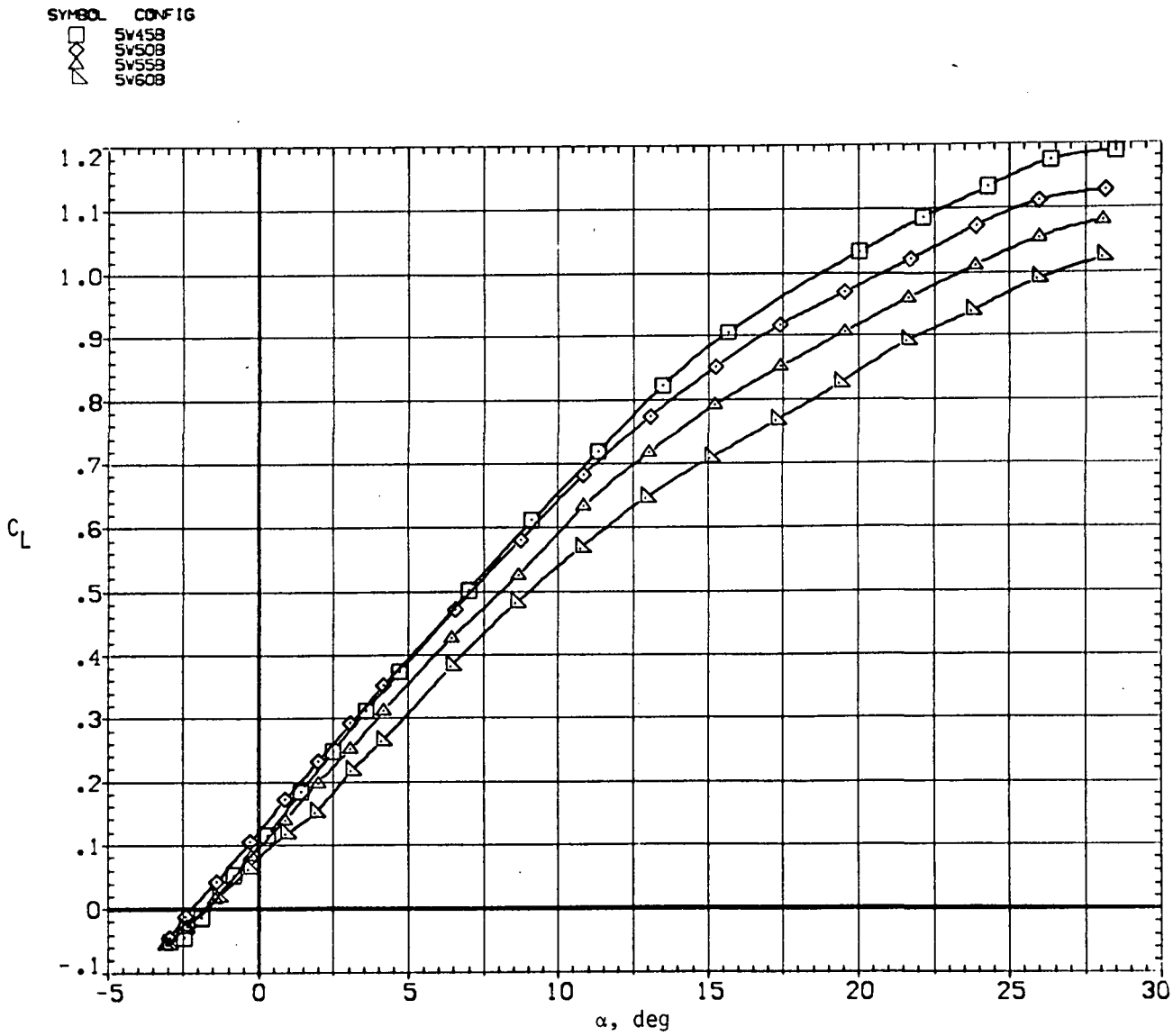

(a) C_L versus α.

Figure 12.– Longitudinal stability characteristics of the oblique wing with intermediate bend, $M = 1.4$, $\beta = 0$.

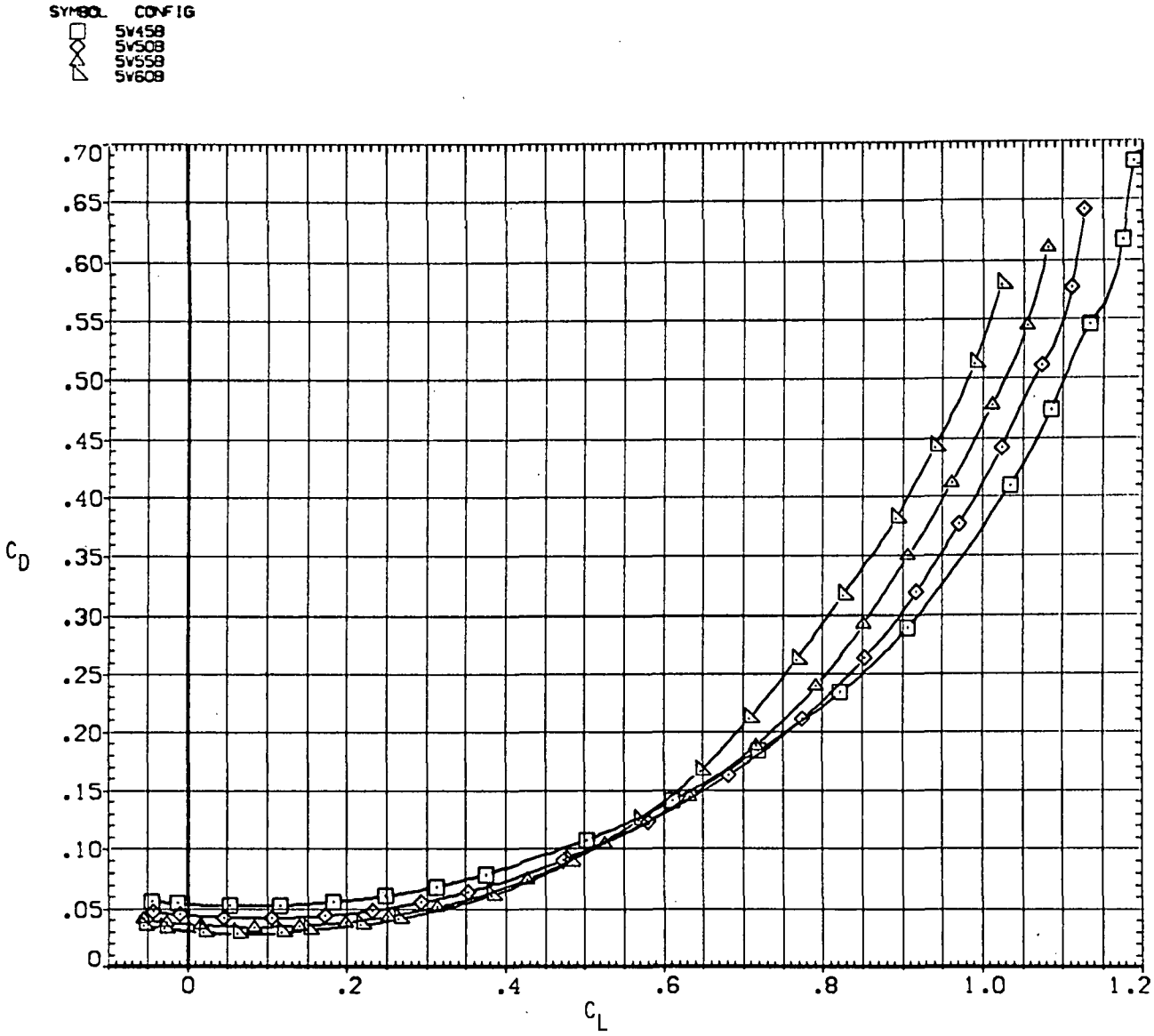

(b) C_D versus C_L.

Figure 12.– Continued.

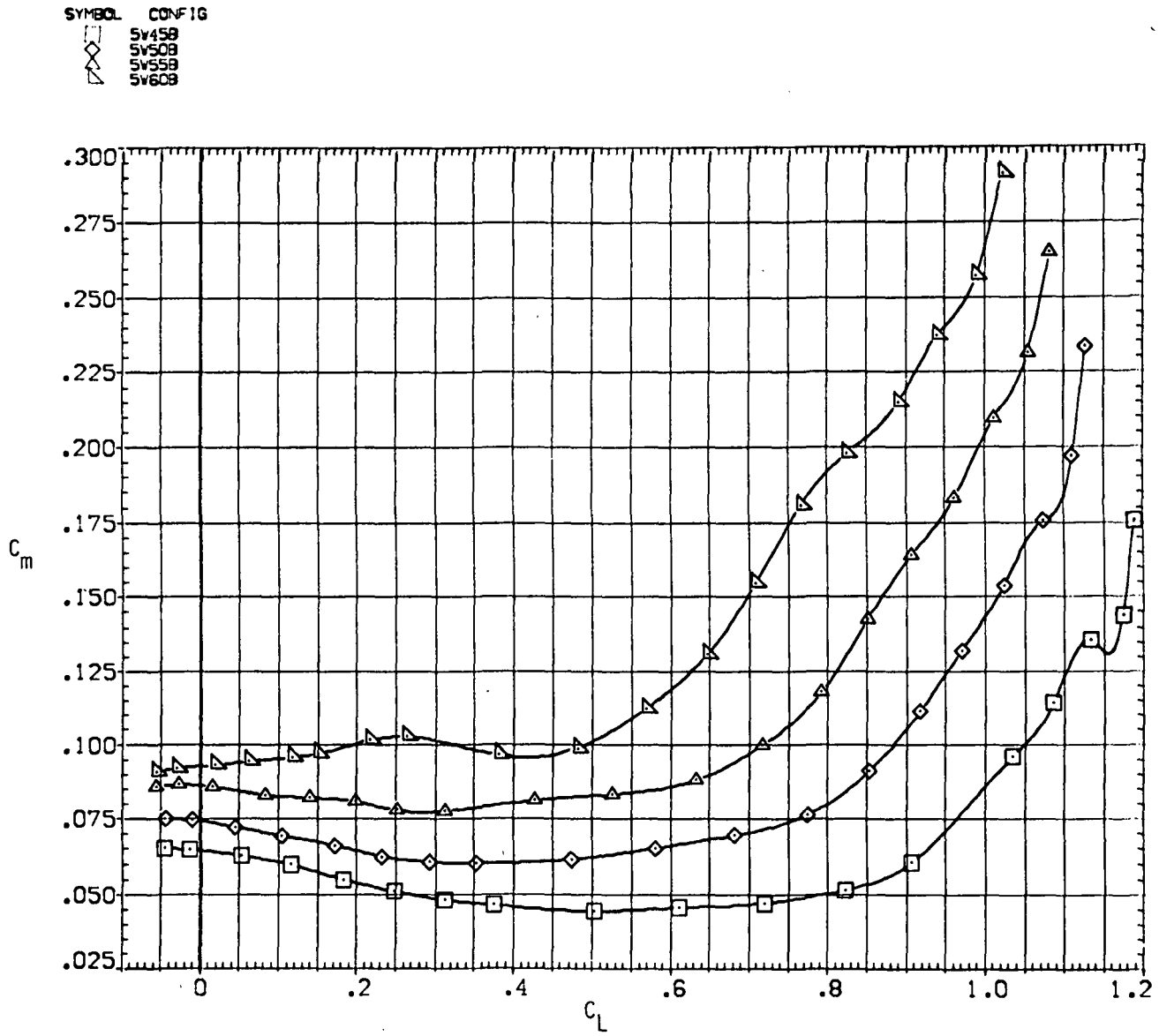

(c) C_m versus C_L.

Figure 12.– Continued.

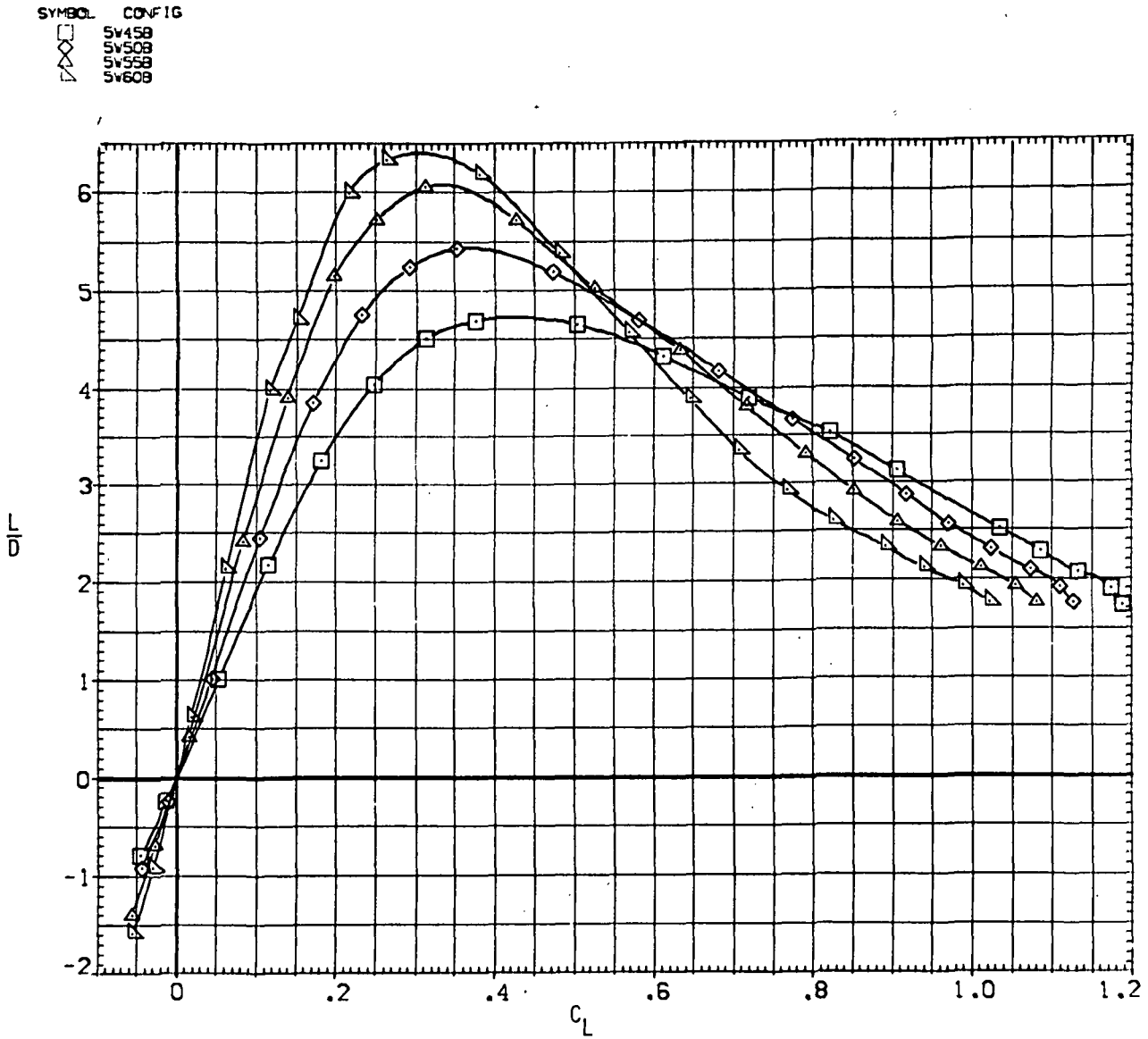

(d) L/D versus C_L.

Figure 12.– Continued.

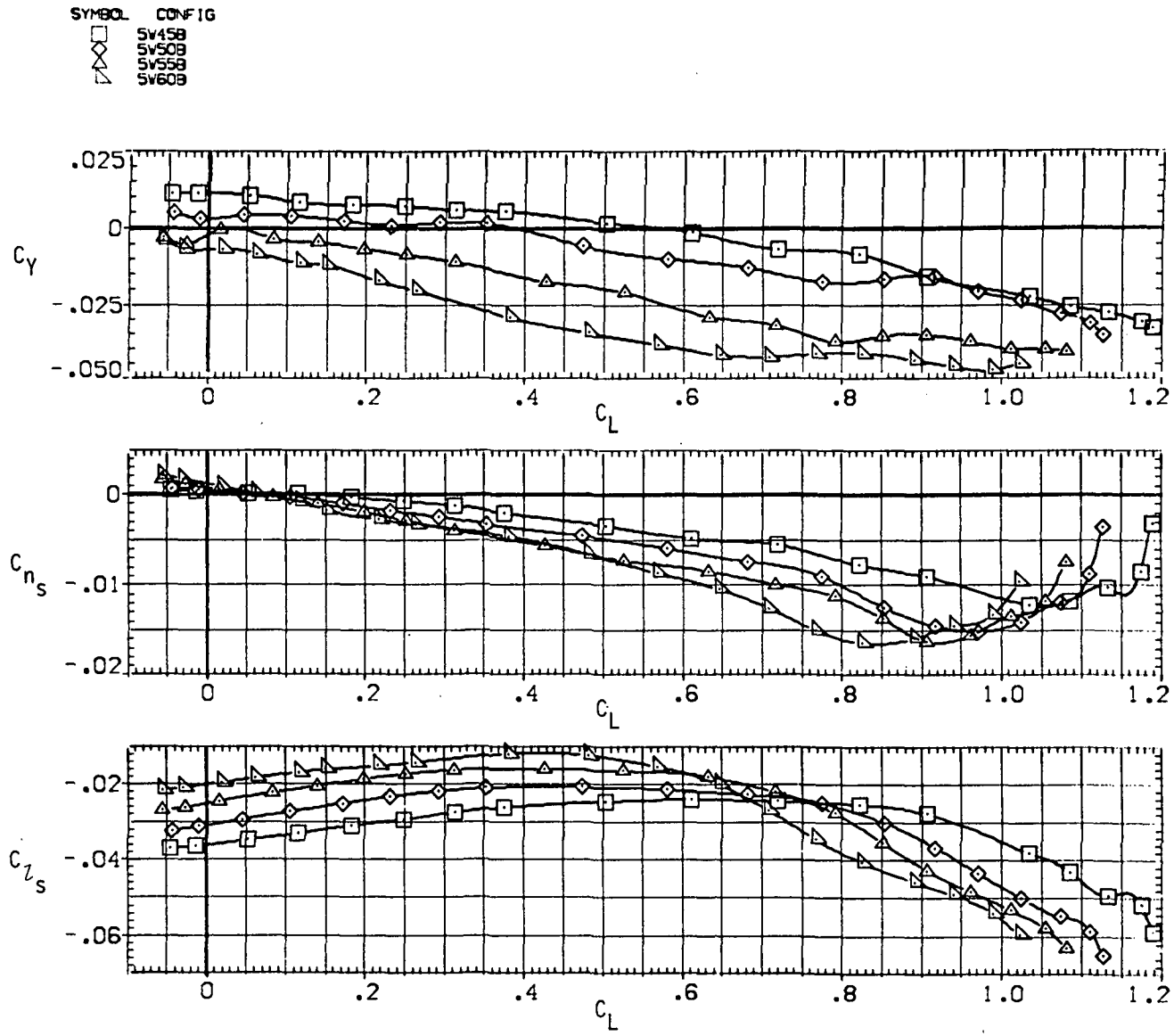

(e) C_Y, C_{n_s} and C_{l_s} versus C_L.

Figure 12.– Continued.

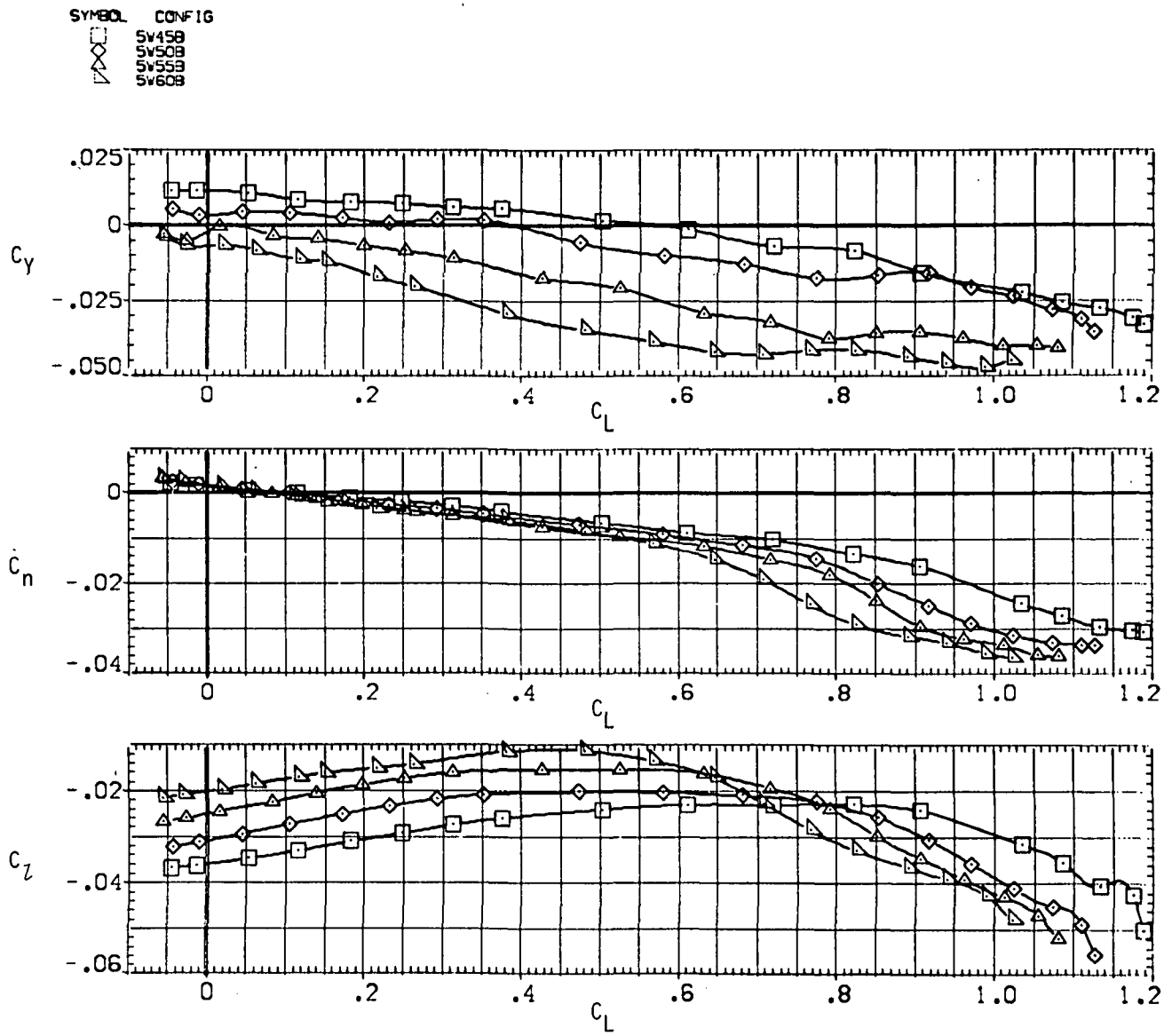

(f) C_Y, C_n and C_l versus C_L.

Figure 12.– Concluded.

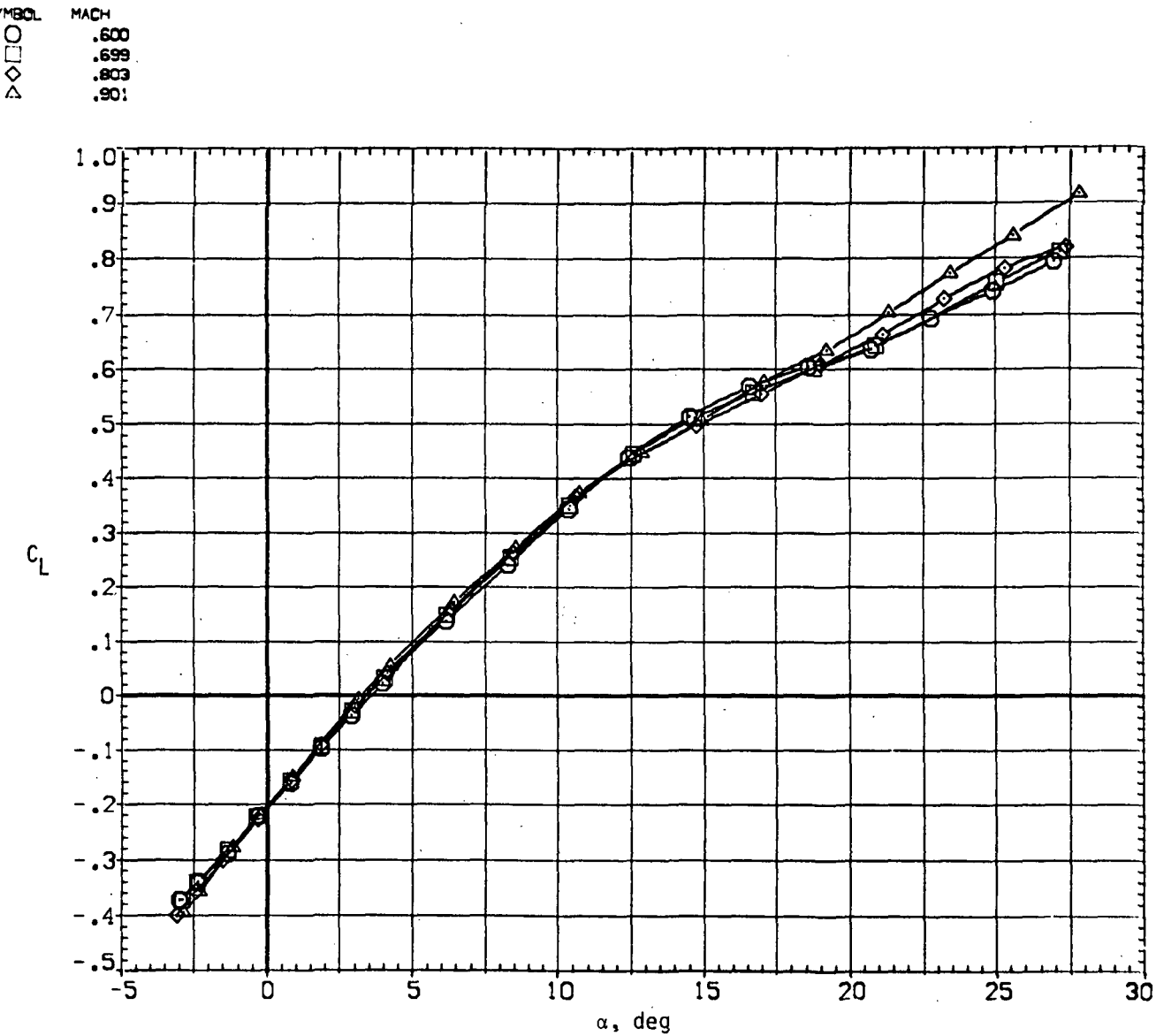

(a) C_L versus α (M = 0.6–0.9).

Figure 13.– Longitudinal stability characteristics of the oblique wing with intermediate bend mounted inverted, $\Lambda = 45°$, $\beta = 0$.

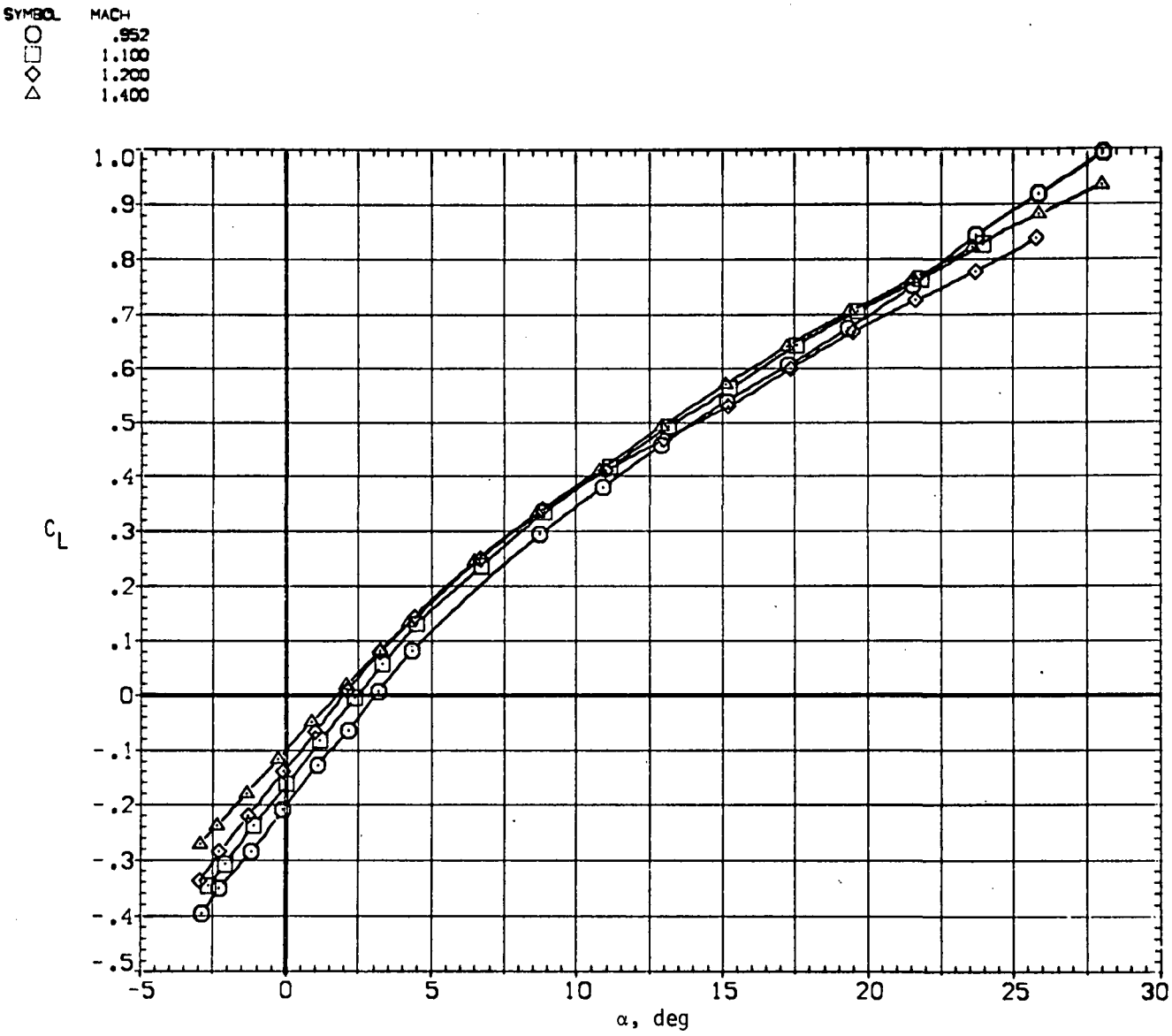

(b) C_L versus α (M = 0.95–1.4).

Figure 13.– Continued.

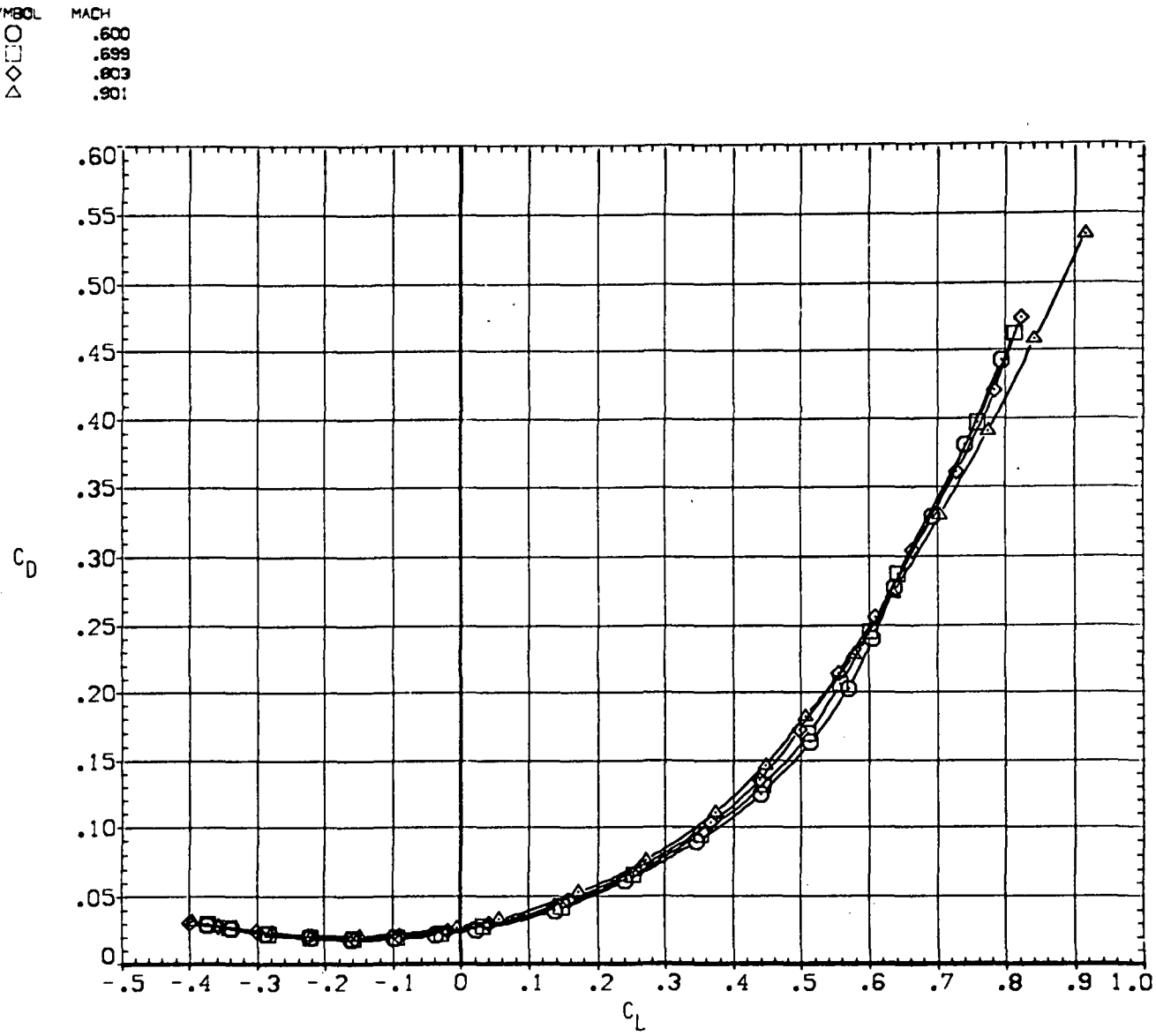

(c) C_D versus C_L (M = 0.6–0.9).

Figure 13.– Continued.

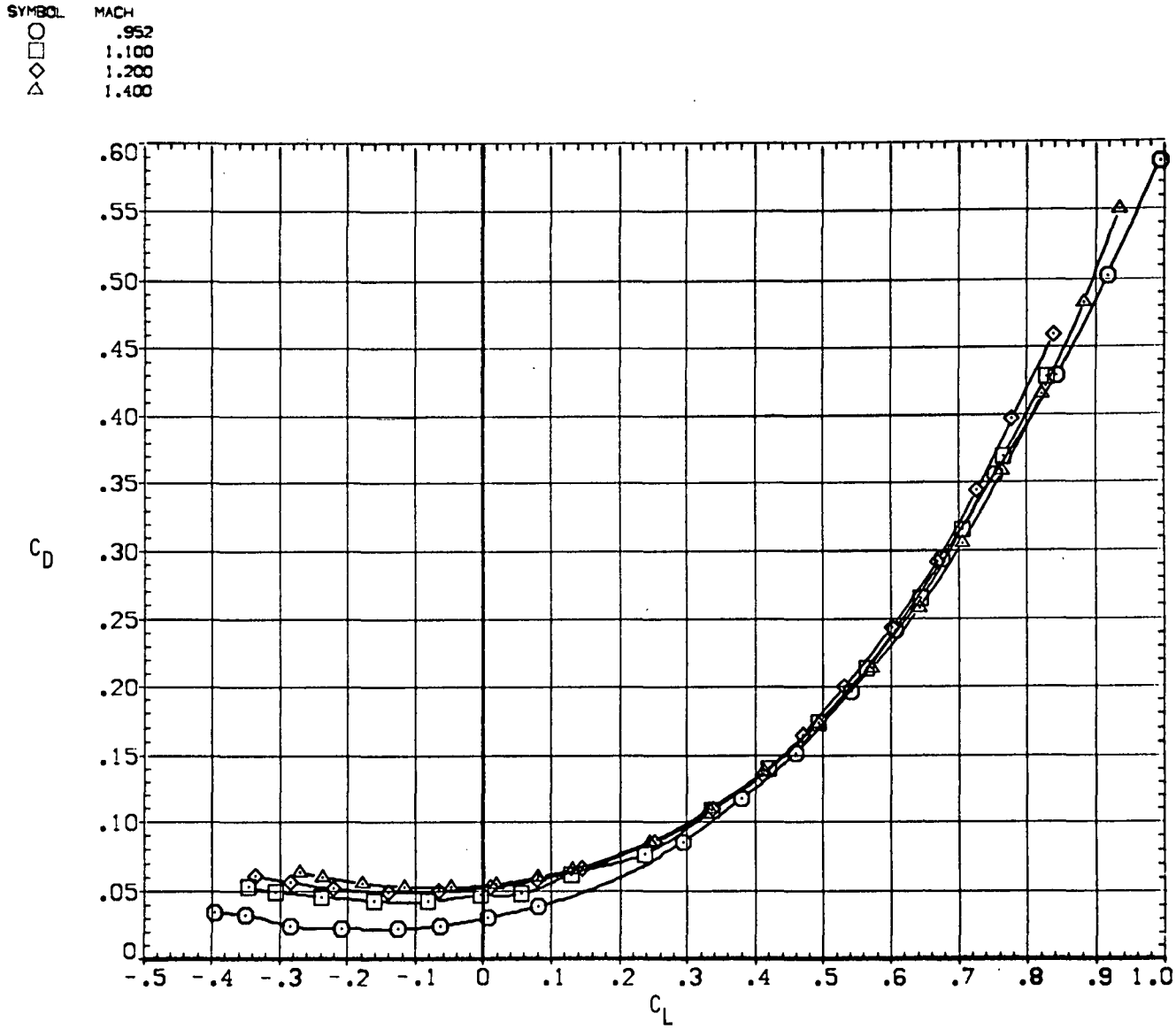

(d) C_D versus C_L (M = 0.95–1.4).

Figure 13.– Continued.

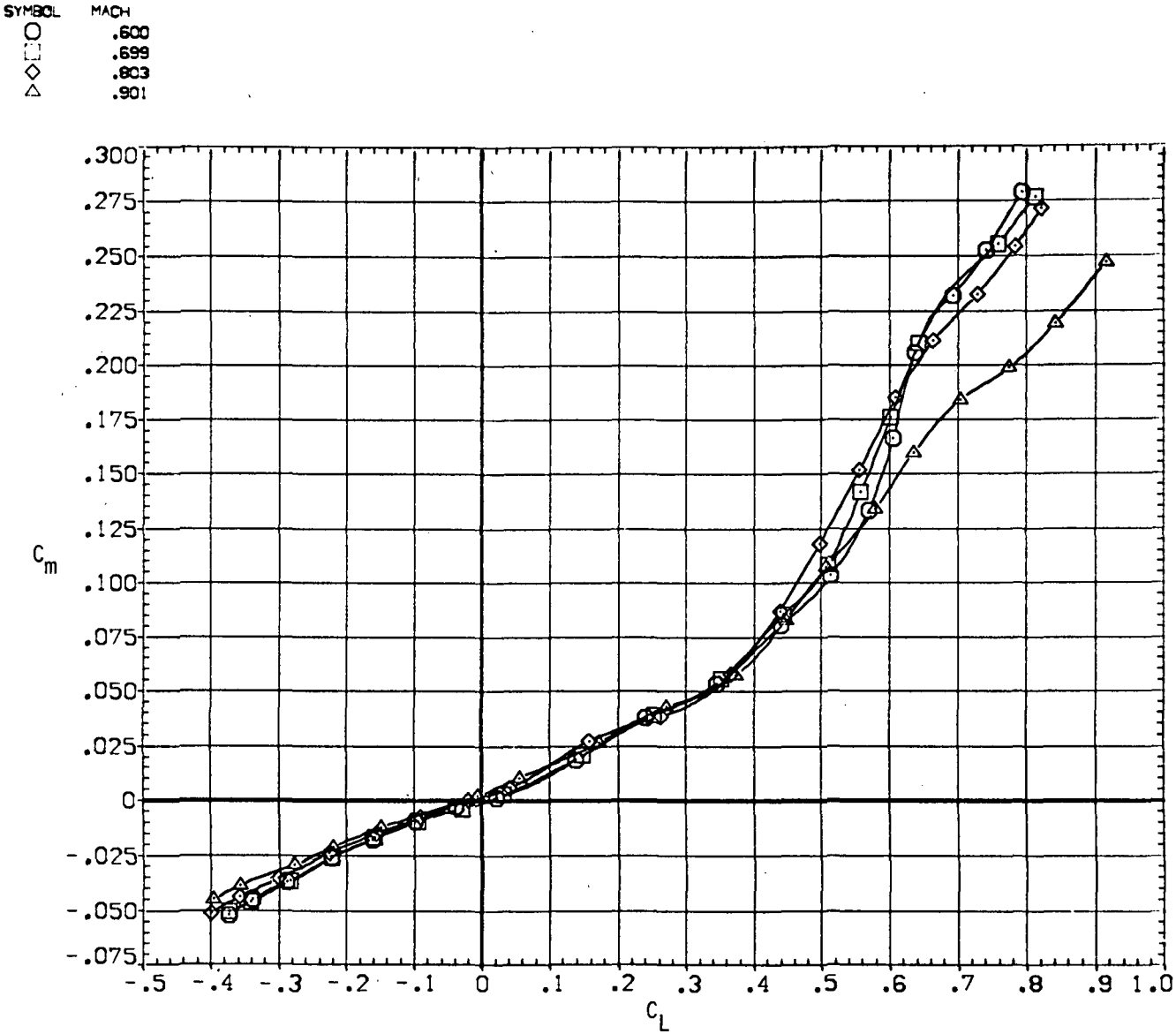

(e) C_m versus C_L (M = 0.6–0.9).

Figure 13.– Continued.

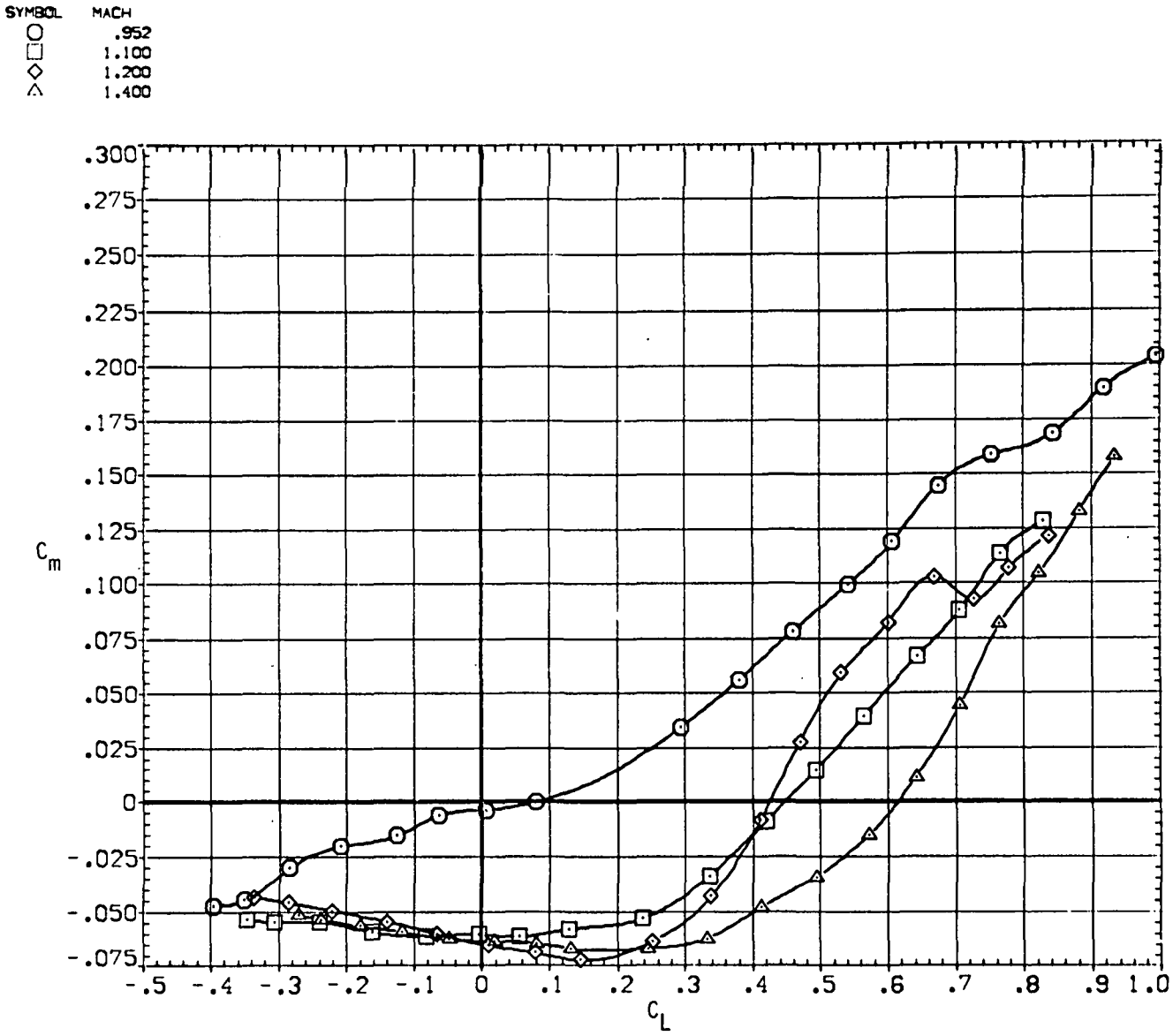

(f) C_m versus C_L (M = 0.95–1.4).

Figure 13.– Continued.

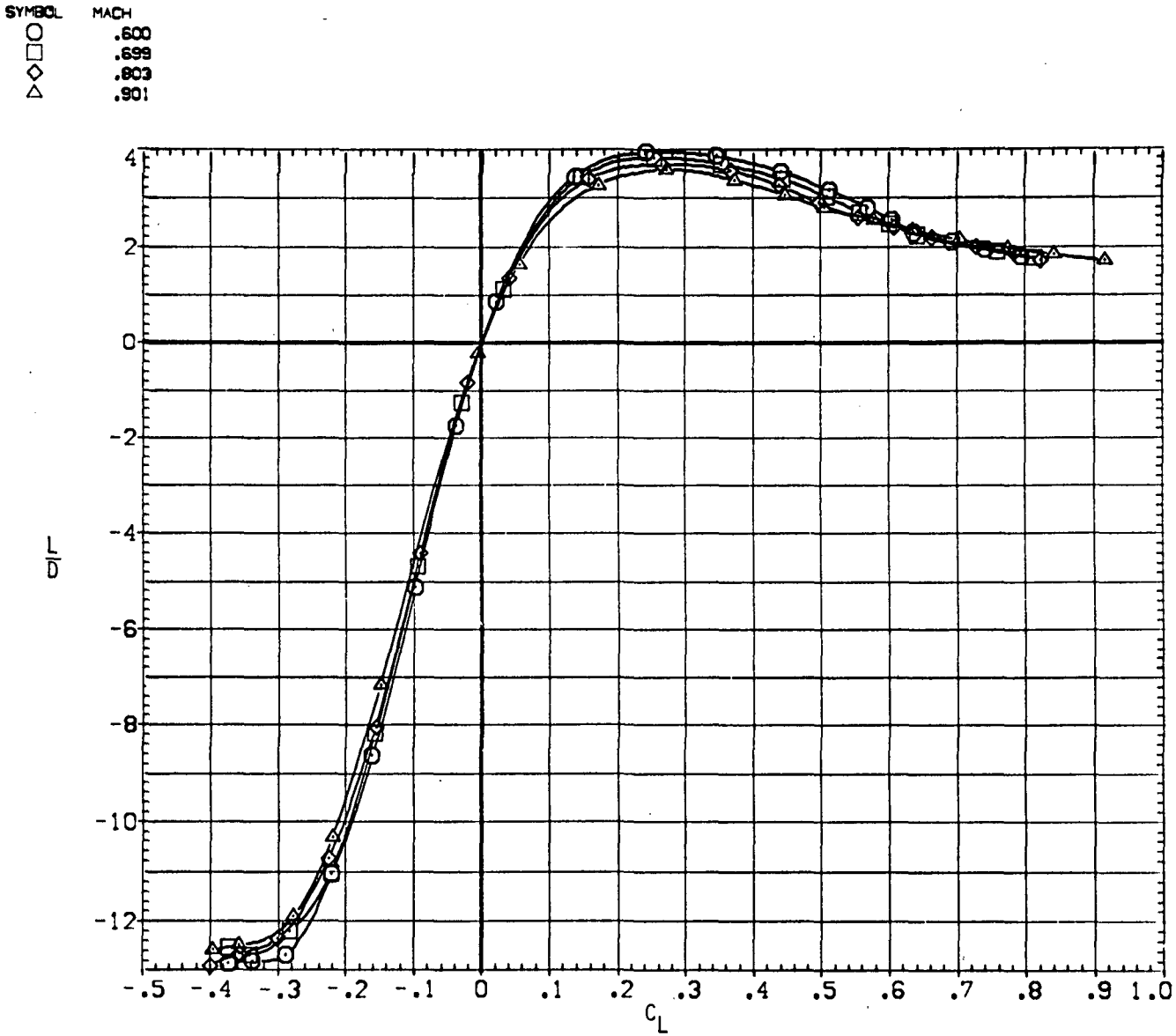

(g) L/D versus C_L ($M = 0.6$–0.9).

Figure 13.– Continued.

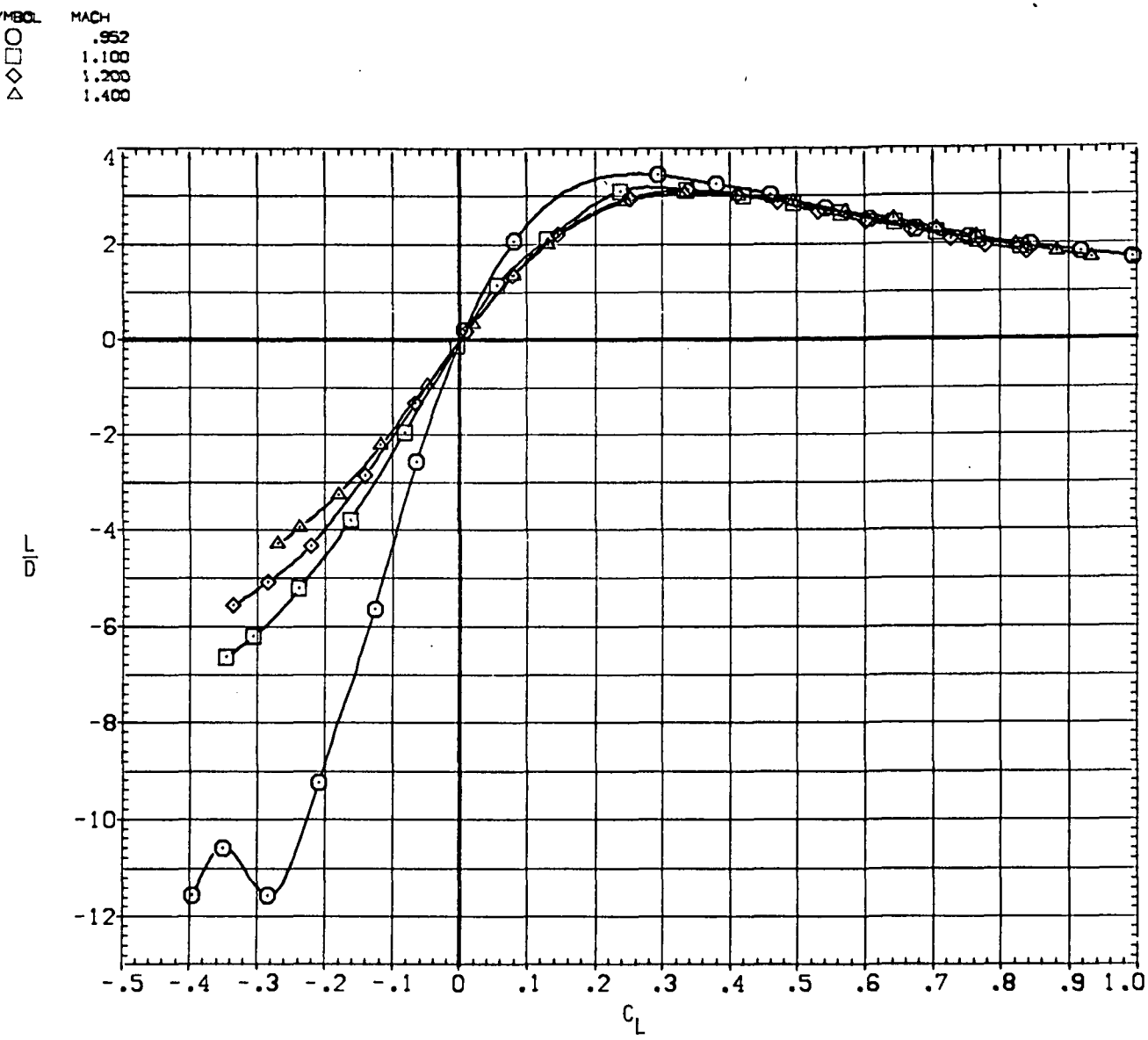

(h) L/D versus C_L ($M = 0.95–1.4$).

Figure 13.– Continued.

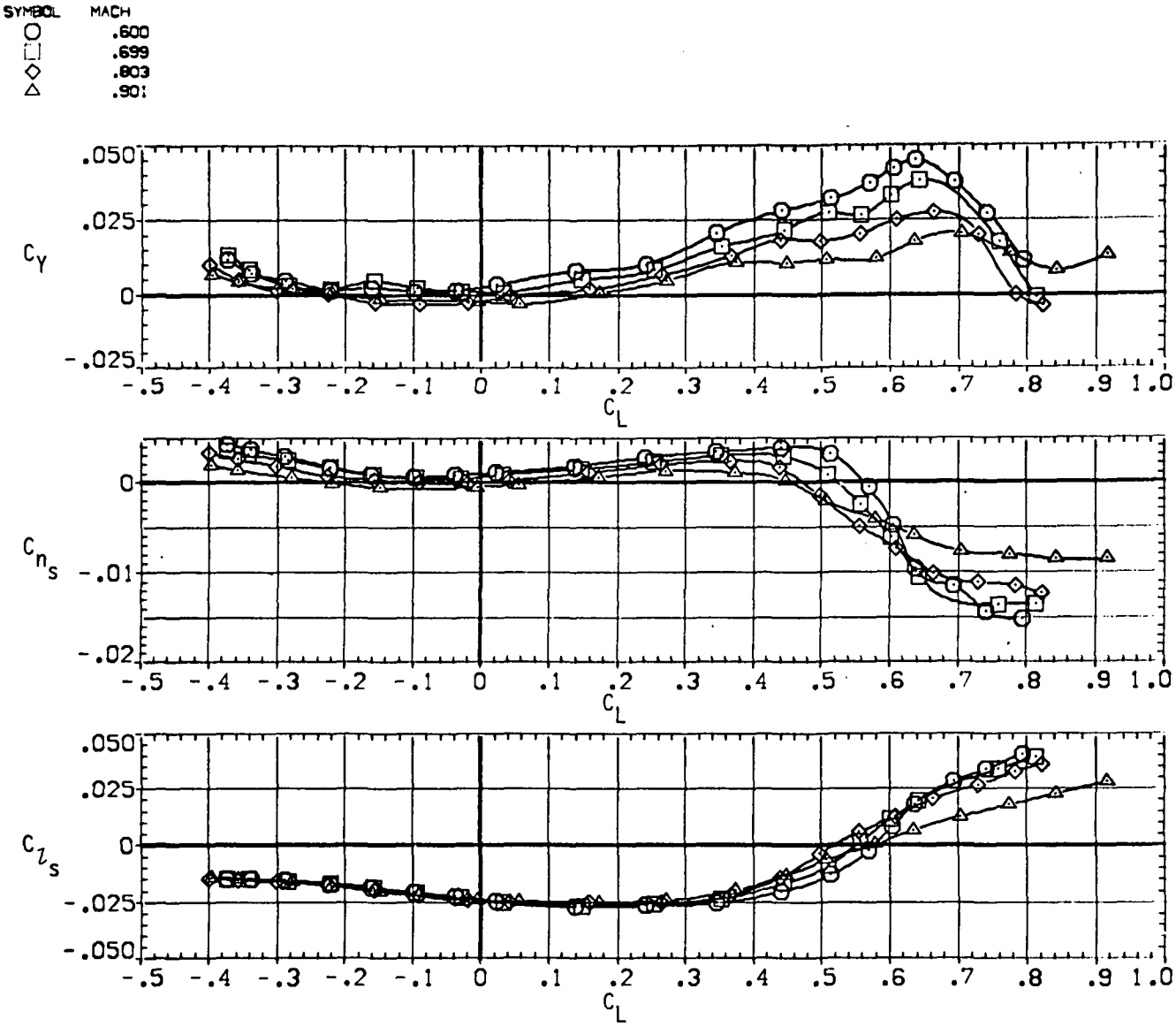

(i) C_Y, C_{n_s} and C_{l_s} versus C_L (M = 0.6–0.9).

Figure 13.– Continued.

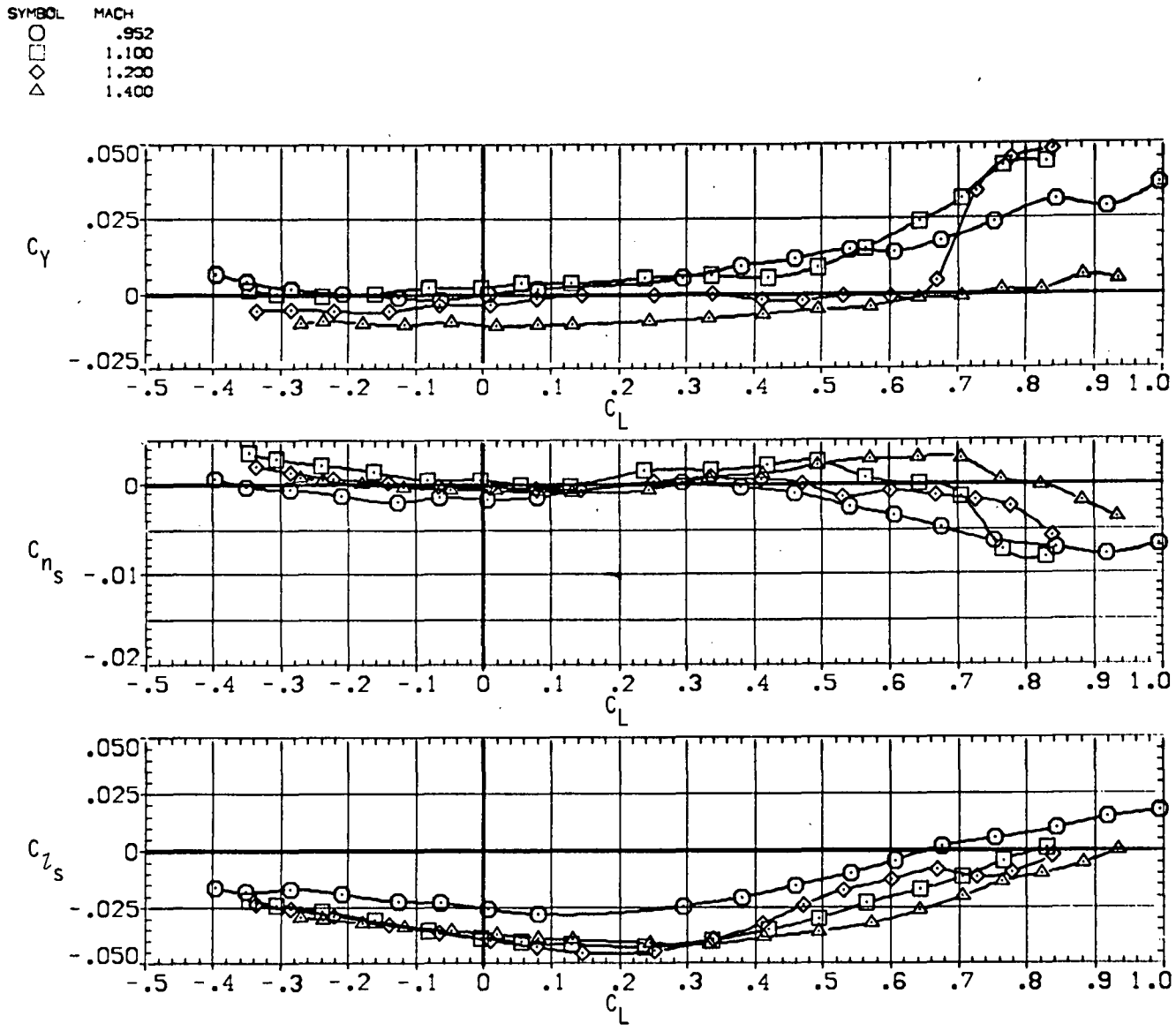

(j) C_Y, C_{n_s} and C_{l_s} versus C_L (M = 0.95–1.4).

Figure 13.– Continued.

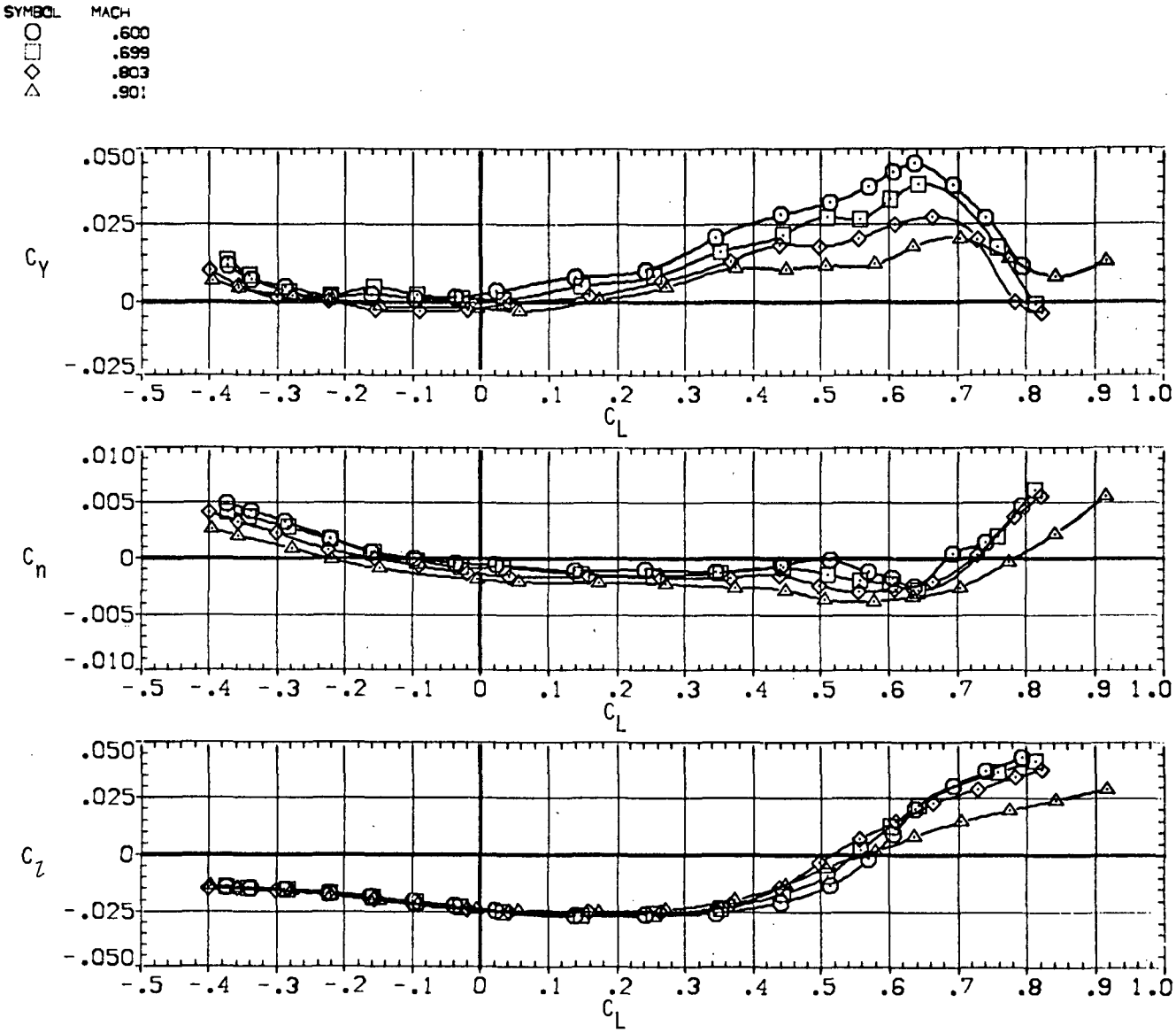

(k) C_Y, C_n and C_l versus C_L (M = 0.6–0.9).

Figure 13.– Continued.

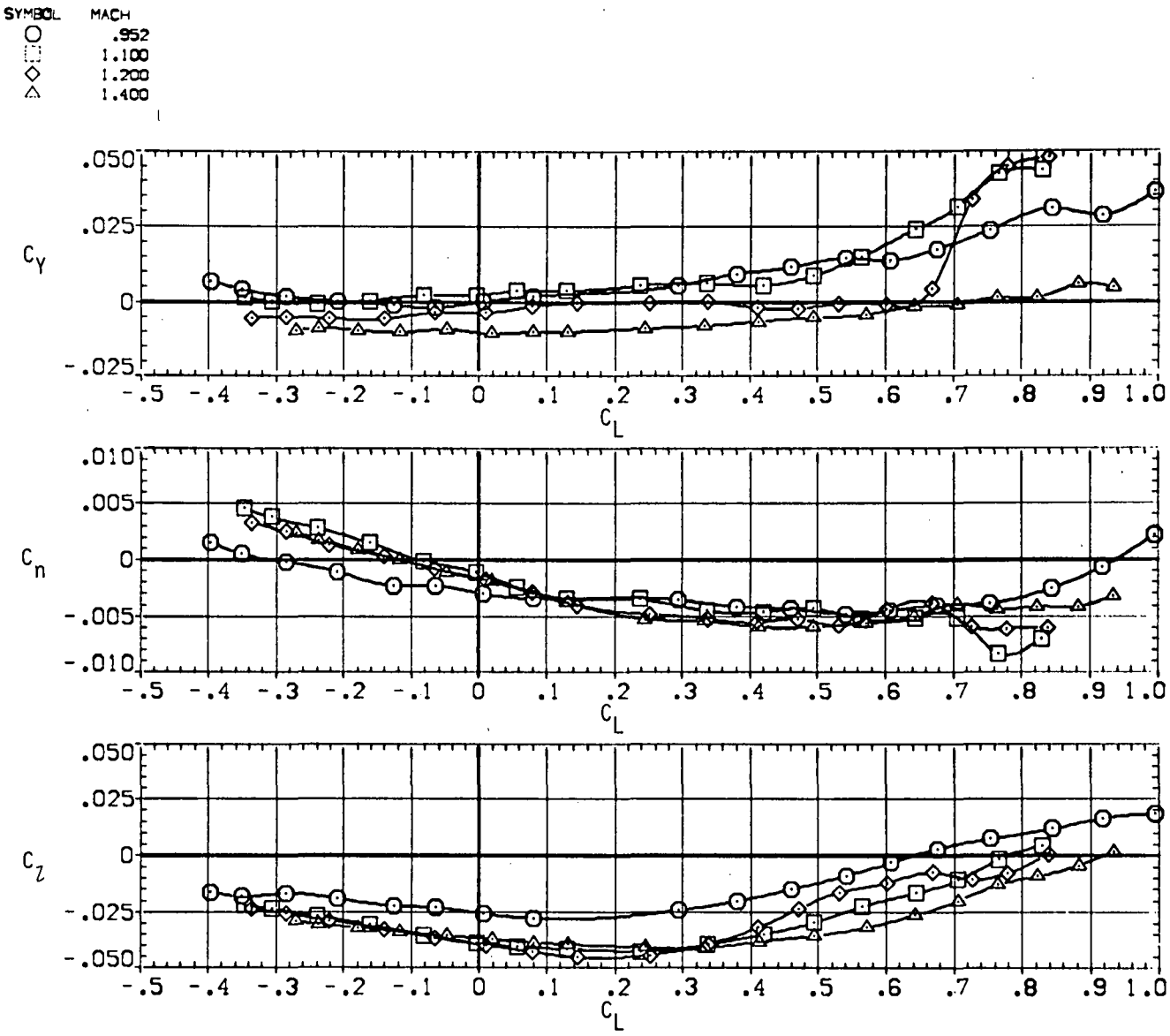

(l) C_Y, C_n and C_l versus C_L (M = 0.95–1.4).

Figure 13.– Concluded.

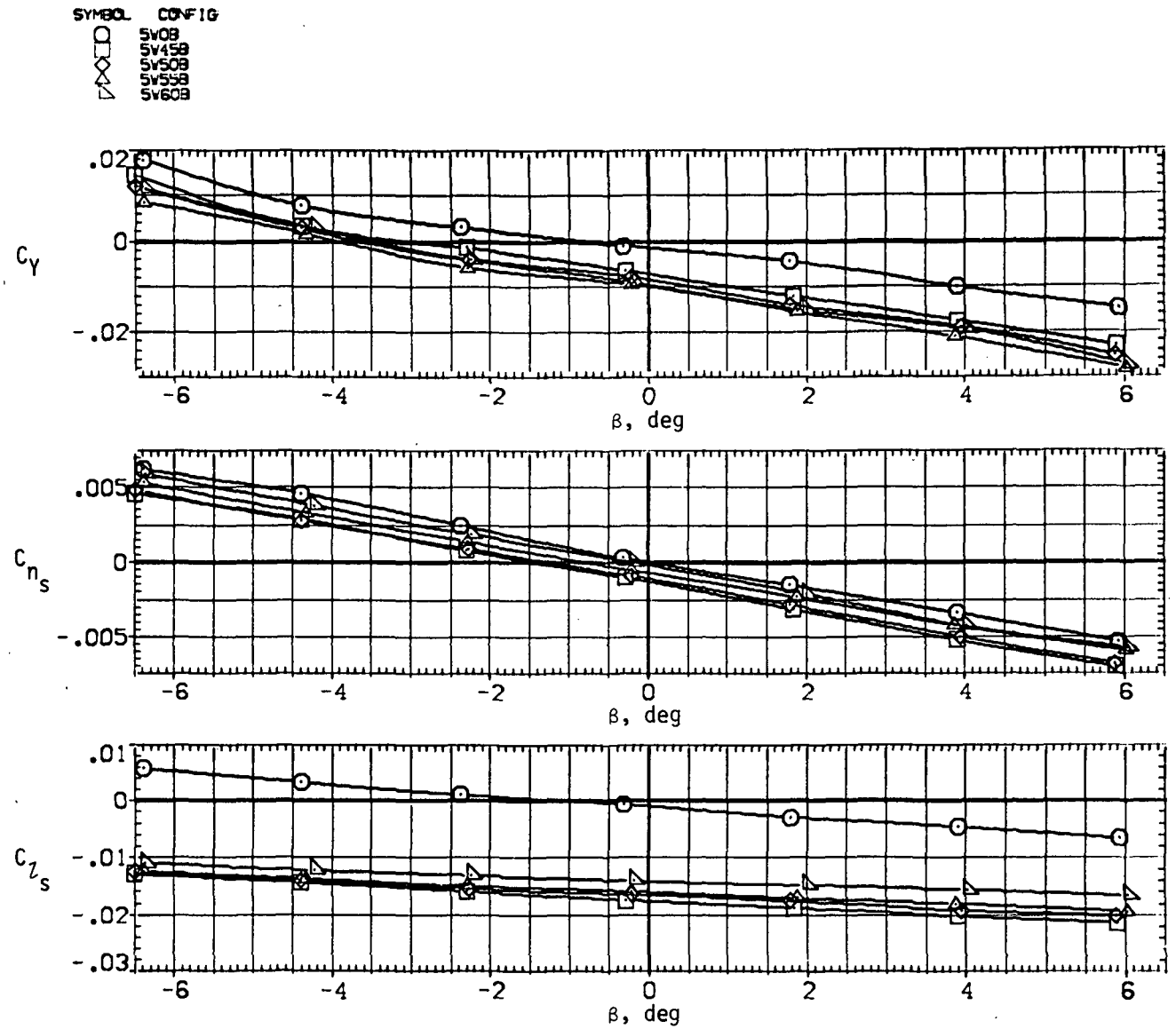

(a) C_Y, C_{n_s} and C_{l_s} versus β ($M = 0.6$).

Figure 14.– Lateral/directional stability characteristics of the oblique wing with intermediate bend, $\alpha = 0$.

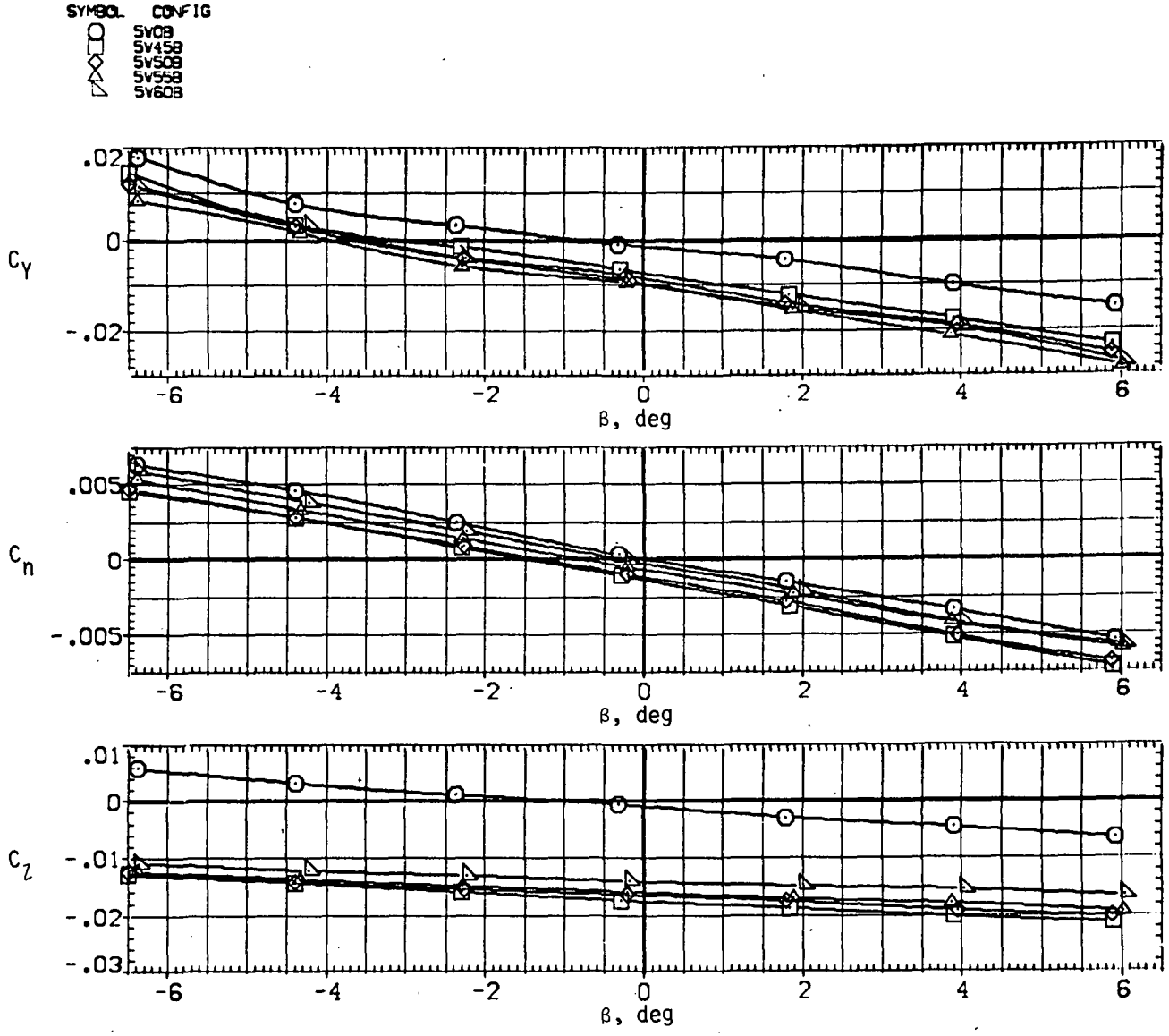

(b) C_Y, C_n and C_l versus β ($M = 0.6$).

Figure 14.– Continued.

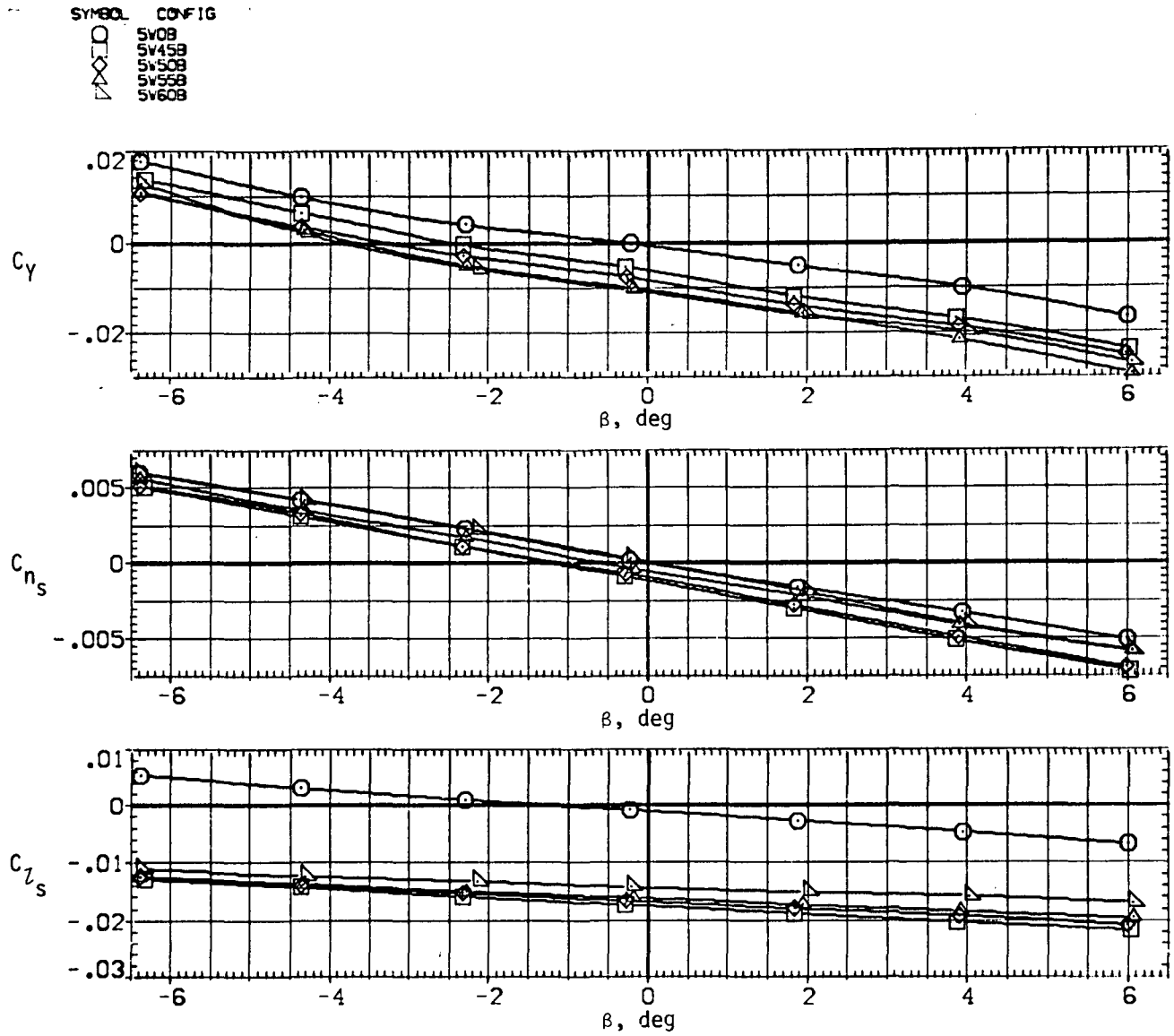

(c) C_Y, C_{n_s} and C_{l_s} versus β ($M = 0.7$).

Figure 14.– Continued.

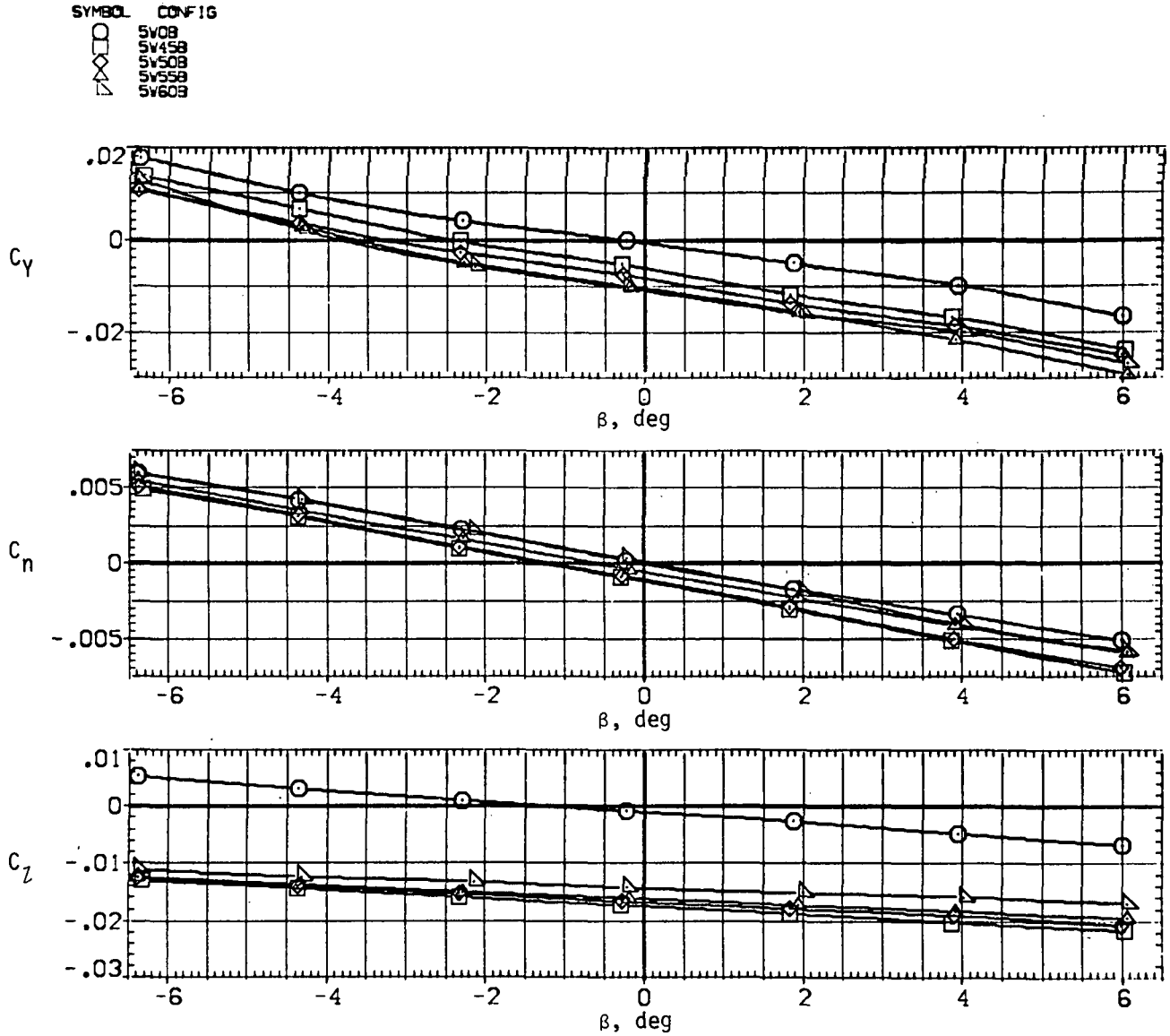

(d) C_Y, C_n and C_l versus β ($M = 0.7$).

Figure 14.– Continued.

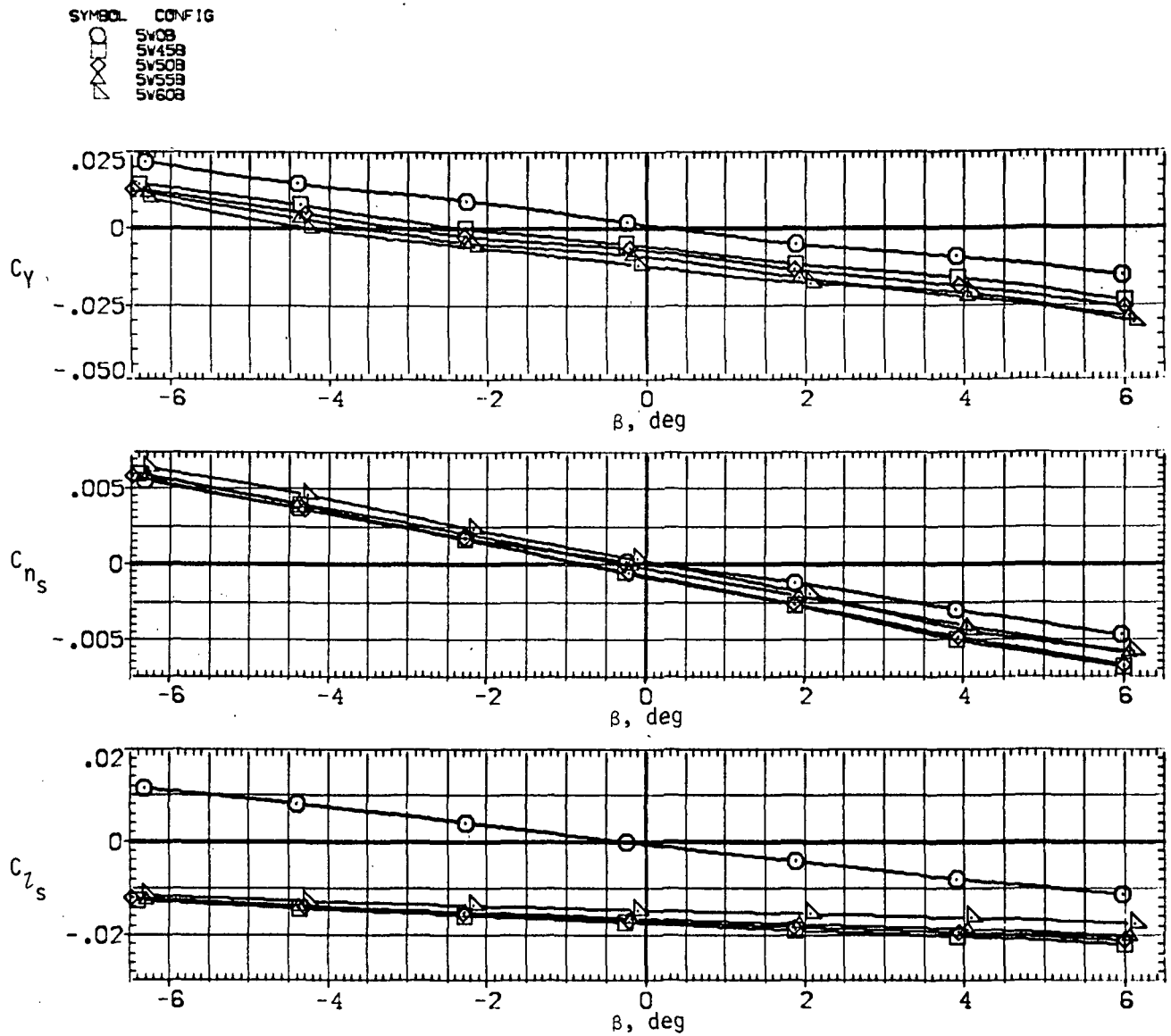

(e) C_Y, C_{n_s} and C_{l_s} versus β ($M = 0.8$).

Figure 14.– Continued.

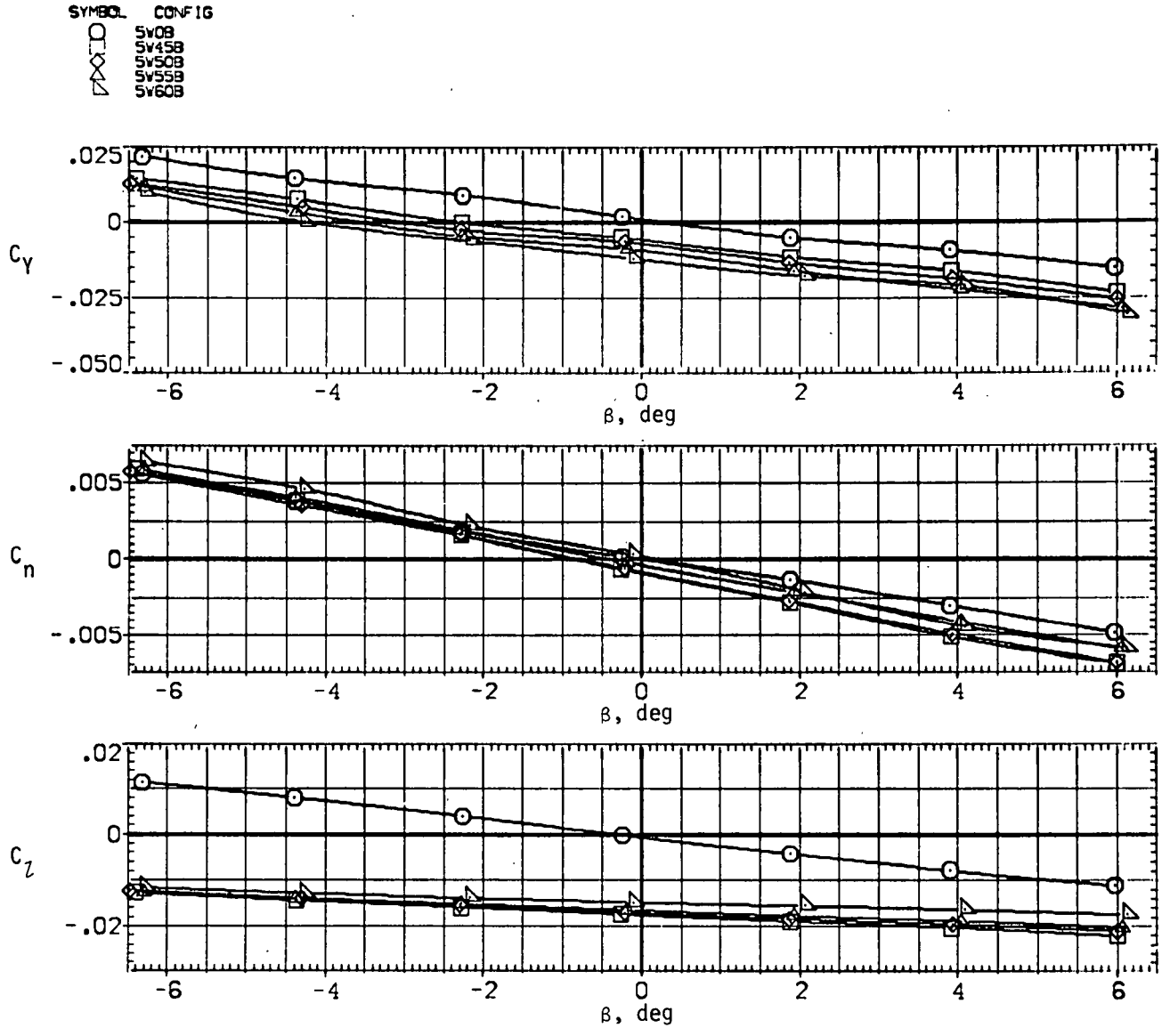

(f) C_Y, C_n and C_l versus β ($M = 0.8$).

Figure 14.– Continued.

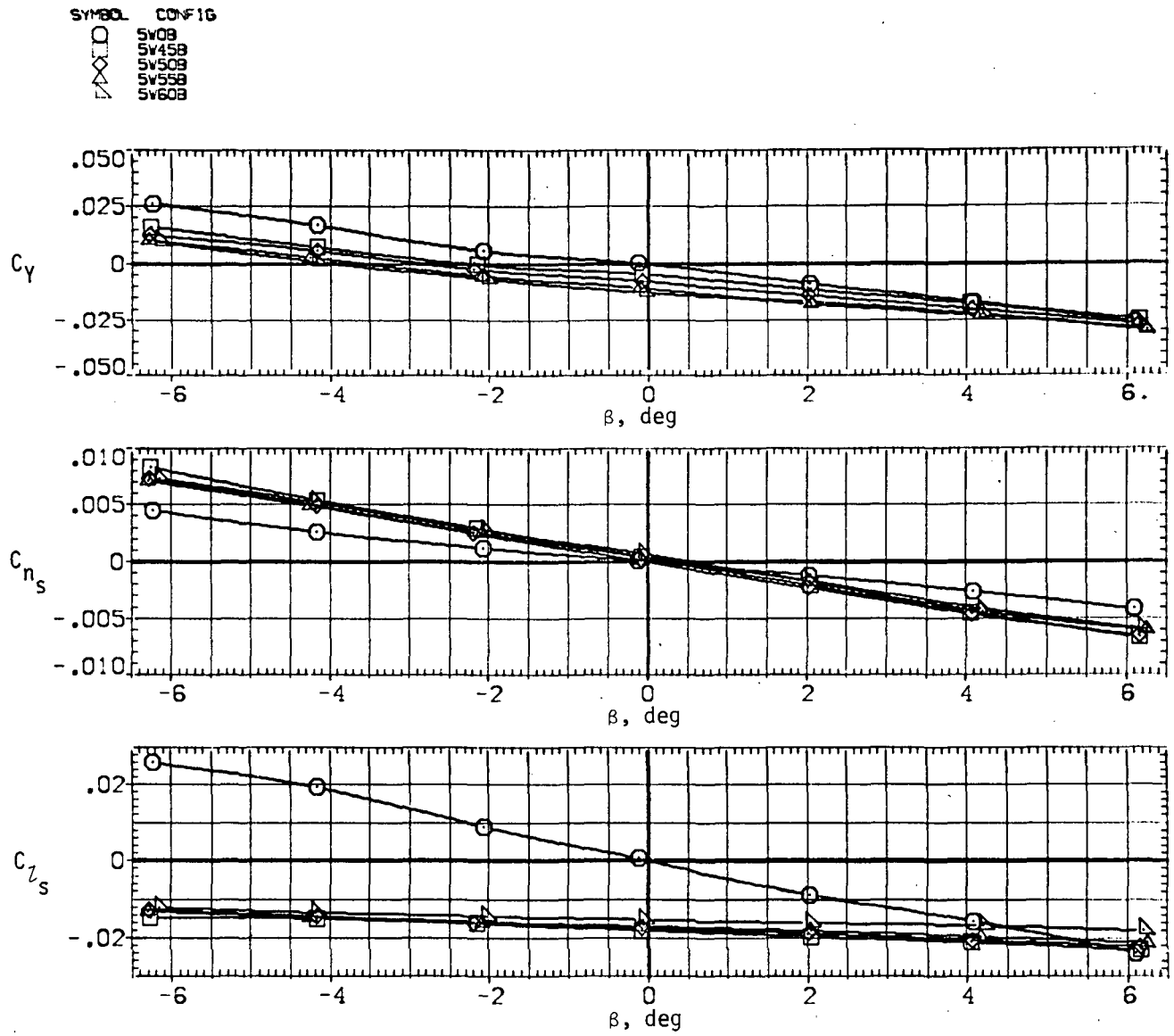

(g) C_Y, C_{n_s} and C_{l_s} versus β ($M = 0.9$).

Figure 14.– Continued.

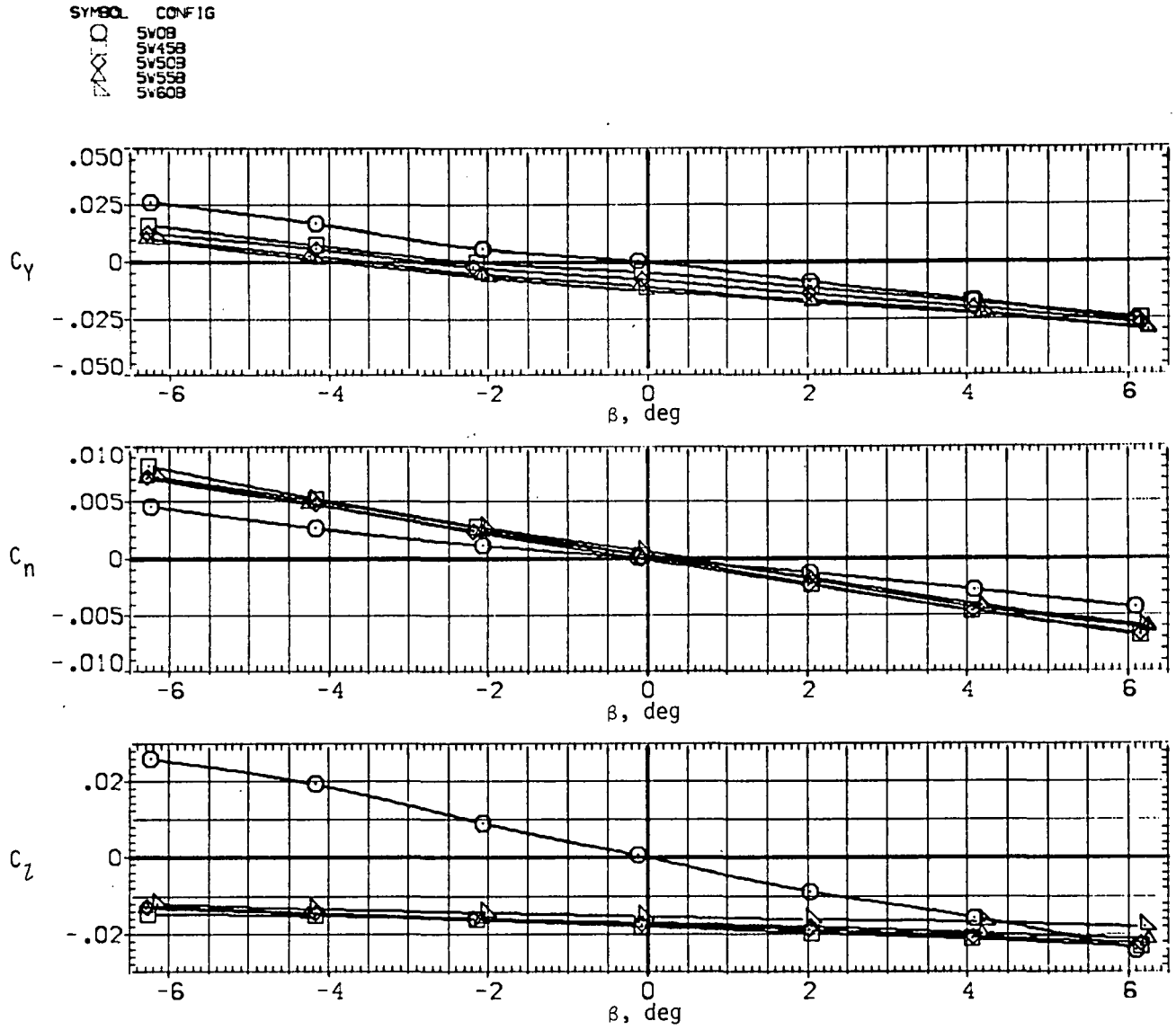

(h) C_Y, C_n and C_l versus β ($M = 0.9$).

Figure 14.– Continued.

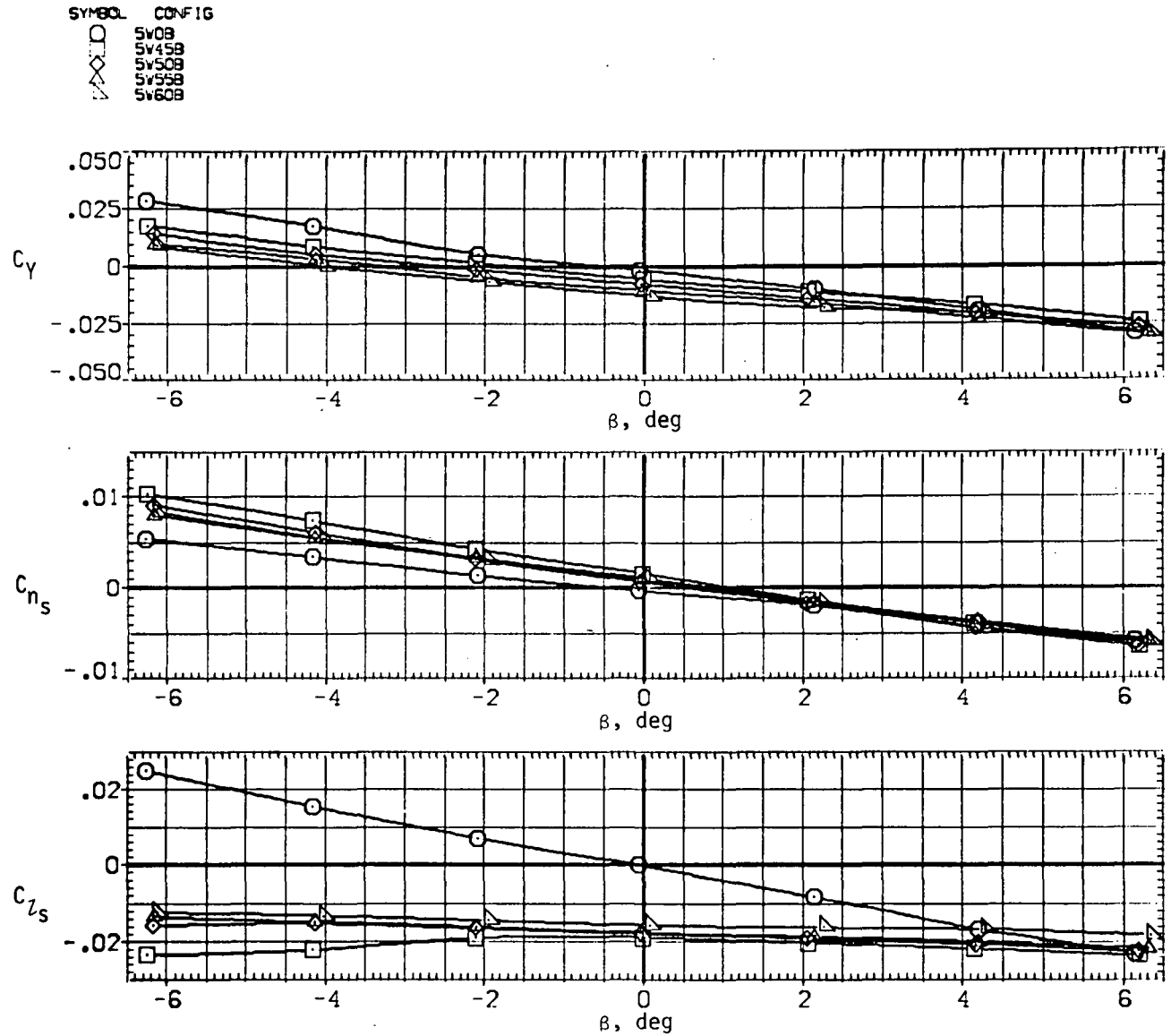

(i) C_Y, C_{n_s} and C_{l_s} versus β ($M = 0.95$).

Figure 14.–Continued.

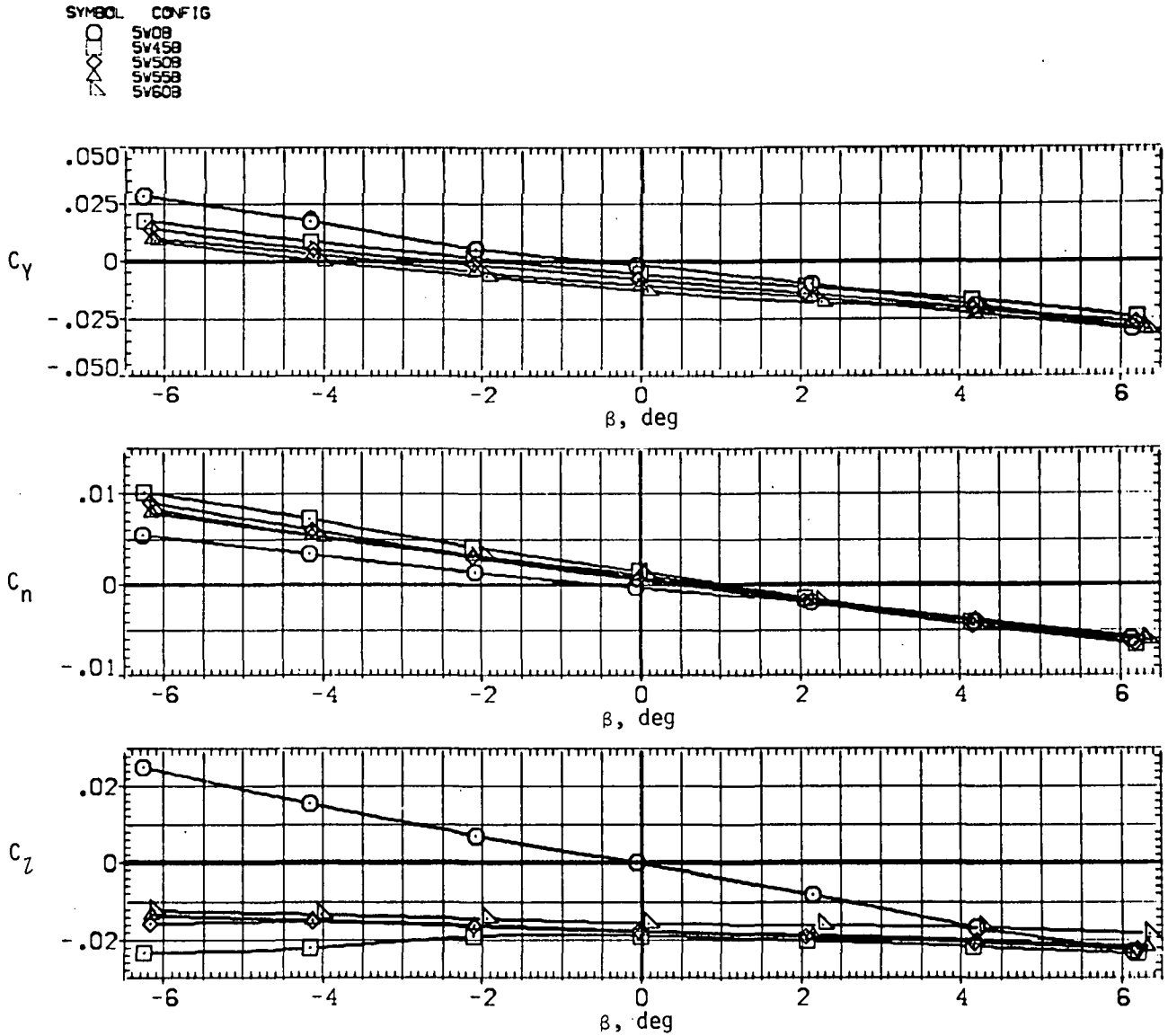

(j) C_Y, C_n and C_l versus β ($M = 0.95$).

Figure 14.– Continued.

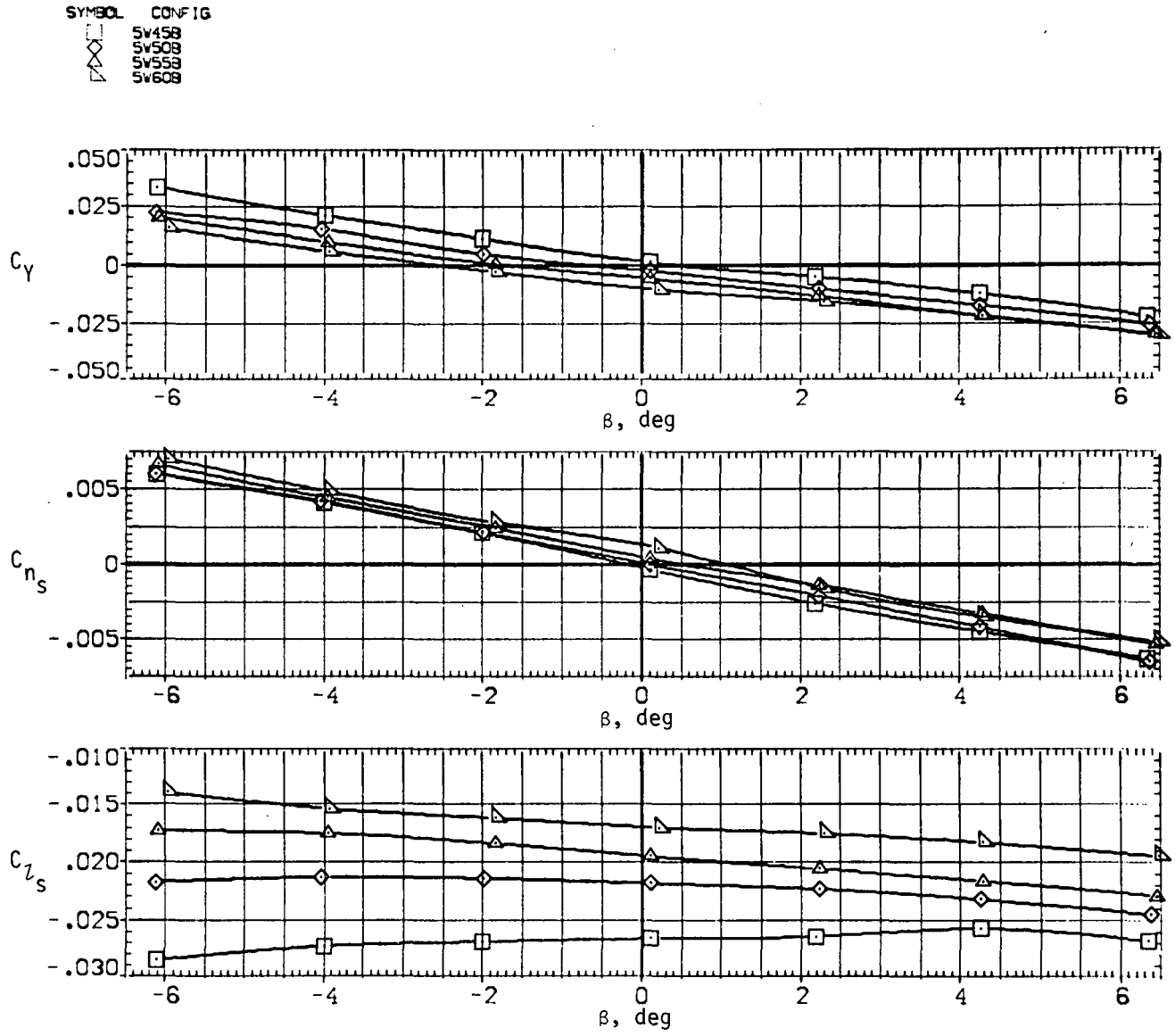

(k) C_Y, C_{n_s} and C_{l_s} versus β (M = 1.1).

Figure 14.– Continued.

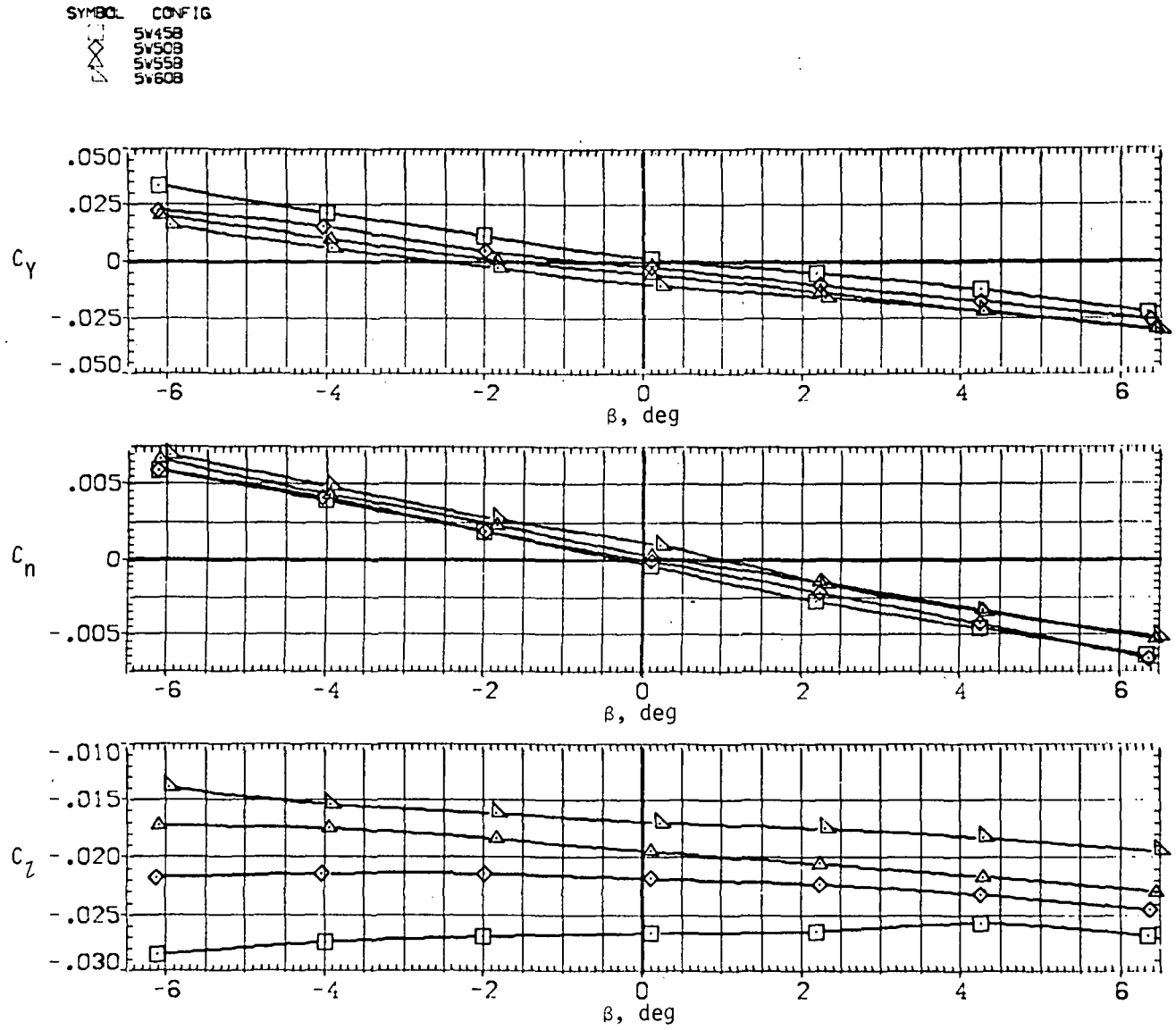

(l) C_Y, C_n and C_l versus β (M = 1.1).

Figure 14.– Continued.

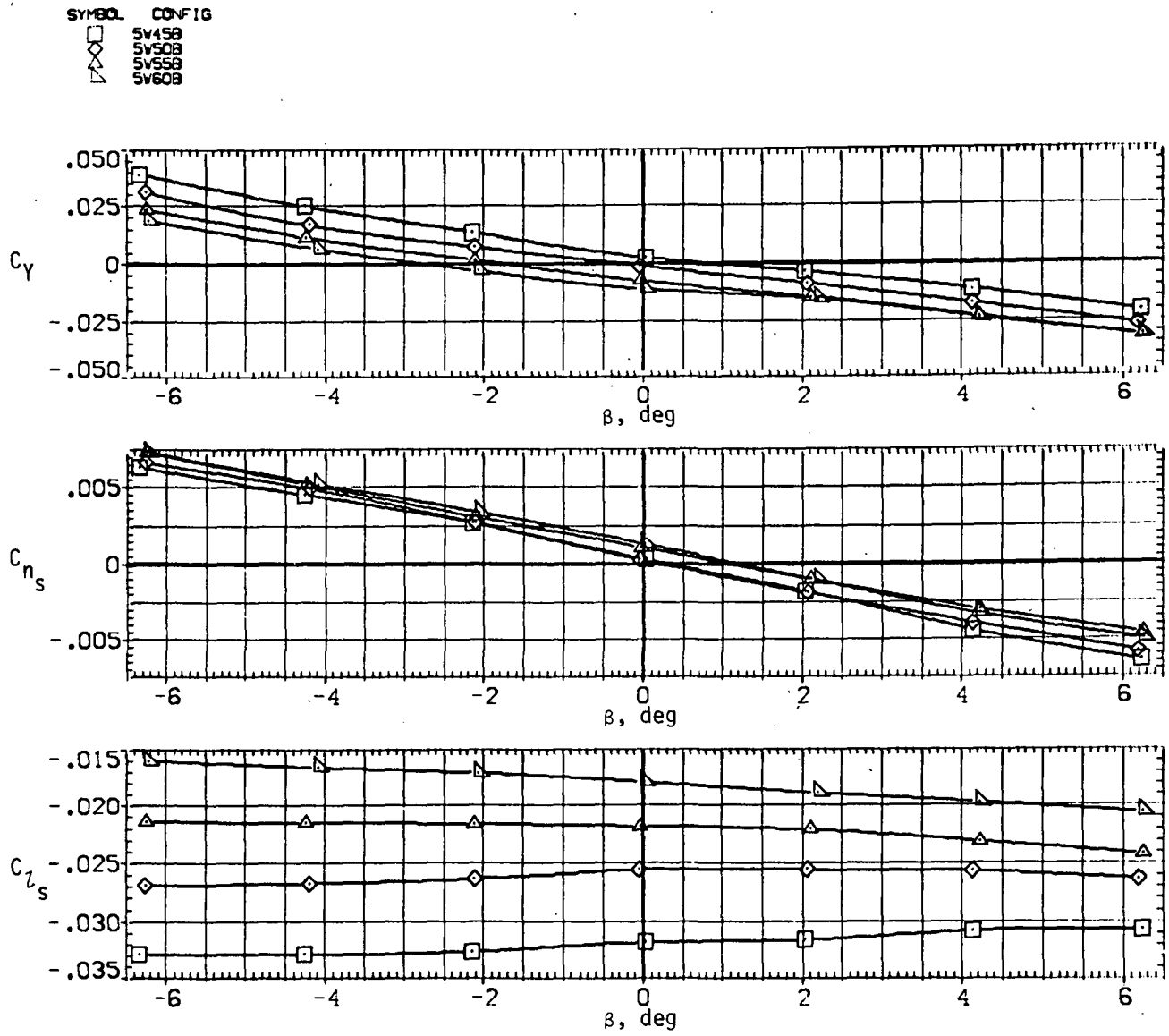

(m) C_Y, C_{n_s} and C_{l_s} versus β (M = 1.2).

Figure 14.– Continued.

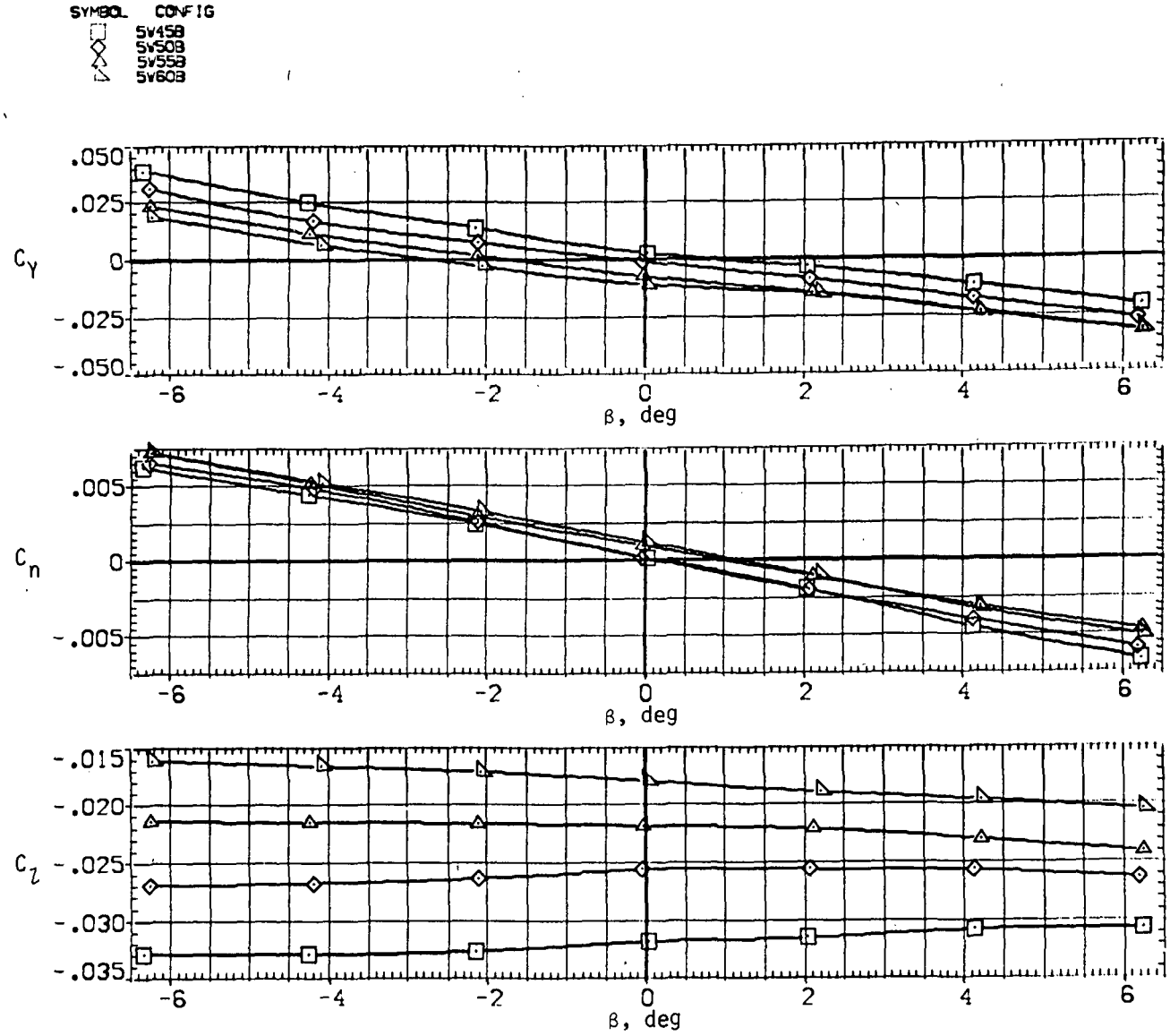

(n) C_Y, C_n and C_l versus β (M = 1.2).

Figure 14.– Continued.

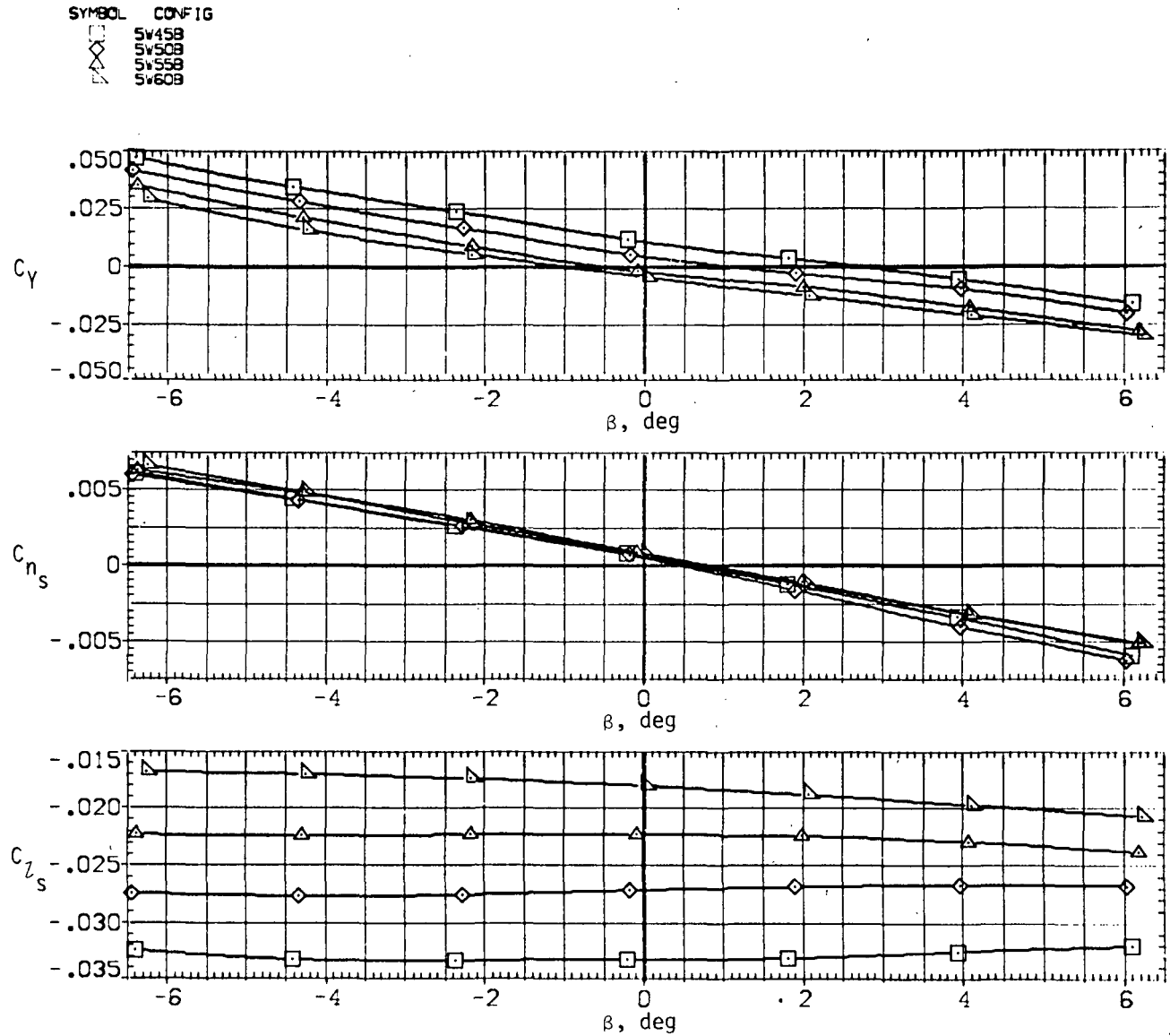

(o) C_Y, C_{n_s} and C_{l_s} versus β (M = 1.4).

Figure 14.– Continued.

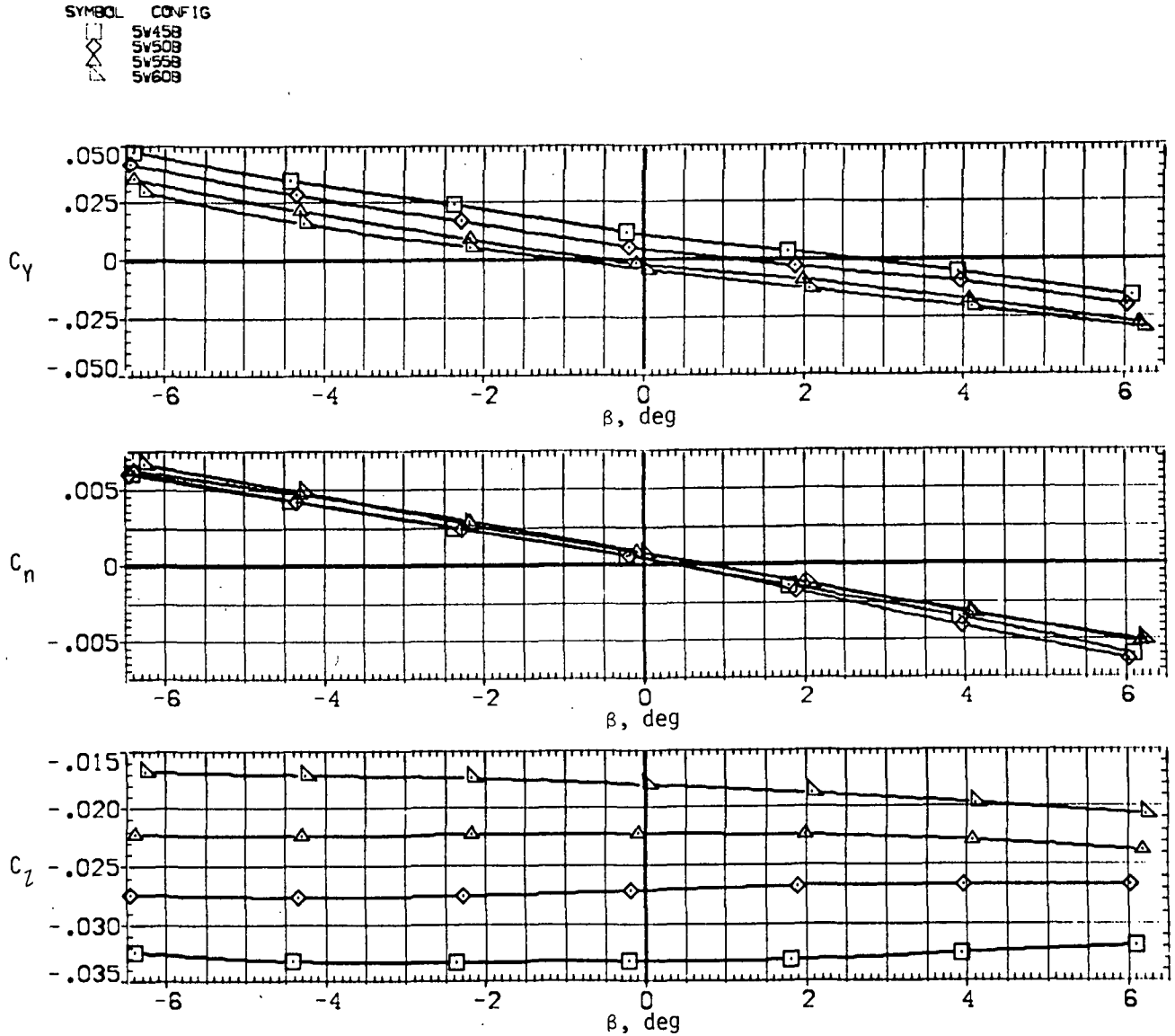

(p) C_Y, C_n and C_l versus β (M = 1.4).

Figure 14.– Concluded.

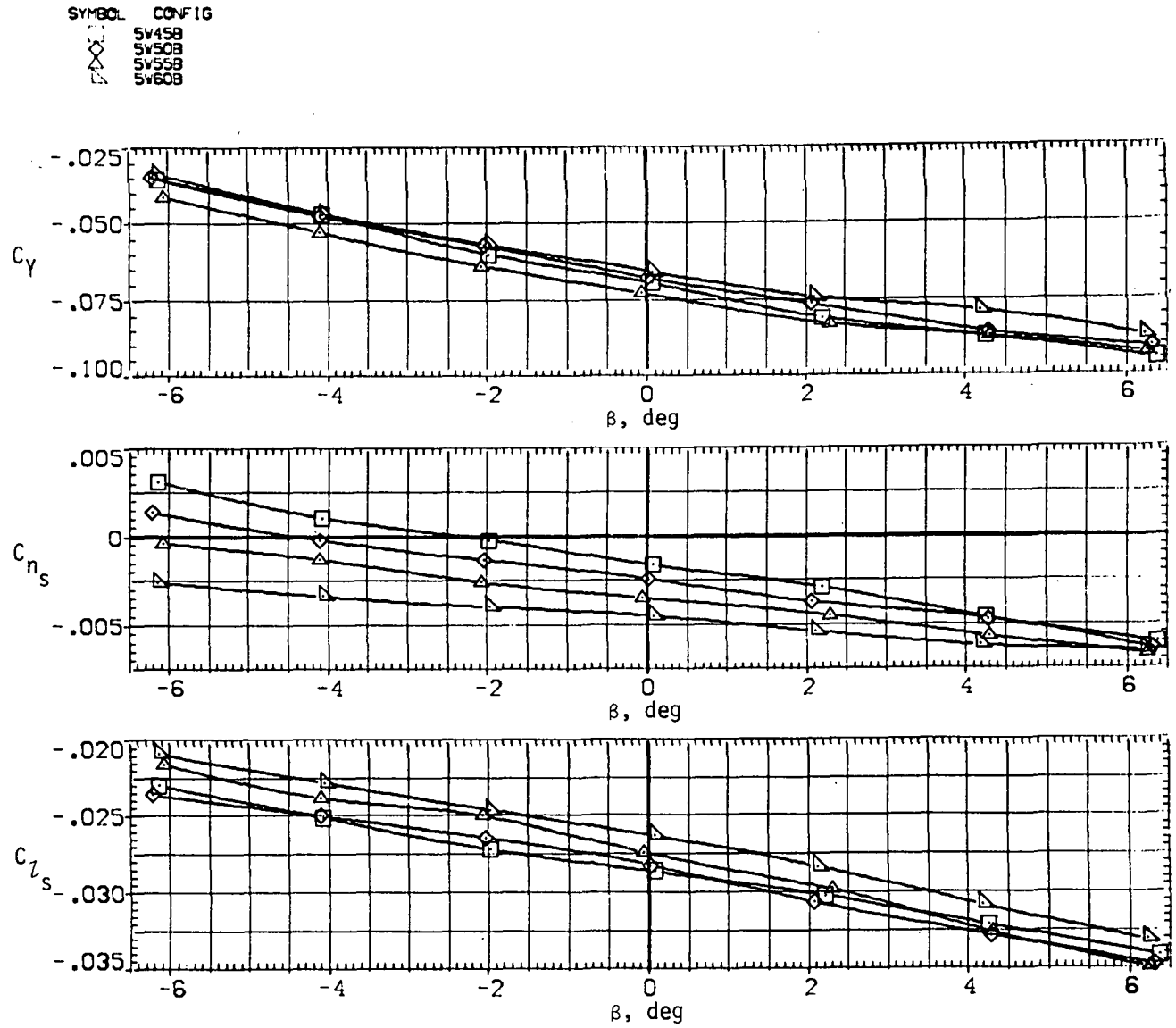

(a) C_Y, C_{n_s} and C_{l_s} versus β ($M = 0.6$).

Figure 15.– Lateral/directional stability characteristics of the oblique wing with intermediate bend, $\alpha = 10°$.

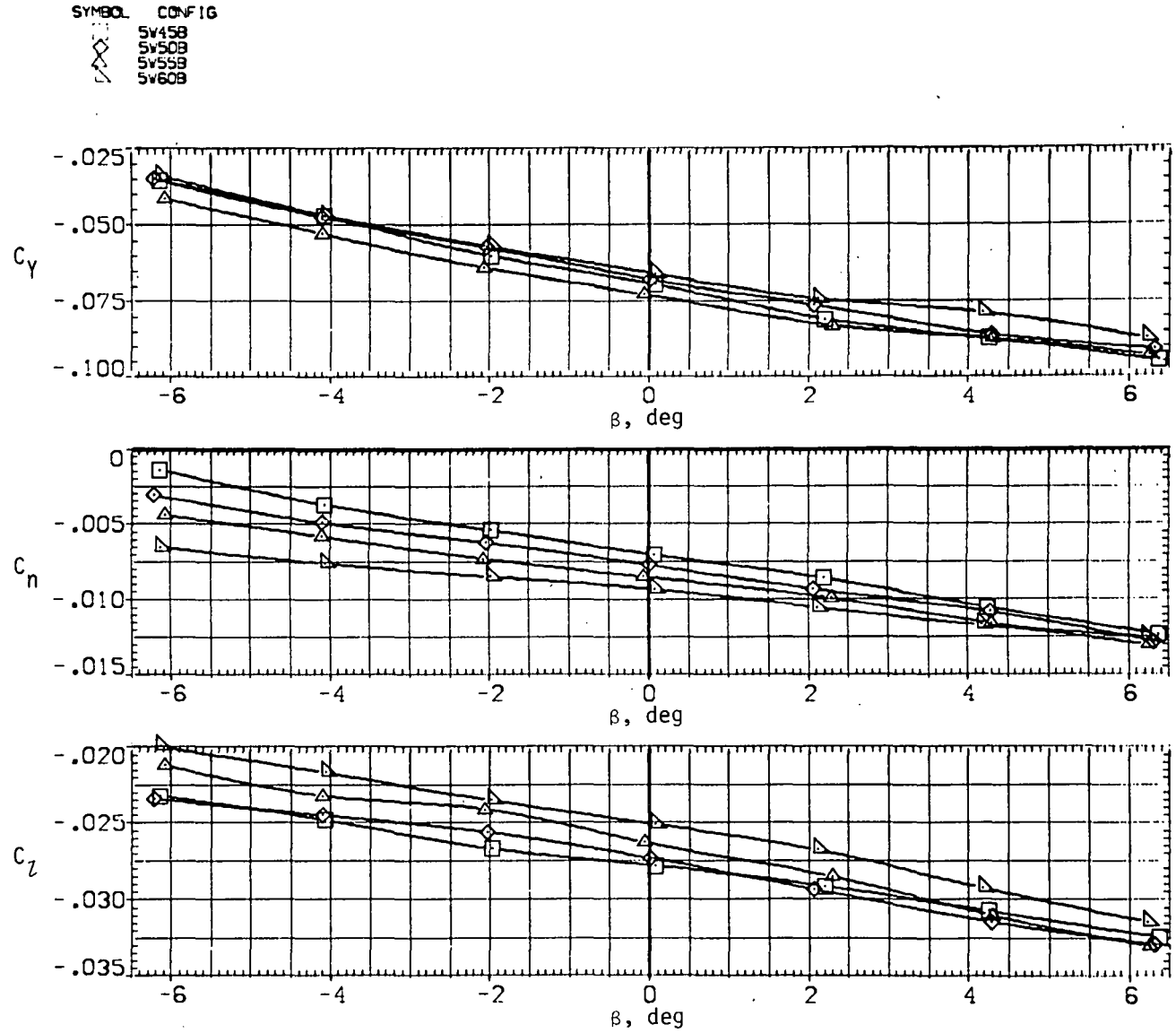

(b) C_Y, C_n and C_l versus β ($M = 0.6$).

Figure 15.– Continued.

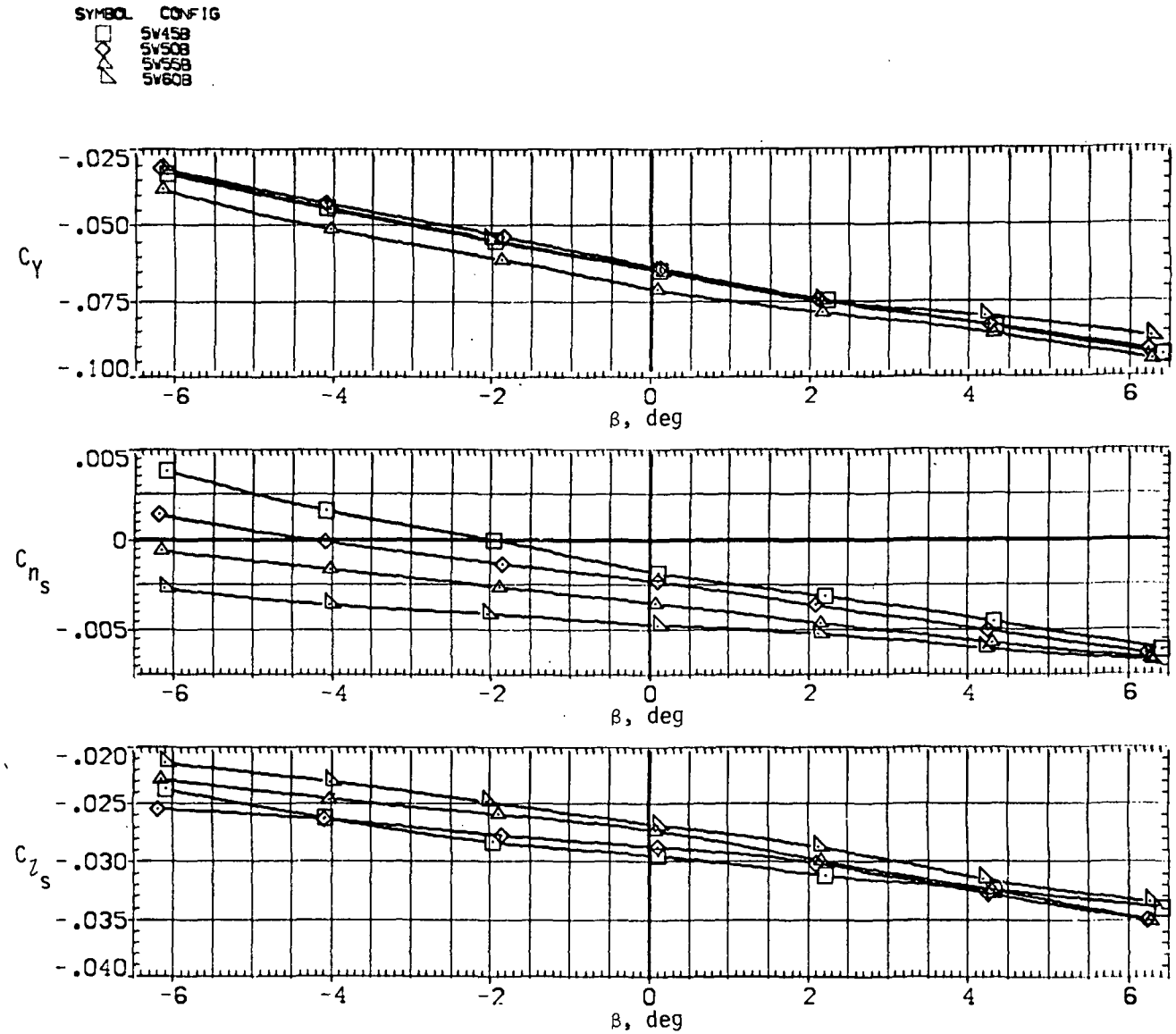

(c) C_Y, C_{n_s} and C_{l_s} versus β ($M = 0.7$).

Figure 15.– Continued.

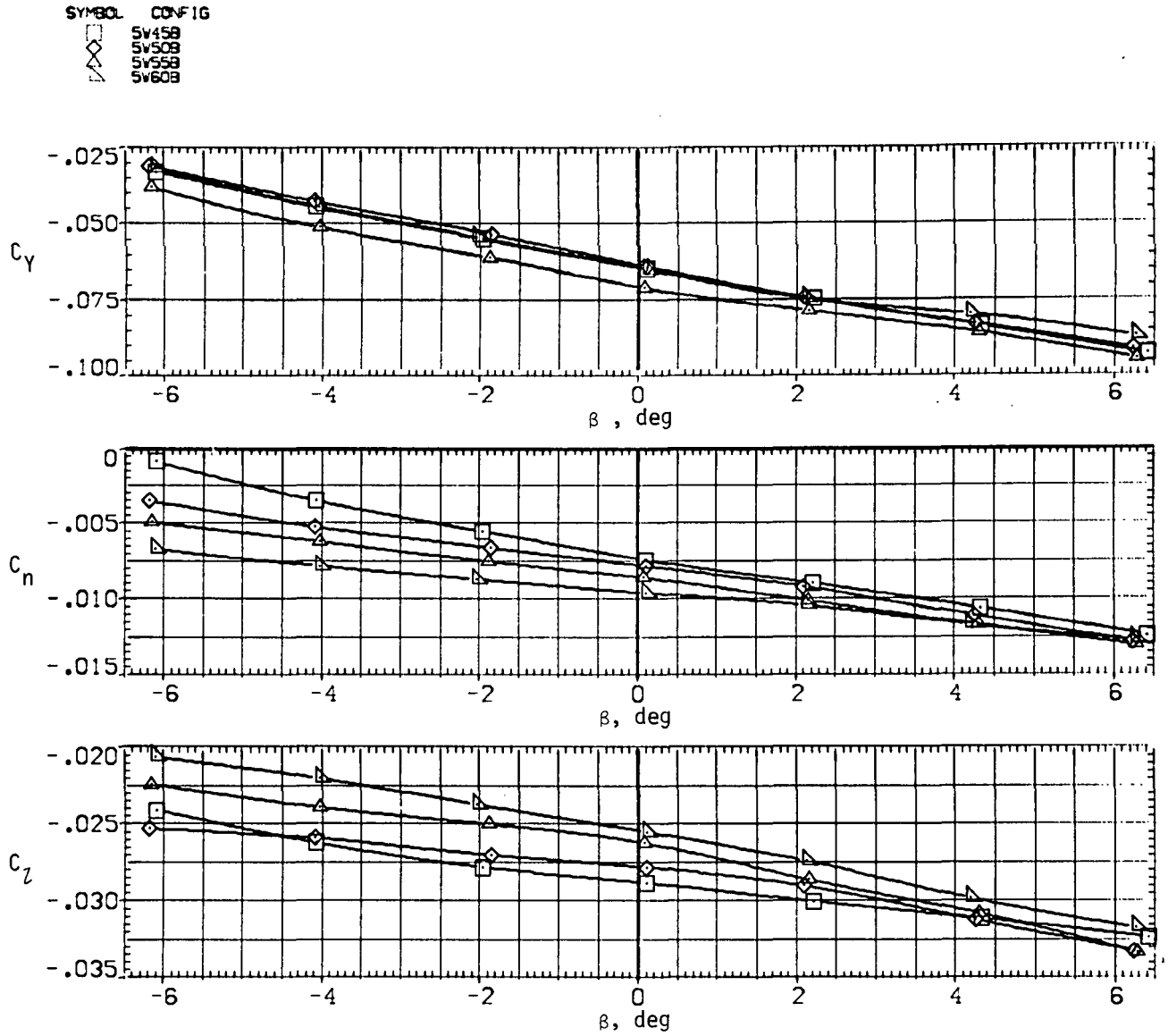

(d) C_Y, C_n and C_l versus β ($M = 0.7$).

Figure 15.– Continued.

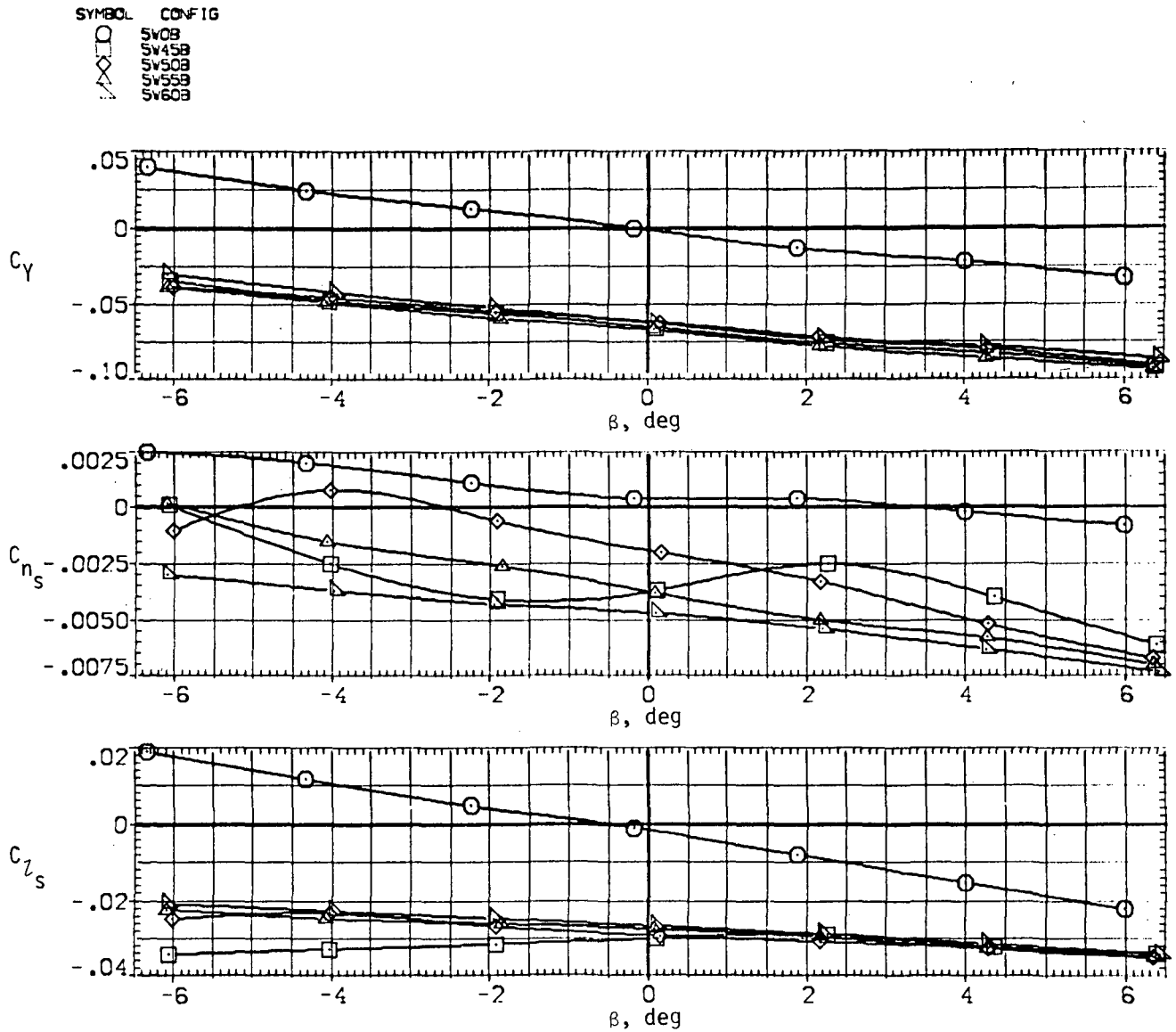

(e) C_Y, C_{n_s} and C_{l_s} versus β ($M = 0.8$).

Figure 15.– Continued.

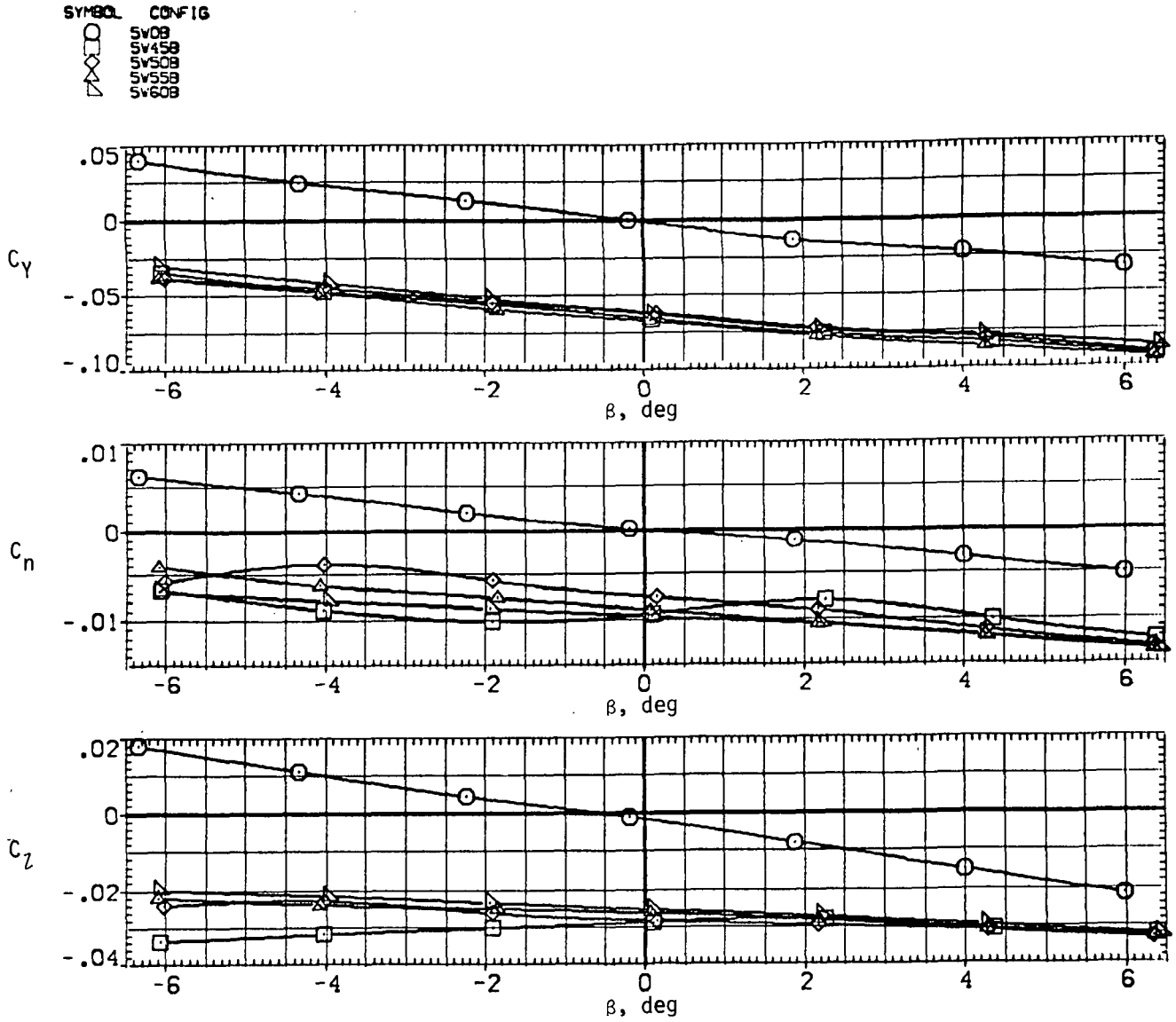

(f) C_Y, C_n and C_l versus β (M = 0.8).

Figure 15.– Continued.

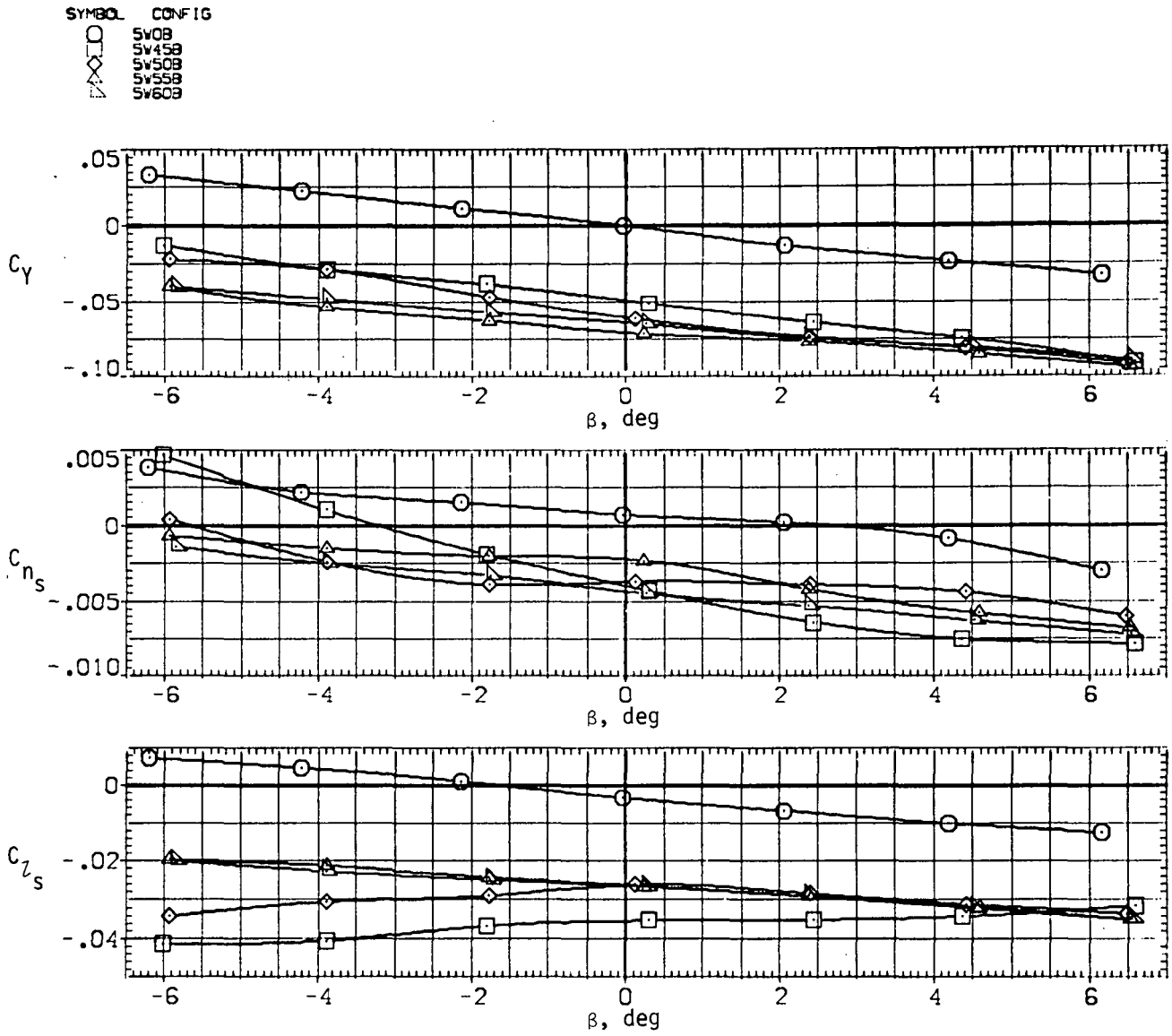

(g) C_Y, C_{n_s} and C_{l_s} versus β ($M = 0.9$).

Figure 15.– Continued.

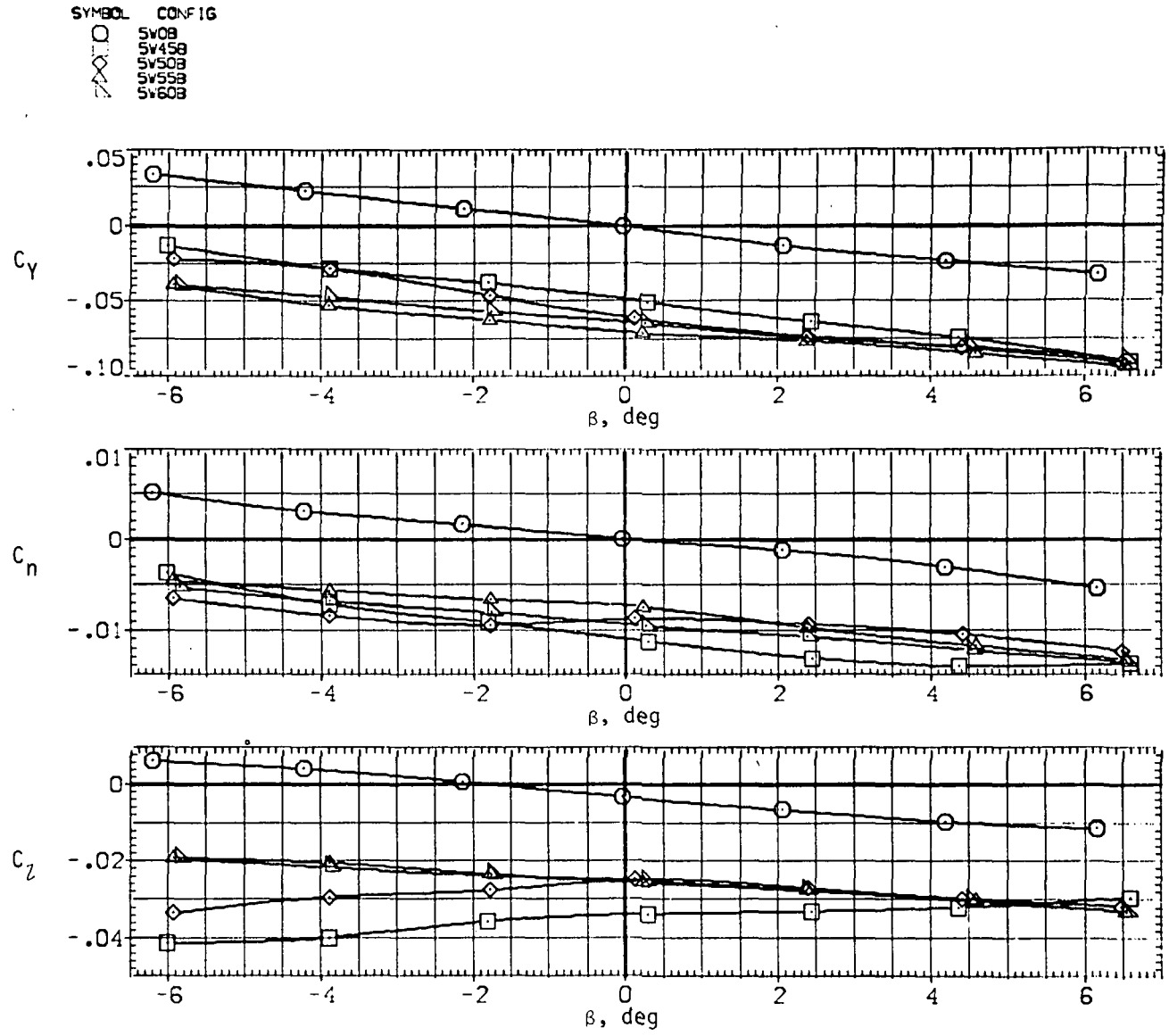

(h) C_Y, C_n and C_l versus β ($M = 0.9$).

Figure 15.– Continued.

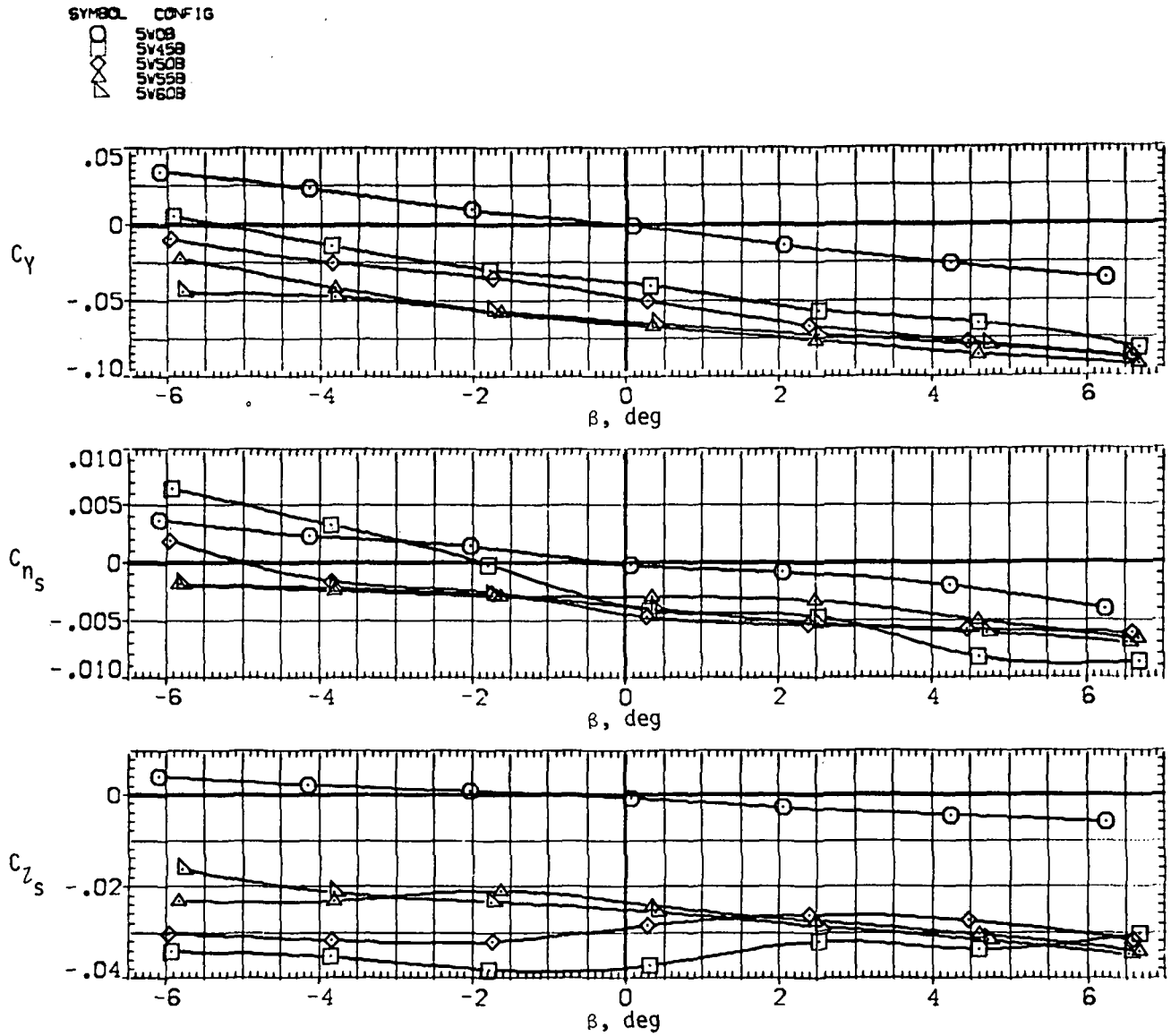

(i) C_Y, C_{n_s} and C_{l_s} versus β ($M = 0.95$).

Figure 15.– Continued.

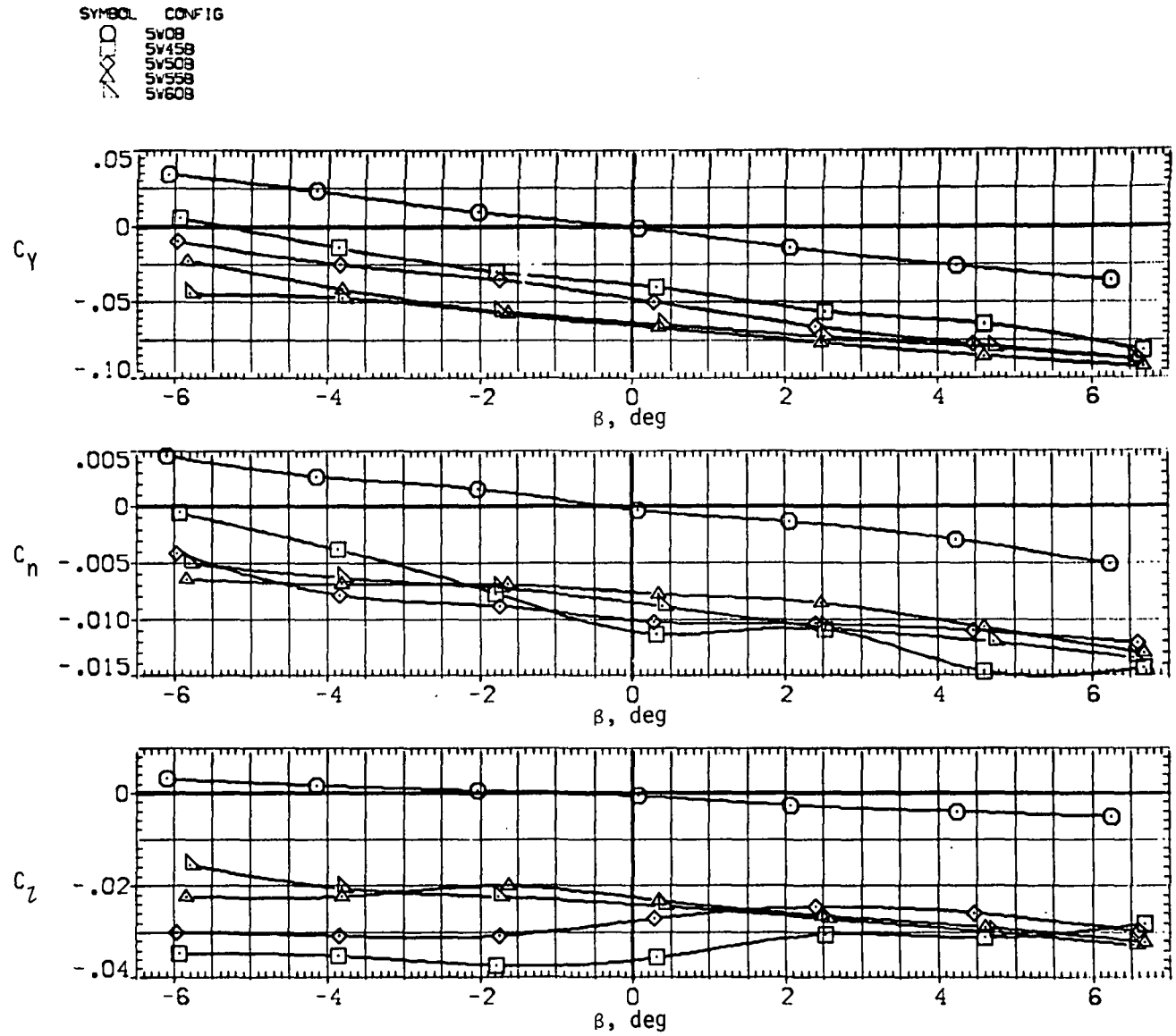

(j) C_Y, C_n and C_l versus β ($M = 0.95$).

Figure 15.– Continued.

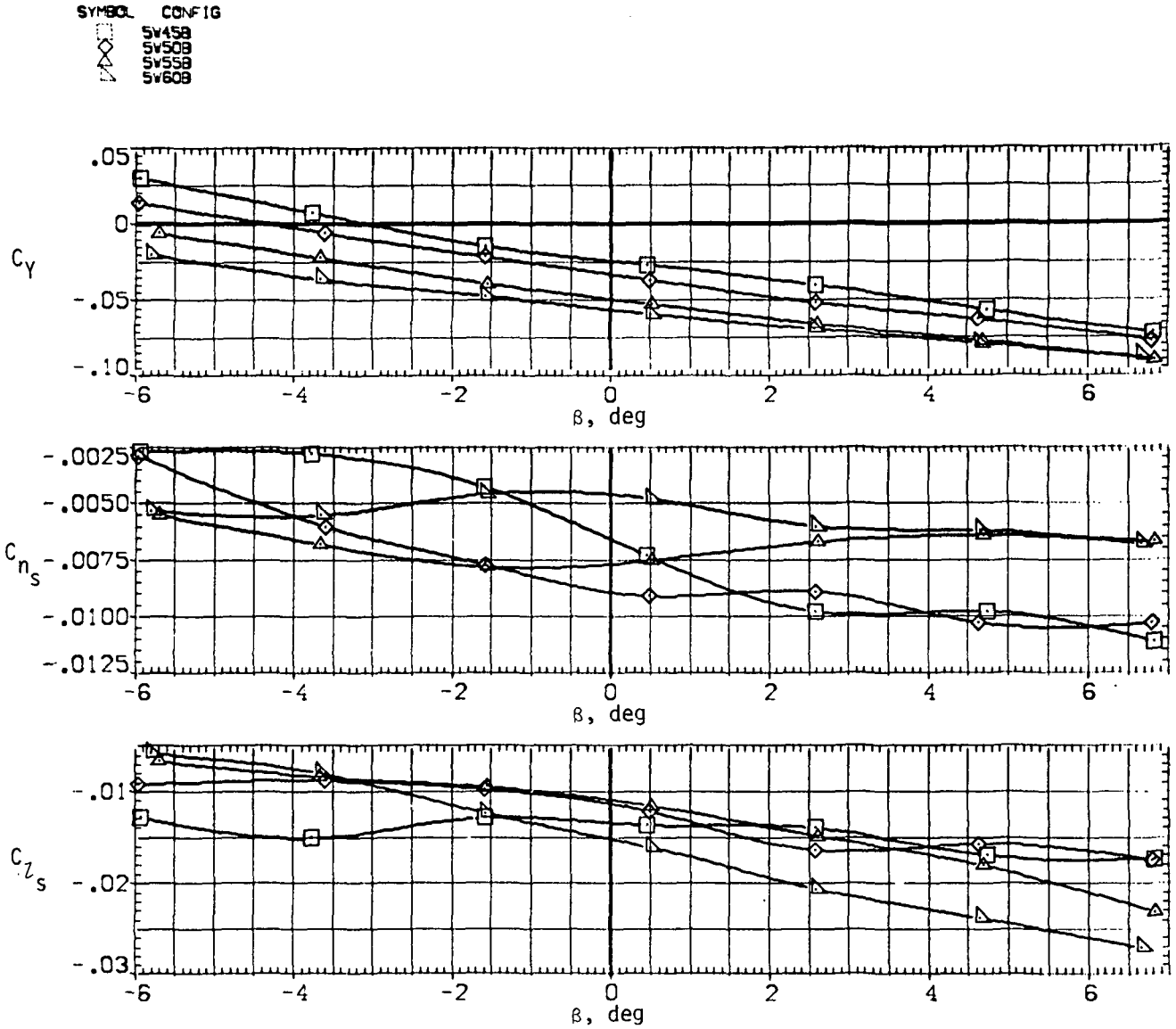

(k) C_Y, C_{n_s} and C_{l_s} versus β (M = 1.1).

Figure 15.– Continued.

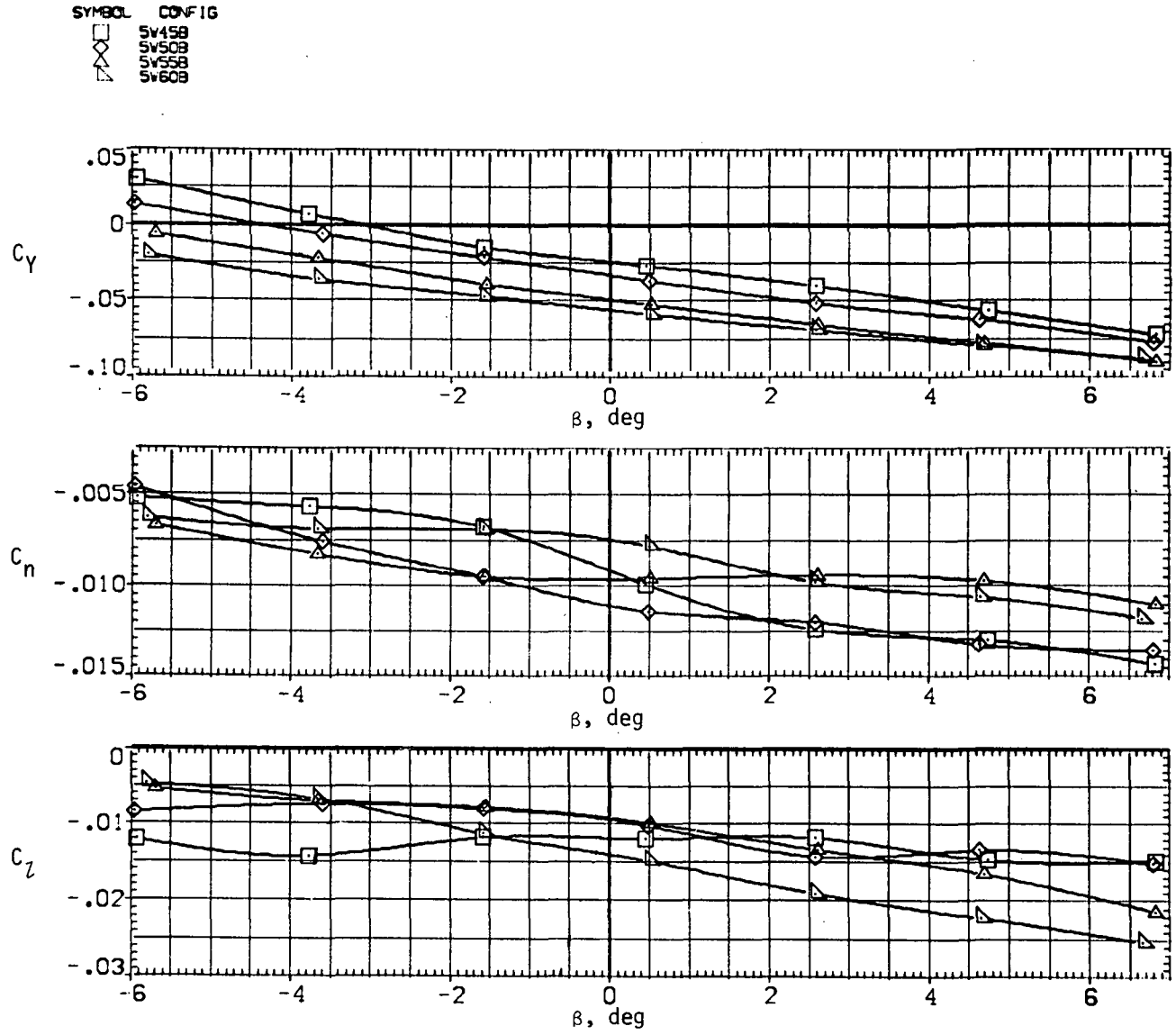

(l) C_Y, C_n and C_l versus β (M = 1.1).

Figure 15.– Continued.

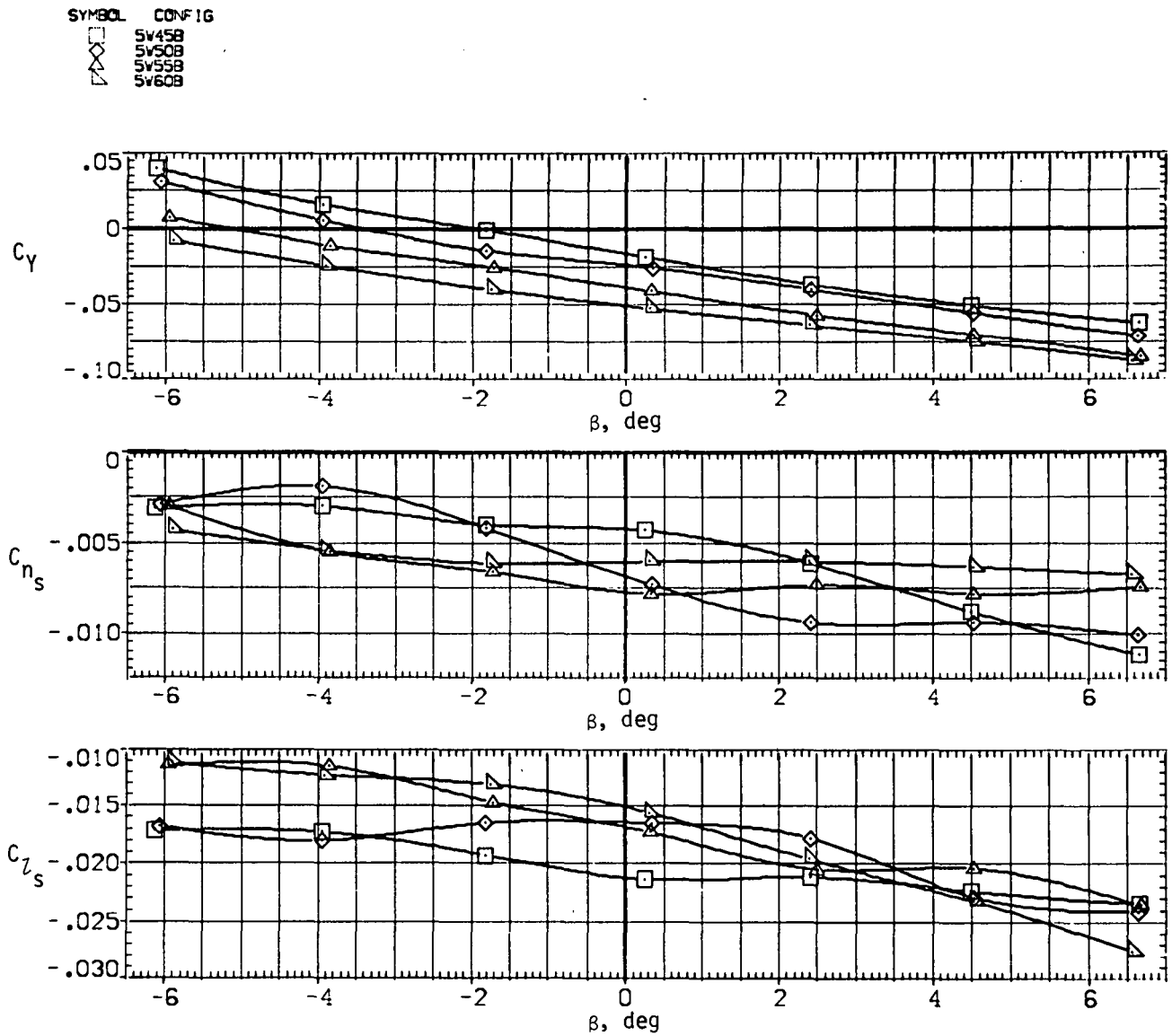

(m) C_Y, C_{n_s} and C_{l_s} versus β (M = 1.2).

Figure 15.– Continued.

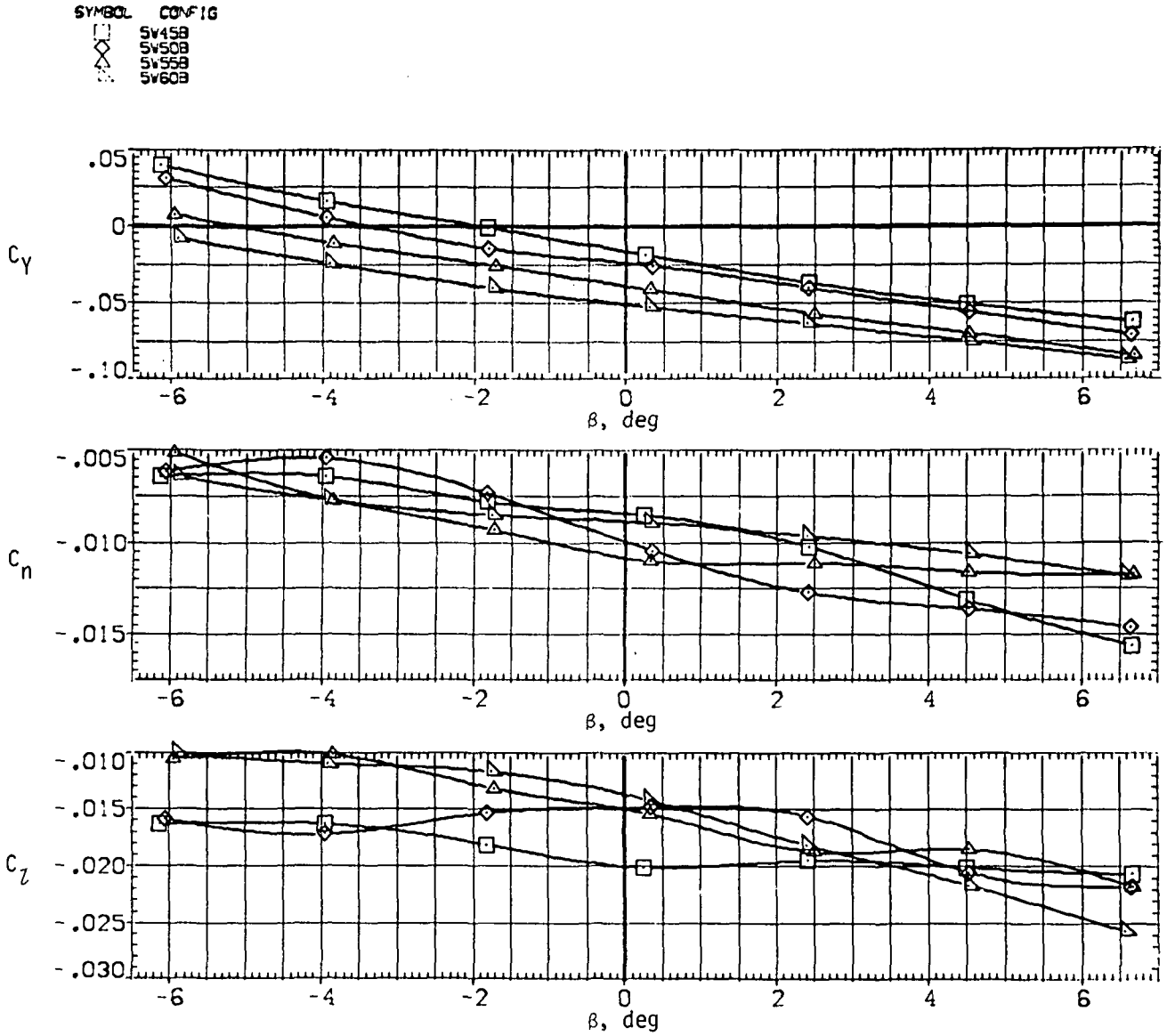

(n) C_Y, C_n and C_l versus β (M = 1.2).

Figure 15.– Continued.

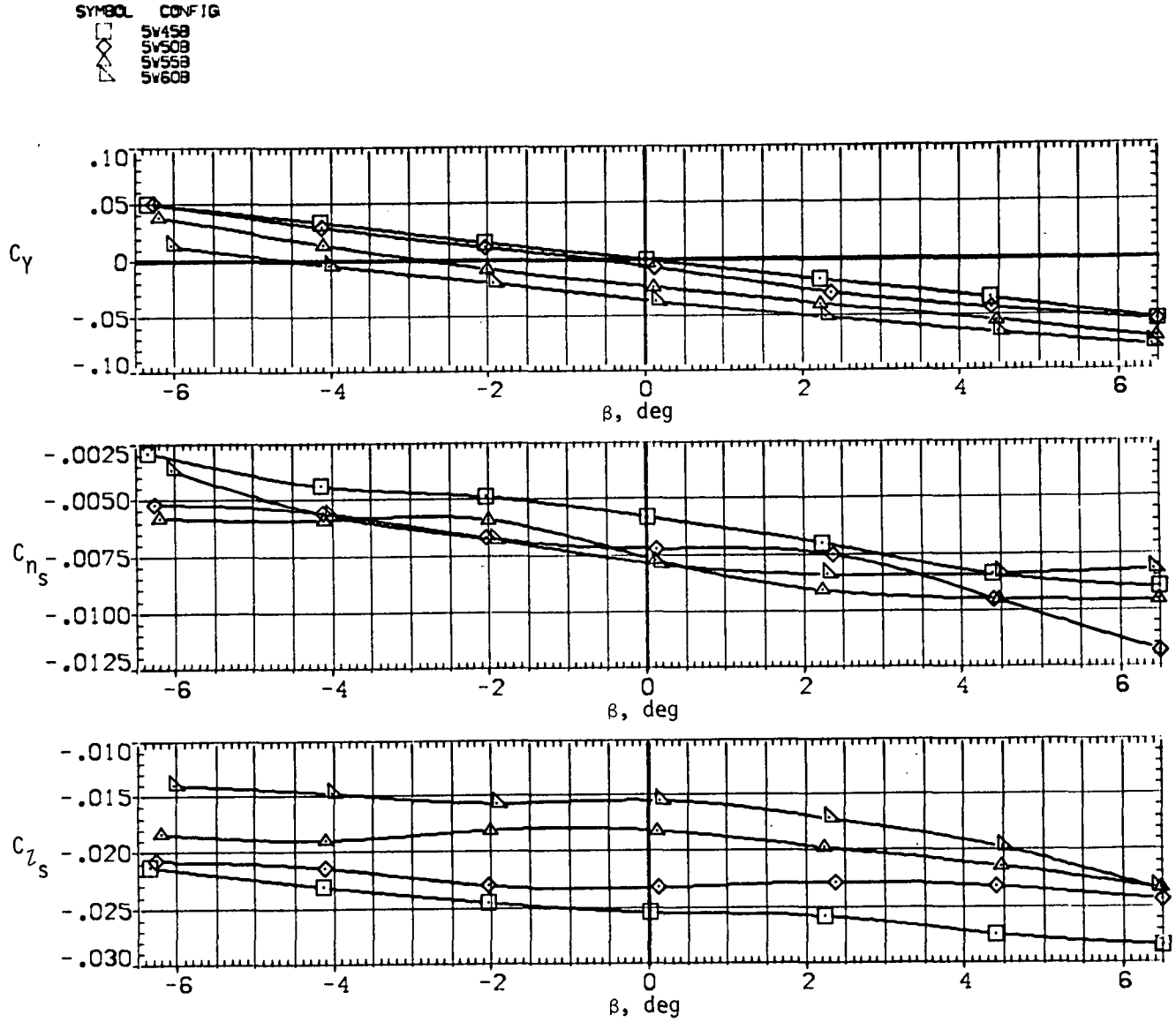

(o) C_Y, C_{n_s} and C_{l_s} versus β (M = 1.4).

Figure 15.– Continued.

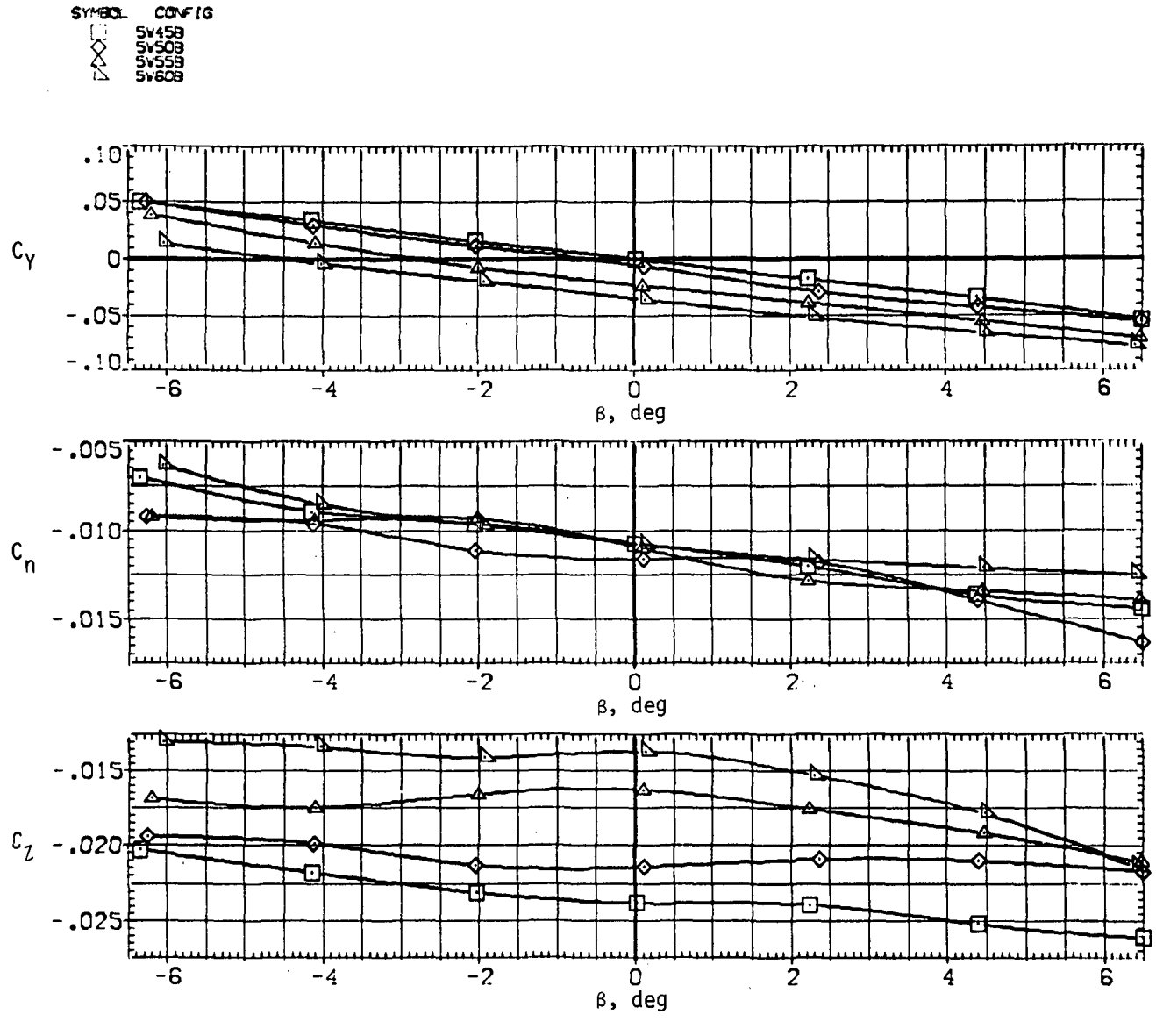

(p) C_Y, C_n and C_l versus β (M = 1.4).

Figure 15.– Concluded.

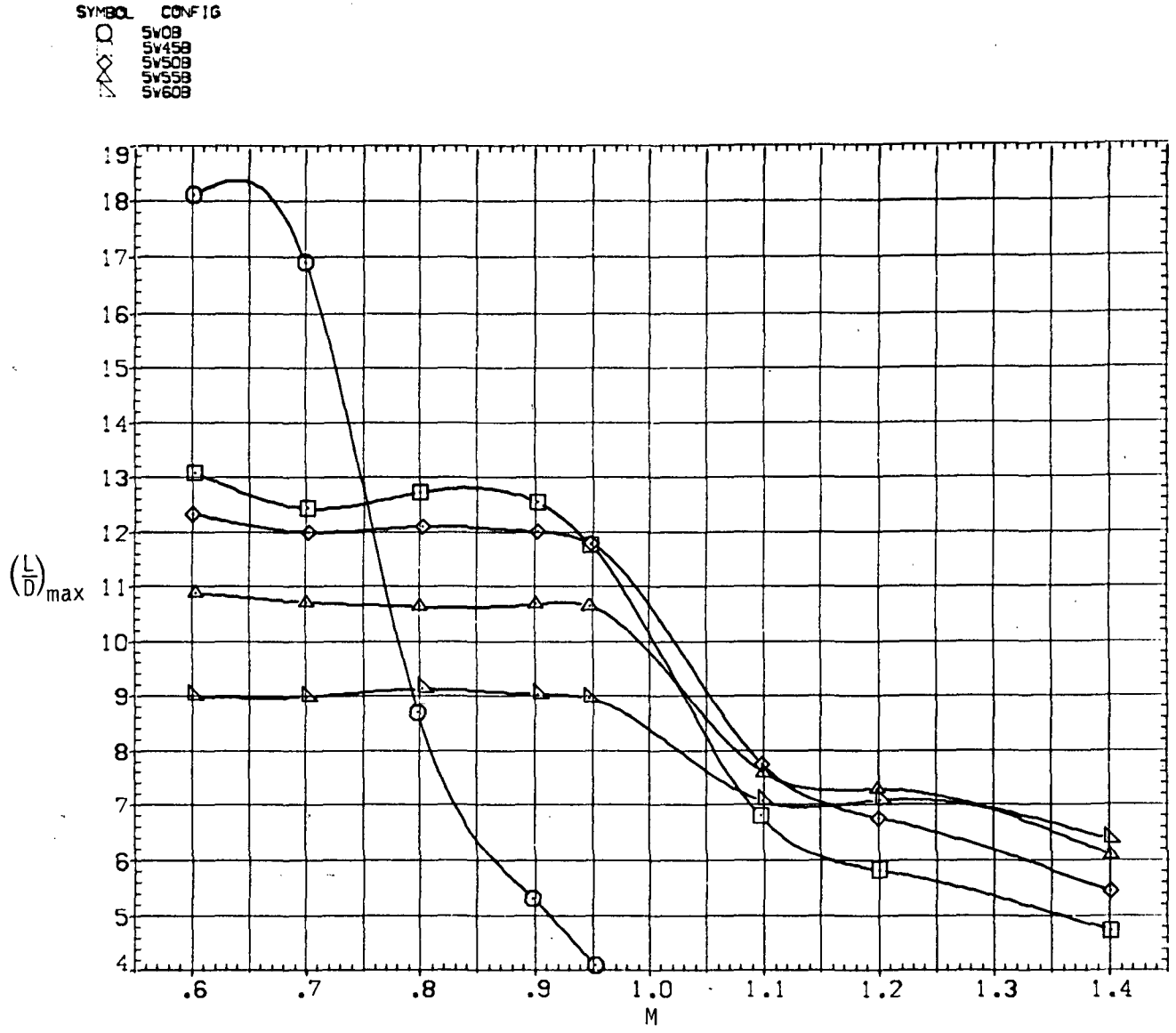

(a) $(L/D)_{max}$ versus M.

Figure 16.– Summary of the longitudinal stability characteristics of the oblique wing with intermediate bend.

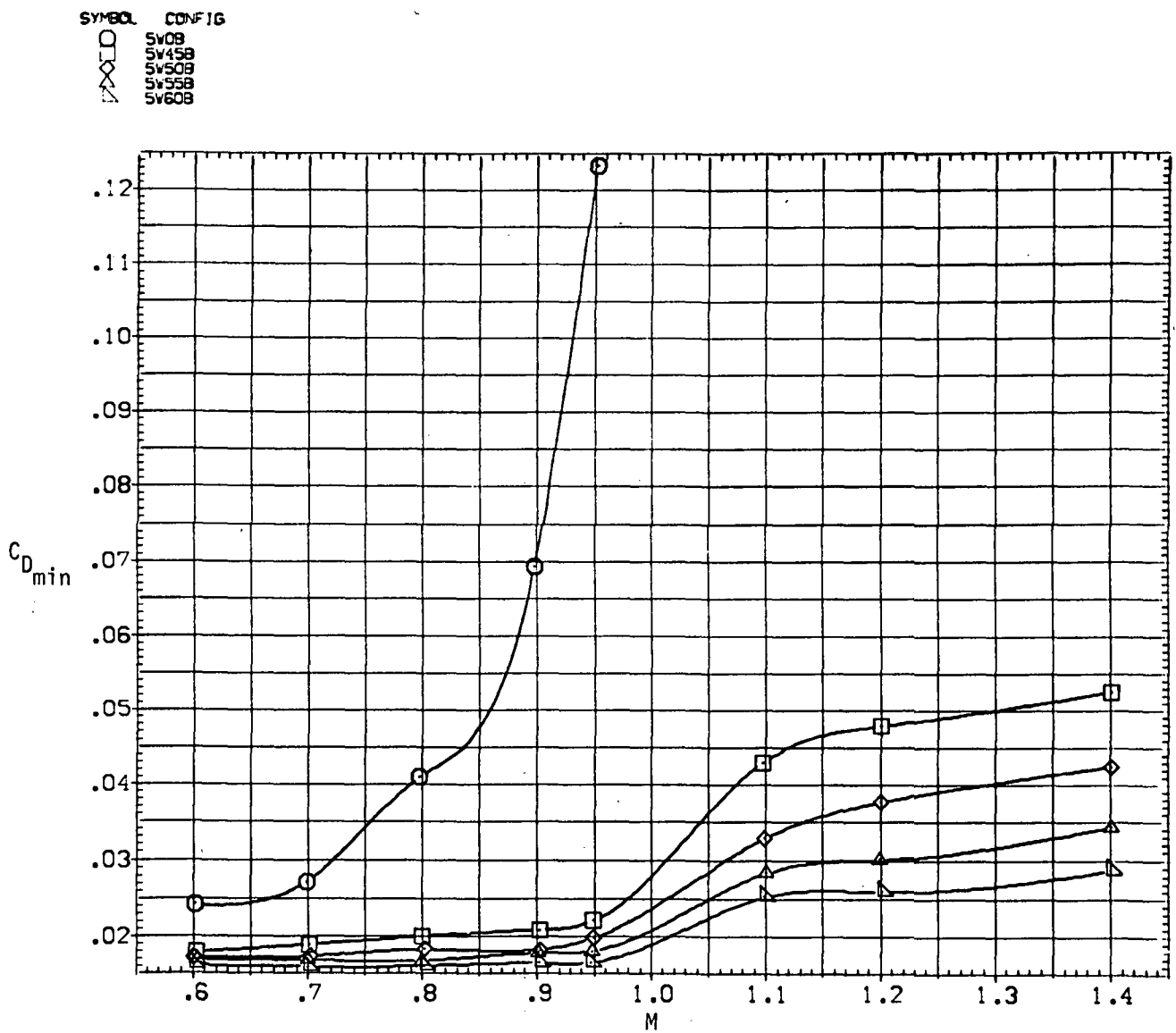

(b) $C_{D_{min}}$ versus M.

Figure 16.– Continued.

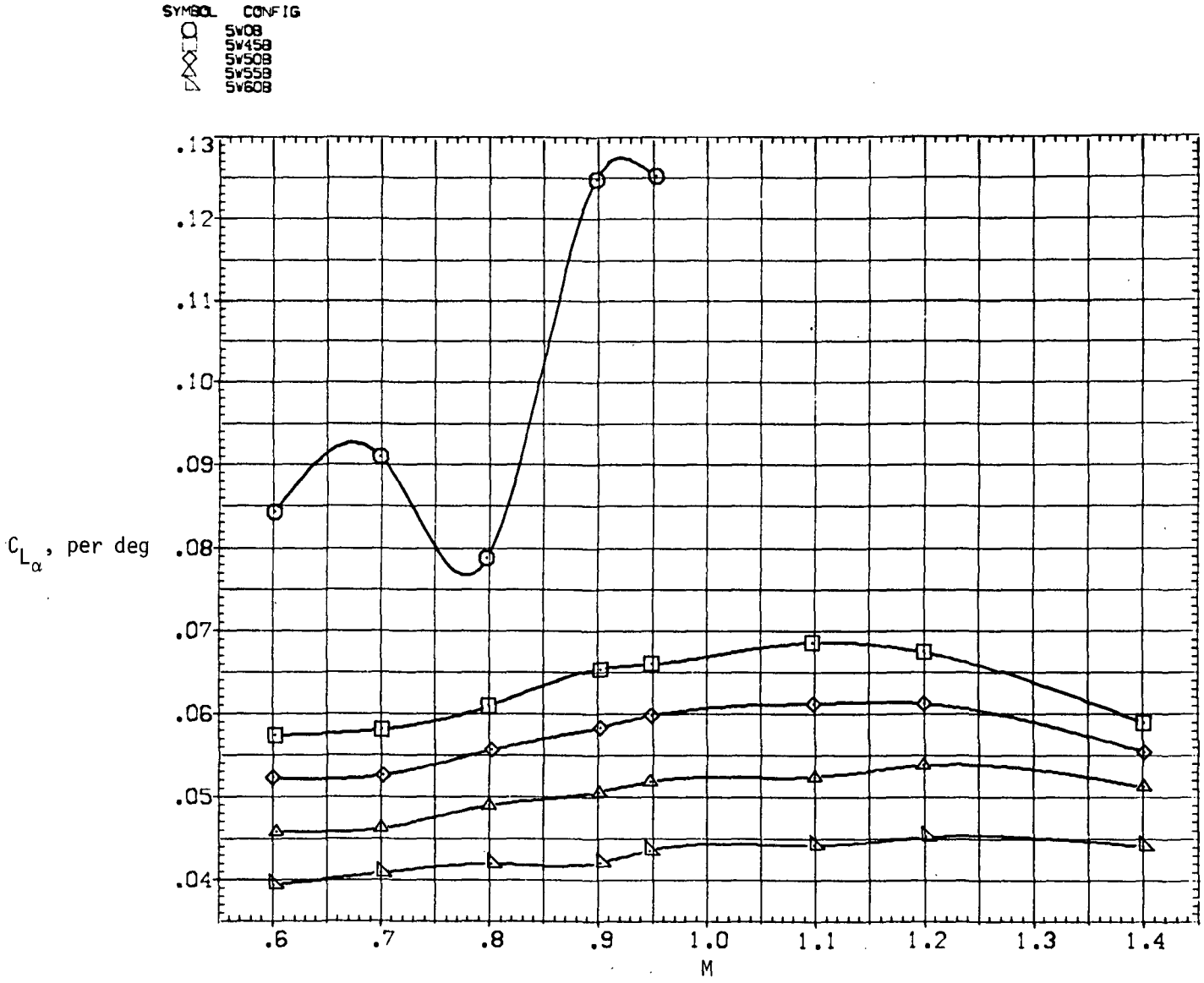

(c) C_{L_α} versus M.

Figure 16.– Continued.

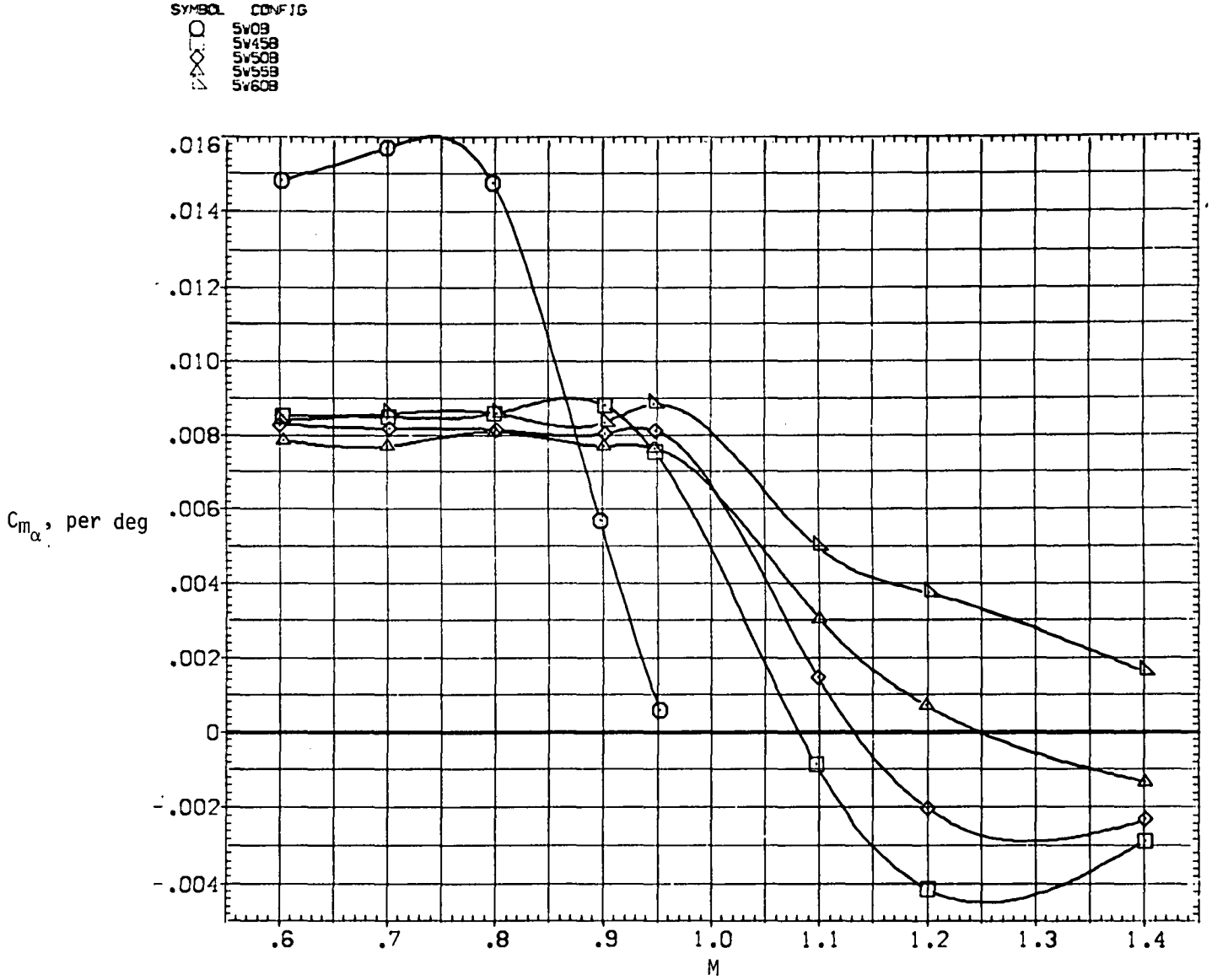

(d) C_{m_α} versus M.

Figure 16.– Concluded.

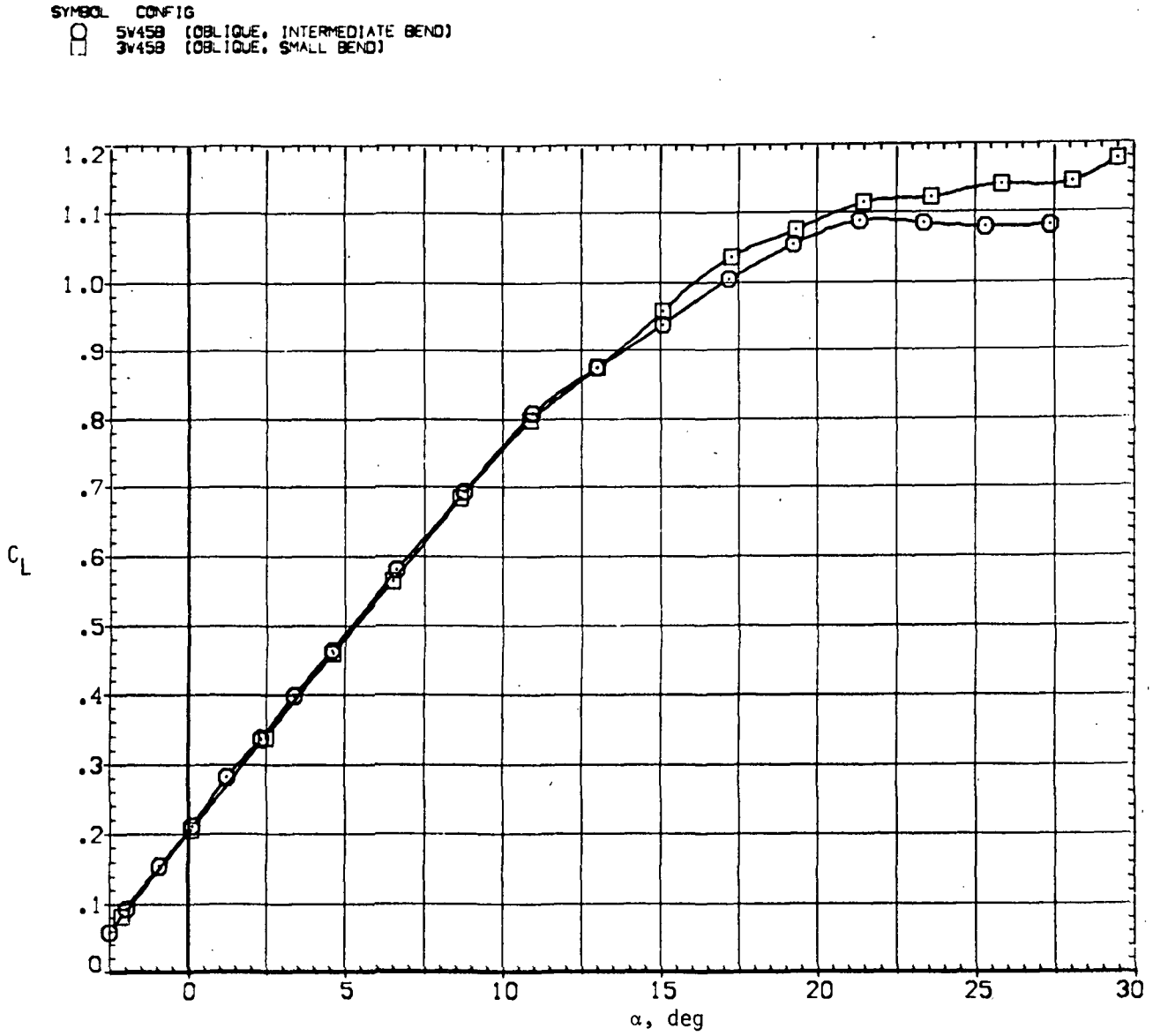

(a) C_L versus α.

Figure 17.– Effect of wing bend on the longitudinal stability characteristics of the oblique wing, $M = 0.6$.

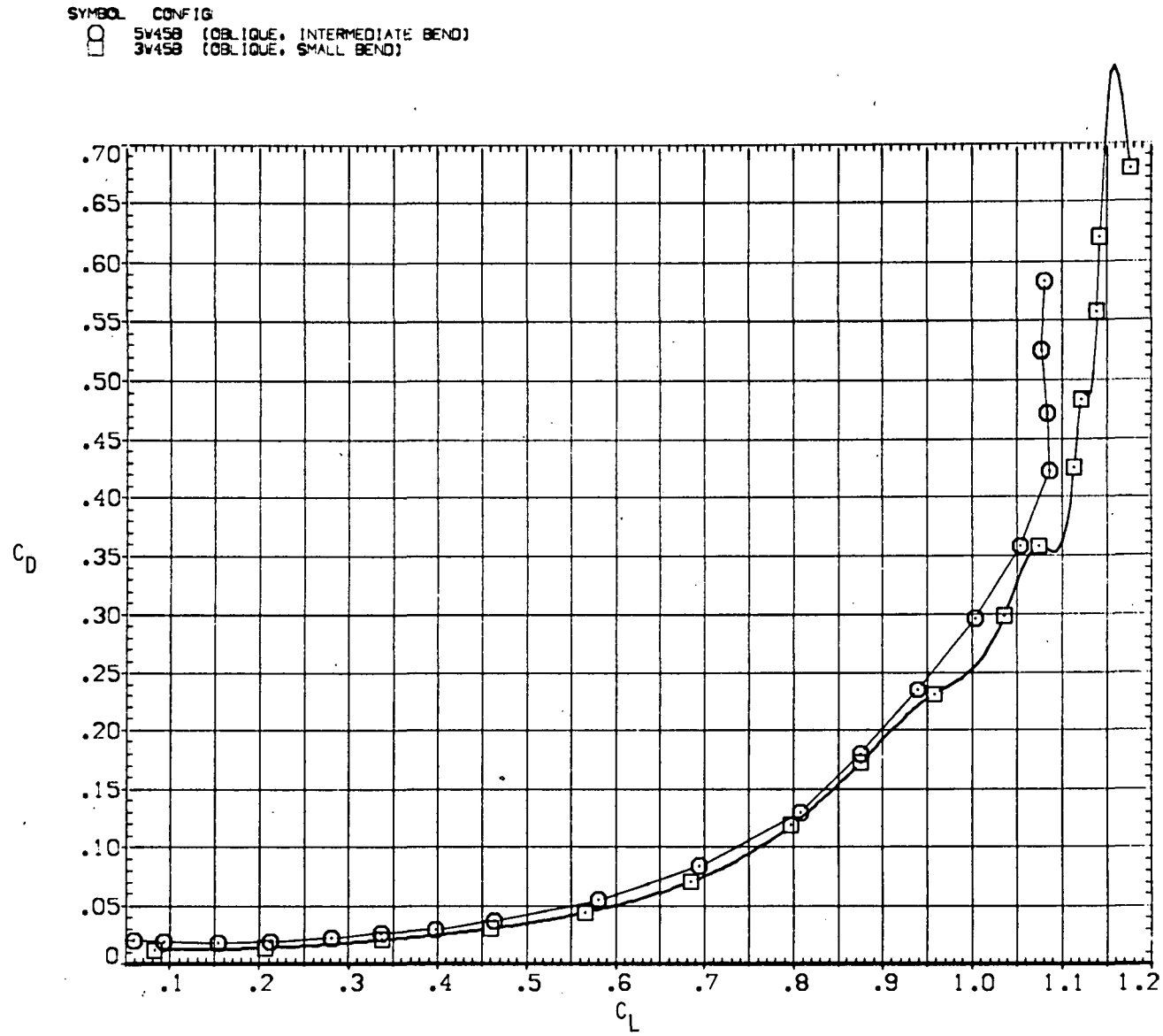

(b) C_D versus C_L.

Figure 17.– Continued.

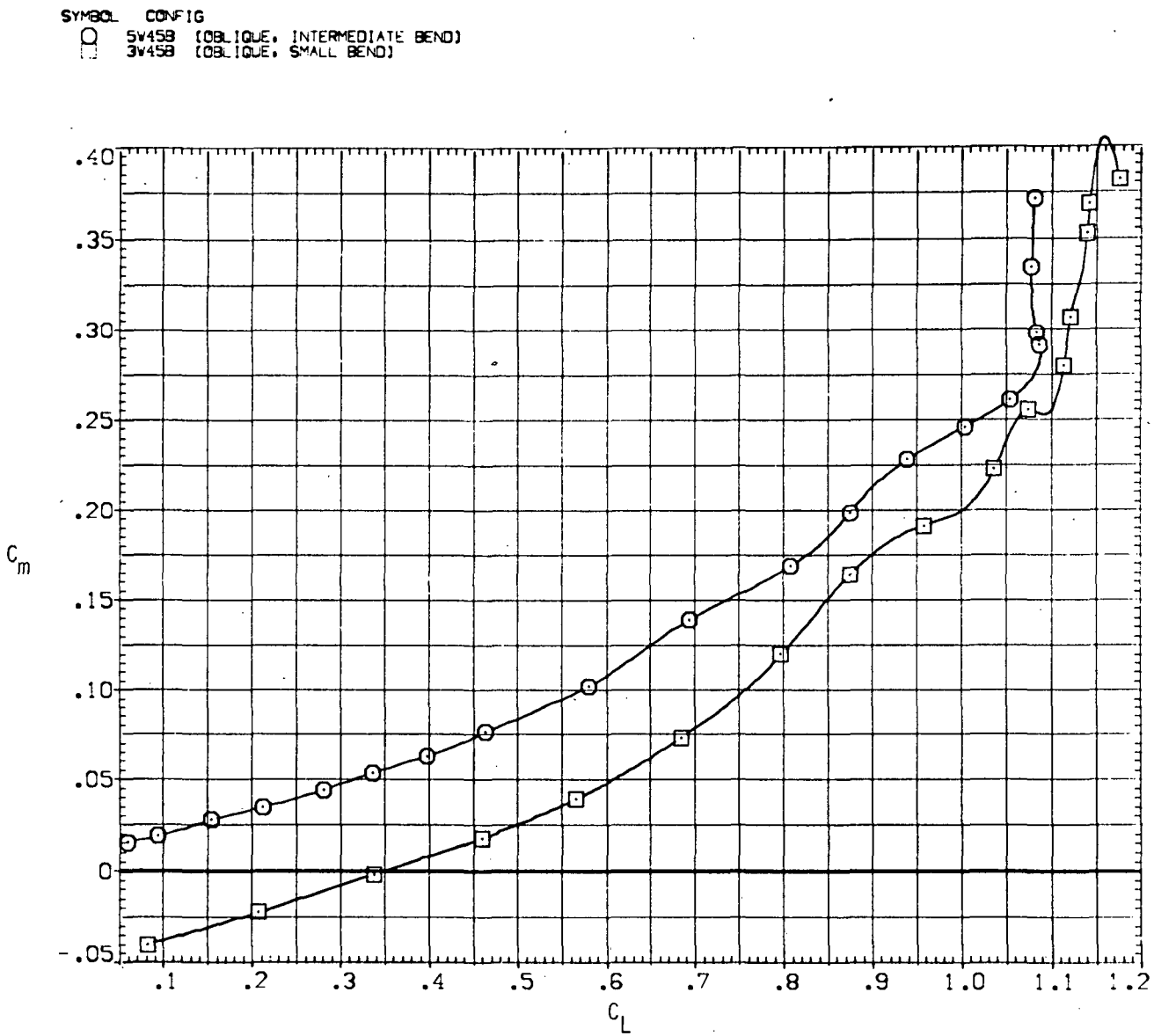

(c) C_m versus C_L.

Figure 17.– Continued.

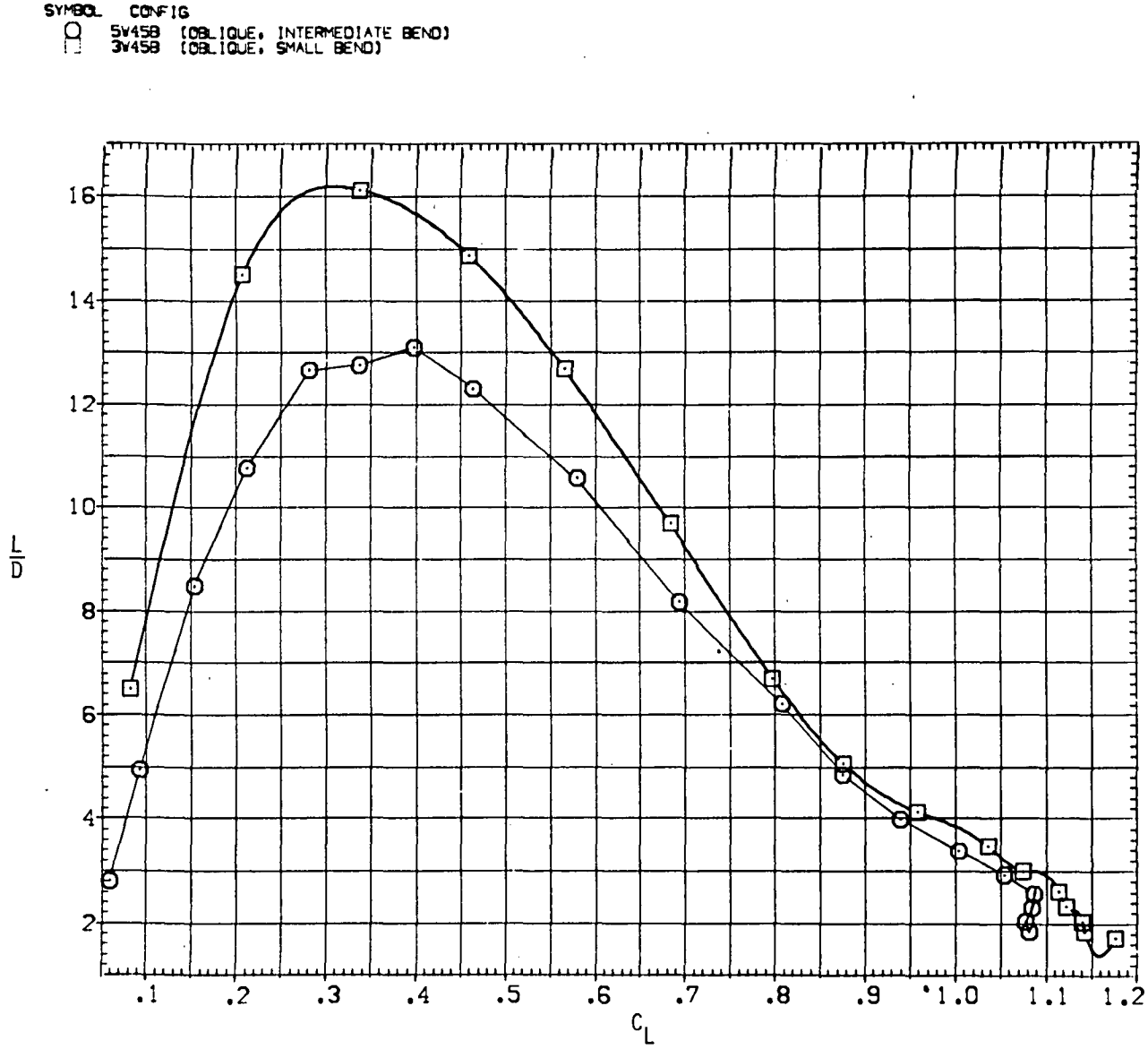

(d) L/D versus C_L.

Figure 17.– Continued.

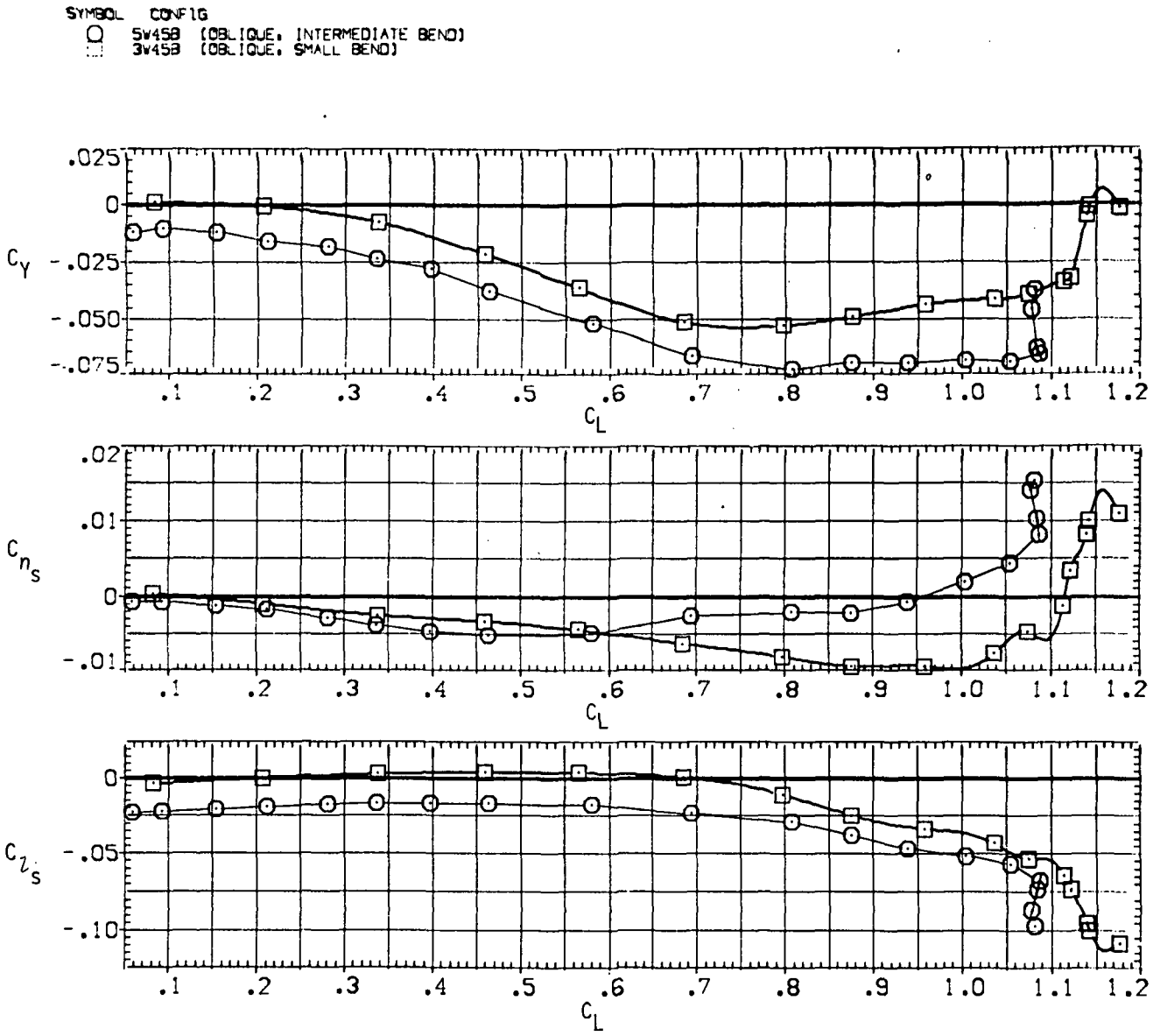

(e) C_Y, C_{n_s} and C_{l_s} versus C_L.

Figure 17.– Continued.

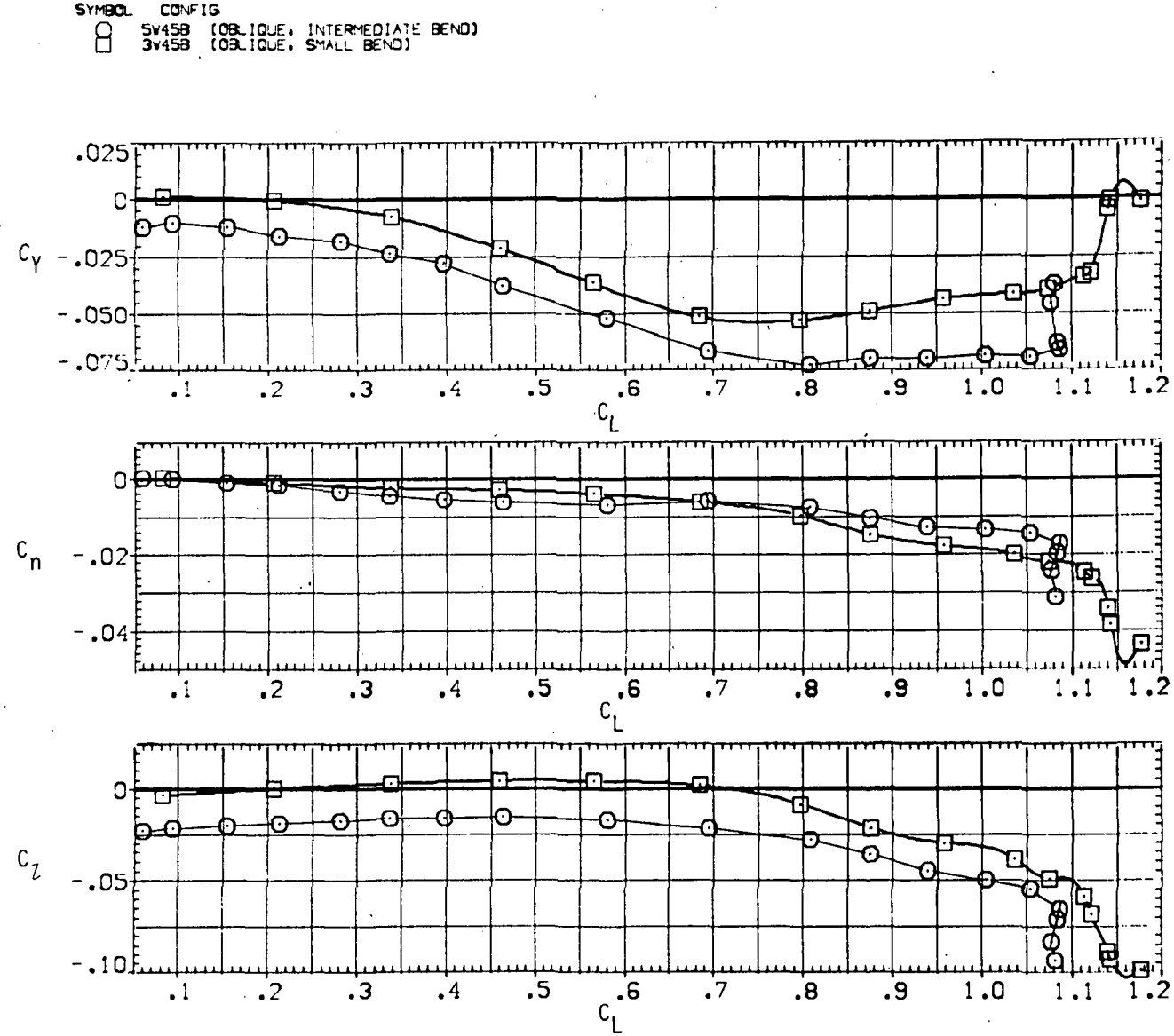

(f) C_Y, C_n and C_l versus C_L.

Figure 17.– Concluded.

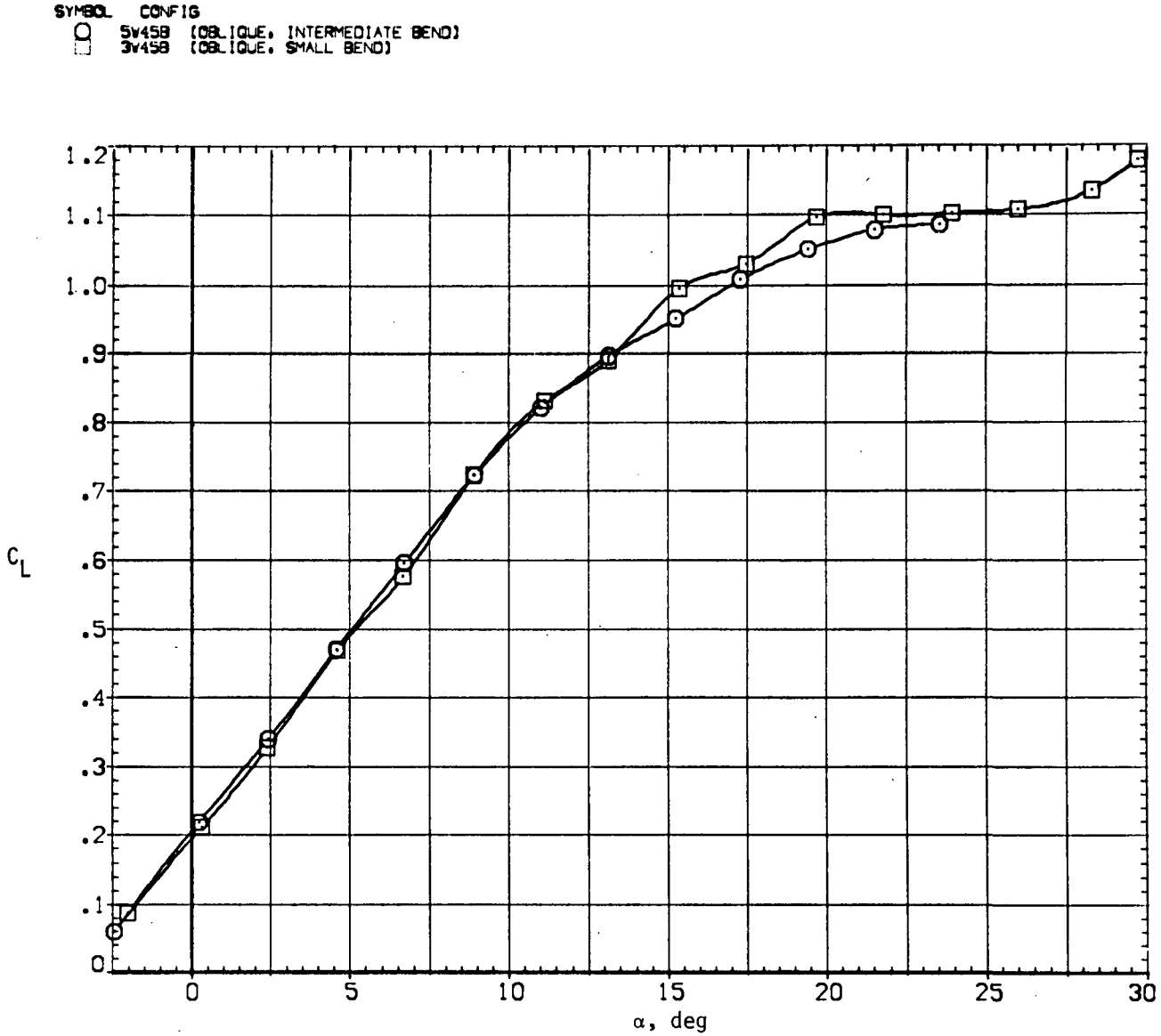

(a) C_L versus α.

Figure 18.– Effect of wing bend on the longitudinal stability characteristics of the oblique wing, $M = 0.7$

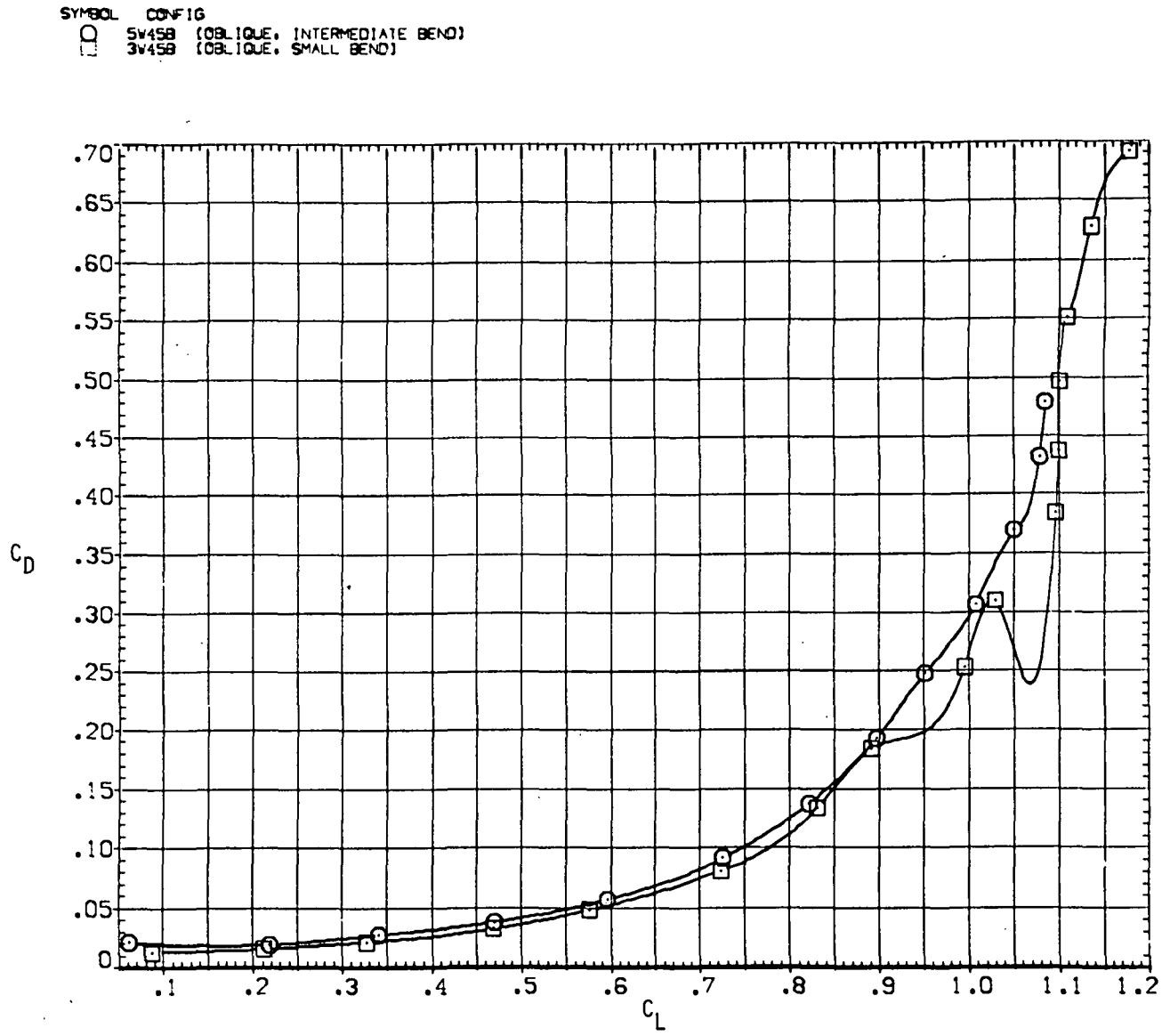

(b) C_D versus C_L.

Figure 18.– Continued.

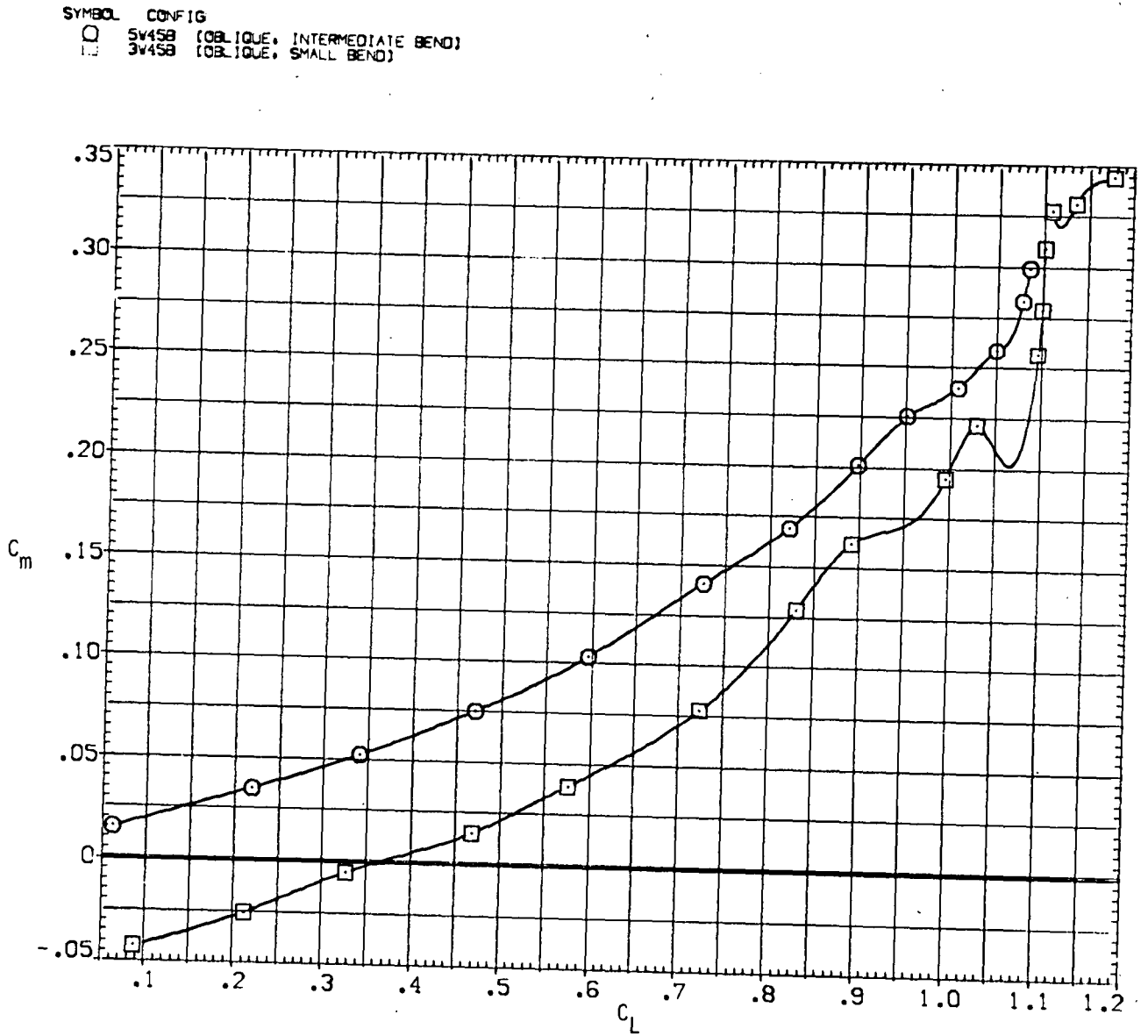

(c) C_m versus C_L.

Figure 18.– Continued.

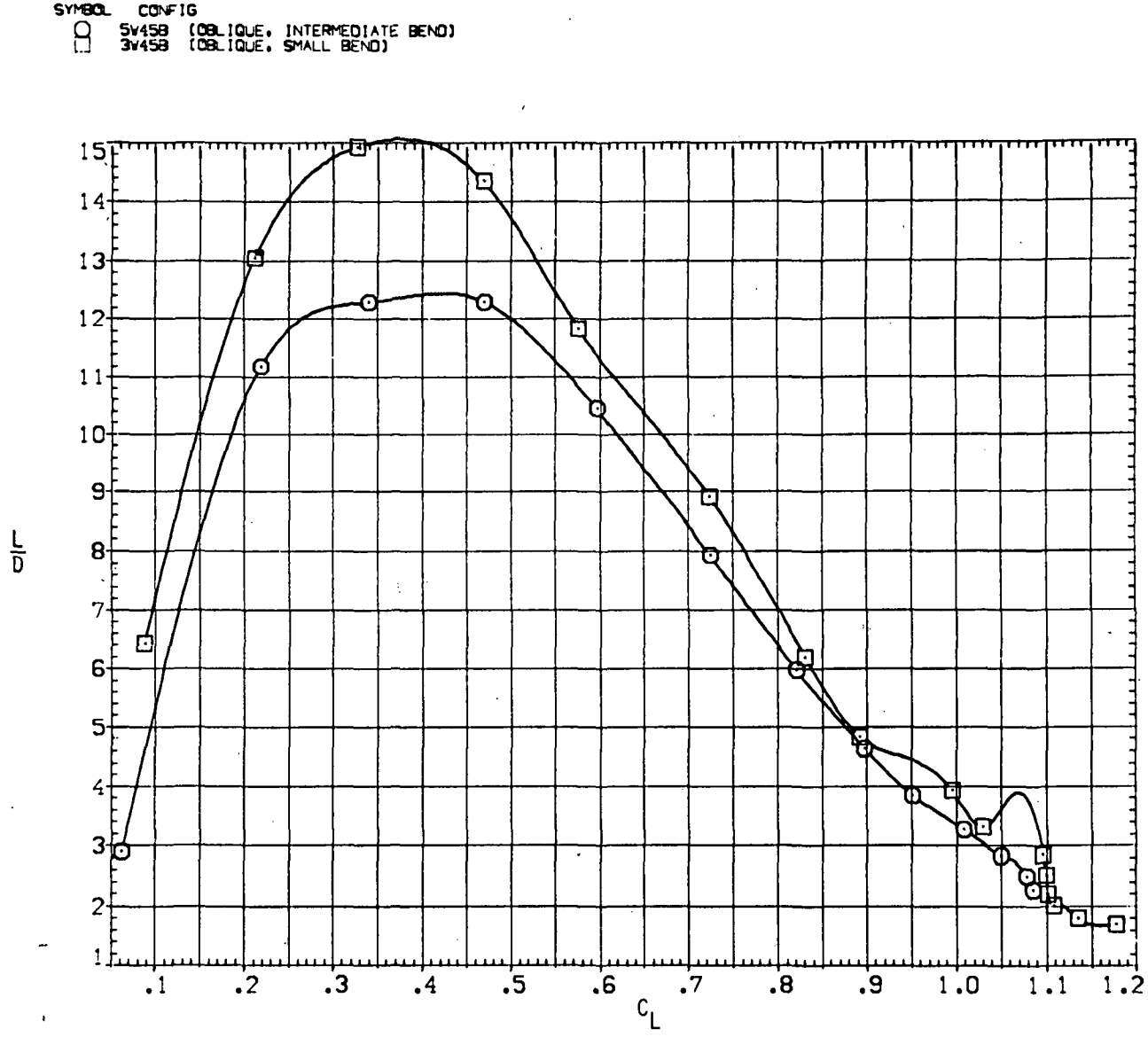

(d) L/D versus C_L.

Figure 18.– Continued.

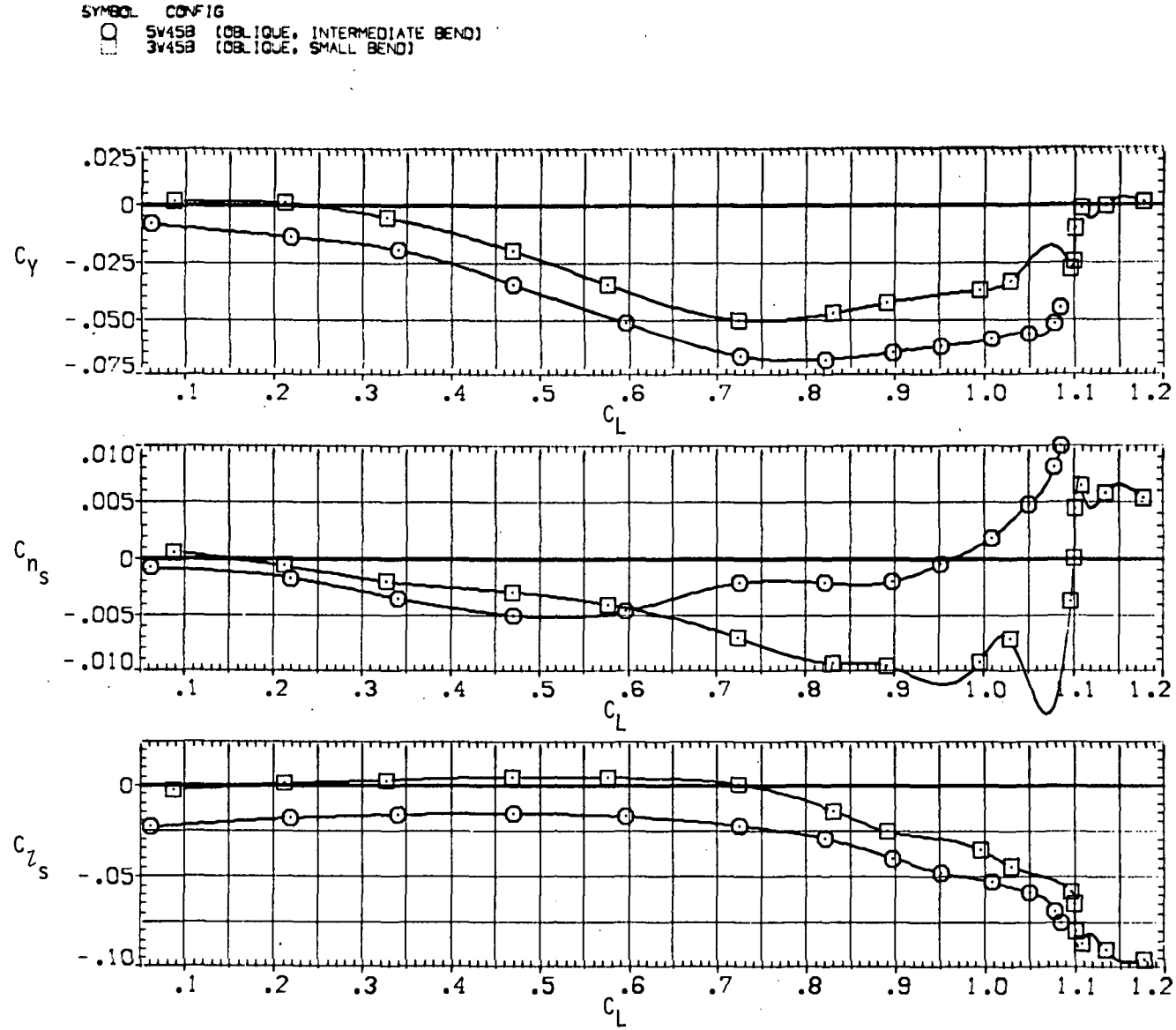

(e) C_Y, C_{n_s} and C_{l_s} versus C_L.

Figure 18.– Continued.

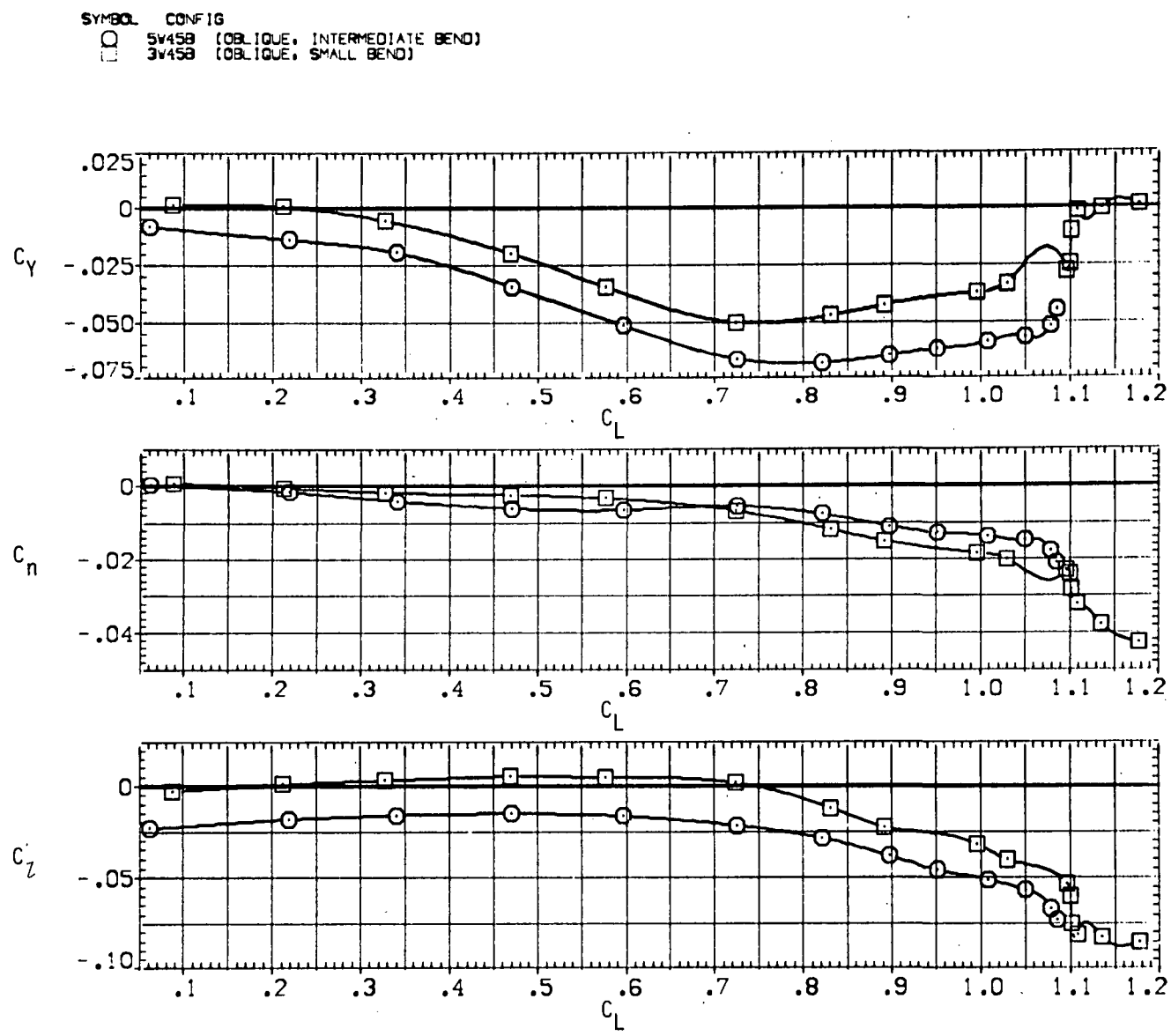

(f) C_Y, C_n and C_l versus C_L.

Figure 18.– Concluded.

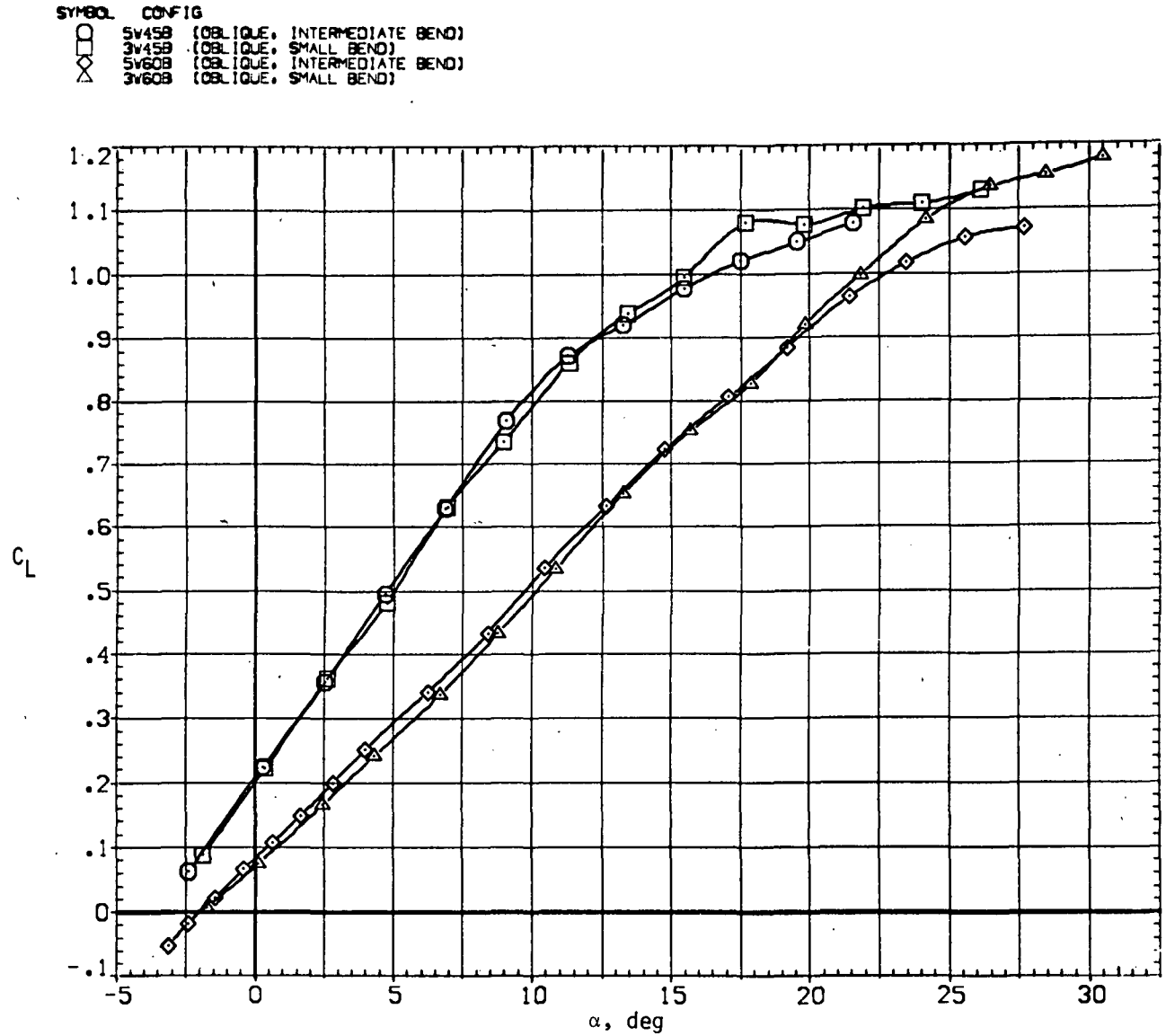

(a) C_L versus α.

Figure 19.– Effect of wing bend on the longitudinal stability characteristics of the oblique wing, $M = 0.8$.

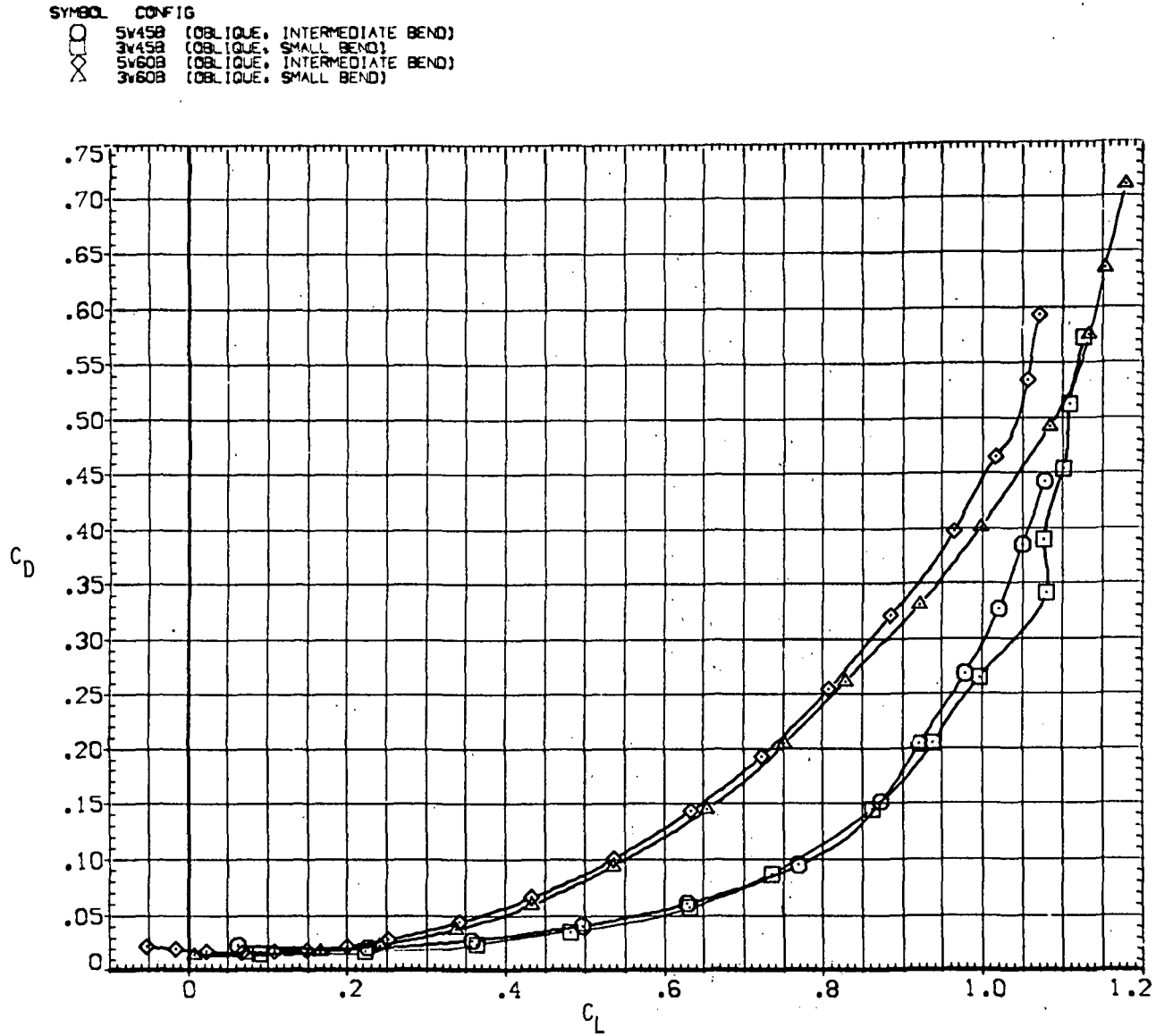

(b) C_D versus C_L.

Figure 19.– Continued.

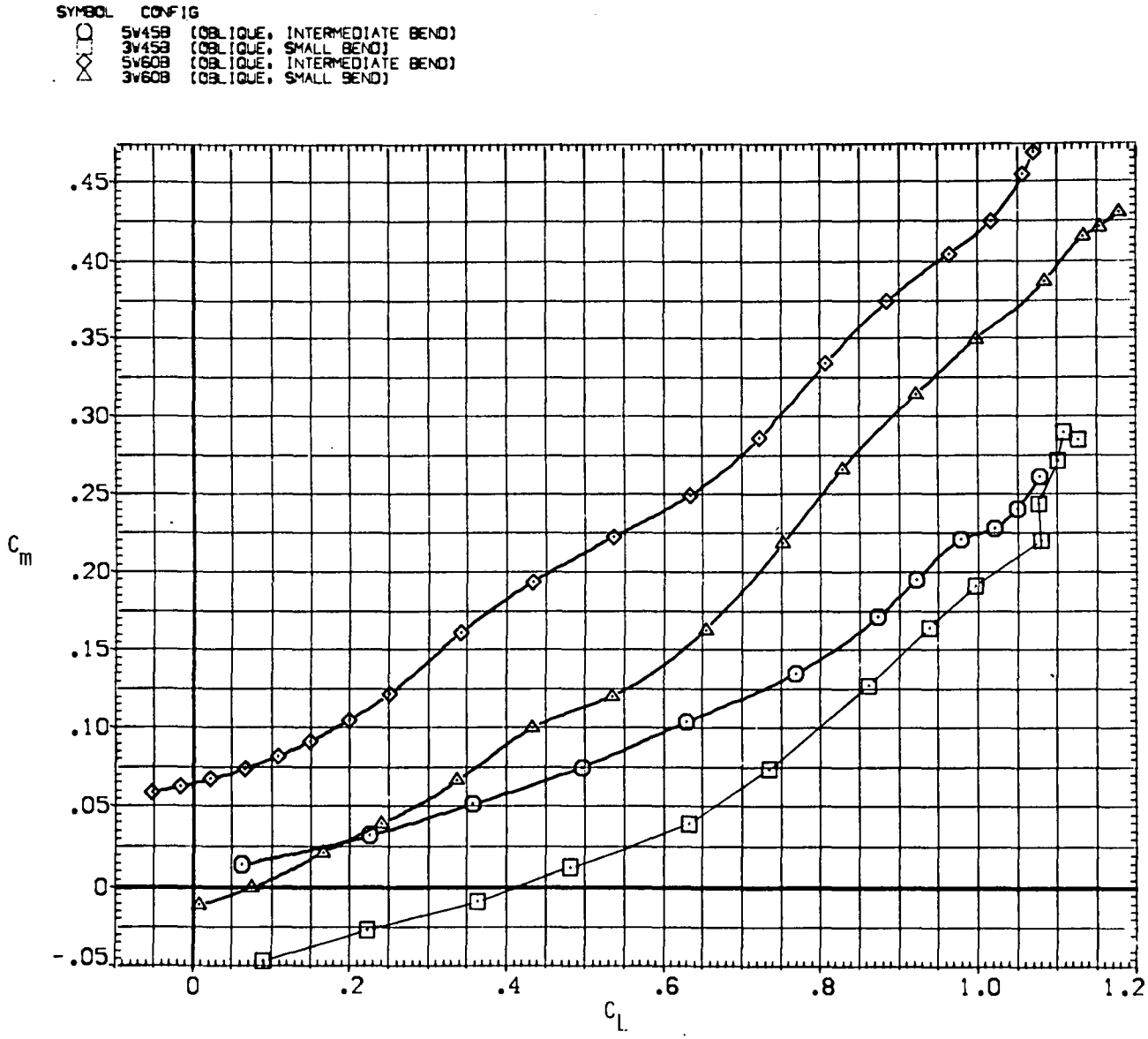

(c) C_m versus C_L.

Figure 19.– Continued.

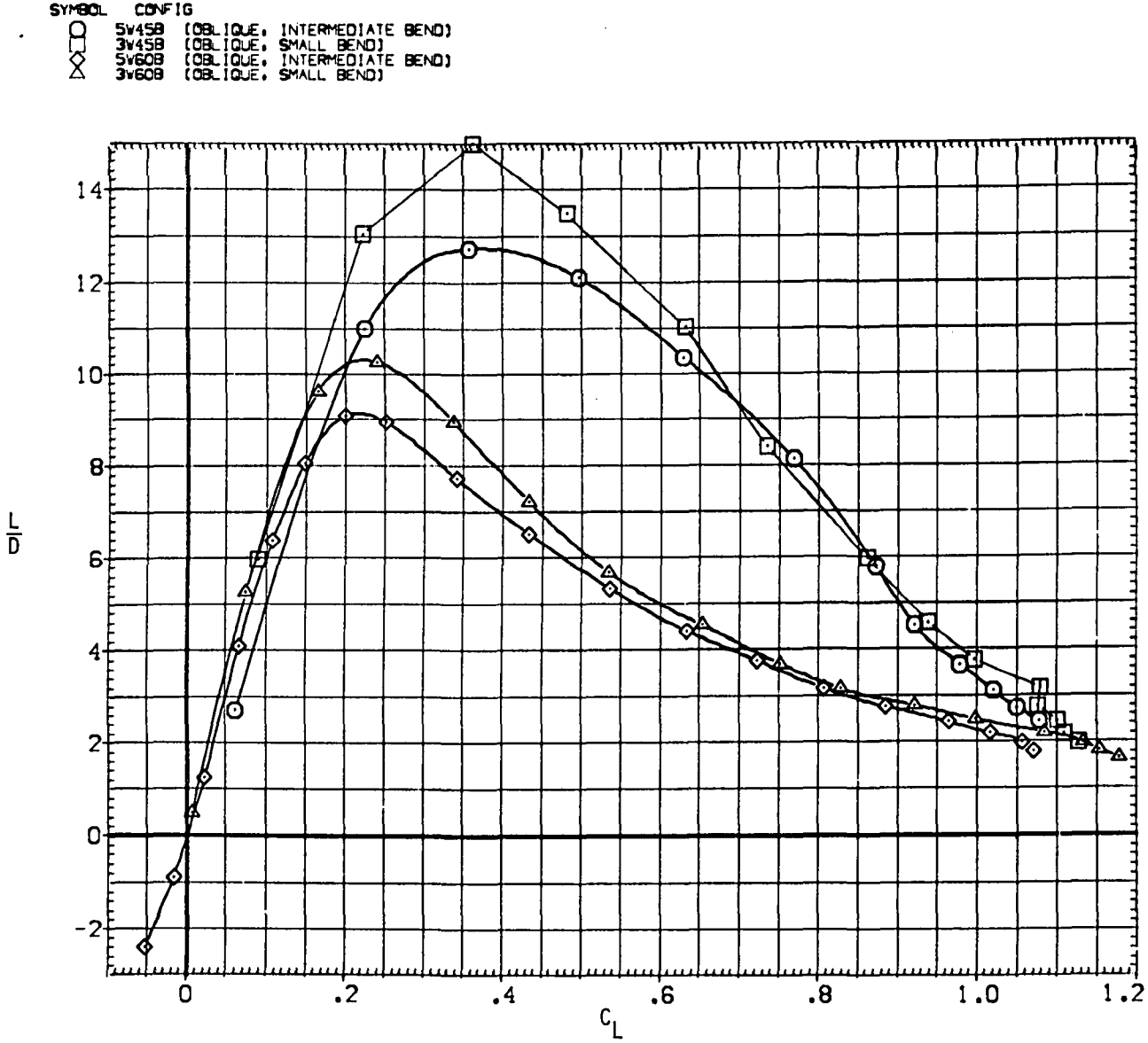

(d) L/D versus C_L.

Figure 19.– Continued.

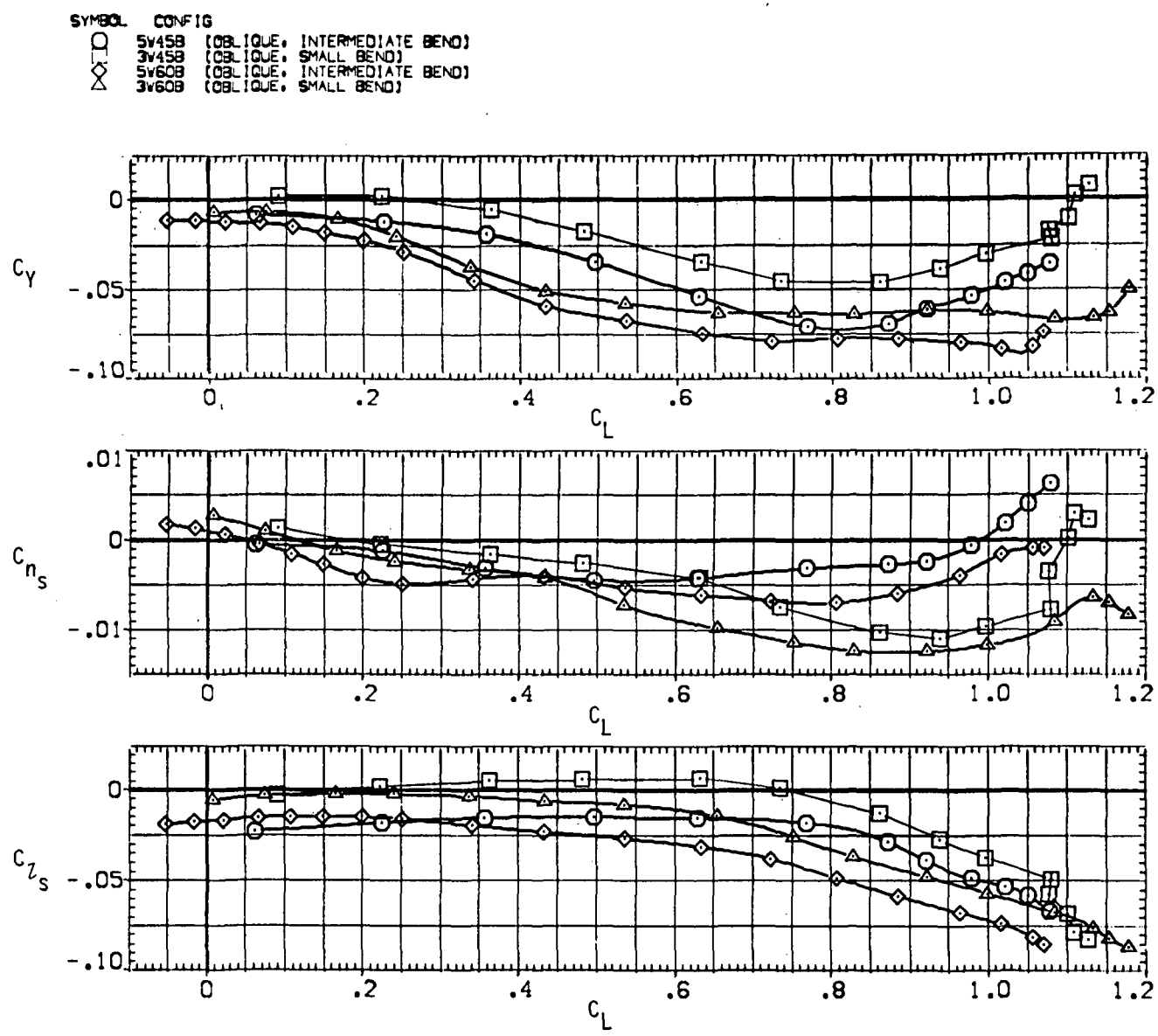

(e) C_Y, C_{n_s} and C_{l_s} versus C_L.

Figure 19.– Continued.

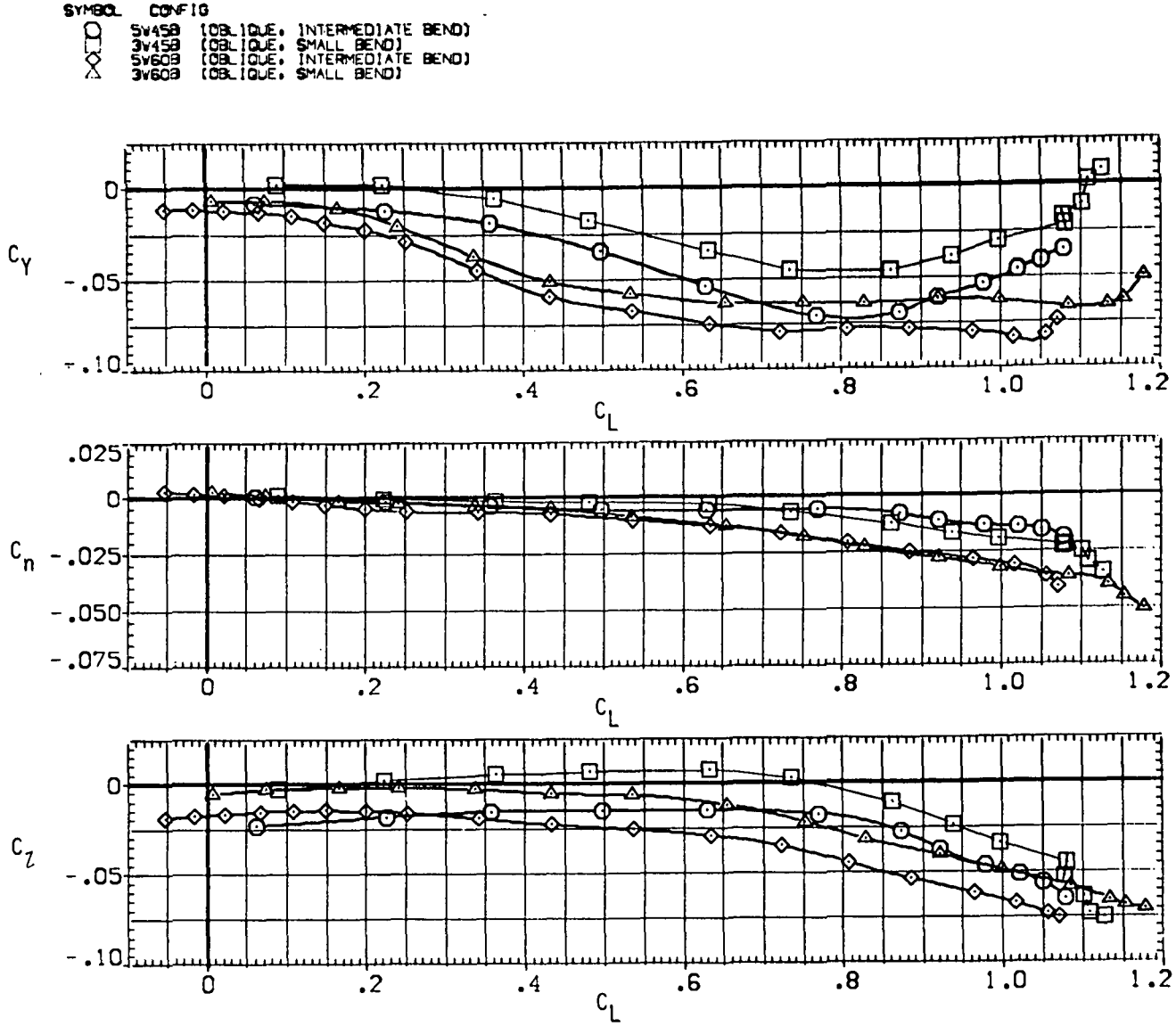

(f) C_Y, C_n and C_l versus C_L.

Figure 19.– Concluded.

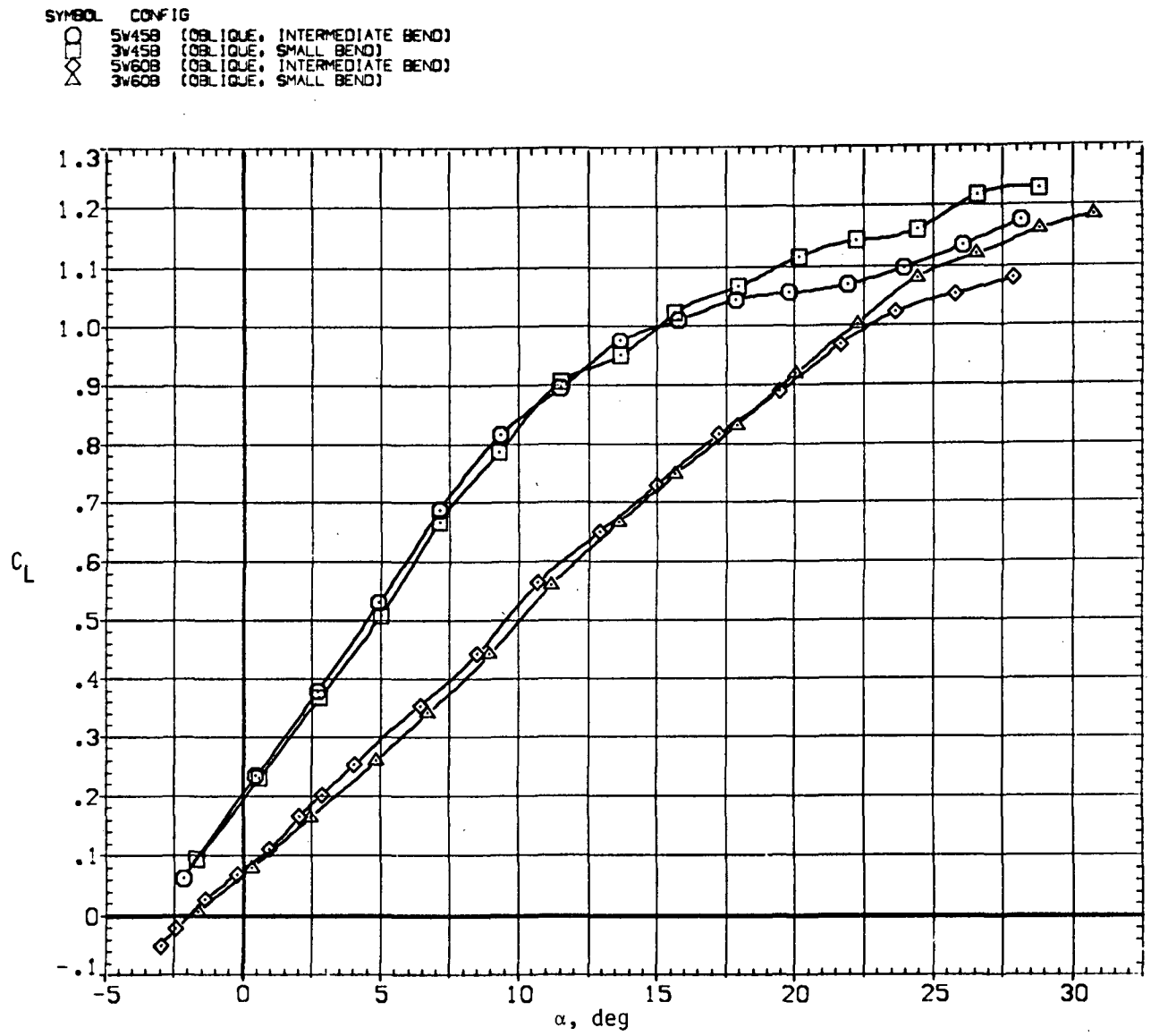

(a) C_L versus α.

Figure 20.– Effect of wing bend on the longitudinal stability characteristics of the oblique wing, $M = 0.9$.

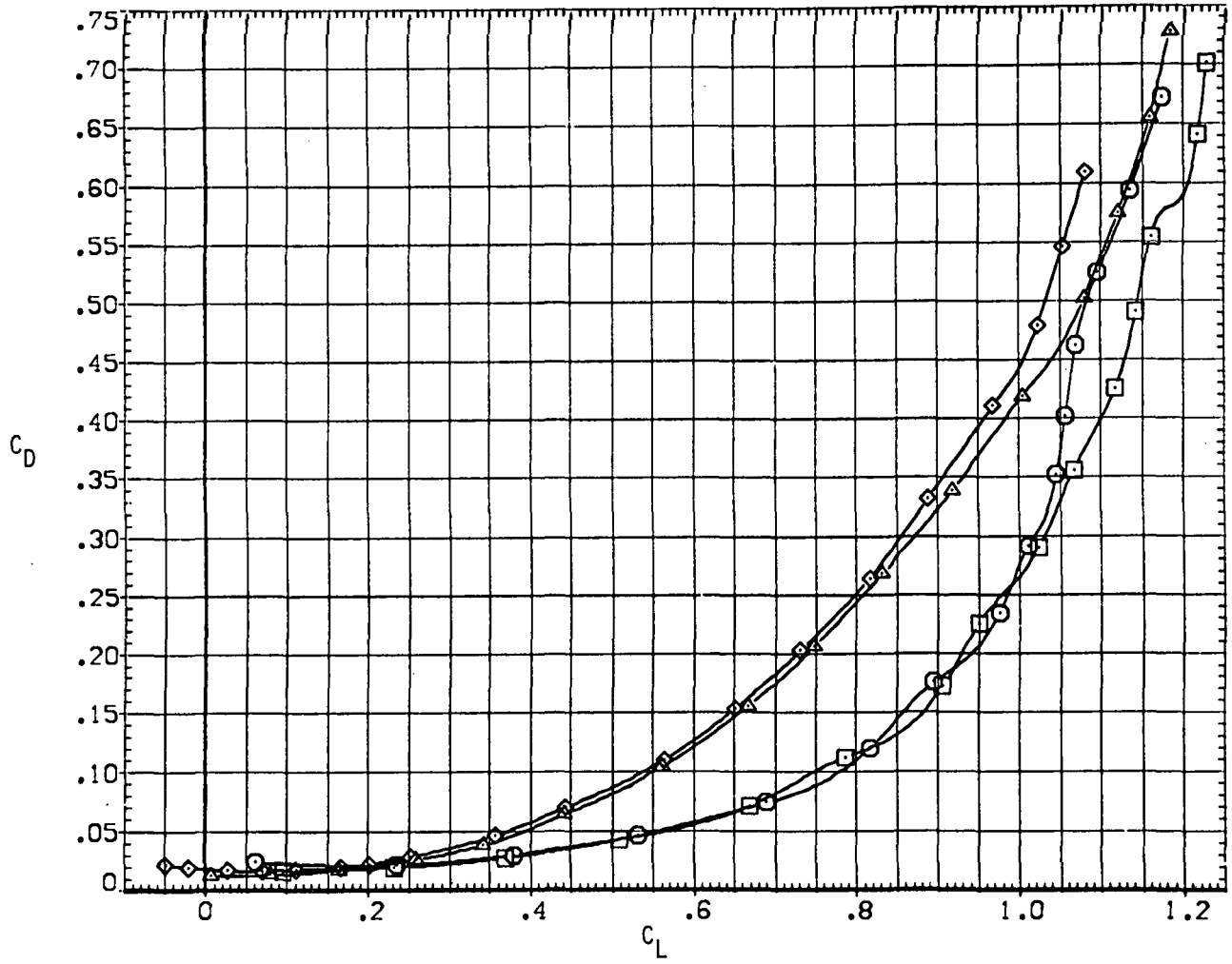

(b) C_D versus C_L.

Figure 20.– Continued.

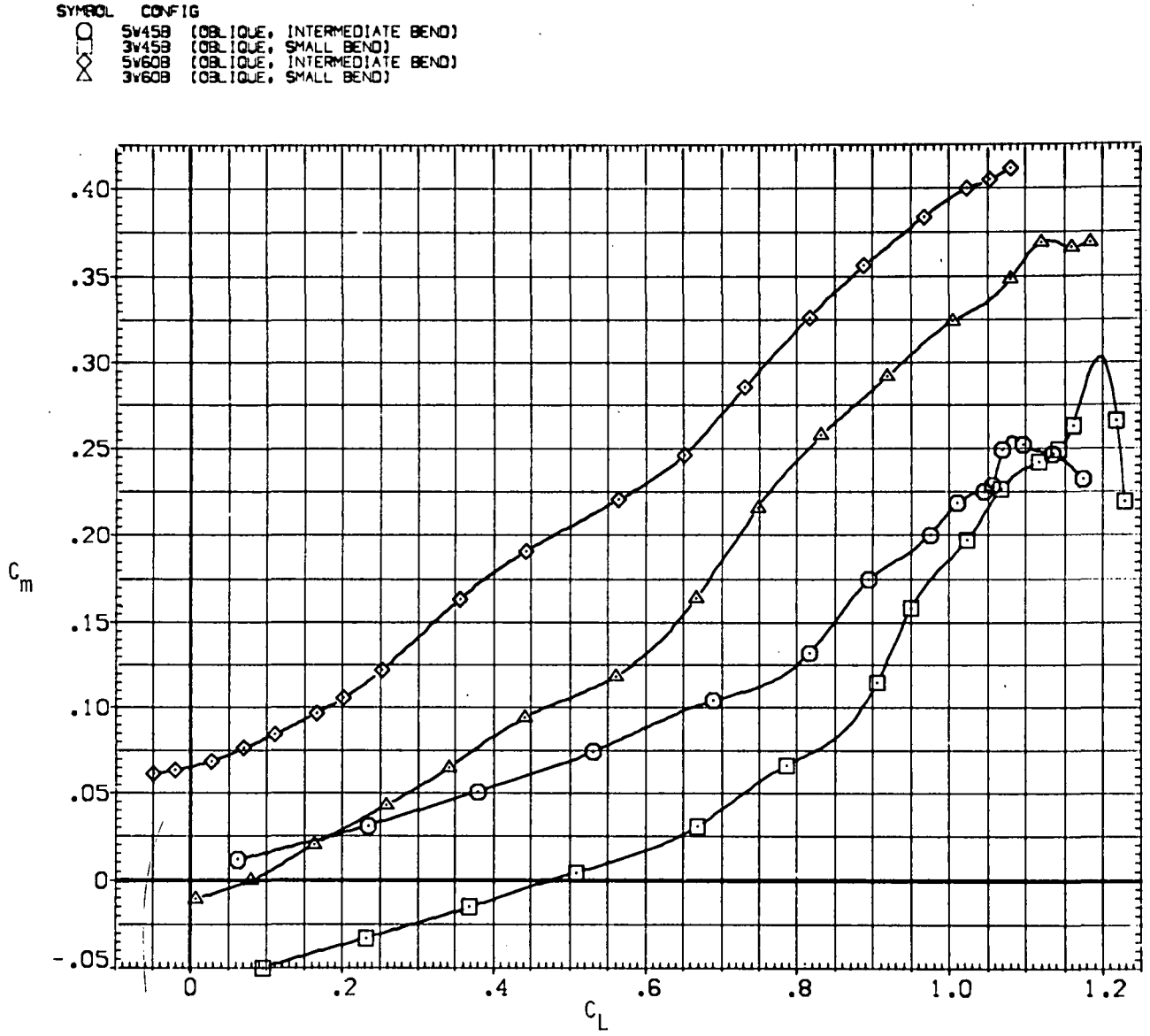

(c) C_m versus C_L.

Figure 20.– Continued.

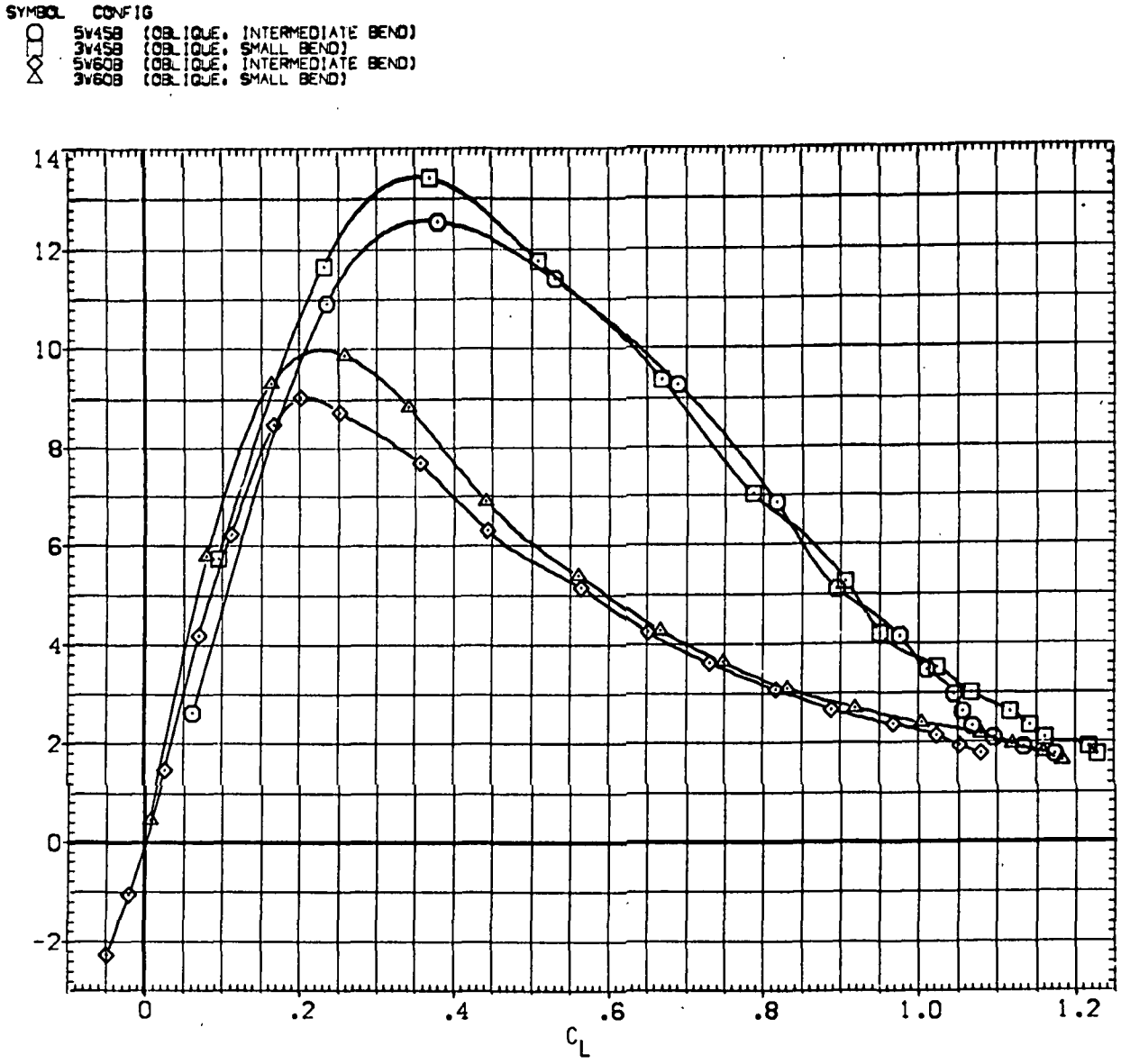

(d) L/D versus C_L.

Figure 20.– Continued.

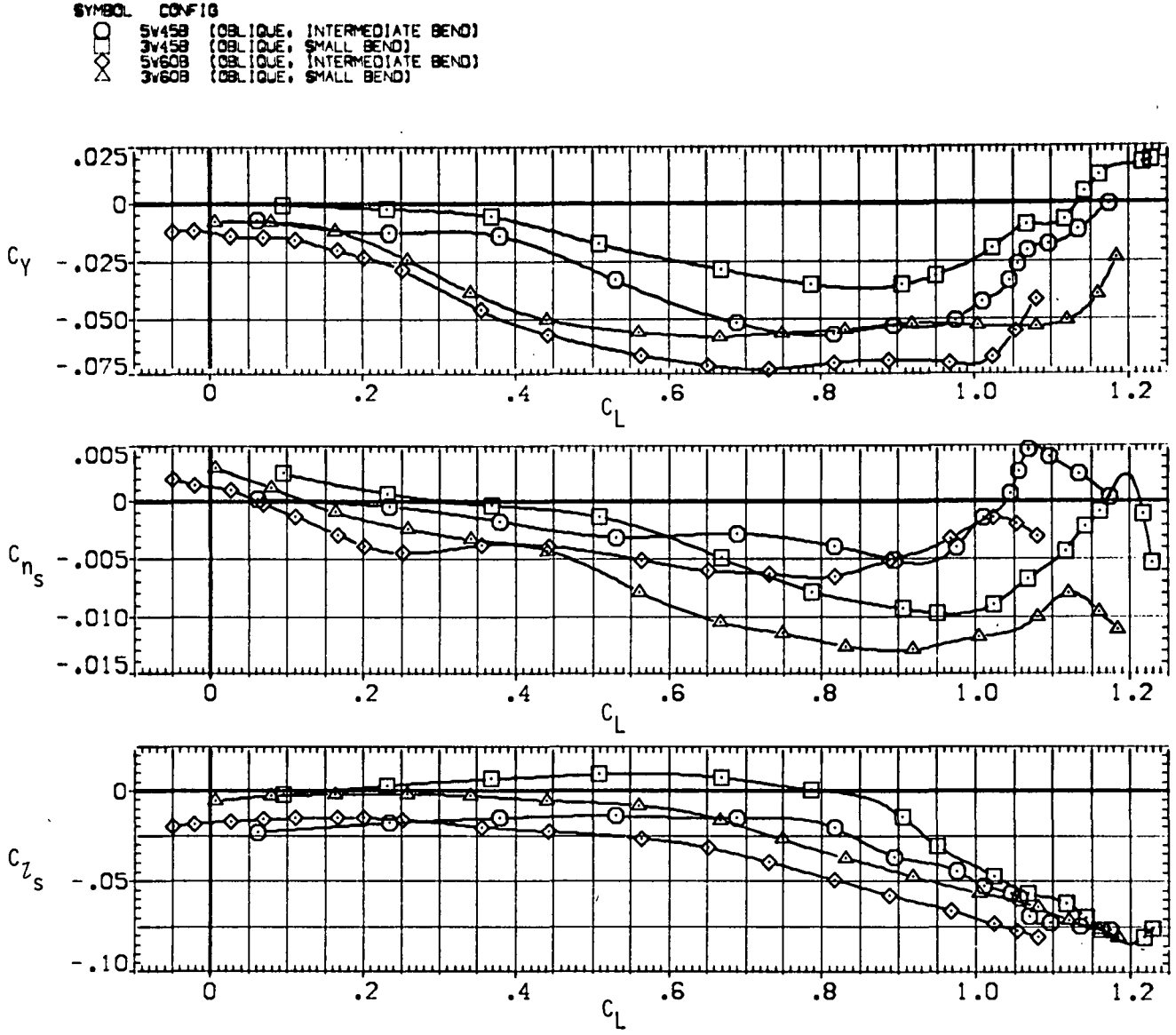

(e) C_Y, C_{n_s} and C_{l_s} versus C_L.

Figure 20.– Continued.

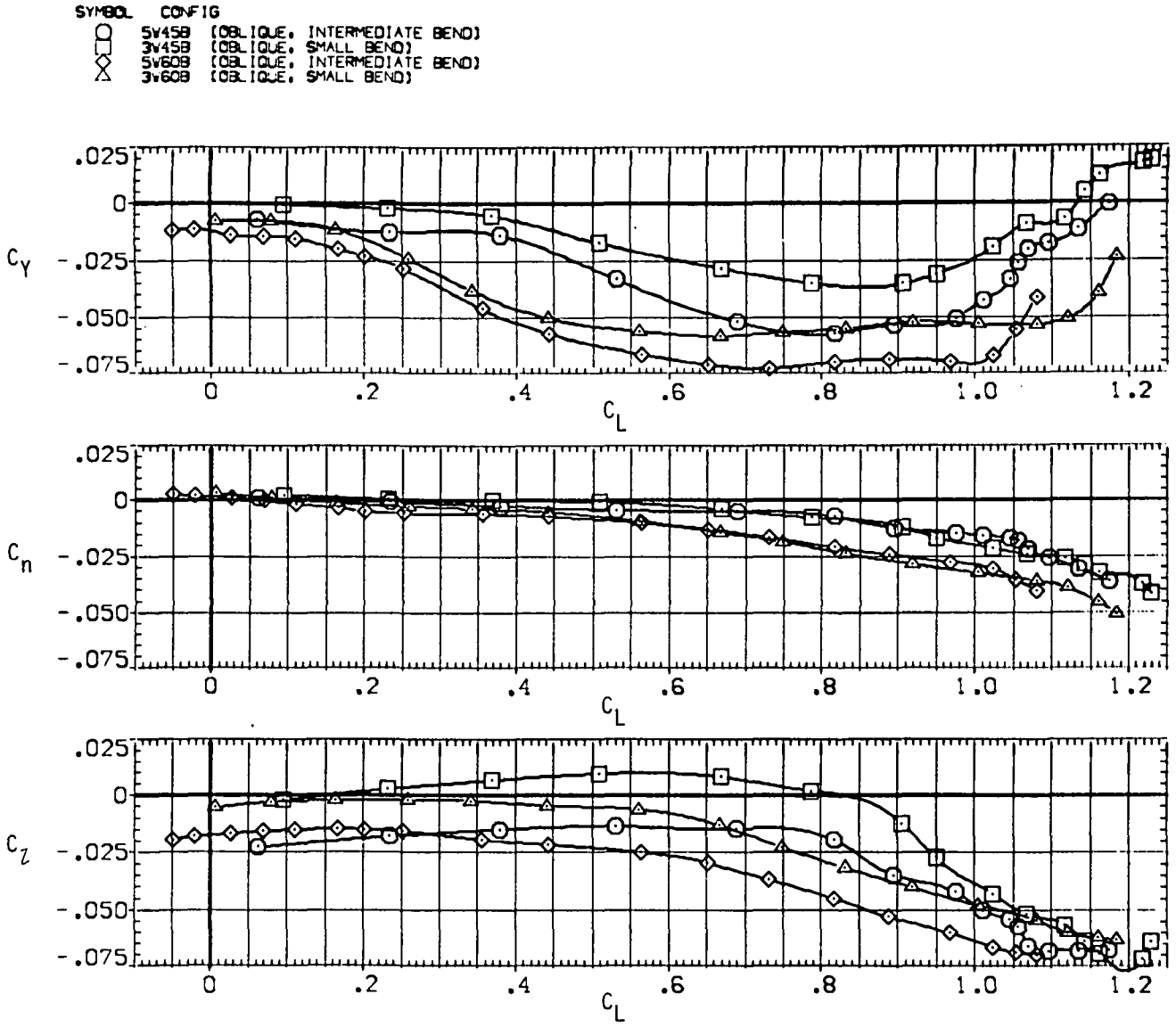

(f) C_Y, C_n and C_l versus C_L.

Figure 20.– Concluded.

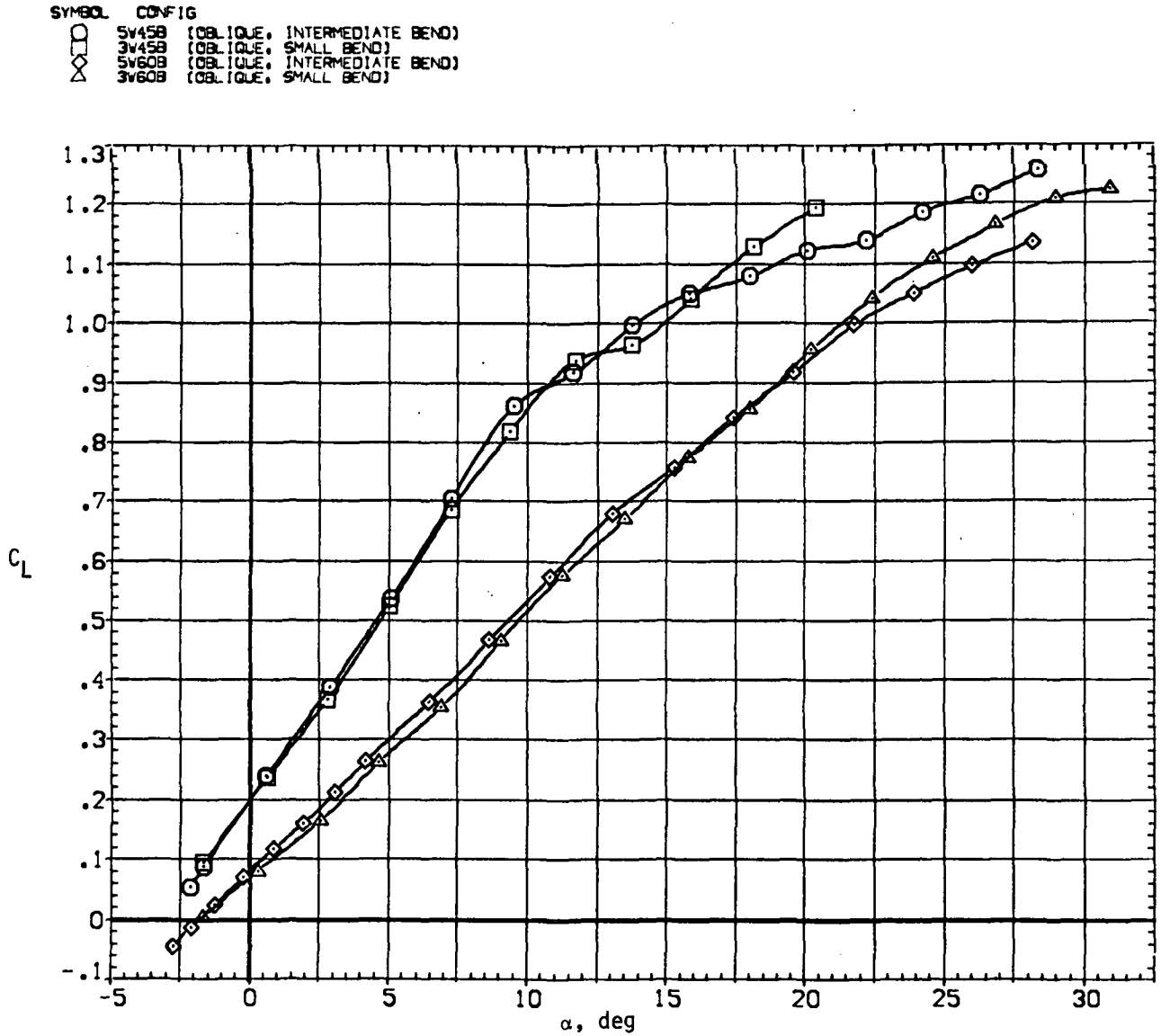

(a) C_L versus α.

Figure 21.– Effect of wing bend on the longitudinal stability characteristics of the oblique wing, $M = 0.95$.

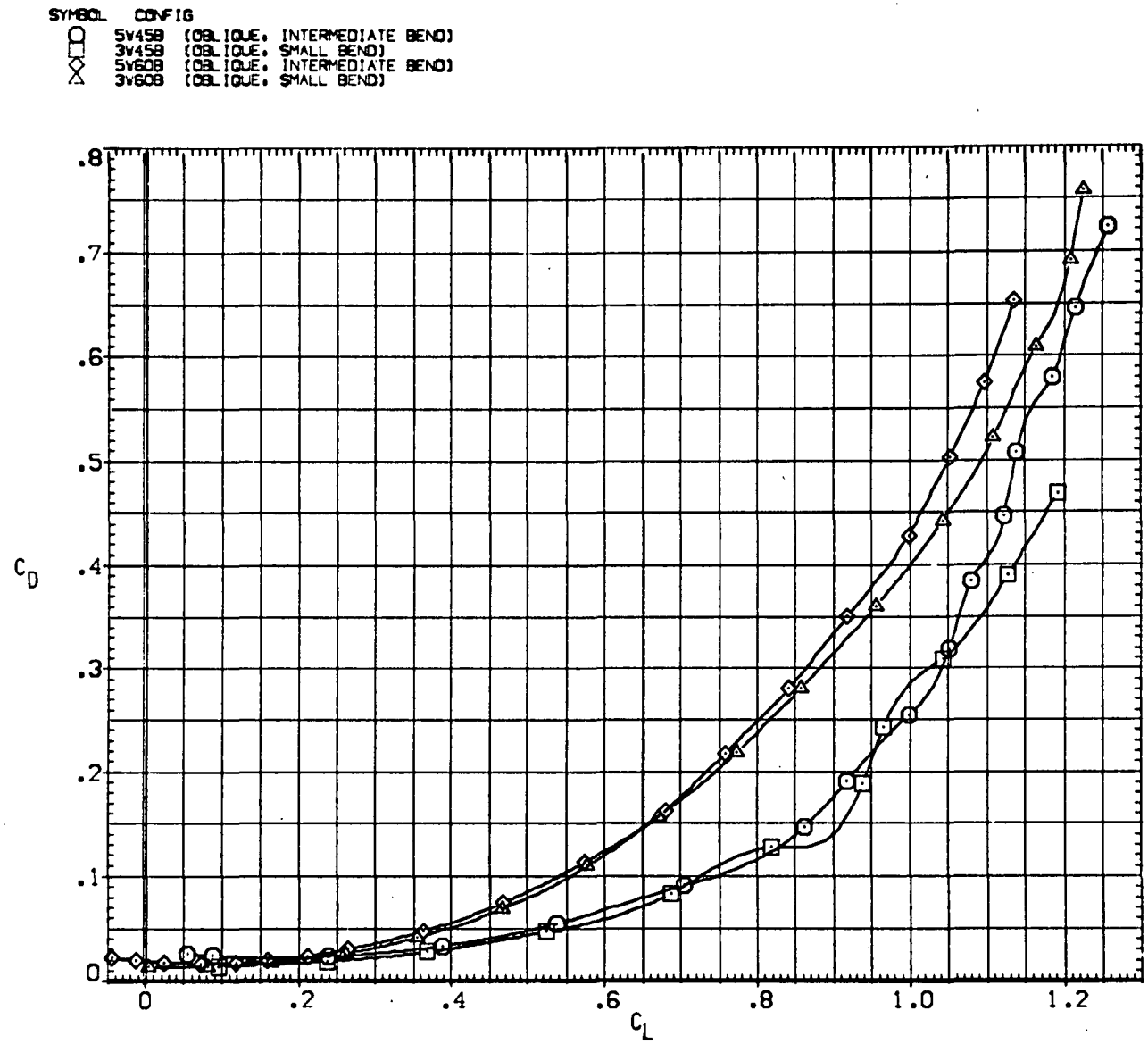

(b) C_D versus C_L.

Figure 21.– Continued.

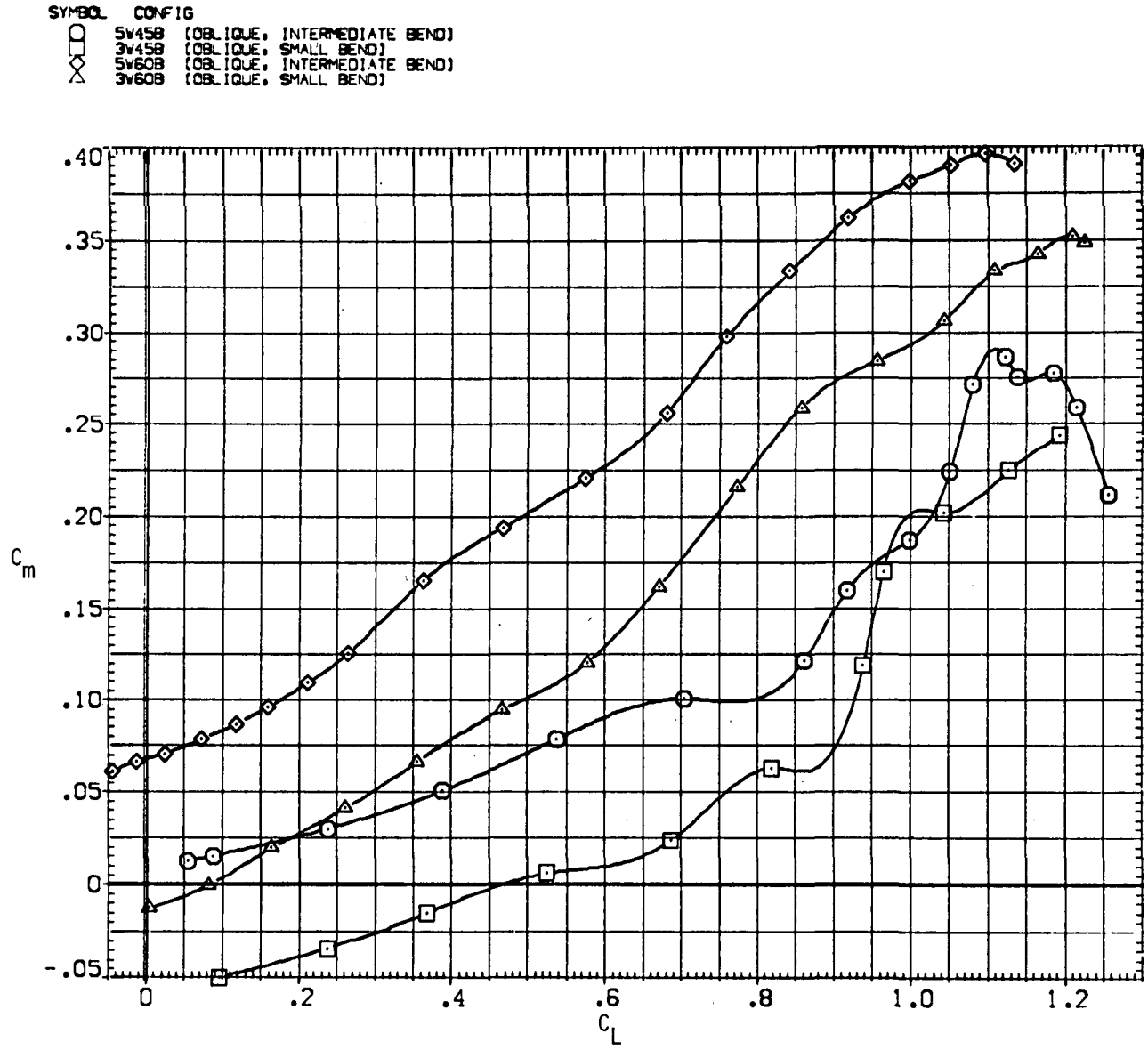

(c) C_m versus C_L.

Figure 21.– Continued.

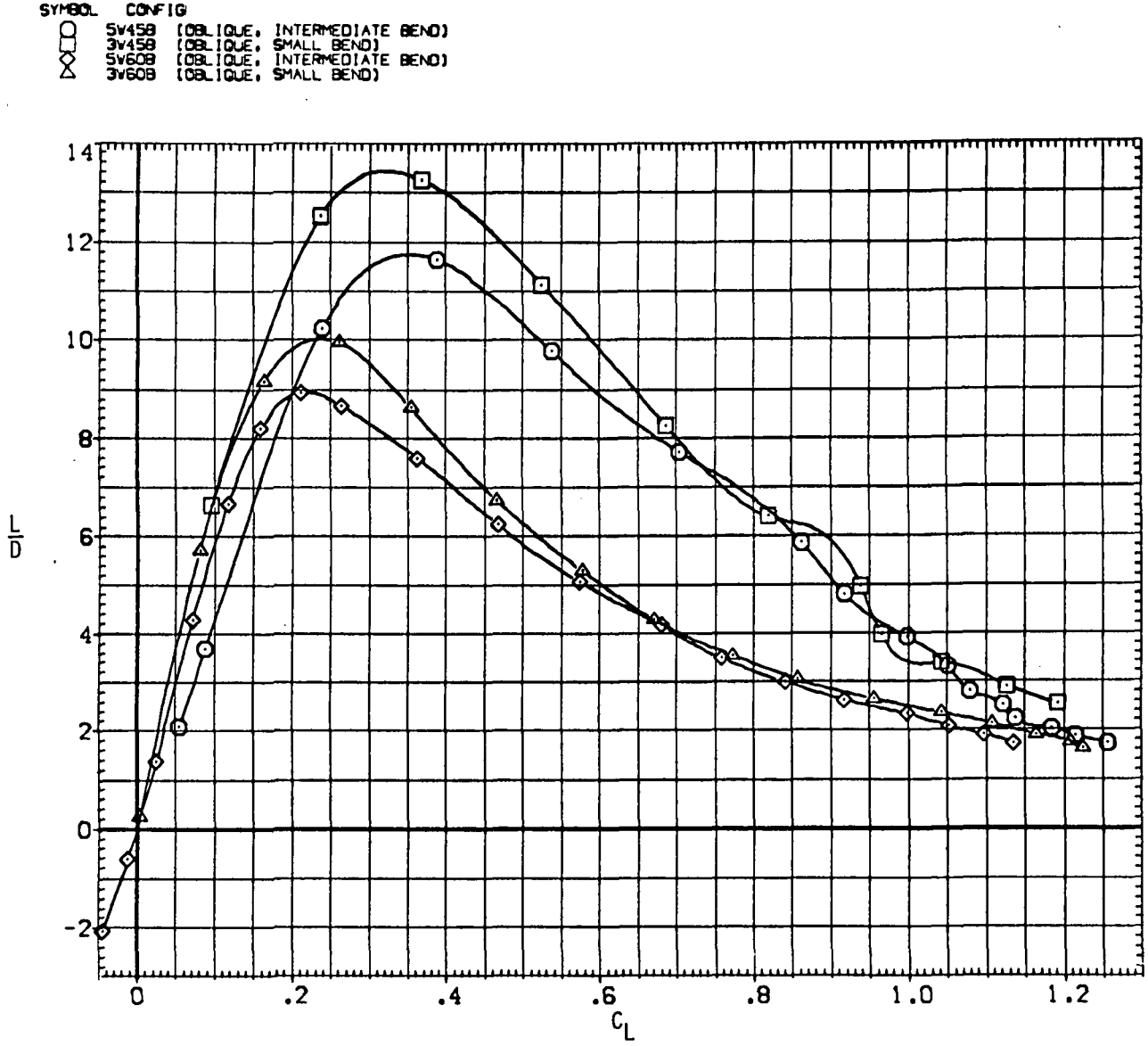

(d) L/D versus C_L.

Figure 21.– Continued.

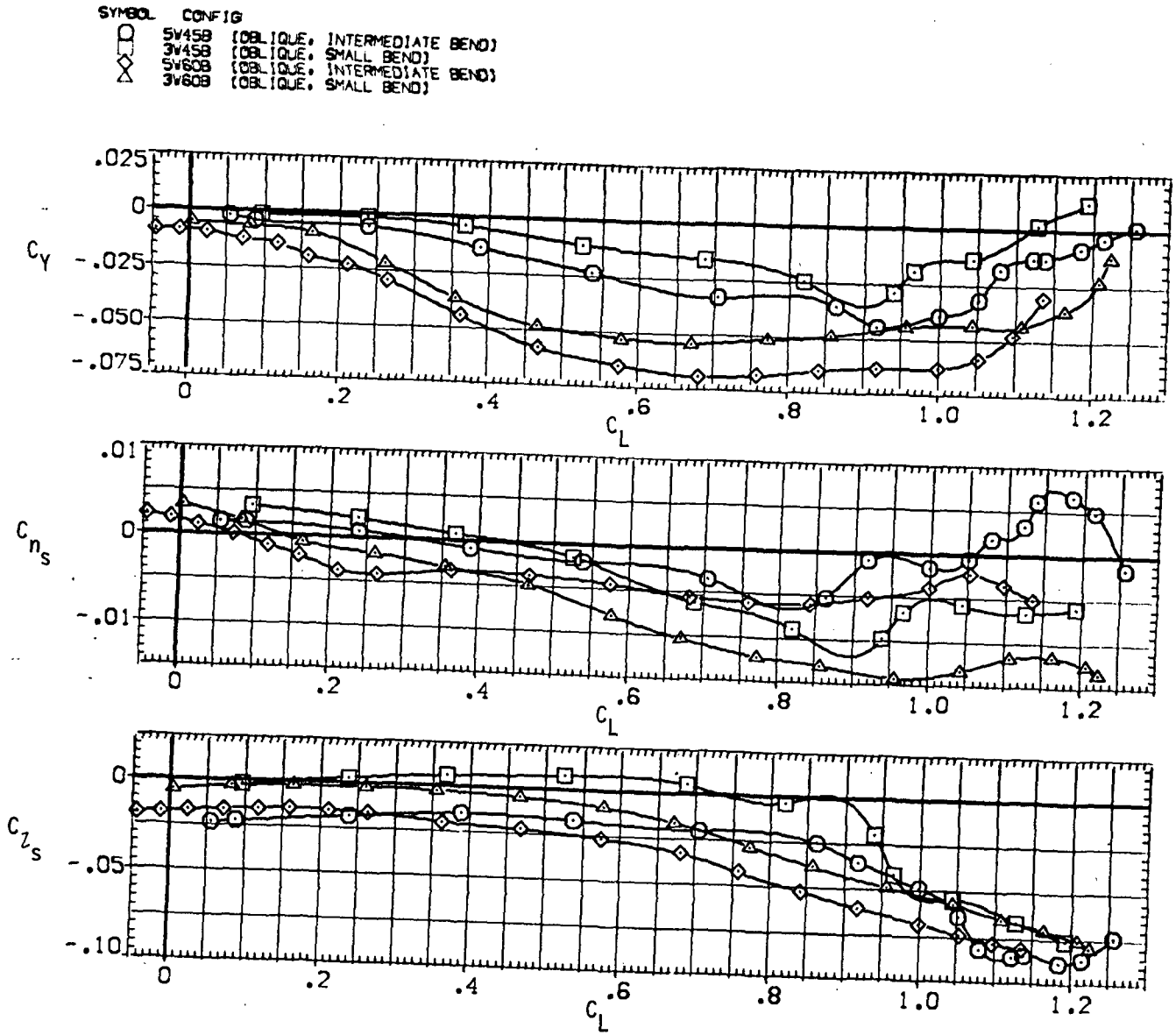

(e) C_Y, C_{n_s} and C_{l_s} versus C_L.

Figure 21.– Continued.

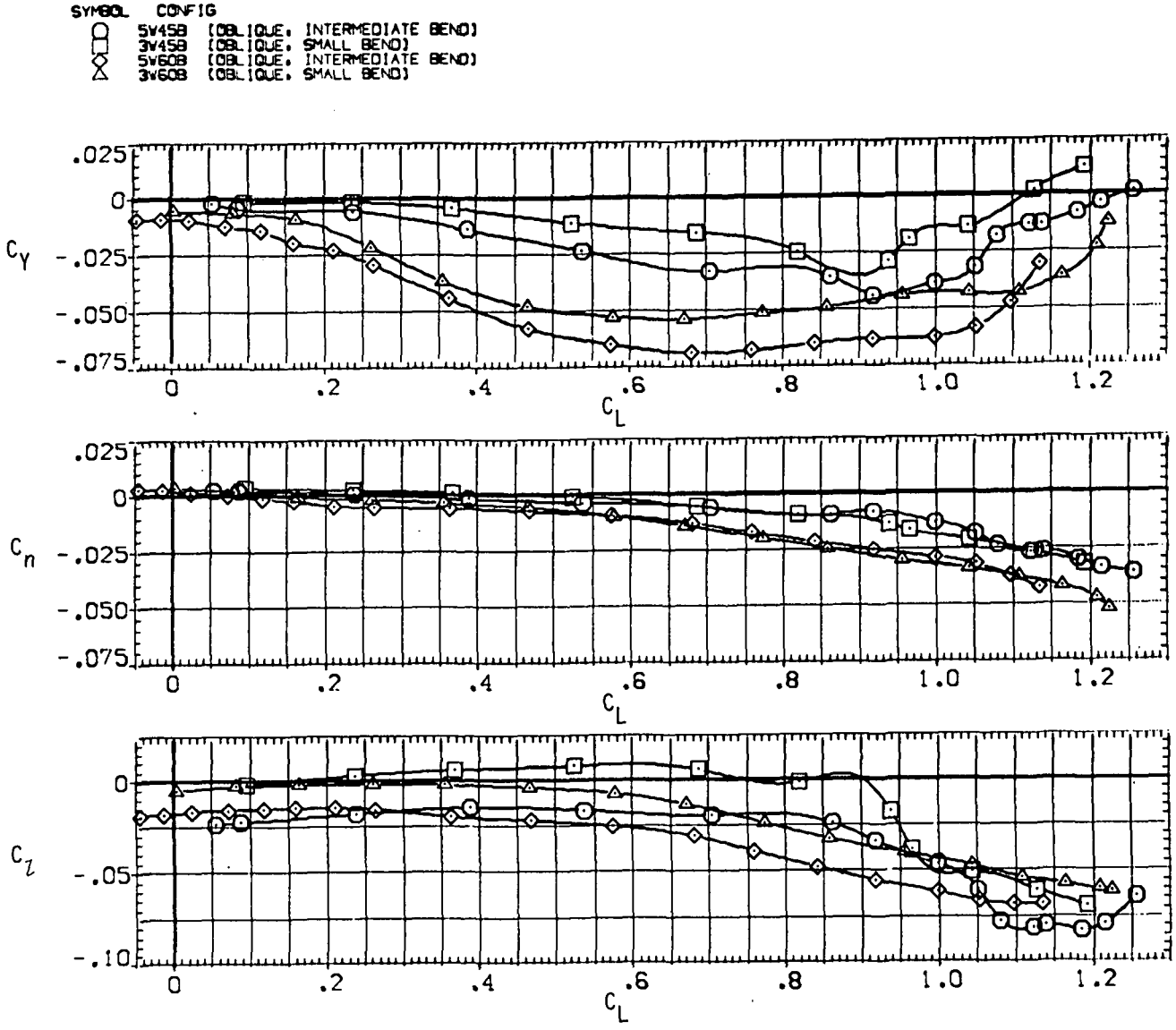

(f) C_Y, C_n and C_l versus C_L.

Figure 21.– Concluded.

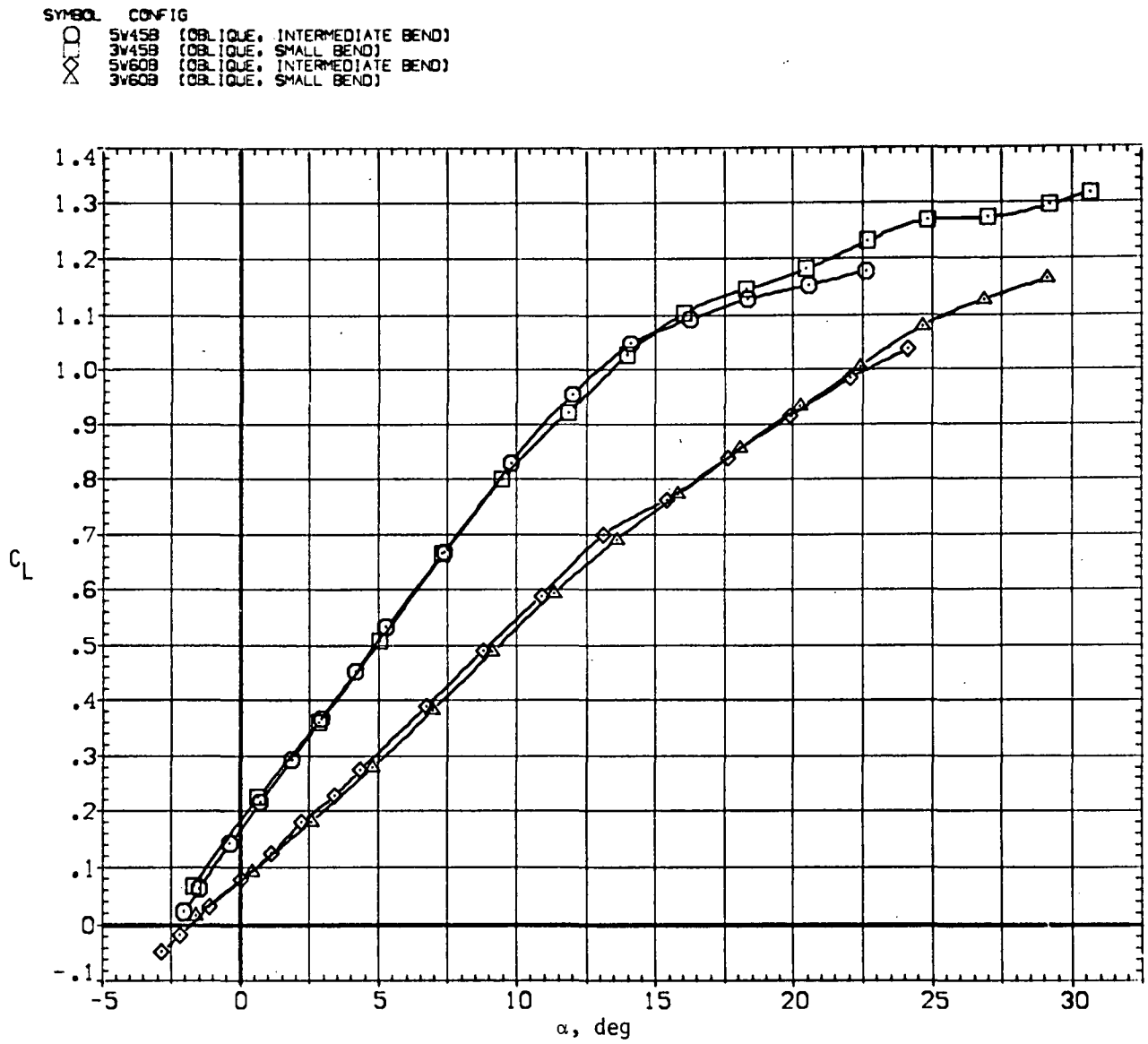

(a) C_L versus α.

Figure 22.– Effect of wing bend on the longitudinal stability characteristics of the oblique wing, $M = 1.1$.

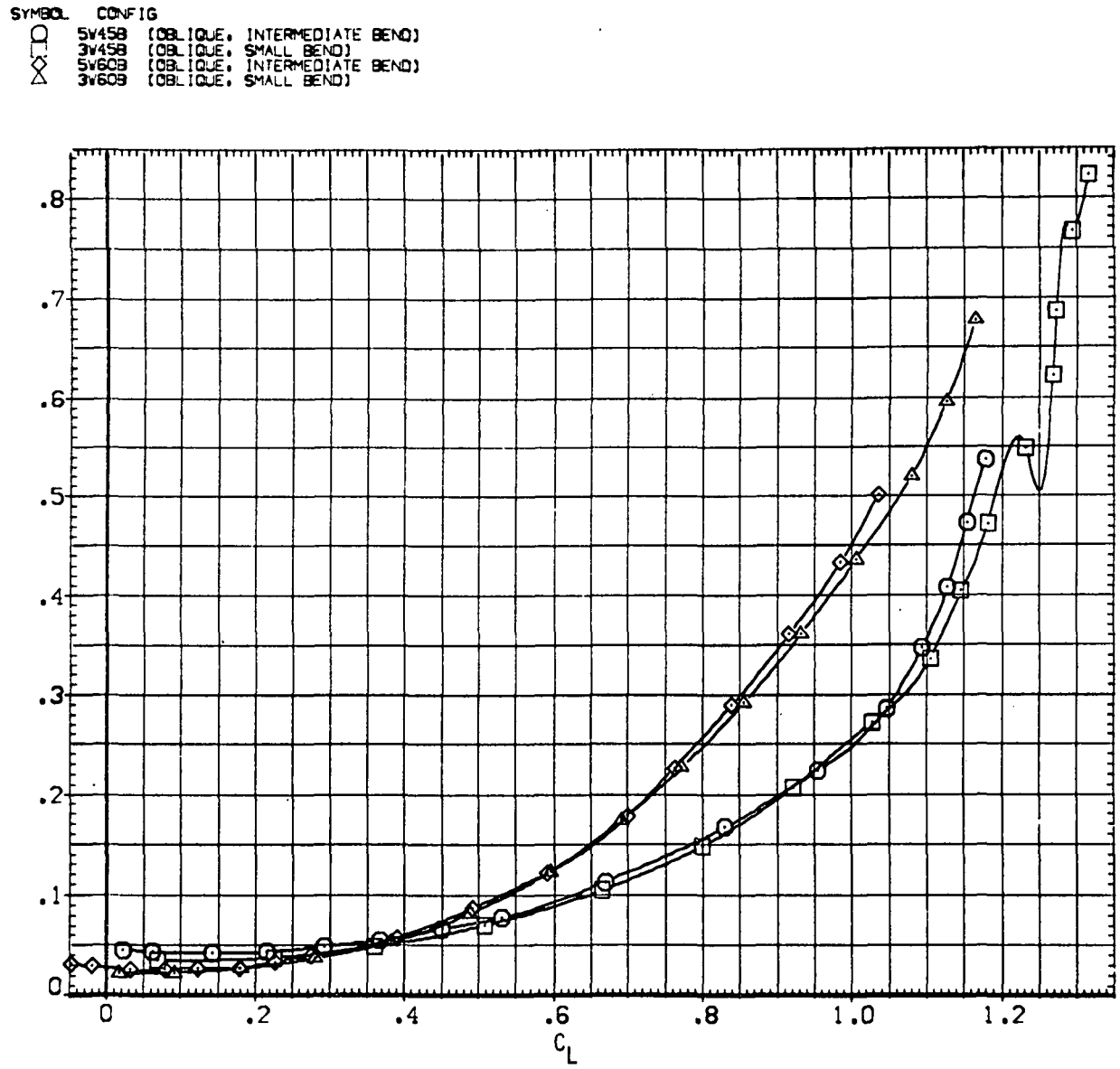

(b) C_D versus C_L.

Figure 22.– Continued.

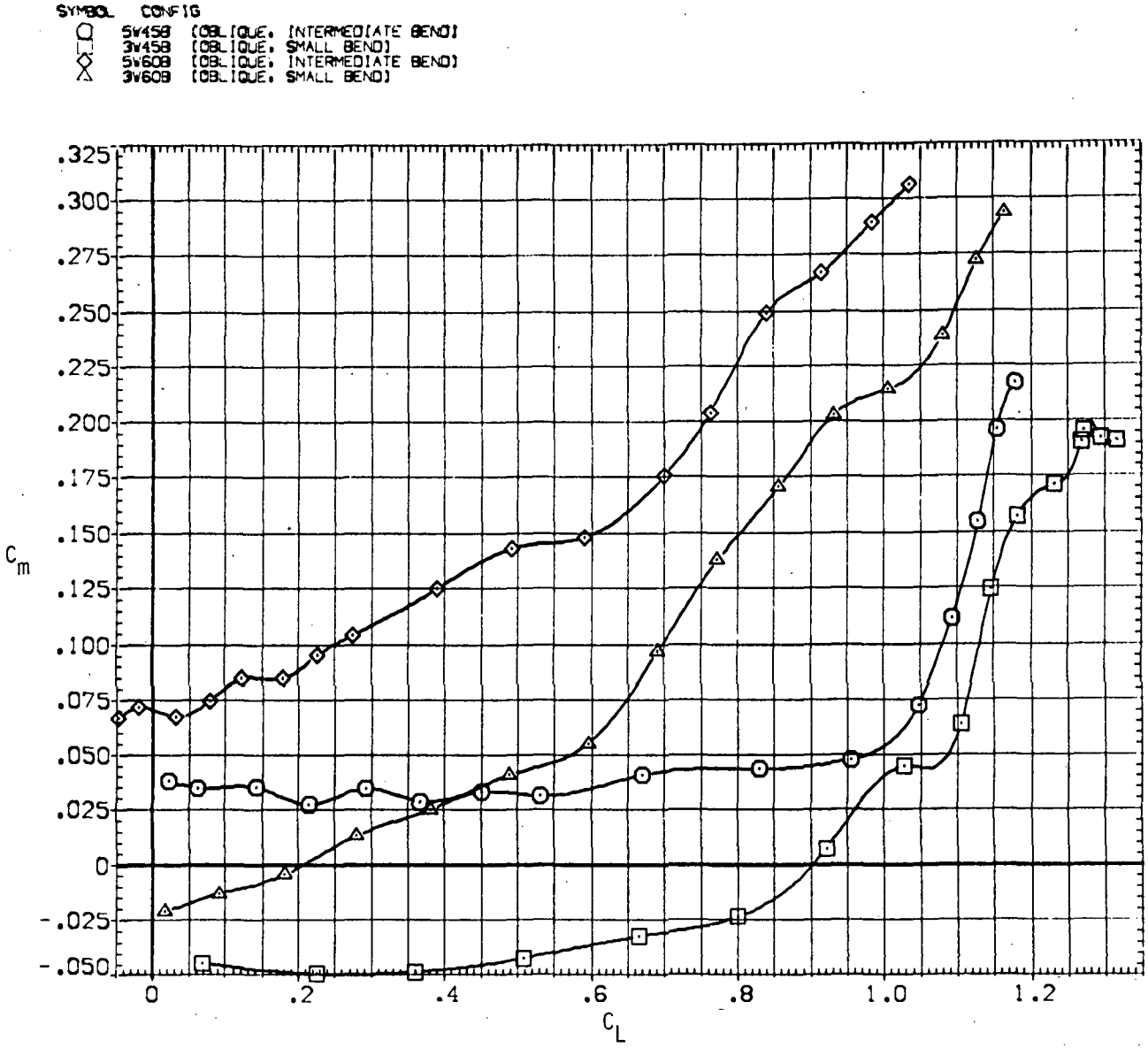

(c) C_m versus C_L.

Figure 22.– Continued.

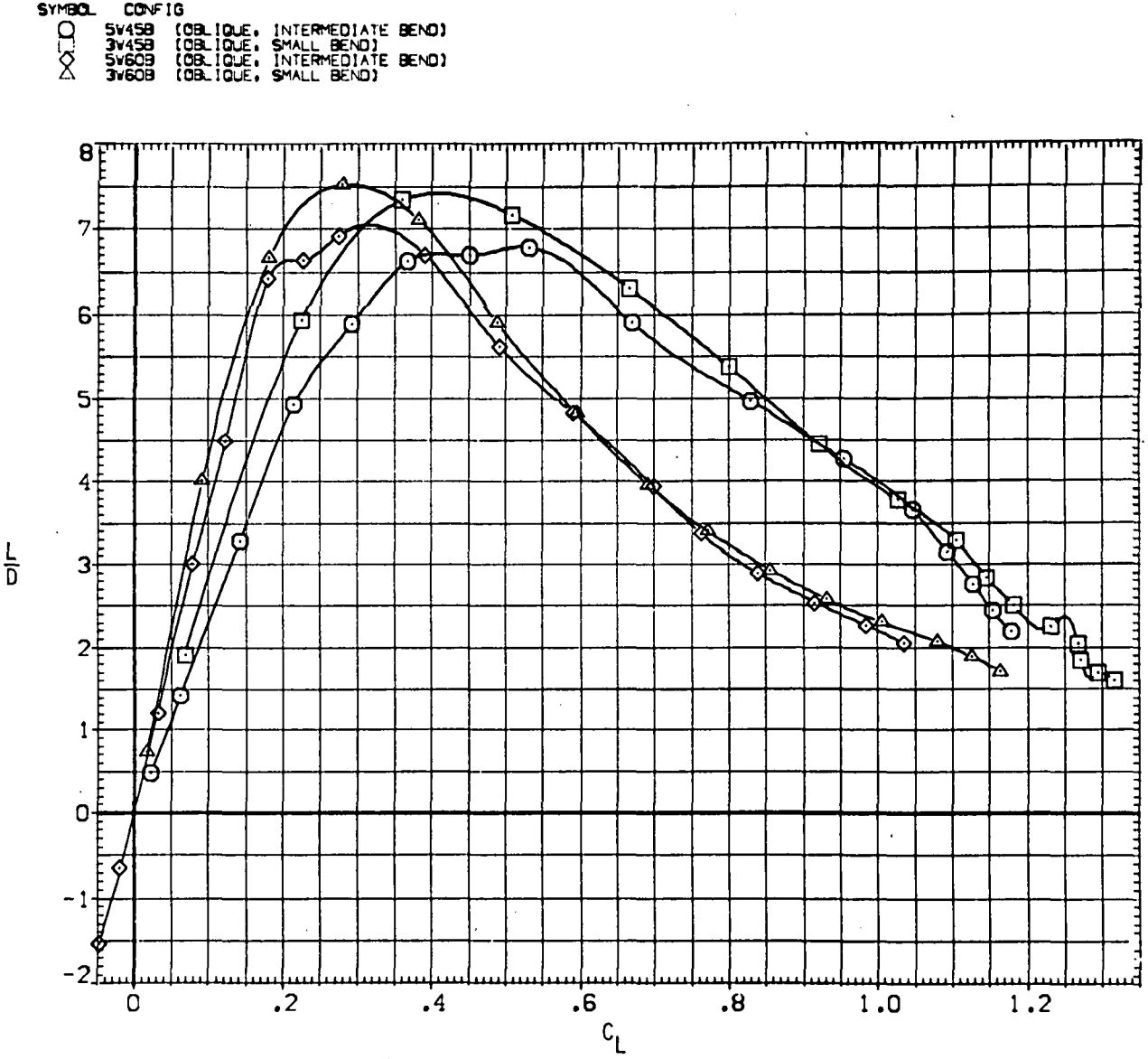

(d) L/D versus C_L.

Figure 22.– Continued.

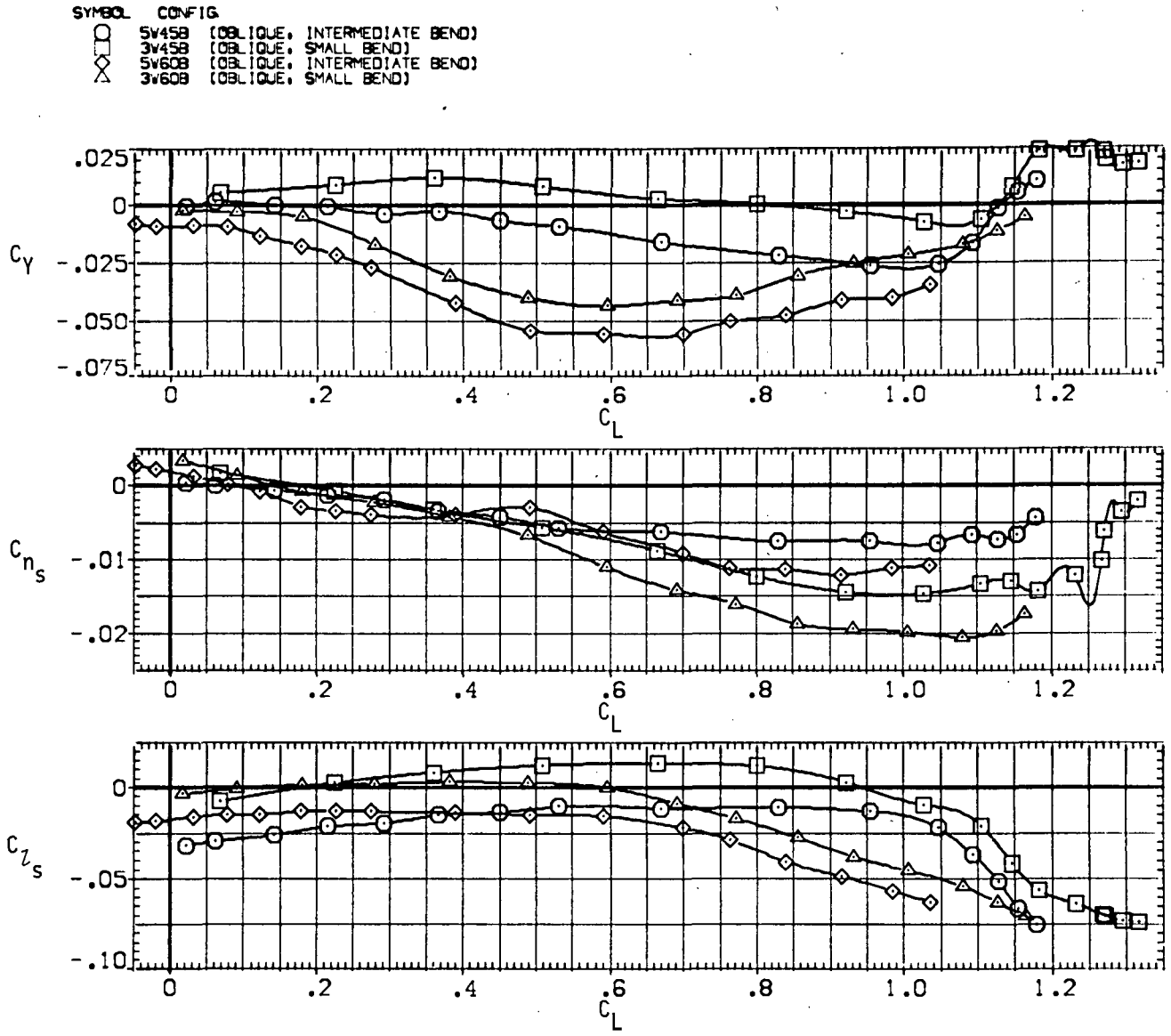

(e) C_Y, C_{n_s} and C_{l_s} versus C_L.

Figure 22.– Continued.

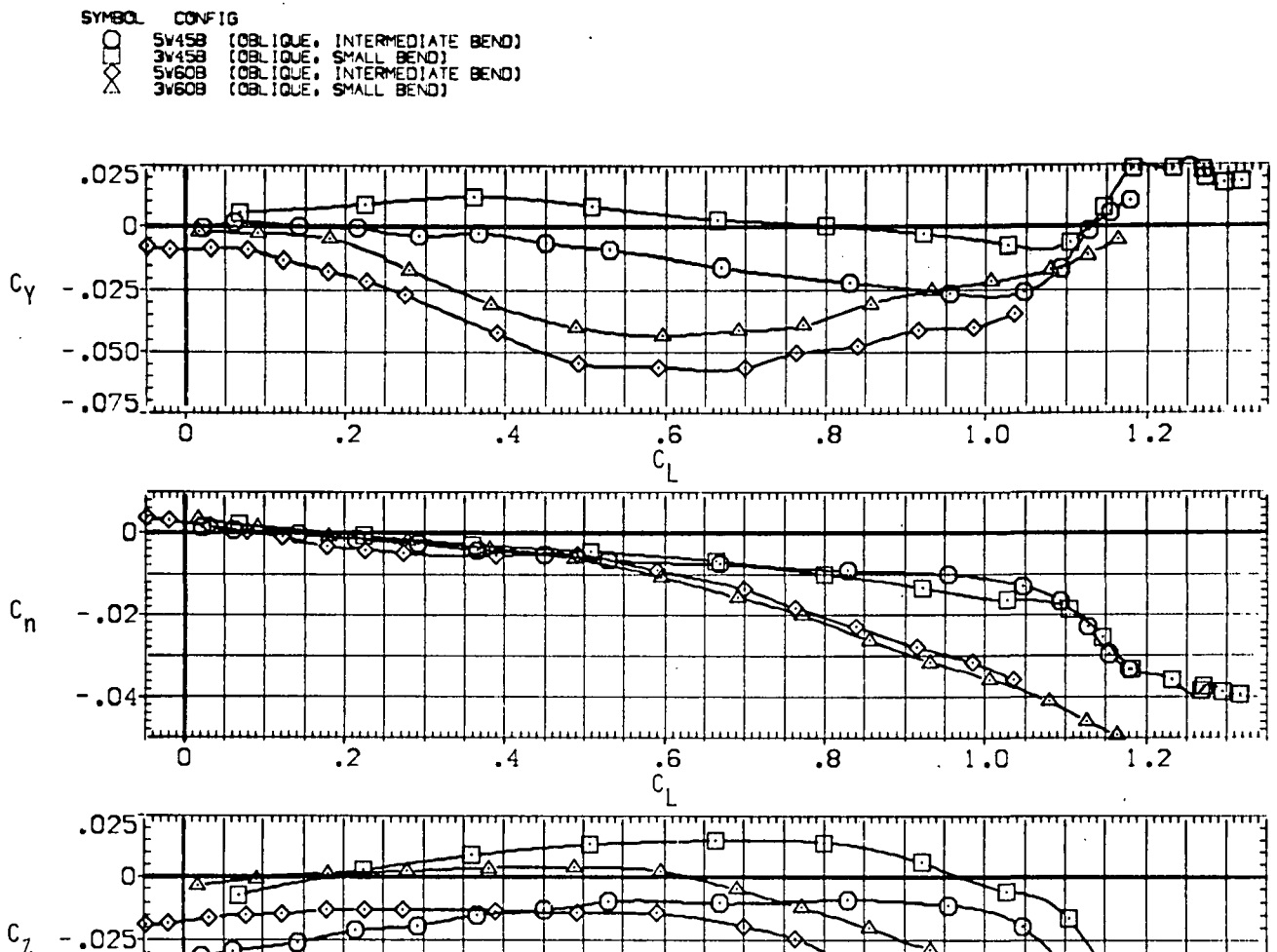

(f) C_Y, C_n and C_l versus C_L.

Figure 22.– Concluded.

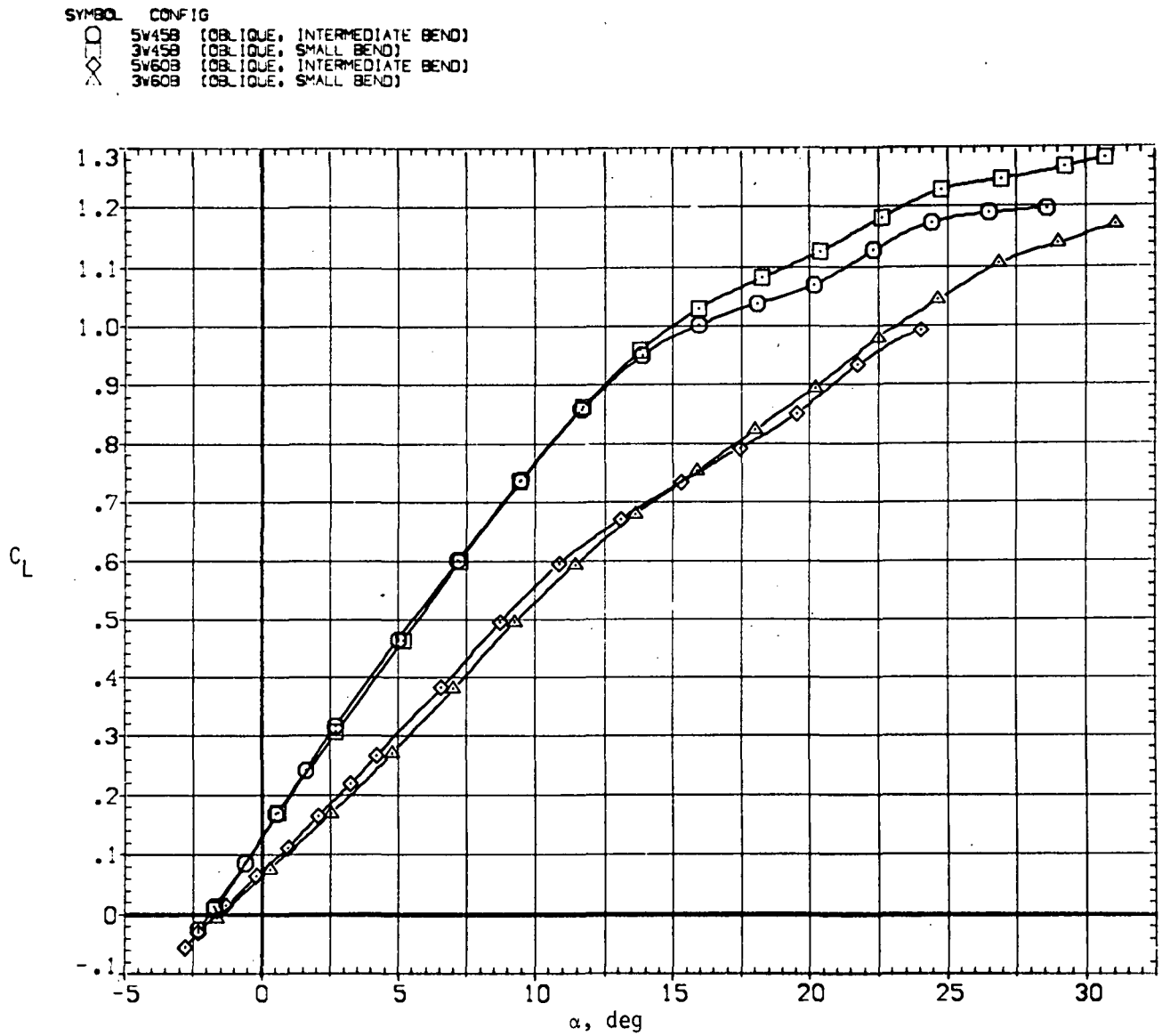

(a) C_L versus α.

Figure 23.– Effect of wing bend on the longitudinal stability characteristics of the oblique wing, $M = 1.2$.

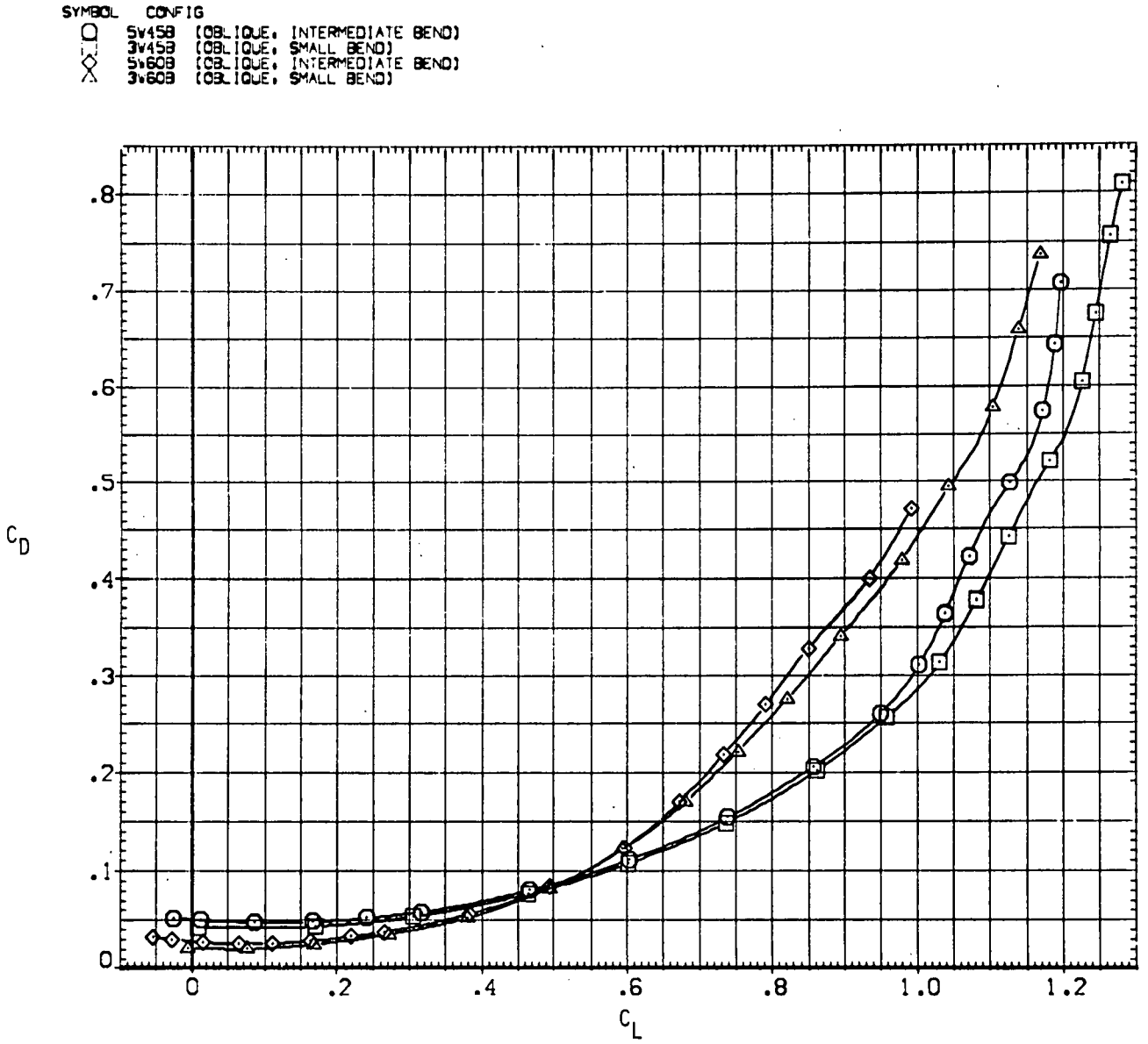

(b) C_D versus C_L.

Figure 23.– Continued.

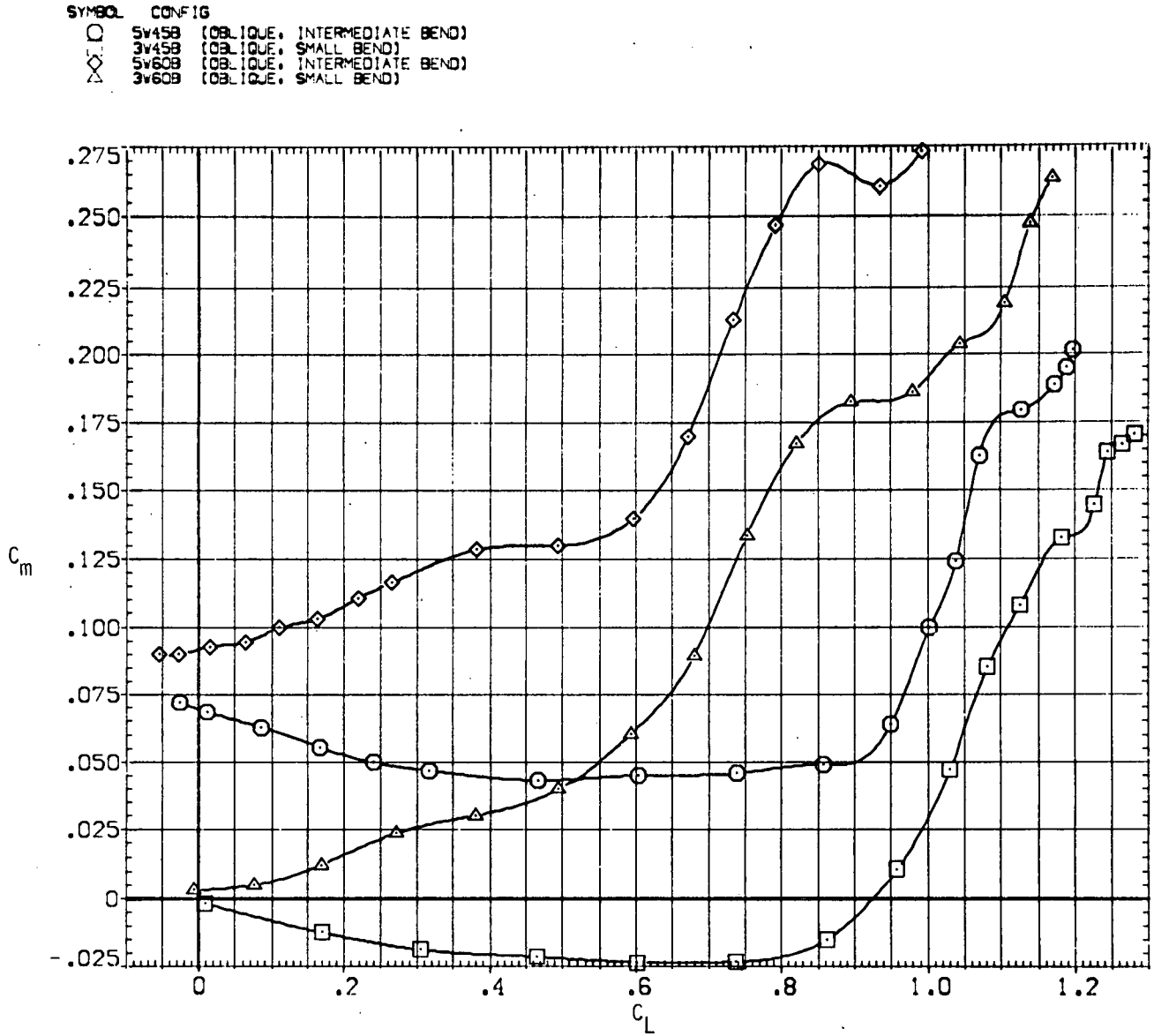

(c) C_m versus C_L.

Figure 23.– Continued.

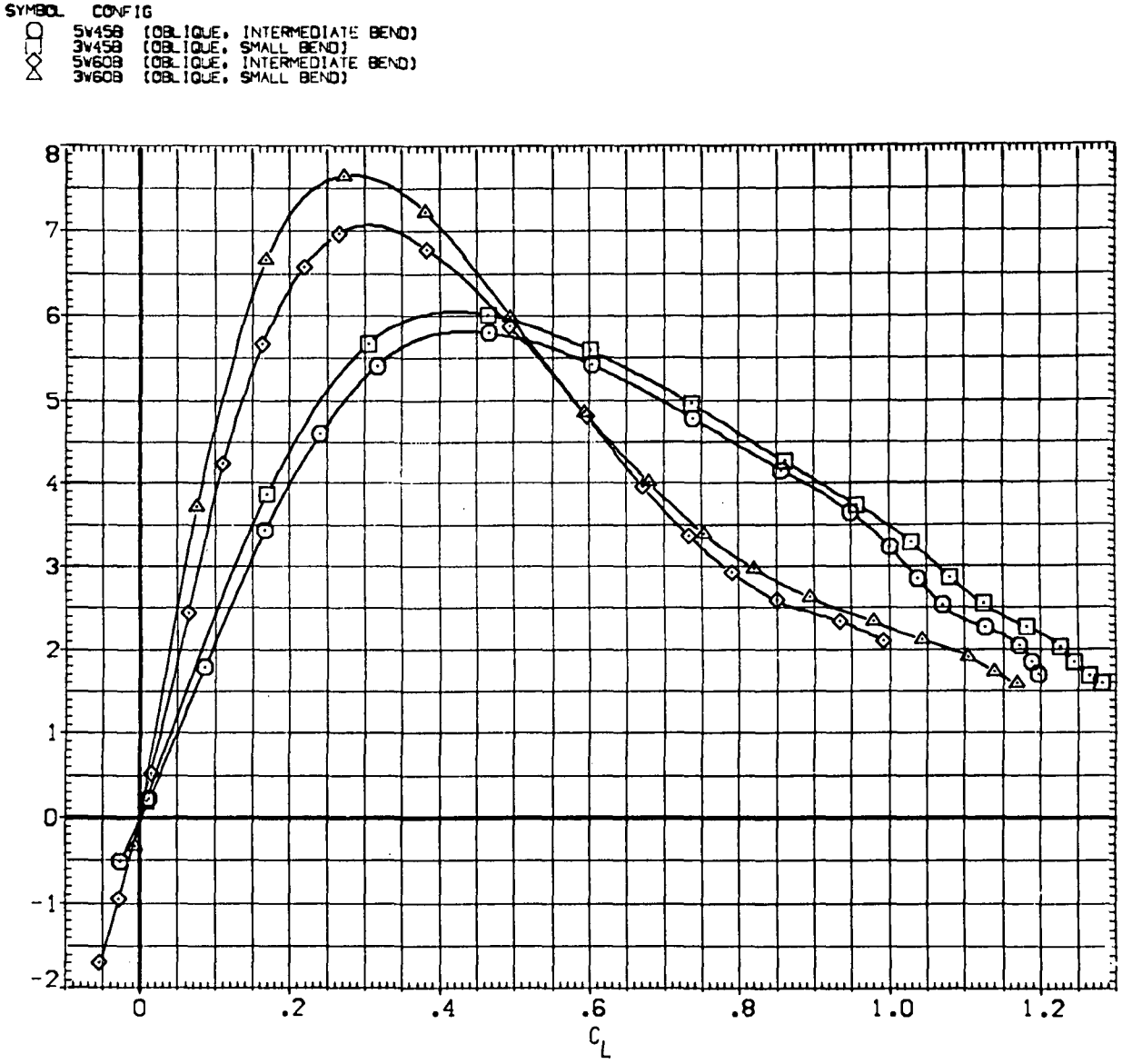

(d) L/D versus C_L.

Figure 23.– Continued.

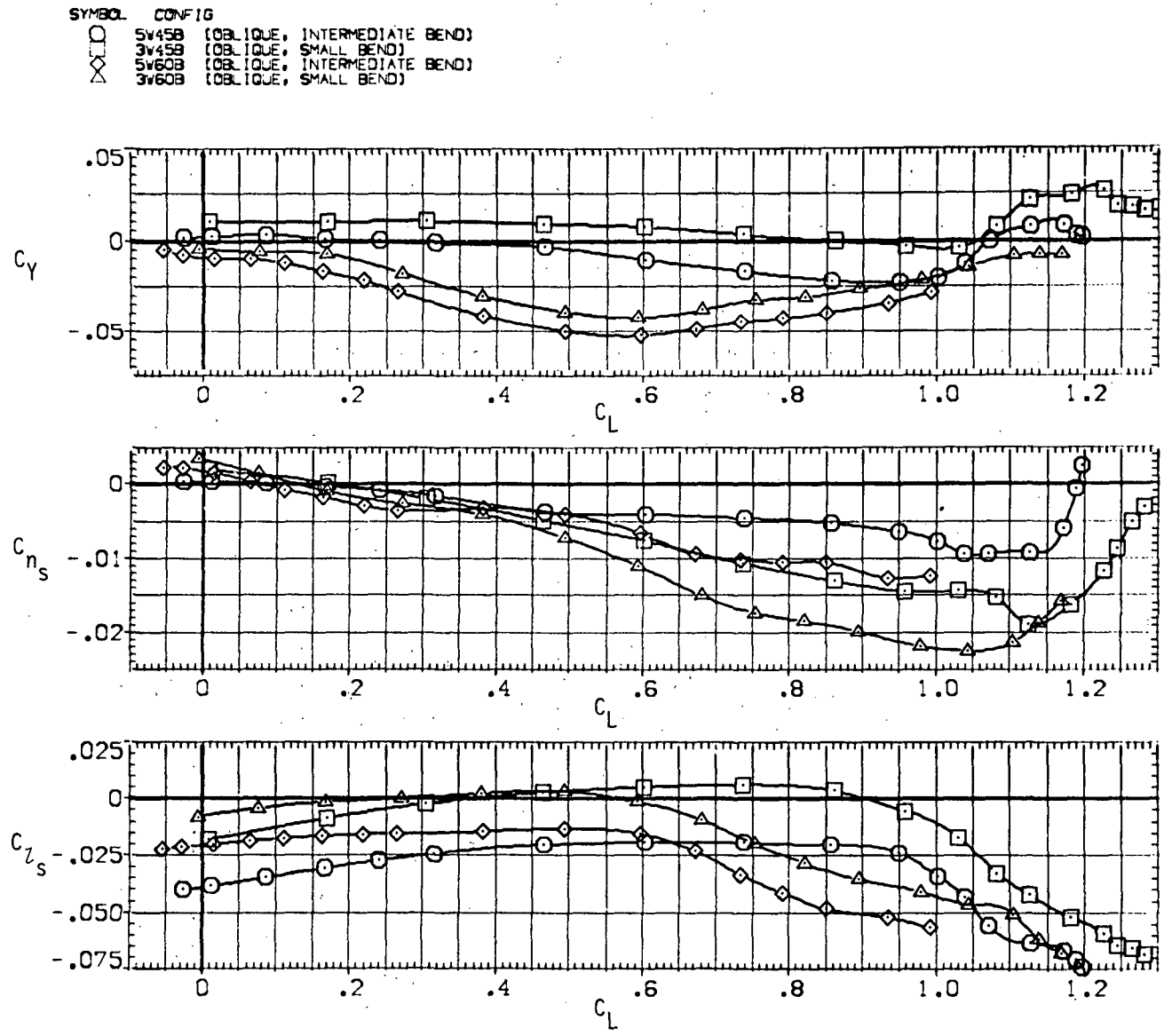

(e) C_Y, C_{n_s} and C_{l_s} versus C_L.

Figure 23.– Continued

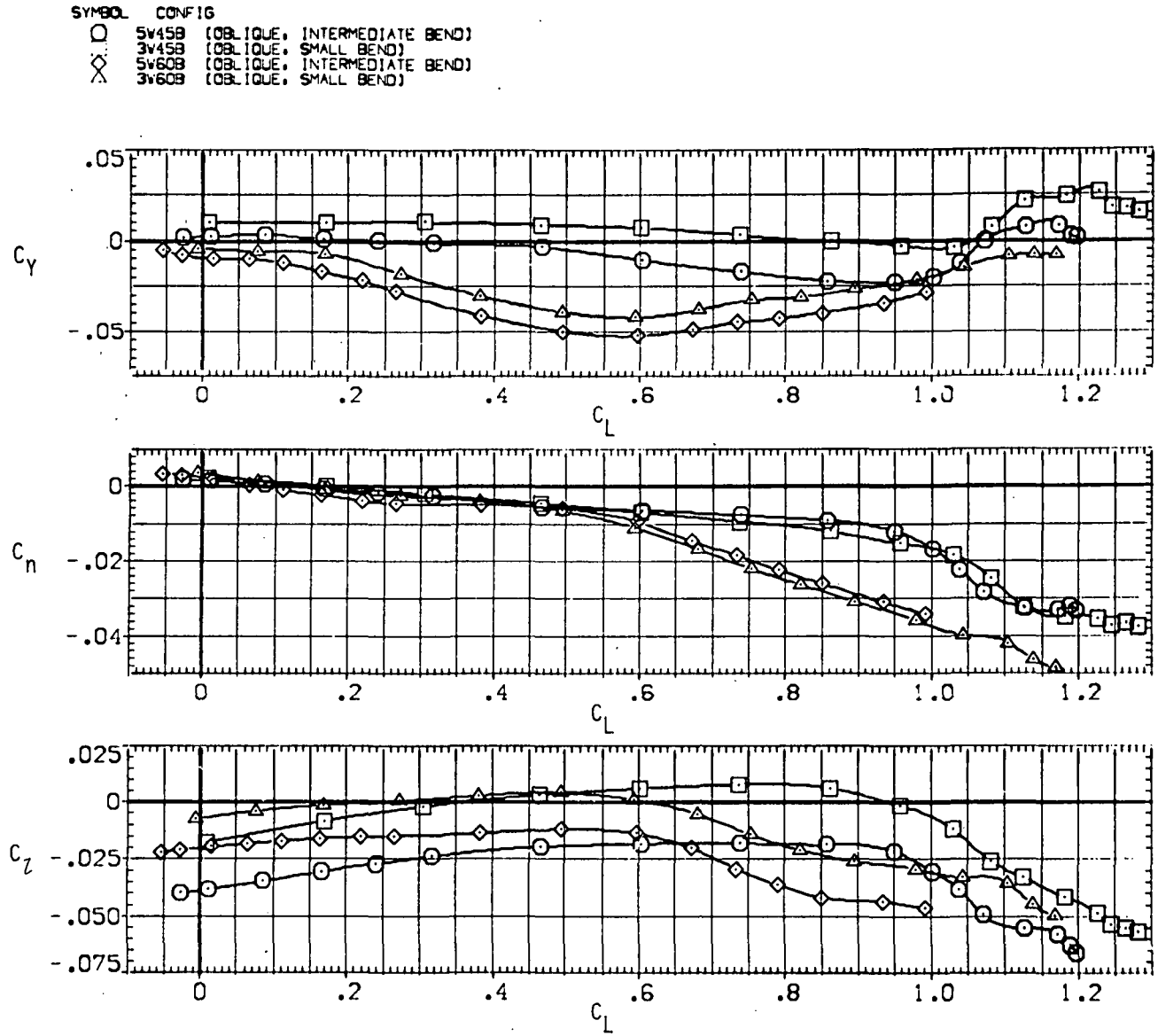

(f) C_Y, C_n and C_l versus C_L.

Figure 23.– Concluded.

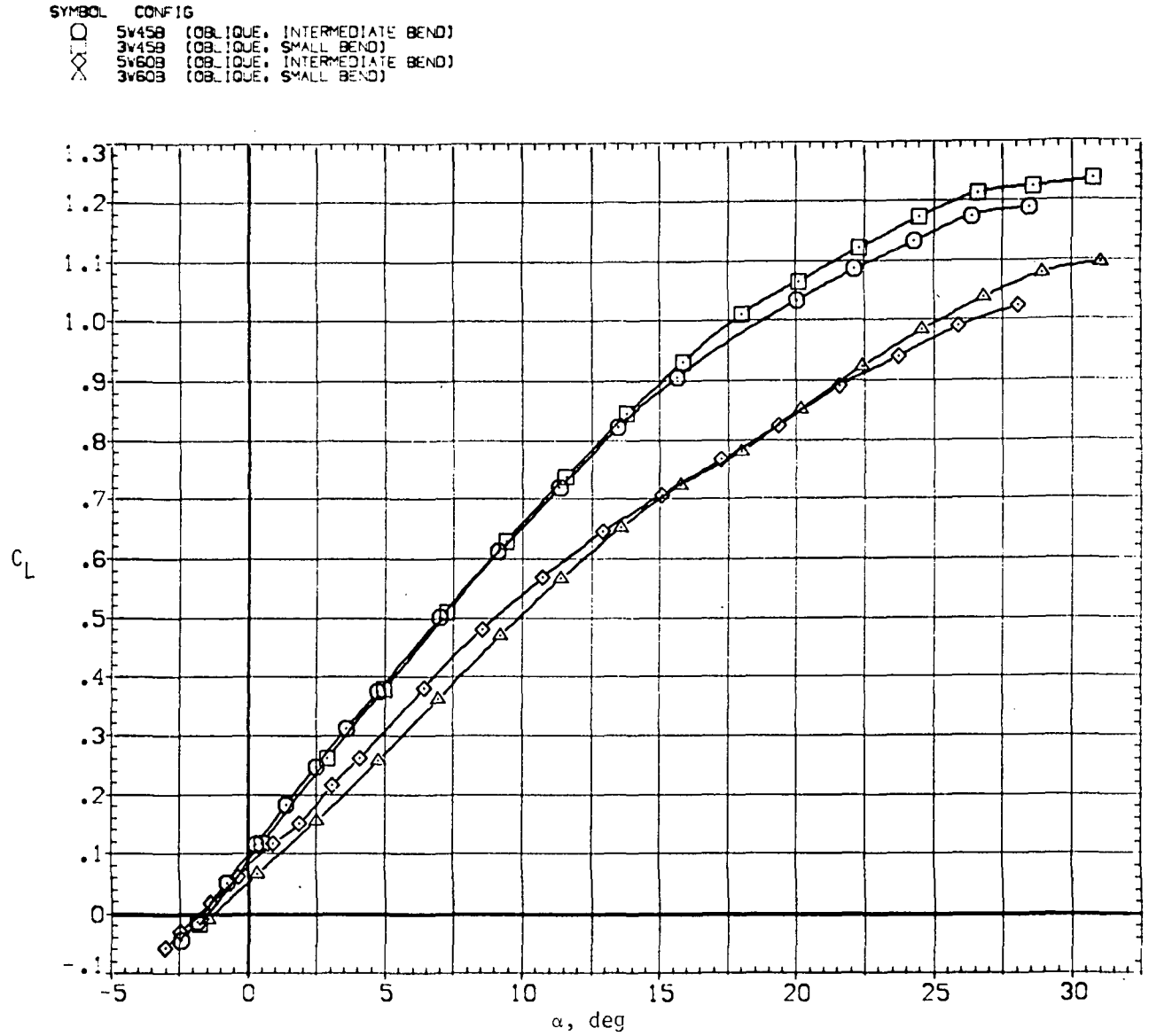

(a) C_L versus α.

Figure 24.– Effect of wing bend on the longitudinal stability characteristics of the oblique wing, $M = 1.4$.

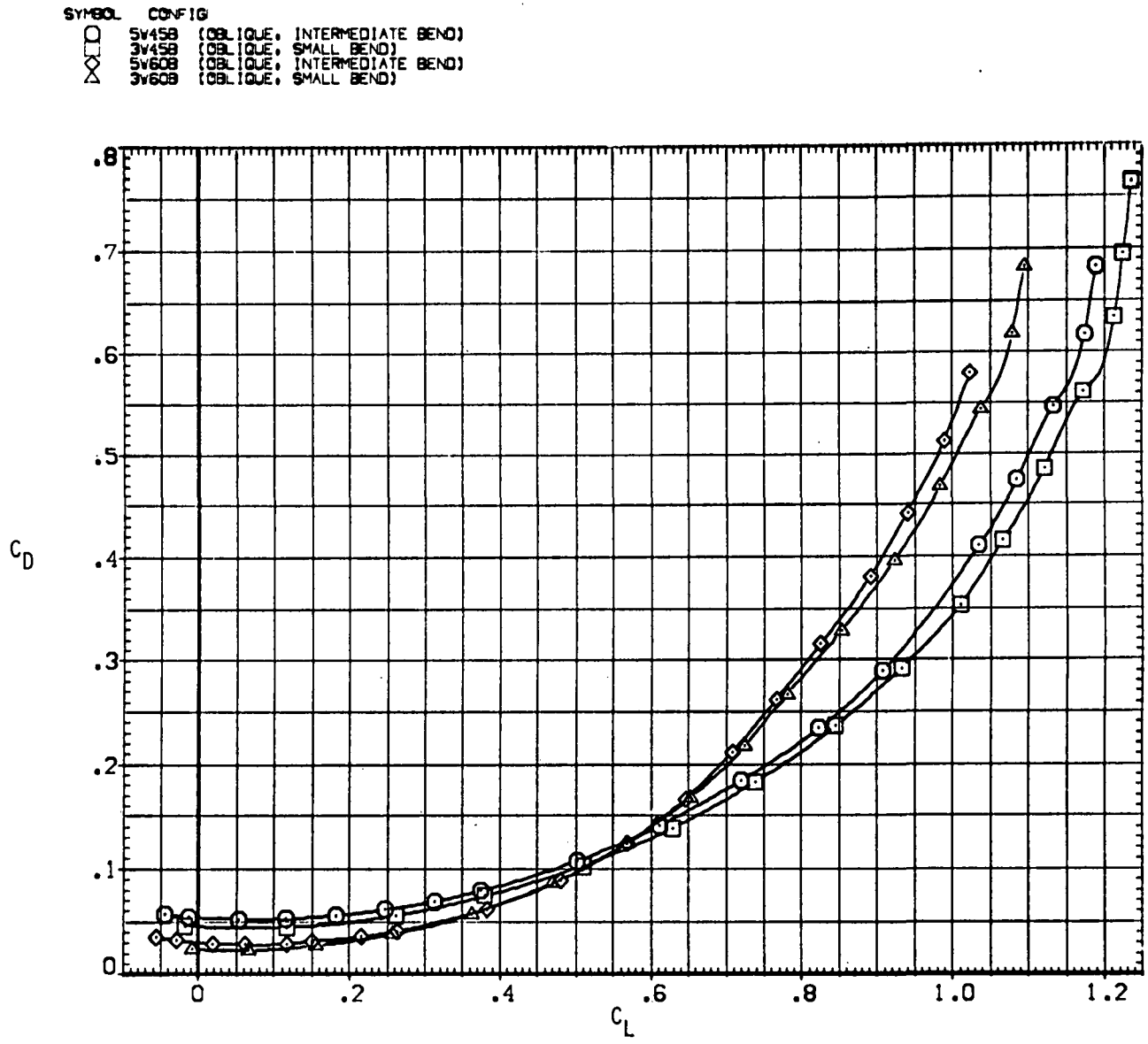

(b) C_D versus C_L.

Figure 24.– Continued.

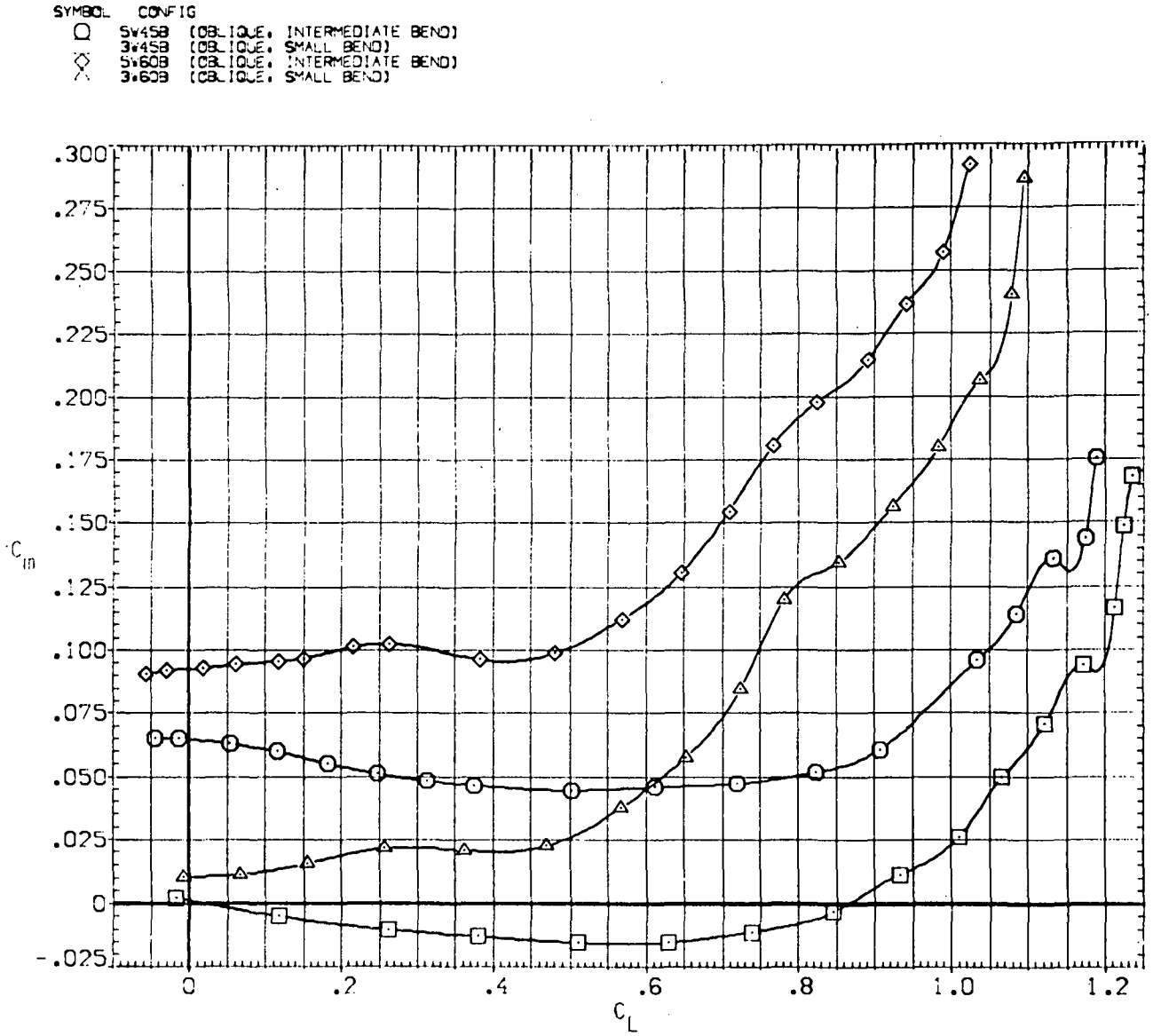

(c) C_m versus C_L.

Figure 24.– Continued.

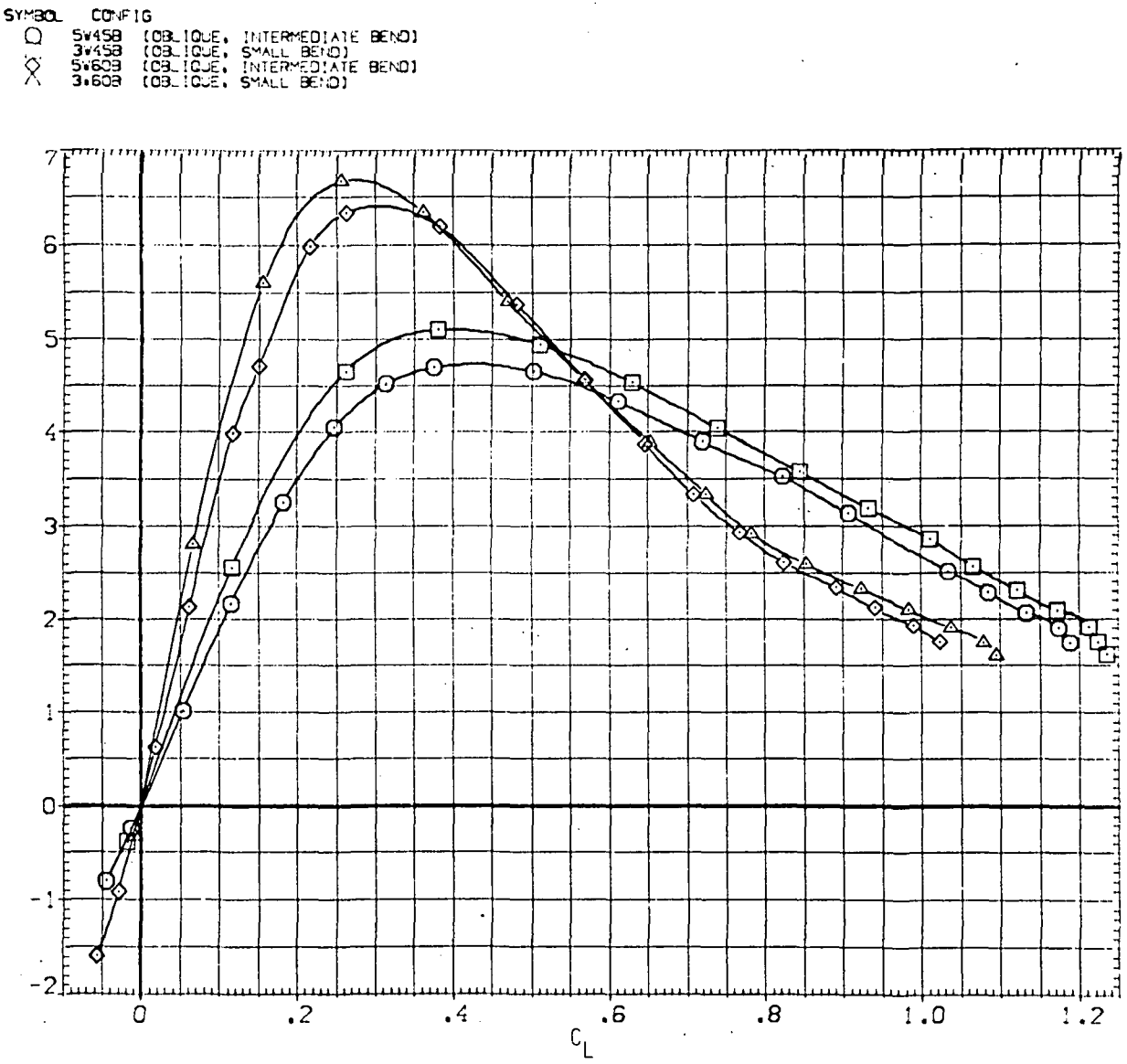

(d) L/D versus C_L.

Figure 24.– Continued.

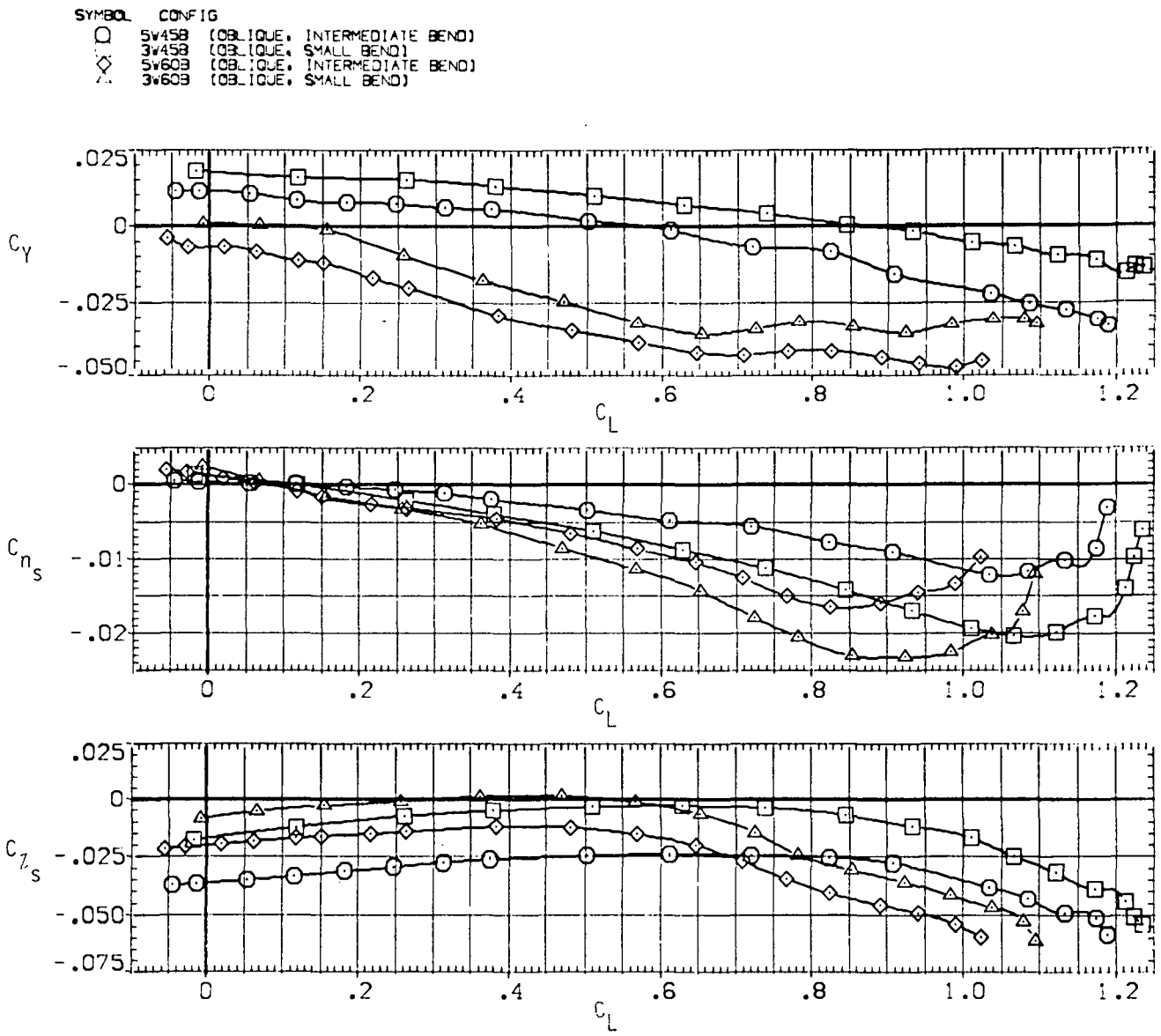

(e) C_Y, C_{n_s} and C_{l_s} versus C_L.

Figure 24.– Continued.

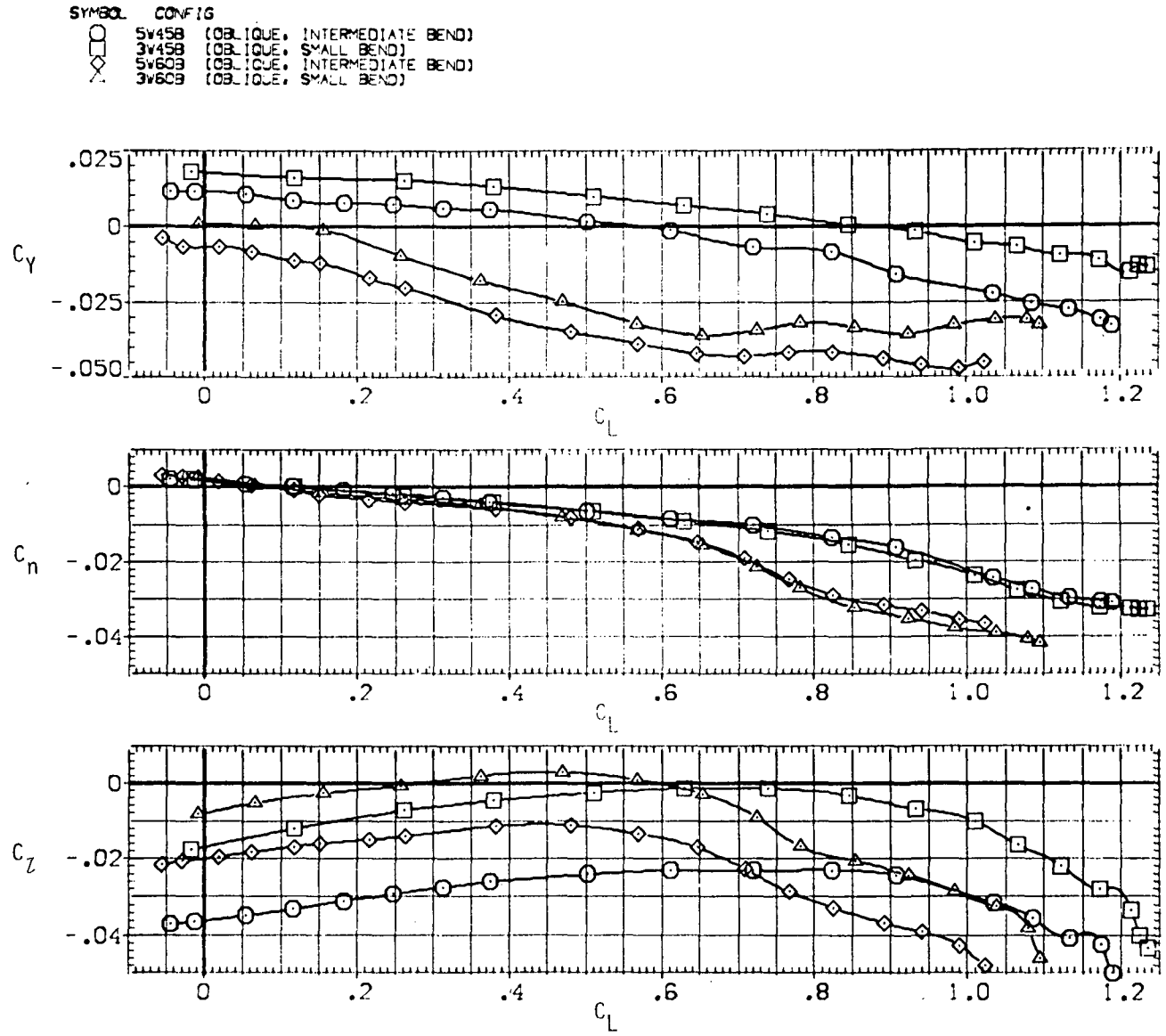

(f) C_Y, C_n and C_l versus C_L.

Figure 24.– Concluded.

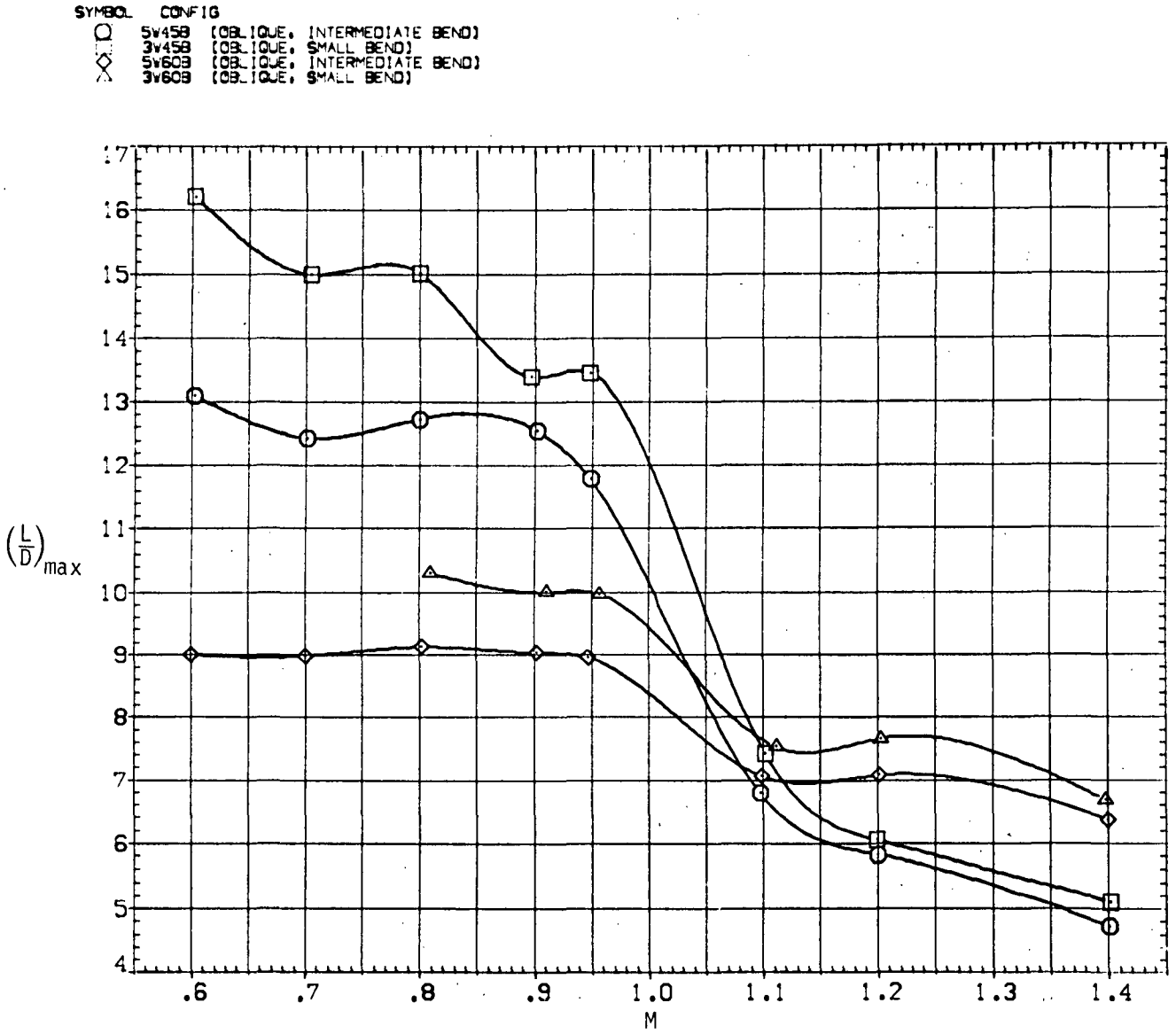

(a) $(L/D)_{max}$ versus M.

Figure 25.– Effect of wing bend on the summary of the longitudinal stability characteristics of the oblique wing, $\Lambda = 45°$ and $60°$.

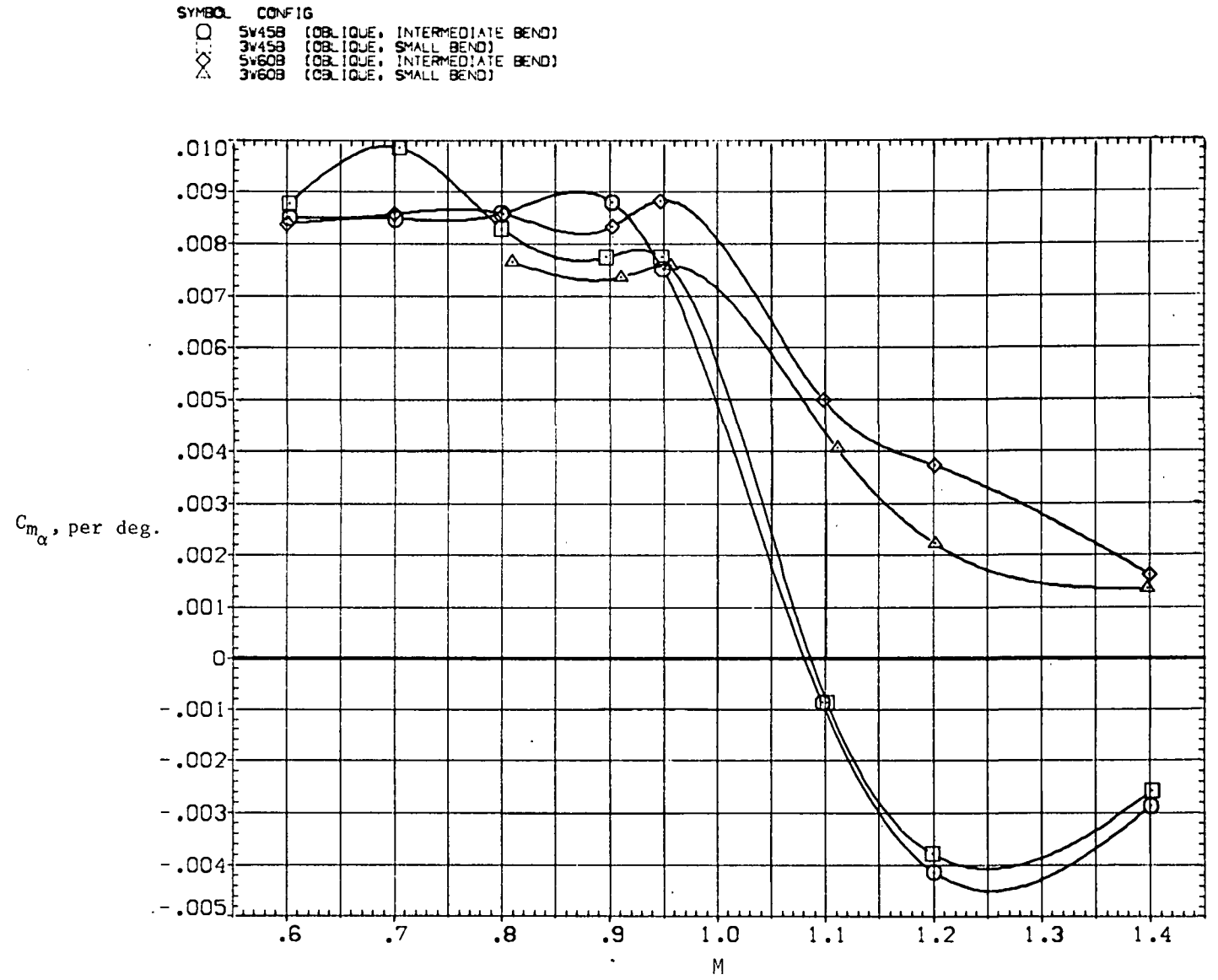

(b) C_{m_α} versus M.

Figure 25.– Concluded.

NATIONAL AERONAUTICS AND SPACE ADMINISTRATION
WASHINGTON, D.C. 20546

OFFICIAL BUSINESS
PENALTY FOR PRIVATE USE $300

SPECIAL FOURTH-CLASS RATE BOOK

POSTAGE AND FEES PAID
NATIONAL AERONAUTICS AND SPACE ADMINISTRATION
451

U.S.MAIL

POSTMASTER: If Undeliverable (Section 158 Postal Manual) Do Not Return

"The aeronautical and space activities of the United States shall be conducted so as to contribute . . . to the expansion of human knowledge of phenomena in the atmosphere and space. The Administration shall provide for the widest practicable and appropriate dissemination of information concerning its activities and the results thereof."

—NATIONAL AERONAUTICS AND SPACE ACT OF 1958

NASA SCIENTIFIC AND TECHNICAL PUBLICATIONS

TECHNICAL REPORTS: Scientific and technical information considered important, complete, and a lasting contribution to existing knowledge.

TECHNICAL NOTES: Information less broad in scope but nevertheless of importance as a contribution to existing knowledge.

TECHNICAL MEMORANDUMS: Information receiving limited distribution because of preliminary data, security classification, or other reasons. Also includes conference proceedings with either limited or unlimited distribution.

CONTRACTOR REPORTS: Scientific and technical information generated under a NASA contract or grant and considered an important contribution to existing knowledge.

TECHNICAL TRANSLATIONS: Information published in a foreign language considered to merit NASA distribution in English.

SPECIAL PUBLICATIONS: Information derived from or of value to NASA activities. Publications include final reports of major projects, monographs, data compilations, handbooks, sourcebooks, and special bibliographies.

TECHNOLOGY UTILIZATION PUBLICATIONS: Information on technology used by NASA that may be of particular interest in commercial and other non-aerospace applications. Publications include Tech Briefs, Technology Utilization Reports and Technology Surveys.

Details on the availability of these publications may be obtained from:

SCIENTIFIC AND TECHNICAL INFORMATION OFFICE

NATIONAL AERONAUTICS AND SPACE ADMINISTRATION

Washington, D.C. 20546